MODELING & ELECTROMAGNETIC ANALYSIS AND MEASUREMENT OF PARTICLE ACCELERATOR CAVITIES

By

SUMIT SOM
Enrolment No.ENGG04201004002
RF Division, Accelerator Technology Group
Variable Energy Cyclotron Centre, Kolkata-700 064

A thesis submitted to the
Board of Studies in Engineering Sciences
In partial fulfillment of requirements
For the degree of

DOCTOR OF PHILOSOPHY

of

HOMI BHABHA NATIONAL INSTITUTE
Bhabha Atomic Research Centre
Mumbai-400 085, India

January, 2016

Homi Bhabha National Institute

Recommendations of the Viva-Voce Board

As members of the viva-voce board, we certify that we have read the dissertation prepared by Sumit Som entitled **"Modeling & Electromagnetic Analysis and Measurement of Particle Accelerator Cavities"** and recommend that it may be accepted as fulfilling the dissertation requirement for the Degree of Doctor of Philosophy.

Chairman:	Prof. (Dr.) D. Sarkar	: Date: 08/01/2016
Guide/Convenor:	Alok Chakrabarti Prof. (Dr.) Alok Chakrabarti	: Date: 08/01/2016
Member1:	Prof. (Dr.) Vijay Sankar Pandit	: Date:
Member2:	Prof. (Dr.) Pitamar Singh	: Date: 8/1/2016
Member3:	Shri Subimal Saha	: Date: 8/1/2016
External Examiner:	D Kanjilal Prof. (Dr.) Dinakar Kanjilal	: Date: 08/01/2016

Final approval and acceptance of this dissertation is contingent upon the candidate's submission of the final copies of the dissertation to HBNI.

I hereby certify that I have read this dissertation prepared under my direction and recommend that it may be accepted as fulfilling the dissertation requirement.

Date: 08-01-2016
Place: VECC, Salt Lake, Kolkata

Alok Chakrabarti
Guide: Prof. (Dr.) Alok Chakrabarti

STATEMENT BY AUTHOR

This dissertation has been submitted in partial fulfillment of requirements for an advanced degree at Homi Bhabha National Institute (HBNI) and is deposited in the Library to be made available to borrowers under rules of HBNI.

Brief quotations from this dissertation are allowable without special permission, provided that accurate acknowledgement of source is made. Request for permission for extended quotation from of reproduction of this manuscript in whole or in part may be granted by the Competent Authority of HBNI when in his or her judgment the proposed use of the material is in the interests of scholarship. In all other instances, however, permission must be obtained from the author.

SumitSom

DECLARATION

I hereby declare that the investigation presented in this thesis has been carried out by me. The work is original and has not been submitted earlier as a whole or in part for a Degree/ Diploma at this or any other institution/ University.

SumitSom

LIST OF PUBLICATIONS

(arising out of the thesis work)

Journal:

1. "Design, Analysis and Multipacting Studies of 650 MHz, β=0.61 Superconducting RF Cavity", by Sumit Som, S. Seth, A. Mandal, S. Ghosh, *Indian Journal of Pure and Applied Physicsin Vol.53 (3), p.160-168 (2015).*

2. "Precision phase control for the radiofrequency system of *K*-500 superconducting cyclotron at Variable Energy Cyclotron Centre, Kolkata", by Sumit Som, Surajit Ghosh, Sudeshna Seth, Aditya Mandal, Saikat Paul, Suprakash Roy, *Review of Scientific Instruments in Vol.84, issue-11, 113303 (2013).*

3. "Radio frequency cavity analysis, measurement and calibration of absolute Dee voltage for *K*-500 superconducting cyclotron at VECC, Kolkata", by Sumit Som, Sudeshna Seth, Aditya Mandal, Saikat Paul, AnjanDuttagupta, *Review of Scientific Instruments in Vol.84, issue-2, 023303 (2013).*

Conferences/Symposiums:

1. "Development of 650 MHz Cavities for the GeV Proton Accelerator in Project-X", Invited Talk by Sumit Som, *Proceedings of the16th International Conference on RF Superconductivity (SRF-2013)* held in Paris, France during 23–27 September, 2013 (*p.1193*).

2. "Amplitude and phase controlled three-phase RF System of *K*-500 superconducting cyclotron with cavity analysis and measurement", Invited Talk by Sumit Som, *Proceedings of DAE-BRNS Indian Particle Accelerator Conference (InPac-2013)* held at VECC, Kolkata during Nov 19-22, 2013 (*p.91*).

3. "Multipacting Analysis on 650 MHz, beta=0.61 Superconducting RF Linac Cavity", by Sudeshna Seth, Sumit Som, A. Mandal, S. Ghosh, S. Saha, *Proceedings of DAE-BRNS Indian Particle Accelerator Conference (InPac-2013)* held at VECC, Kolkata during Nov 19-22, 2013 (*p.246*).

4. "A Journey Through The Indigenous Developments Of High Power CW RF Amplifiers And Cavities For Accelerators At VECC", Invited Talk by Sumit Som, *Proceedings ofNational Symposium on High Power RF & Microwave (HPRFM-2013)* held at IPR, Gandhinagar, Gujrat, during Sep 04-06, 2013 (*p.5*).

5. "Design and development of Efficient Broadband Combiner and impedance transformers", by Jai Shankar Prasad, Surajit Ghosh, Aditya Mandal, Sumit Som, *Proceedings of National Symposium on High Power RF & Microwave (HPRFM-2013)* held at IPR, Gandhinagar, Gujrat, during Sep 04-06, 2013 (*p.150*).

6. "Structural Design of 650MHz β=0.6 Superconducting Radio-Frequency Cavity" , by Pranab Bhattacharyya, Javed Akhtar, Chinmay Nandi, AnjanDuttagupta, Sumit Som, Gautam Pal, AlokChakraborty, *Proceedings of National Symposium on Cryogenics* held at IPR, Ahmedabad, during January 21-24, 2013.

7. "Bead-pull measurement using phase-shift technique in multi-cell elliptical cavity", by Sumit Som, Sudeshna Seth, Aditya Mandal, Surajit Ghosh, *Proceedings of 2nd International Particle Accelerator Conference (IPAC-2011)* held at Kursaal, San Sebastian, Spain, during September 4-9, 2011 (*p.280*).

8. “RF characterization and measurement of a full scale copper prototype of 5-cell elliptical shape Superconducting RF linac cavity", by S. Seth, Sumit Som, Aditya Mandal, *Proceedings of Indian Particle Accelerator Conference (InPac-2011)* held at IUAC, New Delhi during Feb 15-18, 2011 (*paper id: 207*).

9. “Design study on 650 MHz, high-β multi-cell elliptical shape superconducting RF linac cavity”, by S. Seth, Sumit Som, Aditya Mandal, *Proceedings of Indian Particle Accelerator Conference (InPac-2011)* held at IUAC, New Delhi during Feb 15-18, 2011 (*paper id: 208*).

10. “Advanced closed-loop trimmer control system for fine tuning the RF cavity of K500 Superconducting Cyclotron”, by Aditya Mandal, Surajit Ghosh, Sudeshna Seth, Sumit Som, S. Paul, P.R. Raj, S. Roy, S. Saha, R.K. Bhandari, *Proceedings of Indian Particle Accelerator Conference (InPac-2011)* held at IUAC, New Delhi during Feb 15-18, 2011 (*paper id: 240*).

11. “Upgradation of Radiofrequency system for the K130 room temperature cyclotron”, by Aditya Mandal, S. Seth, S. Som, S. Paul, P.R. Raj, P. Ganguly, S. Roy, S. Ghosh, S. Saha, U. Panda, R.K. Bhandari, *Proceedings of Indian Particle Accelerator Conference (InPac-2011)* held at IUAC, New Delhi during Feb 15-18, 2011 (*paper id: 243*).

12. “Commissioning experience of the RF system of K500 superconducting cyclotron at VECC”, S. Som, Saikat Paul, Aditya Mandal, S. Seth, S. Saha, R.K. Bhandari, P. Gangopadhyay, P.R. Raj, *Proceedings of 19th International Conference on Cyclotron and their Applications (Cyclotrons-2010),* held at Institute of Modern Physics, Lanzhou, China, during September 6 –10, 2010 (*p.162*).

13. “Closed loop RF tuning for superconducting cyclotron at VECC”, by Aditya Mandal, S. Som, S. Saha, Saikat Paul, S. Seth, R.K. Bhandari, P.R. Raj, B.C. Mandal, B.K. Das, U. Panda, *Proceedings of 19th International Conference on Cyclotron and their Applications (Cyclotrons-2010),* held at Institute of Modern Physics, Lanzhou, China, during September 6 –10, 2010 (*p.180*).

14. “Development of Power Supplies for 3-Φ, 240 KW RF System with Crowbar protection for Superconducting Cyclotron at VECC”, by S. K. Thakur, T. P. Tiwari, J. S. Prasad, A. De, Y. Kumar, S. Som, S. Saha, R. K. Bhandari, *Proceedings of 19th International Conference on Cyclotrons and their Application (CYCLOTRONS 2010),* held in Lanzhou, China, September 6-10, 2010 (*p.60*).

Workshops:

1. "Testing of inductive output tube based RF amplifier for 650 MHz SRF cavities", Aditya Mandal, Sumit Som, S.K. Manna, Surajit Ghosh, Sudeshna Seth, S.K. Thakur, S. Saha, Uma Shankar Panda, *9th International Workshop on Personal Computers and Particle Accelerator Controls (PCaPAC2012)* held at VECC from December 4-7, 2012.

2. "FPGA based amplitude control system for accelerating cavities",MadhusudanDey, Abhishek Singh, Aditya Mondal, Surajit Ghosh, Sumit Som, *9th International Workshop On Personal Computers and Particle Accelerator Controls (PCaPAC 2012)* held at VECC, 2012.

3. "Comparative Design study and Analysis of 650 MHz, beta=0.61 SCRF Cavity", Sumit Som, Sudeshna Seth, Aditya Mandal, Surajit Ghosh, *2nd International Workshop on Accelerator Driven Sub-critical Systems & thorium Utilization*, held at BARC, Mumbai during December 11–14, 2011.

Signature
(SumitSom)

Dedications

I dedicate this dissertation to my mother

Mrs. Bharati Som

ACKNOWLEDGEMENTS

I wish to express my sincere gratitude to my guide Dr. Alok Chakrabarti for his continuous encouragement, able guidance, inspiration and ample support during this research work. In particular, I would like to thank Dr. Chakrabarti, Associate Director (Accelerator), Variable Energy Cyclotron Centre, Department of Atomic Energy, Government of India, Kolkata, for sparing his valuable time with me in discussing many useful ideas regarding these activities and for many critical reviews of this manuscript.

I also wish to thank Dr. D. Sarkar, Dean-Academic-HBNI for Engineering Sciences, Variable energy cyclotron Centre, Department of Atomic Energy, Government of India, Kolkata, for encouraging me to pursue research related to my work at Variable Energy Cyclotron Centre, Kolkata.

I am extremely thankful to Dr. D.K. Srivastava, Director, VECC, Kolkata, and Dr. R.K. Bhandari, Former Director, VECC, Kolkata, for their valuable guidance and encouragement.

I would like to take this opportunity to thank all members of my doctoral committee and especially to Shri SubimalSaha, Head Accelerator Technology Group, VECC, Kolkata, for giving me valuable technical advices, discussions and encouragement.

I wish to thank entire VECC staff, especially, Shri Aditya Mandal, Smt. Sudeshna Seth and Shri Surajit Ghosh of RF Division, Variable Energy cyclotron Centre, Kolkata for their constant support and also the scientists/engineers from Fermilab, USA (under Indian Institutes Fermilab Collaboration) for valuable technical discussions.

This research work is supported by the Department of Atomic Energy, Government of India.

SumitSom

CONTENTS

Page No.

LIST OF ABBREVIATIONS:

RF	radio frequency
EM	electromagnetic
Hz	Hertz
kHz	kilohertz
MHz	megahertz
GHz	gigahertz
W	watt
kW	kilowatt
eV	electron volt
keV	kilo electron volt
MeV	million electron volt
GeV	giga electron volt
TM	transverse magnetic
TE	transverse electric
TEM	transverse electric and magnetic
DC	direct current
SRF	superconducting radio frequency
LINAC	linear accelerator
AVF	azimuthally varying field
SC	superconducting
NC	normalconducting
SCC	superconducting cyclotron
ppm	parts per million
kV	kilovolt
MV	million volt
P/S	power supply
dB	decibel
I&Q	in-phase & quadrature
I/Q	in-phase /quadrature
PLC	programmable logic controller
RLC	resistive inductive and capacitive
VNA	vector network analyzer
GPIB	General Purpose Interface Bus
LAN	local area network
GUI	graphical user interface
MPa	mega-pascal
GPa	giga-pascal
OFHC	oxygen free high conductivity
VECC	Variable Energy Cyclotron Centre
JLab	Jefferson Laboratory, USA
Fermilab	Fermi National Accelerator Laboratory, USA
TAMU	Texas A &M University, USA
MSU	Michigan State University, USA
MOPA	master oscillator power amplifier
mm.	millimeter
DDS	direct digital synthesis
LLRF	low-level radio frequency
IC	integrated circuit
mA	milliampere
μS	microsecond
μm	micrometer
VSWR	voltage standing wave ratio

PID	Proportional Integral Derivative
PI	Proportional Integral
EPICS	Experimental Physics and Industrial Control System
FIT	finite integration technique
2D	two dimensional
3D	Three Dimensional
CST	Computer Simulation Technologies
Be-Cu	Berrylium-Copper
HV	High Voltage
ASME	The American Society of Mechanical Engineers
BCP	Buffered Chemical Polish
EP	Electro-polish
QWR	Quarter wave resonator
HWR	Half wave resonator
LFD	Lorentz Force Detuning
FPC	Fundamental Power
Coupler	
PLL	Phase Locked Loop
mT	milli-Tesla
HOM	Higher Order Mode
ADSS	Accelerator Driven Subcritical System
CW	Continuous Wave
PC	Personal Computer
USB	Universal Serial Bus
CdTe	Cadmium telluride
PIP	Proton Improvement Plan

SYNOPSIS

Particle Accelerator is one of the most important scientific instruments and probably one of the most fascinating tools for scientific research on high energy physics. The accelerator has enormous potential to reach into the sub-atomic world. Besides scientific research, millions of global population could also avail the facility of getting high class medical treatment by using particle accelerators, like cyclotrons, linacs etc.

Except low energy DC accelerators, all modern accelerators accelerate ion beams using radiofrequency (RF) power. The design of resonant cavities at frequencies ranging from a few MHz to a few GHz is thus an essential part of any particle accelerator design. The RF design is not trivial. It needs to ensure that the right RF mode is generated in the accelerating zone and other undesired electromagnetic modes are minimal at the operating frequencies. The design becomes even more challenging in cyclotrons having multiple accelerating electrodes (or "dees") in which each dee becomes a part of the resonator having perfect phase relationship with the other dees powered by the separate RF amplifiers, but fed from the same low power RF source. In this work, one major portion deals with the design and development of the RF system for the *K*500 Superconducting Cyclotron at VECC, Kolkata. The other major part deals with the design of 5-cell, 650 MHz, β=0.61 superconducting cavity for the acceleration of proton from 177 MeV to 480 MeV. This will be one of the sections of the 1 GeV Proton linear Accelerator planned for the Accelerator Driven Subcritical System (ADSS) programme of DAE, pursued jointly with Fermi National Accelerator Laboratory (FNAL), USA.

The design, analysis, development and measurement of RF parameters for high power RF cavitiesfor*K500* superconducting cyclotron (SCC) have many difficulties and complexities as it has to maintain phase stability within ± 0.1 degree, especially, with wide dynamic range (± 180 degree) of phase correction, between any two cavities in continuous-wave (CW) mode at high RF power within a frequency range of 9 to 27 MHz.The analog type in-phase/quadrature (I/Q) modulation technique is generally used in such type of RF systems for the accelerators. The main disadvantage of this technique is that the dynamic range of automatic phase correction is narrow (within ± 25 degree). The present automatic phase control system has the design feature of having both analog in-phase/quadrature (I/Q) modulator based phase regulator and Direct Digital Synthesis (DDS) based phase shifter in order to achieve both faster response and wide dynamic range (± 180 degree) as well. Moreover, unlike conventional phase controller loop used for each of the three-phase RF system, the present phase control system has the option to change the relative phase difference between any two RF cavities and therefore, only two phase controller loops, instead of three, are required to be used for the three-phase RF system.

The modeling and simulations of the complete RF cavity with a very complicated geometry have been performedusing Finite Integration Technique (FIT), which provides a universal spatial discretization scheme applicable to various electromagnetic problems ranging from static field calculations to high frequency applications in time domain or frequency domain.

Another important feature is the measurement of the amplitude of accelerating RF voltage, without perturbing the cavity fields significantly, thus keeping the resonance characteristics of the cavities almost undisturbed. An indirect and different method using continuous X-ray spectrum (called "Bremsstrahlung") has been employed to measure RF voltage, fairly accurately (within ± 1.5 kV) and quite reliably. The field emitted electrons, accelerated by the RF field, from one electrode impact on the other electrode, the energy of accelerated electrons is transferred to the atoms of electrode material. The electromagnetic radiation takes place by the transition of atomic inner electrons, resulting inthe generation of

X-ray with continuous energy spectrum. The maximum electron energy corresponds to the peak value of Dee voltage. When the electrons collide with the atoms of electrode's material, the transferred energies to the atoms are from zero to the maximum kinetic energy of the accelerated electrons. Detecting the end-point or the maximum energy of the X-ray spectrum, the peak voltage of the RF cavity has been determined.

The superconducting RF (SRF) cavities have enormous potential in building the present-day energy frontier accelerators. The quest of higher and higher energy of a beam of ions has become the necessity for the future energy frontier accelerators. The design of superconducting cavities at various ion velocity ranges require optimization of various parameters defining the RF cavity that ensures proper electric and magnetic field distribution and the mechanical rigidity, the number of cells in the cavity and higher order mode suppression.

The electromagnetic design of a 650 MHz five-cell elliptical cavity has been carried out forβ = 0.61 to be operated at temperature 2K for the proposed 1GeV, 2mA proton linear accelerator in India. The cavity various features such aswide aperture (96 mm) for better acceptance and moderate value of wall slope angle (2.4 degree for mid cells and 4.5 degree for end cells) for better mechanical structural strength and also better accessibility for surface processing. This design could achieve the desired normalized peak surface electric and surface magnetic fields well within the limits, along with better field flatness, and higher value of shunt impedance.

When the ion beam passes through the cavity, the beam induced higher order modes (HOMs) create problems. The detailed investigation of the existence of transverse and longitudinal HOMs of the cavity has been carried out.

Multipacting or Resonant Field Emission analysisisalso important for SRF cavities. 2D Multipacing analysis with simplified model of secondary electron emission, shows no probability of multipacting. However, more rigorous 3D analysis, based on Furman model, which takes into account three kinds of secondary electron emissions –true secondary, elastic back scattered secondary and rediffused secondary electrons, for 650 MHz, β=0.61, SRF cavity, exhibitstrong multipacting possibility within a specific electric field region. Actually, the elastic back scattered and rediffused secondary electrons change the situation drastically and a small convexity in the equator region suppresses the multipacting significantly. This isprobablybecause the remaining electric field lines at the equator region vanishes due to this convexity as the electric field lines cannot be parallel to the metal boundaries. However, the convexity does not change the other cavity parameters, like, peak surface fields, quality factor, R/Q etc. This small convexity gets automatically introduced during electron beam welding, which is thus useful for suppressing multipacting.

Besides these, a fully automated bead pull measurement system, with special feature of using phase-shift technique instead of frequency shift, has been designed and developed to measure the electric fields along the cavity beam axis.

Organization of the chapters in the thesis

The thesis comprises of five chapters. An outline of the individual chapter is presented below.

Chapter 1:

Introduction to particle accelerators and RF cavity

This chapter gives an introduction and research scope in particle accelerators and RF cavities. The need for RF in accelerators and also the RF cavities in particle accelerators are illustrated. The chapter also discusses thoroughly the fundamentals of RF cavity and its theoretical background. The metamorphosis of RF cavity, starting from a simple LC resonant circuit to the formation of a closed resonant cavity, is explained in this chapter. The definitions along with general formula of various RF parameters of a cavity are mentioned in brief.

Chapter 2:

Normal conducting RF for accelerators

This chapter gives detailed design and analysis of normal conducting (copper) transverse electromagnetic (TEM) class cavities along with its low-level closed-loop amplitude and phase controller system, especially, for the three-phase RF system of $K500$ Superconducting cyclotron developed at the Variable Energy Cyclotron Centre (VECC), Kolkata. Each of the three high power coaxial type half-wavelength TEM-mode cavities operates within a frequency range of 9 to 27 MHz. The maximum accelerating voltage being developed in the accelerating electrode located at the median plane of the cyclotron is 80 kV at 27 MHz with maximum delivered RF power of 80 kW for each cavity. The detail simulation and analysis of the cavity using 3D electromagnetic codes have been illustrated here. The variation of RF voltage along the accelerating electrode, due to its length comparable to the operating wavelength, is an important aspect for this type of cavity.

The real-time measurement of quality factor of the cavity,under pulse mode operation, by measuring the cavity voltage time constant, is discussed in this chapter. Also, an indirect measurement technique of the absolute accelerating RF voltage,by detecting the end-point or the maximum energy of continuous X-ray spectrum or "Bremsstrahlung" by the transition of atomic inner electrons, due field emitted (FE) electrons accelerated by the RF field from one electrode impact on the other electrode,has been elaborated here.

A brief discussion on the design and development of stepper motor controlled coarse frequency tuning system and hydraulically driven fine frequency tuner or trimmer for the RF cavity has been made.

The detail design aspects of the amplitude controller to achieve 10 ppm voltage stability and also the phase controller with stringent requirement of $\pm$ 0.1 degree phase stability (with wide dynamic range of phase correction) along with unique features of having a combination of both analog I/Q modulator and Direct Digital Synthesis based phase regulator to achieve both faster response and wide dynamic range, is explained thoroughly.

Besides these, the design and development aspects of high power RF amplifiers/transmitters operating in the frequency range of 9 to 27 MHz, for feeding power to the main cavities, have been discussed in this chapter.

Chapter 3:

Superconductivity in accelerators

This chapter focuses on the basics of superconductivity and also the RF superconductivity along with the basic concepts of Residual Surface Resistance and BCS Surface Resistance and its dependence on various parameters, as obtained from literature surveys. Also, the various types of superconductors and the advantages of superconducting RF cavity have been discussed here.

Chapter 4:

Superconducting RF cavity design

This chapterdiscusses the design aspects of TM-class superconducting RF cavity, especially, for its operation in medium-β region. A brief discussion on low beta TEM- class cavities like, half-wave resonator (HWR), quarter-wave resonator (QWR) etc. is also made for the sake of completeness. The various cavity parameters for medium-β cavity and also the influence of cell geometry on RF parameters for the medium-β cavity have been discussed thoroughly.

A new electromagnetic design of a five-cell TM-class elliptical cavity operating at 650 MHz for β = 0.61 region for the 1 GeV, 2 mA proton linear accelerator, is discussed here. The design aspects of elliptical and re-entrant shape cavities have been compared and the final cavity selection for the target accelerating gradient of 17 MV/m is done.

A thorough investigation of the existence of transverse and longitudinal higher order modes (HOMs) of the cavity, to be operated with proton beam current of 2 mA, is carried out.

As one of the major limitations of SRF cavities is Multipacting or Resonant Field Emission, the detail 2D Multipacting analysis with simplified model of secondary electron emission, and also 3D Multipacting analysis based on Furman model considering true secondary, elastic back scattered secondary and rediffused secondary electrons, for 650 MHz, β=0.61, SRF cavity have been done.

The mechanical modal analysis of the cavity (using 3D Finite Element Model) determines that the natural frequencies of mechanical modes without stiffener are present below 100 Hz, which is not desirable for operation. Because, in that case the cavity may get detuned due to any low frequency vibrations. However, the preliminary analysis with 3D ANSYS Code suggests that the cavity with stiffener placed at the radius of 133 mm, pushes the modal frequencies to above 100 Hz. The SRF cavity is subjected to cryogenic temperature (2K) and external pressure under operating conditions. The simulation and structural analysis of the cavity has been carried out using 3D ANSYS code, assuming operating temperature at 2K and external pressure of 3 atm (which is much higher compared to the operating pressure), with boundary conditions of both ends being fixed. The analysis indicates that the cavity with 4 mm. thick niobium sheet is structurally stable.

The design and development of a fully automated bead pull measurement system, using phase-shift technique instead of frequency shift, have been discussed in this chapter.

Chapter 5:

Summary and discussions

This chapter summarizes the work and discusses the salient conclusions of the results. The material contained in the thesis is mainly elucidation of work reported in the following list of publications by the author.

LIST OF FIGURES:

LIST OF TABLES:

CHAPTER-1

INTRODUCTION

1.1 Research Institution

The work performed in this thesis has been done in support of Variable Energy Cyclotron Centre (VECC), Department of Atomic Energy, Government of India, Sector-1, Block-AF, Bidhan Nagar, Kolkata – 700 064, State-W.B., India.

1.2 Research Scope

This dissertation has developed and applied to the design and analysis of the coaxial cavity and the measurement of absolute accelerating voltage using 'bremstrahllung' X-ray method for the radio-frequency cavity structure of accelerators and also developed low-level RF controls and applied to the design of precision phase control with wide dynamic range of phase correction between any two high power RF cavities of particle accelerators. The present automatic phase control system has a design feature of having both analog in-phase/quadrature (I/Q) modulator based phase regulator and Direct Digital Synthesis (DDS) based phase shifter in order to achieve both faster response and wide dynamic range (± 180 degree) as well. Moreover, unlike conventional phase controller loop used for each of the three-phase RF system, the present phase control system has the option to change the relative phase difference between any two RF cavities and therefore, only two phase controller loops, instead of three, are required to be used for the three-phase RF system.

The dissertation will also enable to proceed further in the design and development of multi-cell superconducting RF cavities to be used for giga-electron volt (GeV) range proton linear accelerator. In particular, this research and development activity is applied to predict and document the design and analysis of multi-cell superconducting RF linear accelerator cavity operating in the medium-β region.

Department of Atomic Energy, Government of India has proposed to build Indian Spallation Neutron Source (ISNS) and Indian Accelerator Driven Sub-critical System (IADSS), which are basically particle accelerators(pulsed/CW) with high energy (~1 GeV) and high current (~ 2 mA or higher) proton beam. When high energy and high current proton beam hits the target of heavy element, such as thorium (Th), plutonium (Pu) or uranium (U) etc., spallation neutron is produced. Spallation target is surrounded by a blanket assembly of nuclear fuel (such as ${}_{90}Th^{232}$, a fissile isotope) which, by emitting two β-particles, breeds to ${}_{92}U^{233}$ and sustaining fission chain reaction takes place. Since a significant portion of these accelerators call for several numbers of superconducting RF(SRF) cavities, with different $\beta(=\frac{v}{c}=\frac{\text{speed of electromagnetic wave}}{\text{speed of light}})$ as well,proper modeling and electromagnetic analysis is necessary as a feasible method of designing the cavities.

This dissertation will concentrate on a new electromagnetic design of a five-cell elliptical shape superconducting RF cavity to be operated at 650 MHz, and at temperature 2K in$\beta = 0.61$ region for the proposed 1GeV, 2mA proton linear accelerator. The cavity features are comprised of wide aperture (96 mm) for better acceptance and moderate value of wall slope angle (2.4 degree for mid cells and 4.5 degree for end cells) for better mechanical rigidity and also better accessibility for surface processing. The design would achieve desired target values of normalized peak surface electric and peak surface magnetic fields well within the maximum limits, along with better field flatness, and higher value of shunt impedance ensuring less cryogenic load.

1.3 Need for RF in accelerators

In an accelerator, charged particles or ions of various elements are desired to be accelerated to higher energy. In order to impart energy to the charged particle, it is necessary to let the ion move across a region of high electric field, which is developed in the direction towards the desired motion of the charged particle. The energy gain (ΔE) of the charged particle is given by the following equation.

$$\Delta E = \int \vec{F}.d\vec{s} = q\int \vec{E}.\vec{v}dt$$

[Where, $\vec{F}$= Lorentz force acting on the charged particle,$\vec{s}$ = Displacement of the particle in motion, q = Charge of the particle, $\vec{E}$ = Electric field, $\vec{v}$ = velocity of the particle = $\frac{d\vec{s}}{dt}$, t =time].

It is to be noted that the generalized form of Lorentz force [1] on a charged particle under both electric and magnetic fields is given by,

$$\vec{F} = q\vec{E} + q\vec{B} \times \vec{v} \text{[where, } \vec{B} \text{ is the magnetic field]}$$

In a particle accelerator like cyclotron (as shown in Fig.1.3.1), the direction of magnetic field ($\vec{B}$) is perpendicular to the direction of the motion ($\vec{v}$) of the particle and so the ($\vec{B} \times \vec{v}$) component also is perpendicular to both $\vec{B}$ and $\vec{v}$. Hence the contribution of force due to magnetic field in the Lorentz force equation is zero and thus the Lorentz force toward the particle motion becomes $\vec{F} = q\vec{E} + \vec{0} = q\vec{E}$.

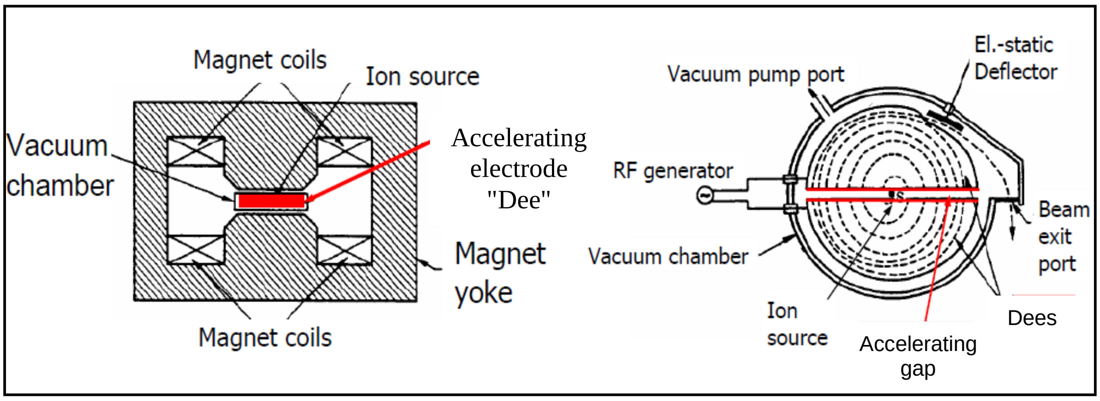

Fig.1.3.1 A cross-sectional view of classical cyclotron and simplified view of a cyclotron with most essential parts [2]

In accelerators, Radio-frequency (RF) system produces a region filled with electromagnetic (EM) energy and this energy is partially transferred to the charged particles while crossing this region. A high power RF transmitter (or amplifier)supplies the necessary RF power, through a Coupler, to the resonant cavity.

1.3.1 RF Cavity in Particle Accelerator

In particle accelerators (such as linear or cyclic accelerators), charged particles or ions are accelerated by crossing strong synchronized electric fields, several times. To maintain the electric fields efficiently and to synchronize the electric fields, RF cavities or resonators are required. The parallel resonant circuit with lumped components (e.g., inductors, capacitors, resistors) cannot be used in place of resonant cavities, because at high power applications a very low inductance with very high quality factor is necessary. Cavities are integral part of many particle accelerators that require fast time varying synchronized accelerating voltage. The resonant cavities are used to efficiently develop high voltages at the gaps of the accelerating electrodes and the charged particles, while crossing through these gaps, get accelerated. To develop high electric fields at the accelerating gaps, without using resonant cavities, would require the energy stored in electric fields to be removed as heat in each cycle. In resonant cavities, the stored energy alternates between electric and magnetic energy each RF cycle rather than being dissipated as heat. For example, the *K*500 Superconducting Cyclotron at VECC (as shown in Fig.1.3.1.1), Kolkata, has three resonant cavities operating in the frequency range of 9to 27 MHz and can develop peak accelerating voltage of 80 kV (maximum at the highest frequency)at the accelerating gap consuming RF power of 64kWper cavity at 27 MHz.

Fig.1.3.1.1 *K*500 Superconducting Cyclotron at VECC, Kolkata, India.

1.3.2 Fundamentals of RF cavity

It is understood from Lorentz Force equation (given in section 1.3) that an accelerating cavity needs to provide an electric field ($\vec{E}$) in the direction of the motion of the charged particle. However, magnetic field ($\vec{B}$) does not provide any acceleration, but provides bending of the charged particle in case of cyclic accelerator (cyclotron). Now the question arises - what about DC electric field?

DC electric field can provide energies only up to a few MeV (million electron-volt).[1 eV= 1.6 x 10^{-19} Joule (approx.)]. The energies of charged particles beyond a few MeV can be obtained only by transfer of energies from travelling waves to generate standing waves in resonant circuits and then to the particles being accelerated. The energy from a wave can be transferred to particles efficiently, only if both propagate at the same velocity.

In case of linear accelerator (linac), RF cavity works in Transverse magnetic (TM) mode, where the direction of magnetic field ($\vec{B}$) is perpendicular or transverse to the direction of propagation of the particle and the direction of electric field ($\vec{E}$) is longitudinal to the direction of propagation. TM-class cavity is considered as mode transformer converting from transverse electromagnetic mode (*TEM)* to transverse magnetic mode (TM), because the RF power, originating from high power RF amplifier, passes through the rigid coaxial transmission line (operating in TEM mode) and then is fed to the cavity (operating in TM mode) in order to develop high electric field gradient at the accelerating gaps. The cavity is also considered as an impedance transformer as the RF power is fed from the generator having low output impedance (generally, 50 Ohm) to the cavity with high shunt impedance (a few tens of kΩ to

MΩ). The higher the shunt impedance of the cavity, the less is the power dissipation in the cavity wall.

$$P_{diss} = \frac{{V_P}^2}{2R_{sh}} = \frac{\left(\frac{V_P}{\sqrt{2}}\right)^2}{R_{sh}}$$

[where, P_{diss} is the power dissipationin the cavity wall, V_P is the peak accelerating voltage and R_{sh} is the shunt impedance of the cavity].

The cavity is a space under vacuum (~ 1 x 10^{-8} mbar or better) enclosed by normal conducting (copper)(as shown in Fig.1.3.2.1(a))or superconducting (niobium) walls and it can sustain an infinite number of resonant electromagnetic modes (as shown in Fig.1.3.2.1(b)). However, a particular cavity shape is designed to make so that only the desired mode is excited and can efficiently transfer its energy to the charged particles (or ions) being accelerated. An isolated mode can be modeled by an RLC circuit. The metamorphosis of the resonant cavity is discussed below[3].

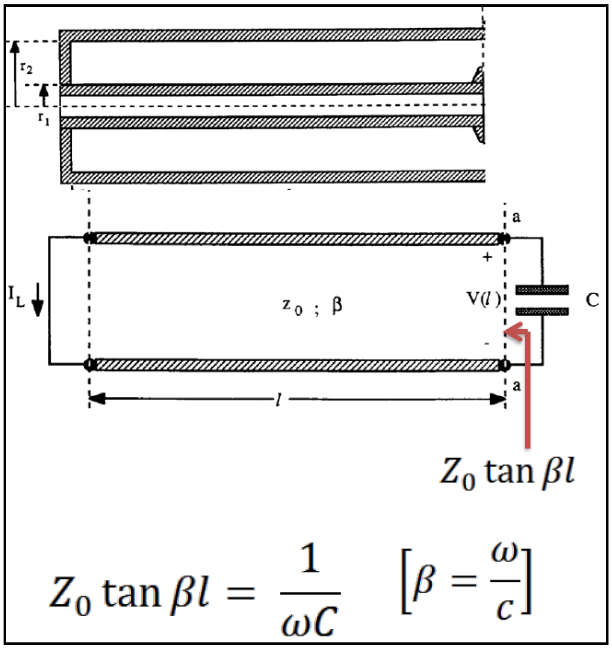

Fig.1.3.2.1 (a)One-end short circuited coaxial cavity with length 'ℓ', characteristic impedance 'Z_0', phase constant 'β', open end capacitance 'C', angular frequency 'ω', wave propagation velocity 'c'[3]

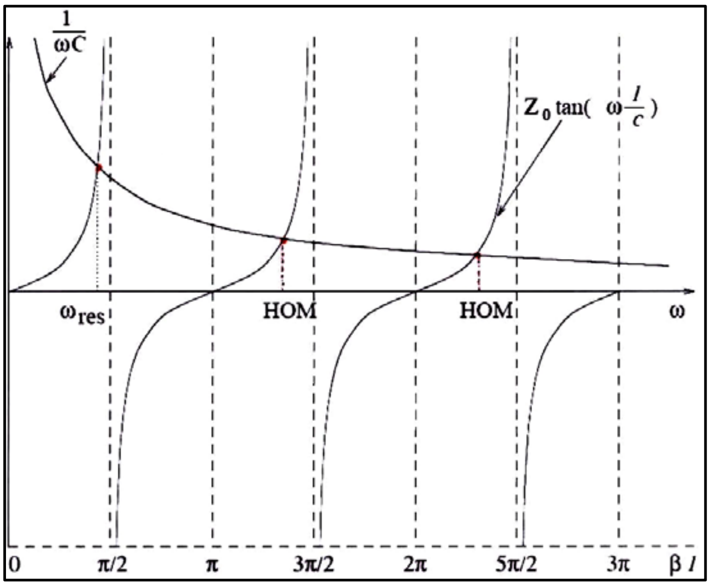

Fig.1.3.2.1 (b)Plot of $Z_0 \tan \beta l$ vs. ω and also plot of $\frac{1}{\omega c}$ vs. ω of one-end short circuited coaxial transmission line. The intersect points of these two plots show that there are infinite number of modes existing in a cavity

If we consider [3] two equal round discs made from copper (a perfect conductor), axially separated by a very small gap and with a negligible hole area. The two discs (as shown in Fig.1.3.2.2(a)) form a capacitor with capacitance value "C". If this capacitor is charged then we can simply say that the lines of force of the electric field are nearly uniform at the inside and spread outside to have zero intensity at infinity. Now, if two discs are connected with a copper loop (as shown in Fig.1.3.2.2(b)) having inductance value "L", a parallel resonant circuit is formed with a resonant frequency, $f_1 (\approx \frac{1}{2\pi\sqrt{LC}})$, power dissipation being considered very small and negligible.

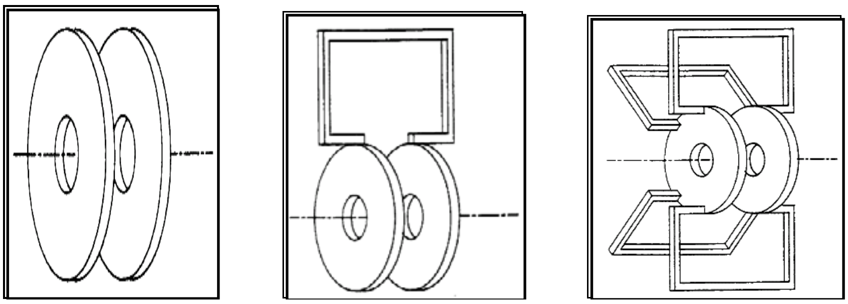

(a) (b) (c)

Fig. 1.3.2.2 The figure represents (a) two discs; (b) two discs connected with a loop; (c) two discs connected with four loops[3].

Next, if one more loop, equal and opposite to the first one, is added (as shown in Fig.1.3.2.2(c)),the resonant frequency will be f_2 ($=\frac{1}{2\pi\sqrt{\frac{L}{2}.C}} = \sqrt{2}f_1$),ignoring the small mutual coupling between the two loops. If the number of loops is kept on increasing and for 'n' number of loops the resonant frequency (f_n) will not be $f_n = \frac{1}{2\pi\sqrt{\frac{L}{n}.C}} = \sqrt{n}f_1$, as expected. Because there will be significant mutual couplings between the loops and cannot be ignored. So, increasing the number of loops tends to increase the inductance of each loop together with their mutual couplings, instead of reducing the total inductance due to parallel combination. So, when the loops are well separated, magnetic lines of force (as shown in Fig.1.3.2.3(a))very weakly (or does not) interact with each other. But, when the loops are very close to each other, magnetic lines of force (as shown in Fig.1.3.2.3(b))strongly interact with each other trying to enhance the field inside and to cancel the field between the wires.

The closed cavity means the infinitely large number of loops and therefore, the resonant frequency of the closed cavity increases, of course, within a limit. The electromagnetic fields remain confined inside the dielectric volume of the cavity made of perfect conductor and consequently, the electromagnetic fields are not radiated.

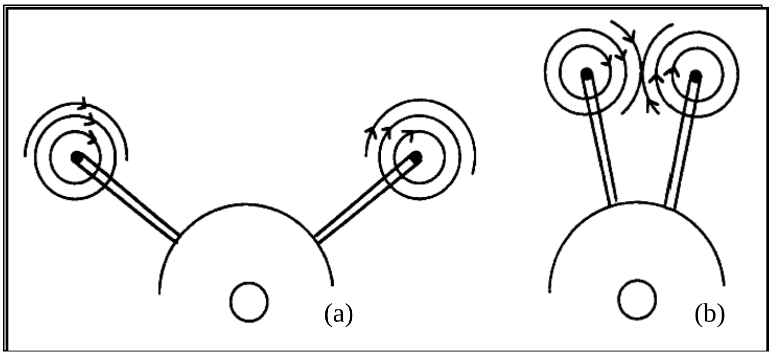

Fig.1.3.2.3 The figure represents (a) two loops well separated; (b) two loops very close to each other[3]

The basic resonant cavity is a “pill-box” cavity[4].For the sake of completeness, the theory [5] of RF cavity is briefly discussed in APPENDIX-1.

The cavity is characterized by various parameters. The operating frequency, *f* is one of the most important parameters. The dimension of the cavity is of the order of the wavelength ($\lambda = \frac{c}{f}$) of the operating frequency (*f*). The cavity dimension at the operation frequency of 300 MHz becomes of the order of its wavelength ($\lambda = \frac{3.0\ x\ 10^8\ m/s}{300\ 10^6 Hz} = 1\ m$) and at 30 GHz, the dimension becomes of the order of tens of mm ($\lambda = \frac{3\ \ 10^8\ m/s}{30\ \ 10^9 Hz} = 0.01\ m = 10\ mm$). So, the operating frequency below several MHz gives the cavity dimension very large and expensive. On the other hand, at frequencies higher than several GHz the cavity becomes too small to fabricate.

CHAPTER – 2

NORMAL CONDUCTING RF FOR ACCELERATORS

2.1 Basics of particle accelerators

Prof. Ernest Lawrenceof University of California, Berkeley, USA, invented and also patented the cyclotron, which was first operated there in 1932 and Prof. Lawrence got the Nobel Prize for it. The detail discussion on various particle accelerators has been given in the book[6].

2.2 Normal conducting RF cavities for K500 Superconducting Cyclotron

After a reasonably good exposure with the construction, commissioning and operation of *K*130 azimuthally varying sector focussed (AVF) cyclotron at Variable Energy Cyclotron Centre (VECC), Kolkata, and also based on Michigan State University (MSU) *K*500 and Texas A&M University (TAMU) *K*500 Superconducting cyclotrons, the three-phase radio-frequency system of Superconducting (SC) cyclotron[7] has been developed at Variable Energy Cyclotron Centre (VECC).The role of radio-frequency (RF) system in a cyclotron is to develop high RF voltage across the accelerating electrodes, and impart energy to the charged particles each time they cross the electrodes gap. In our case, the electrodes along with the tuning elements form RF cavity working in the frequency range of 9 to 27 MHz. Because of geometrical and mechanical constraints, we have vertical coaxial resonator system in the superconducting cyclotron (SCC), which has three accelerating electrodes (called 'dees') placed 120 degree apart in the valleys. The RF cavity (as shown in Fig.2.2.1) of *K500* superconducting cyclotron (SCC) at VECC consists of three half-wave ($\lambda/2$) cavities placed vertically 120 degree apart. Here, 'λ' is the wavelength at the operating frequency. Each half-wave cavity consists of two quarter-wave ($\lambda/4$) cylindrical cavities tied together at the centre and symmetrically placed vertically about median plane of the cyclotron. Each quarter-wave cavity is made up of a short circuited non-uniform coaxial transmission line (called "dee-stem") terminated by accelerating electrode (called "Dee"). The cavities that handle high RF power are made of normal conducting oxygen free high conductivity (OFHC) copper. These cavities are cooled by low conductivity water (LCW) with conductivity around 0.5 μS (micro-siemens). The use of superconducting magnet in SCC provides high bending power and its effective utilization needs to use high energy-gain per turn to extract the beam. This is achieved by having multiple (in our case, three) “dees”. Also, the use of fundamental mode (corresponding to harmonic number, h=1) requires a three-phase RF system, *i.e.,* three dees are fed with RF power separately from three chains of high power amplification system maintaining 120±0.1 degree phase difference between each of them. A wide frequency variation (1:3) is mostly selected to facilitate acceleration of a large cross section of the ions. The handling of high RF power, high dee voltage and high RF current requires very special precision fabrication techniques, clean and high vacuum conditions, special materials and components. The challenges involved are in the attainment of stringent amplitude stability (10 ppm) and phase stability ($\pm 0.1^0$), maintaining 120 degree phase difference between the RF phases of various dees. Each dee along with half-wave coaxial cavity develops peak voltage of 80 kV having fed with RF power (~80kW) from each of the three high power final RF amplifiers[8]. Like main Dee-cavity, each amplifier has similar type of cavity, which is also tuned by moveable sliding short. Each of the four identical Bridge-T Network in the grid is driven with maximum power of 250 watts. The amplifier, based on Eimac 4CW#150000E tetrode and operated in class-AB mode with power gain 22 dB, requires dc power supplies (P/S) like, Filament P/S 15.5V/215A, Grid P/S -500V /0.5A, Anode P/S 20kV/22.5A and Screen P/S 1.5kV/1A, at its four terminals. A personal computer (PC) based stepper motor controlled sliding-short movement system is used for coarse tuning of the cavities at different frequencies. The closed-loop amplitude and phase regulators are based on RF modulator and In-phase and Quadrature (I&Q) modulation technique respectively. Dee voltage pick-off signals are used as feedback. A programmable logic controller (PLC) based interlock system protects the RF system as well as operating personnel. The details of radiofrequency (RF) system are briefly discussed and explained in the following subsections.

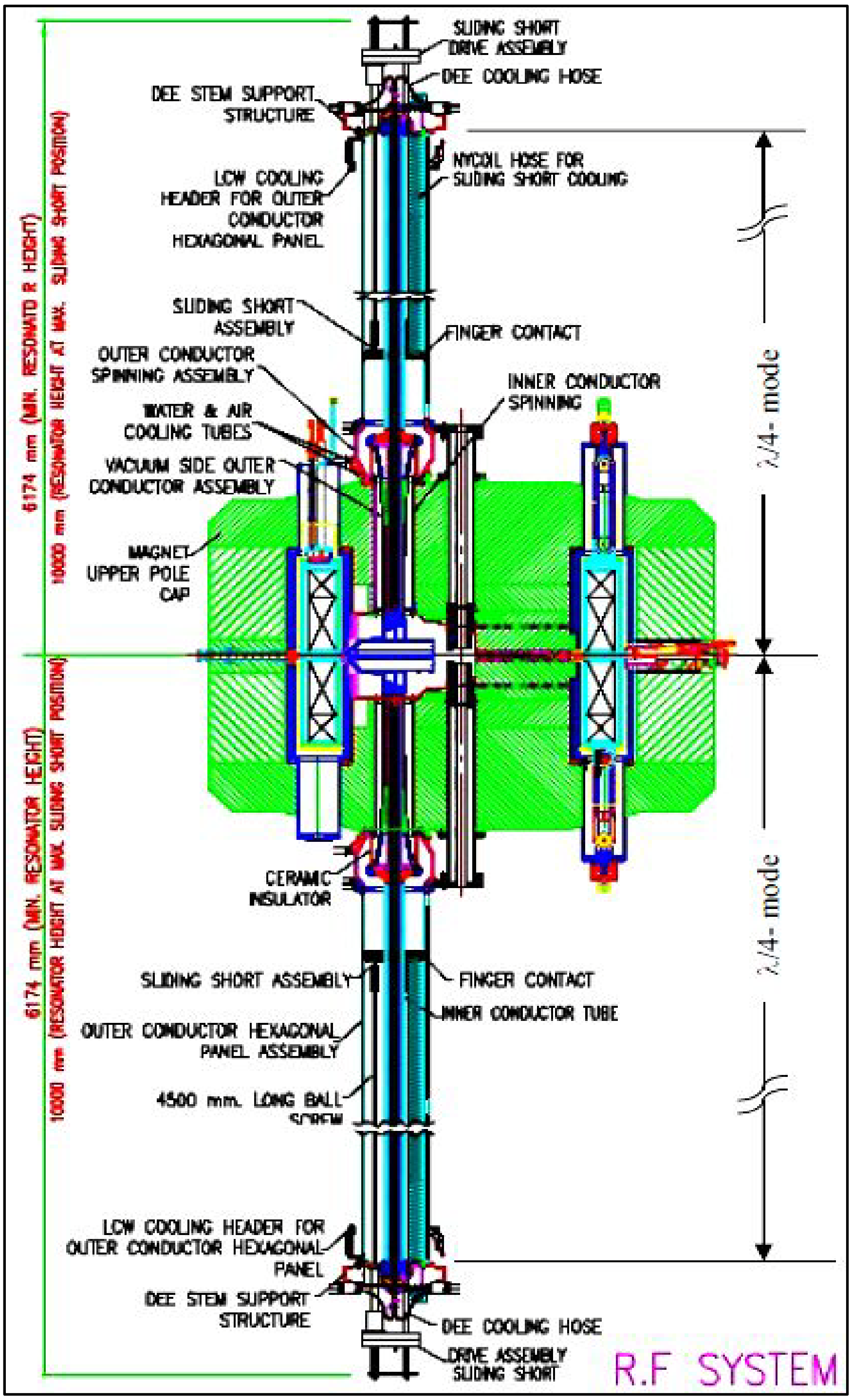

Fig.2.2.1 Half-wave Coaxial RF Cavity for *K500* Superconducting Cyclotron at VECC

2.3. Low-level RF system for *K*500 Superconducting Cyclotron

The RF system of *K*500 superconducting cyclotron at VECC has been designed for the frequency range of 9 - 27 MHz with frequency stability of 0.1ppm (or 1 x 10^{-7}), maximum Dee voltage of 80 kV with amplitude stability of 10 ppm (1 x 10^{-5}) and phase stability of ±0.1 degree between any two dees of the three-dee system. The block diagram of the said RF system is shown in Fig.2.3.1.

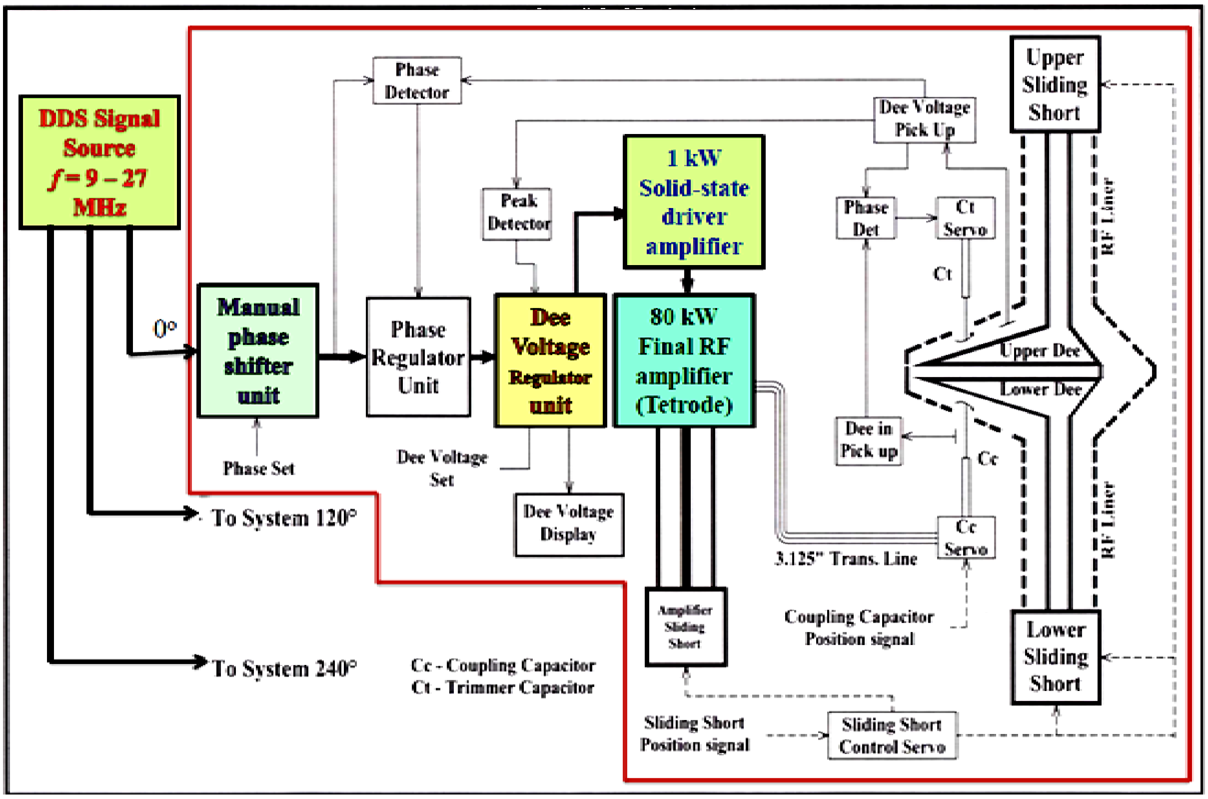

Fig.2.3.1 Block Diagram of the RF system of K500 superconducting cyclotron

The RF system comprises of three separately excited resonating cavities and each cavity consists of two fore-shortened quarter-wave (λ/4) rigid coaxial line terminated by upper and lower Dees at the median plane. The RF system is operating in a Master-Oscillator-Power-Amplifier (MOPA) configuration, in which the highly stable RF signal, from Direct Digital Synthesis (DDS) signal source, enters into Manual phase shifter unit to get adjusted of the relative phase manually, if required due to any phase asymmetry appears between three signals. Then the signal passes through two closed loop systems –Dee voltage regulator unit (DVR) for amplitude regulation and Phase regulator unit for phase regulation. As Phase loop produces some residual amplitude modulation, amplitude loop precedes the phase loop. After phase regulator unit the signal is directly amplified up to 1 kW power level by wideband solid-state driver amplifiers and then to 80kW level by Eimac tetrode based tuned final rf power amplifier for feeding to the main Dee cavity of the cyclotron. The RF power from final amplifieris capacitivelycoupled to the cavity via hydraulically driven coupler with proper impedance matching. The coarse frequency tuning of the cavity is accomplished be the movement of the stepper motor controlled sliding shorts and the fine frequency tuning is carried out using closed loop hydraulically driven trimmer capacitors. As the magnetic field of the superconducting cyclotron is very high (~ 5 Tesla), generally any stepper motors, in proximity to the magnet, are not used to drive trimmers and couplers, instead they are driven hydraulically.

Manual phase shifter:

It is sometimes required to shift the phase manually in order to compensate for any unbalance or asymmetry. The manual phase shifter (as shown in Fig.2.3.2& Fig.2.3.3) is based on classical In-phase & Quadrature (I&Q) modulation using quadrature hybrid (Make-M/ACOM, Model:QH-6-4), electronic attenuator (Make-Minicircuits, Model:MCL-ZAS-3) and power splitter (Make-Minicircuits, Model:MCL-ZFSC-2-1). In normal operation$\pm 15^{o}$ variation is sufficient and output signal balance is $<<\pm 0.05$ dB with harmonic content <-38dBc.

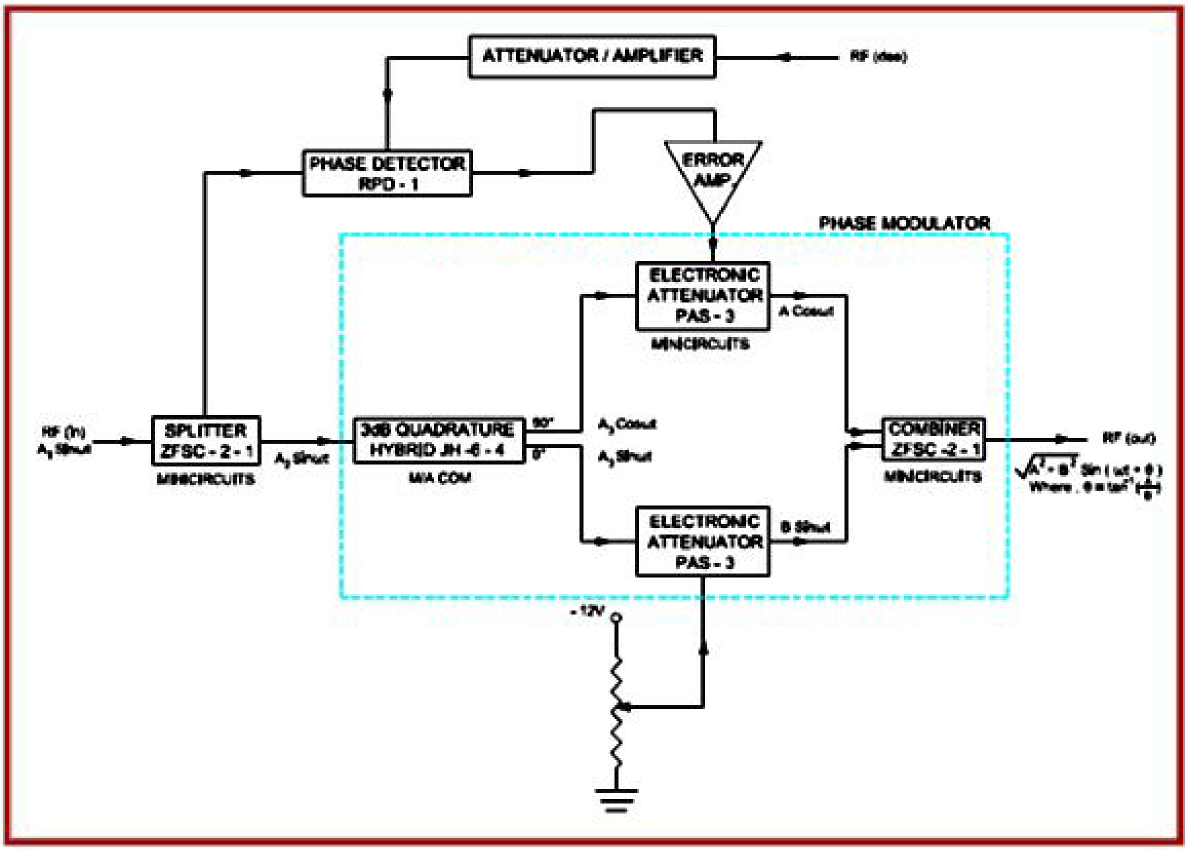

Fig.2.3.2 Block diagram of Manual Phase Shifter for the RF system of *K*500 Superconducting Cyclotron

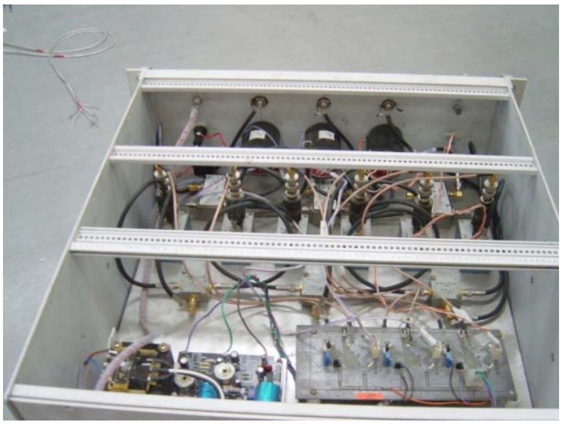

Fig.2.3.3 Manual Phase Shifter unit for the RF system of *K*500 Superconducting Cyclotron.

2.3.1 Amplitude Regulation Loop

It is necessary to achieve amplitude stability in each of the three channels within ±10ppm. A closed loop amplitude control loop or Dee Voltage Regulator (DVR) has been designed (as shown in Fig.2.3.1.1) based on RF Modulator (Analog Devices #AD834JN) that modulates the RF drive signal according to the error signal between highly stable dc reference (REF01) and the feedback sample obtained from Dee pick-up signal. When amplitude loop is closed, the deviation (as shown in Fig. 2.3.1.2) in Dee voltage with respect to time is within the specified value from the set Dee voltage value.

Fig. 2.3.1.1 Dee Voltage Regulator (DVR) unit for the RF system of *K*500 Superconducting Cyclotron.

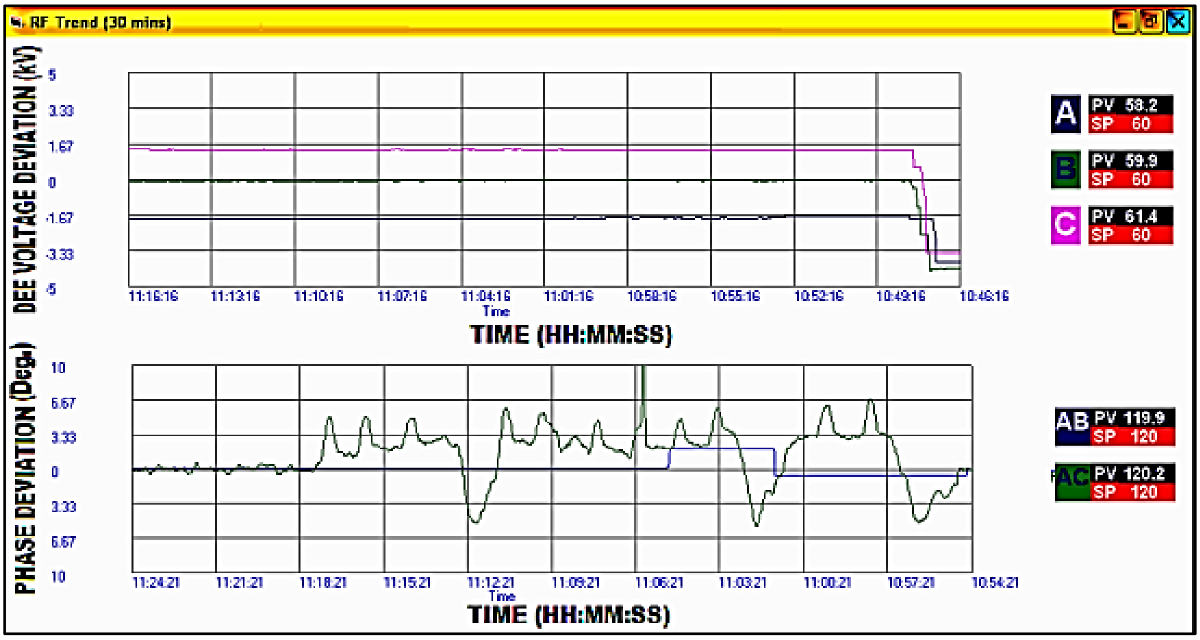

Fig.2.3.1.2 The Amplitude stability (Top Plot) for 30 minutes where A, B & C amplitude loops were CLOSED.

2.3.2 Phase Regulation Loop

The three-phase RF system of Superconducting cyclotron has been developed in the frequency range 9– 27 MHz with very stringent phase stability of $\pm 0.1^0$. The phase control system[9]takes care of varying the relative phase difference between any two RF cavities and also maintain the phase stability within $\pm 0.1^0$ during round-the-clock cyclotron operation. Three individual low-level radiofrequency (LLRF) control loops are used for controlling the RF parameters in three cavity resonators (Cavity-A, Cavity-B and Cavity-C) as shown in Fig.2.3.1.Only relative phase between cavities is required to be maintained at 120 ± 0.1 degree and hence two phase loops instead of three have been used. The DDS (direct digital synthesis) source generates phase synchronous RF signal for three cavities. A programmable logic controller (PLC) produces the control word for DDS[10] unit in order to set the amplitude, phase and frequency of three sinusoidal signals to be generated. The analog phase modulators[11] are also installed in the loop to mitigate the dynamic phase variations caused by system due to fluctuation of various RF parameters.

RF CAVITY RESPONSE TO SINUSOIDAL MODULATIONS :

An electrical equivalent parallel resistive-inductive-capacitive circuit [12] model of a resonant RF cavity has been shown in Fig.2.3.2.1. The cavity transfer function denoting the impedance of this circuit is given by the following equation.

$$Z(s) = \frac{R_{sh}Ls}{R_{sh}LCs^2+Ls+R_{sh}} = \frac{\left(s.\frac{R_{sh}\omega_0}{Q_0}\right)}{s^2+\frac{\omega_0}{Q_0}.s+\omega_0{}^2} \qquad \text{....................(2.3.2.1)}$$

[Where, Q_o is the unloaded quality factor and ω_o is resonant frequency given in radian/second and $s=j\omega$, with $j=\sqrt{-1}$and $\omega$is the angular frequency as per standard notation].

At different frequencies in the range of 9–27 MHz, a substantial variation of shunt resistance (R_{sh}), inductance (L) and capacitance (C) is observed and these dictate the transient response of RF cavity at different frequencies.

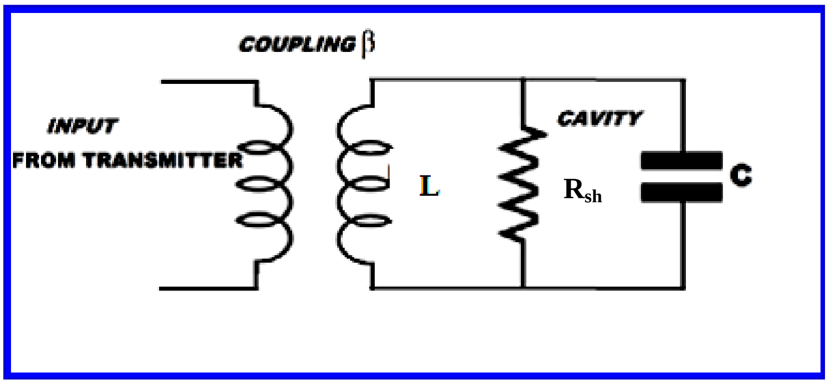

Fig.2.3.2.1 Electrical equivalent circuit of a cavity, where L, R_{sh} and C represent equivalent inductance, shunt resistance and capacitance of the cavity respectively and β represents the inductive coupling coefficient

The unloaded Quality factor (Q_0) and shunt impedance (R_{sh}) values, obtained from 3D EM simulation of *K*500 RF cavity using CST Microwave Studio® 2011, at different frequencies for the said cavity are given in Table-1. The complete RF cavity has been modeled and sliding short length has been changed for different frequencies as shown in Fig.2.3.2.2.

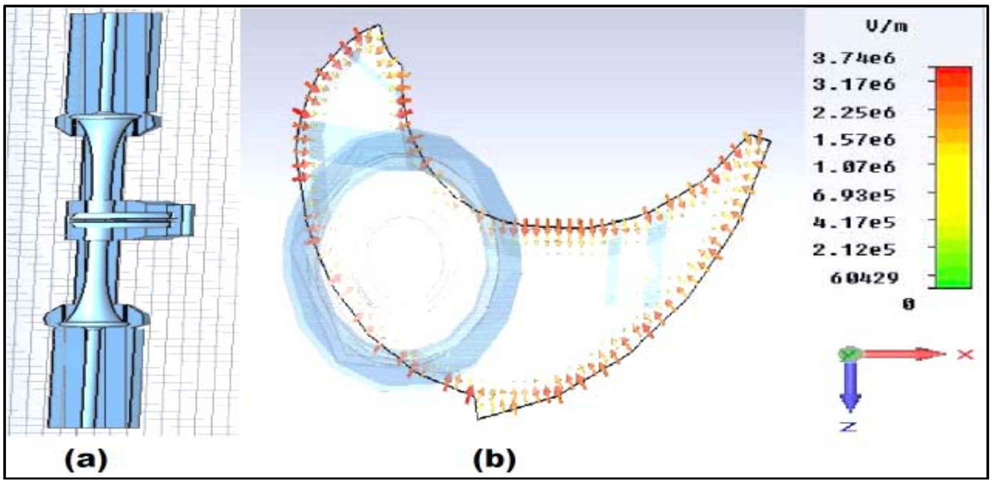

Fig.2.3.2.2 (a) Cross-section of Computer model of single half-wave resonant cavity with sliding short, dee stem and dee at the operating frequency of 19 MHz; and (b) Electric field lines in dee-liner region of the cavity (simulated in CST Microwave Studio®)

An RF cavity, when excited by amplitude and phase modulated carrier signal centered at the resonant frequency (ω_0), is characterized [13] by four different transfer functions, $G_{aa}(s)$, $G_{pp}(s)$, $G_{ap}(s)$ and $G_{pa}(s)$, as defined below.

$G_{aa}(s)$ = transfer functionfor the transmission of amplitude into amplitude modulation,

$G_{pp}(s)$ = transfer function for the transmission of phase into phase modulation,

$G_{ap}(s)$= transfer function for the transmission of amplitude into phase modulation,

$G_{pa}(s)$= transfer function for the transmission of phase into amplitude modulation.

$$G_{aa}(s) = G_{pp}(s) = \frac{\sigma s + \sigma^2[1+(\tan\varphi_z)^2]}{s^2+2\sigma s+\sigma^2[1+(\tan\varphi_z)^2]} \qquad \text{.....................(2.3.2.2)}$$

$$G_{pa}(s) = -G_{ap}(s) = \frac{\sigma s \tan\varphi_z}{s^2+2\sigma s+\sigma^2[1+(\tan\varphi_z)^2]} \qquad \text{.......................(2.3.2.3)}$$

Where, $\omega_0 = \frac{1}{\sqrt{LC}}$; resonant frequency, ω_c is carrier frequency and σ is the damping rate,

$\sigma = \frac{\omega_0}{2Q_0}$; and

$$\tan\varphi_z = \frac{(\omega_c - \omega_0)}{\sigma} \qquad \text{......................(2.3.2.4)}$$

Table-1: RF parameter chart for different frequencies of *K500* Superconducting cyclotron

Frequency (MHz)	Q_0	R_{sh} (kΩ)	$\sigma = \frac{\omega_0}{2Q_0}$
9	4433	123.7	6378
10	4568	119.4	6877
11	4690	114.8	7368
12	4796	109.0	7860
13	4863	105.0	8398
14	4896	101.4	8983
15	4921	97.7	9576
16	4915	101.7	10226
17	4925	91.5	10844
18	4883	86.5	11580
19	4857	84.6	12289
20	4840	81.2	12981
21	4766	79.9	13842
22	4716	77.4	14655
23	4589	73.8	15745
24	4553	72.3	16560
25	4432	70.1	17721
26	4356	67.8	18751
27	4281	67.1	19813

The responses of amplitude and phase at a single frequency are shown in Fig.2.3.2.3(a) and Fig.2.3.2.3(b). The fine frequency control system always maintains the frequency shift within 100 Hz and so the assumptions of (ω_c–ω_0) = 0, reduced the above equations to a first order low pass system (as shown in Fig.2.3.2.3(c)) for the cavity of VECC K500 superconducting cyclotron. A more sluggish response is observed as σ decreases with decrease in frequency.

$$G_{aa}(s) = G_{pp}(s) = \frac{\sigma}{s+\sigma} \quad \text{……………………….. (2.3.2.5)}$$

$$G_{pa}(s) = G_{ap}(s) = 0 \quad \text{………………………….. (2.3.2.6)}$$

THE PHASE REGULATOR LOOPS:

The overall phase regulation system (as shown in Fig.2.3.1)comprises of a DDS RF signal source (make Analog Devices[14]). The RF signal is passed through a signal splitter, which gives Reference signals used for phase measurement and synchronization purposes. The voltage controlled phase shifter in the LLRF loop, takes care of dynamic phase disturbances generated in the chain of LLRF components, amplifiers and RF cavity. In order to maintain only relative phase shift between resonators, two instead of three phase loops have been employed. The relative phase shift (φ_{AB}) between Cavity-A and Cavity-B and also relative phase shift (φ_{AC}) between Cavity-A and Cavity-C, have been detected by two phase detectors. The voltage controlled phase shifter actually shifts the phase according to the error signal of φ_{AB} and φ_{AC} and they are installed in cavity-B and cavity-C.

The phase detector:

It consists of a Dual Demodulating Logarithmic Amplifiers and Phase Detector integrated circuit (IC) of Analog Devices (AD8302)[15], having both the magnitude and the phase outputs. Comparing the phases of two RF signals, it gives a voltage proportional to the phase difference (10 mV/degree).

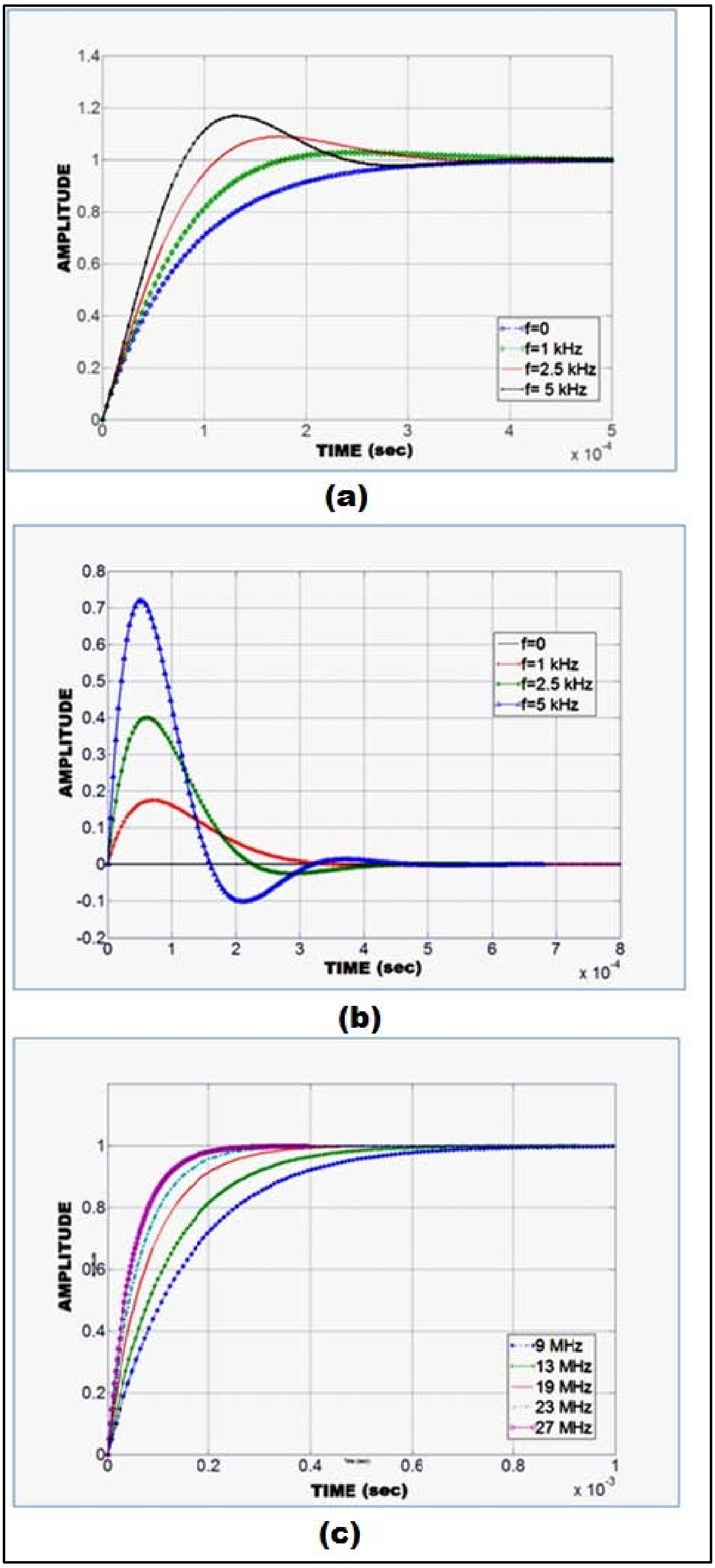

Fig.2.3.2.3 Step response of (a) $G_{aa}(s)/ G_{pp}(s)$ at 19MHz, for Δf=0, 1kHz, 2.5kHz,5kHz; (b) $G_{pa}(s)/G_{ap}(s)$ at 19MHz, for Δf=0, 1kHz, 2.5kHz, 5kHz; and (c) $G_{aa}(s)/ G_{pp}(s)$ at 9MHz, 13MHz, 19MHz, 23MHz and27 MHz

For a phase change of 180º within the frequency range of 9–27 MHz, this IC gives a fairly linear phase response, operating on the principle of zero-crossing followed by a XOR (Exclusive OR) gate and as a result the phase output is unaffected by its amplitude. The output voltage increases with the phase change from θ = 0º to 180º, however, decreases with the phase change from 180º to 360º, forming an 'inverted V' shape, as shown in Fig.2.3.2.4.

The detector output voltage, however, is observed as the same for +θ degree or–θ degree (|θ|<180 degree). In order to overcome this problem, the output voltage along with its slope has been considered. A small predefined phase shift ($+\Delta\theta = 1^0$) from the source DDS is introduced and the corresponding voltage change (+ΔV) is measured to evaluate ΔV/Δθ. It is observed that ΔV/Δθ is positive between 0 to 180 degree and is negative between 180 to 360 degree. This is a dynamic system and it needs to take care of wide phase variations (360 degree) due to system transients of cascaded different other systems in LLRF loop. Besides these, a low pass filter, which makes small signal envelope bandwidth from DC to 500 kHz has been added. The step response for 8 degree phase shift centred at 90 degree has been shown in Fig.2.3.2.5.

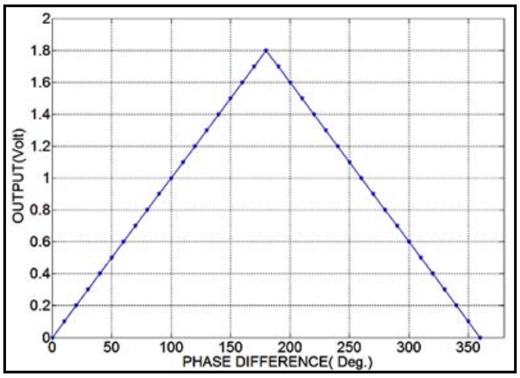

Fig.2.3.2.4 Phase Detector response. The output voltage with respect to phase change increases from θ = 0º to 180º but decreases from 180º to 360º forming an 'inverted V' shape.

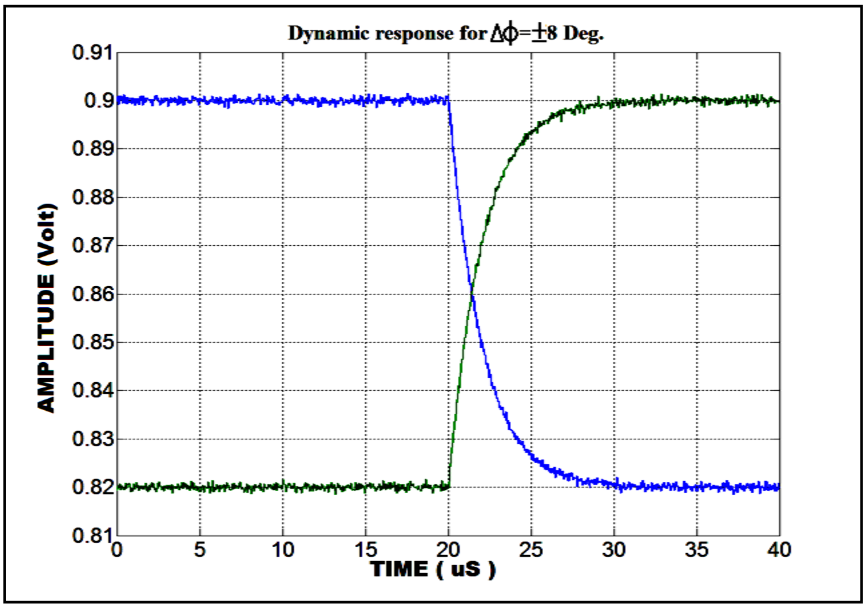

Fig.2.3.2.5 Phase Detector dynamic response centered at 90 degree.

I/Q modulator as Phase shifter:

The In-phase/quadrature (I/Q) modulator based phase shifter has been used for this system within the frequency range 9 to 27 MHz. The quadrature modulator consists of a quadrature hybrid[16], two RF modulators, one signal splitter and one signal combiner as shown in Fig.2.3.2.6. It works as a voltage controlled phase shifter having a phase shift range of $\pm 25^0$. The response time of the phase shifter is 90 μs, limited by the rise time of the RF modulator.

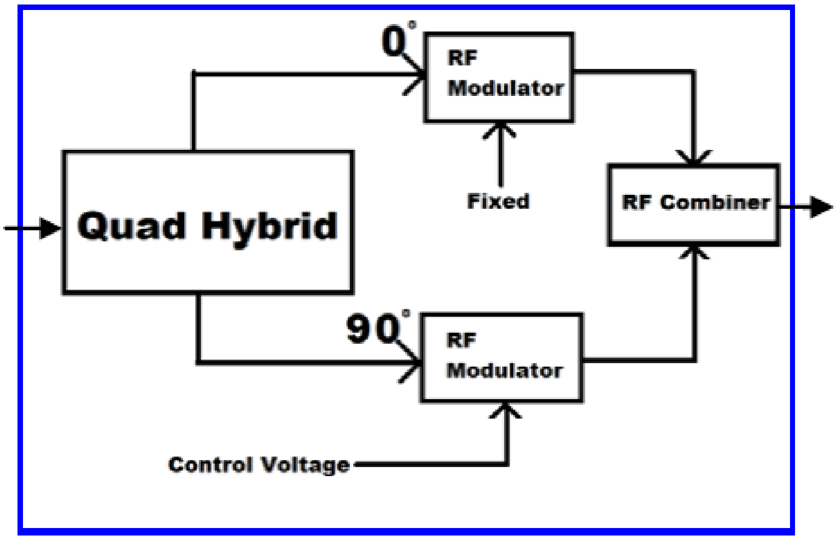

Fig.2.3.2.6 In-phase/Quadrature (I/Q) modulator as phase shifter

The phase shifter drives a control signal from arbitrary waveform generator and measures the output at phase detector end at different frequencies. The phase shifter, modeled as first order low pass filter, has a bandwidth of 11.1 kHz. The plot of output phase shift with input control voltage at different frequencies is shown in Fig.2.3.2.7. In order to keep the amplitude of RF waveform within the limit of amplitude loop, the system is limited to operate within ±0.7V.

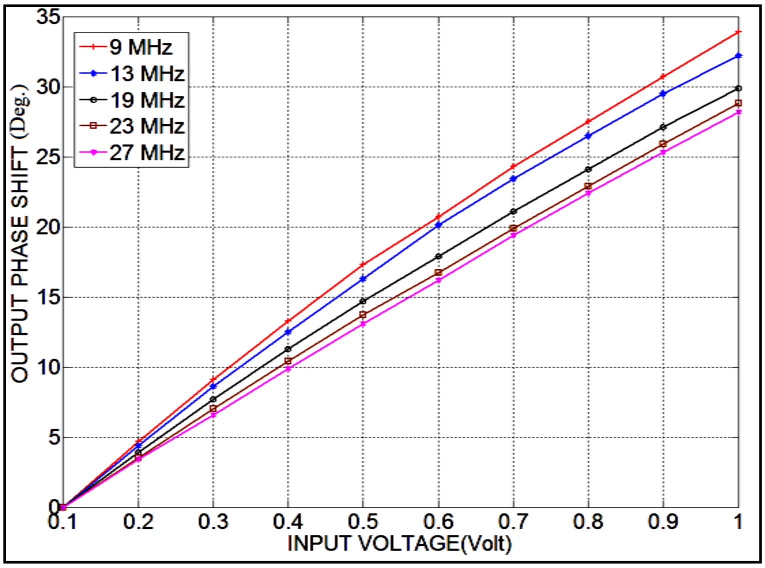

Fig.2.3.2.7 Output phase variation with control voltage at different frequencies. The phase deviation reduces with frequency at a fixed input voltage

The Integrator:

The controller output produces a phase modulated signal for feeding to the RF cavity. The controller bandwidth is kept much smaller than the RF cavity bandwidth in order to keep the frequency shift of the cavity within the permissible limit of amplitude and frequency tuning loop, with respect to the resonant frequency. The performance of the control system is made independent of the cavity parameters by keeping the cut off frequency of the controller[17] less than $\sigma/10$. An active filter with bandwidth 100 Hz has been put in series with the controller to limit the frequency response. The system includes a integrator ,*i.e.*, a pole at origin to have an excellent steady state behavior. The controller transfer function is given by the following equation (2.3.2.7). The value of time constant (RC) has been evaluated from root locus technique.

$$G_c = \frac{1}{RCs(s+2\pi f)} \text{ ....(2.3.2.7)}$$

The DDS as 360^0 phase shifter:

DDS source generates reference signals for the three cavities. As the dynamic range of the analog phase control loops is limited, *i.e.*, $\pm 25^o$, it is necessary to introduce a phase offset to bring the system back to the range of analog regulators. A PLC based system examines (as per algorithm shown in Fig.2.3.2.8) the phase controller output and gives a phase offset when the analog controller gets saturated. It also examines whether the phase shift is in the 0^0–180^0range or 180^0–360^0 range by evaluating $\Delta V/\Delta\theta$ along with +/– sign.

Results of simulation and experiment:

The simulation of the control system has been done withMATLAB/Simulink. The equivalent baseband model is shown in Fig.2.3.2.9.The poles of phase, time constant (RC) of the controller have been obtained from the root locus plot as shown in Fig.2.3.2.10. The critical gain for the system is obtained from root locus as $Kc = 1.27 \times 10^4$. It is required to keep time constant $RC \geq 1/K_C$ to maintain stability.

$$RC \geq 1/K_C = 78.7\ \mu S.$$

The closed loop transfer function is given by $\frac{G(s)}{1+G(s)H(s)}$, where $H(s)=1$ and

$$G(s) = \frac{2.045 .10^{18}}{s^5 + 3.226 .10^6 .s^4 + 2.673 .10^{11} .s^3 + 3.424 .10^{15} .s^2 + 2.045 .10^{18} .s} \text{ .... (2.3.2.8)}$$

The value of RC has been chosen as 800 μs and bandwidth of low pass filter (LPF) as 100 Hz. A low pass filter has been introduced in order to restrict the amplitude modulations caused by phase controller within 100 Hz, so that the amplitude controller takes care of these modulations.

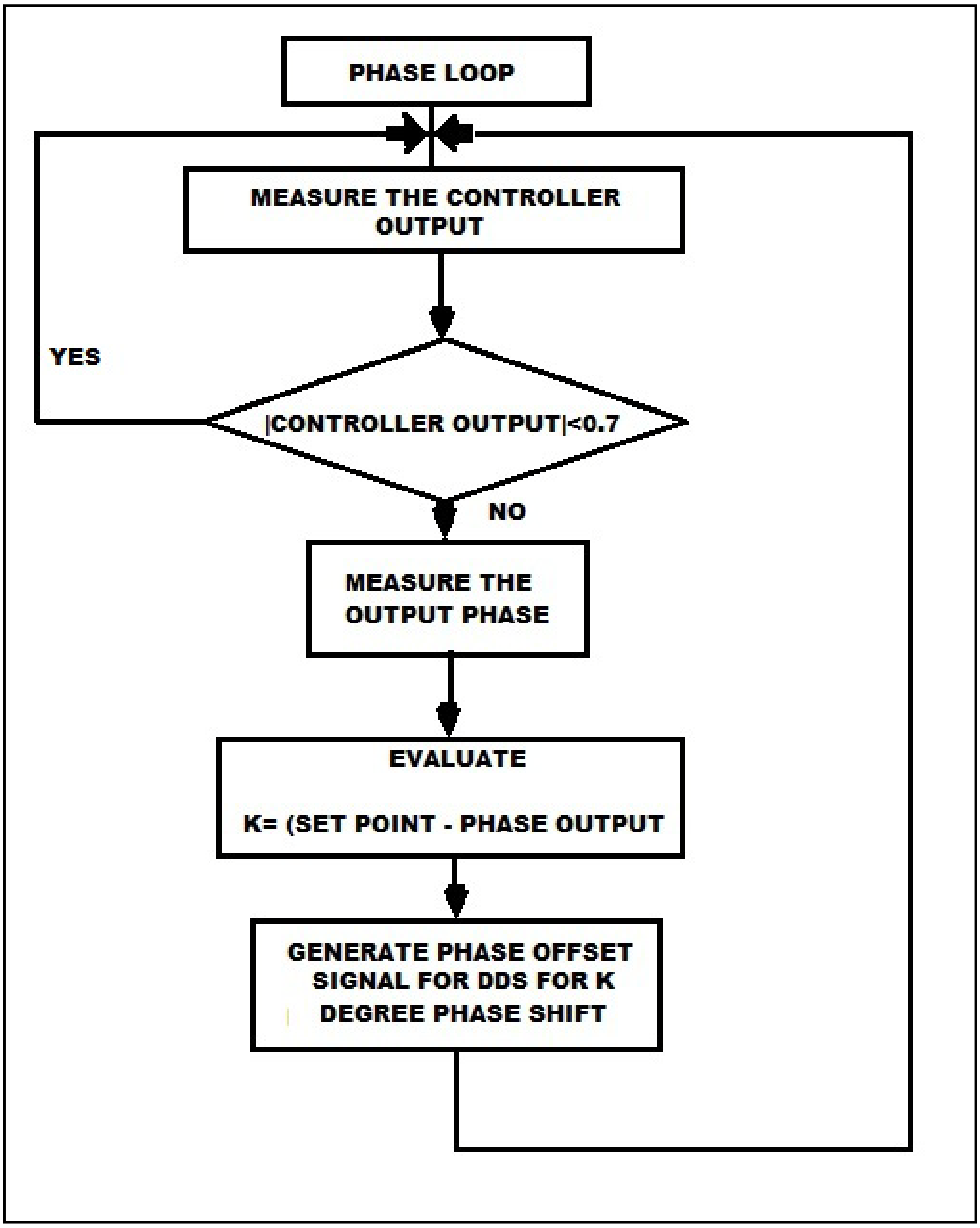

Fig.2.3.2.8 Algorithm to examine phase controller output of the phase regulation loop for the RF system of *K*500 Superconducting Cyclotron

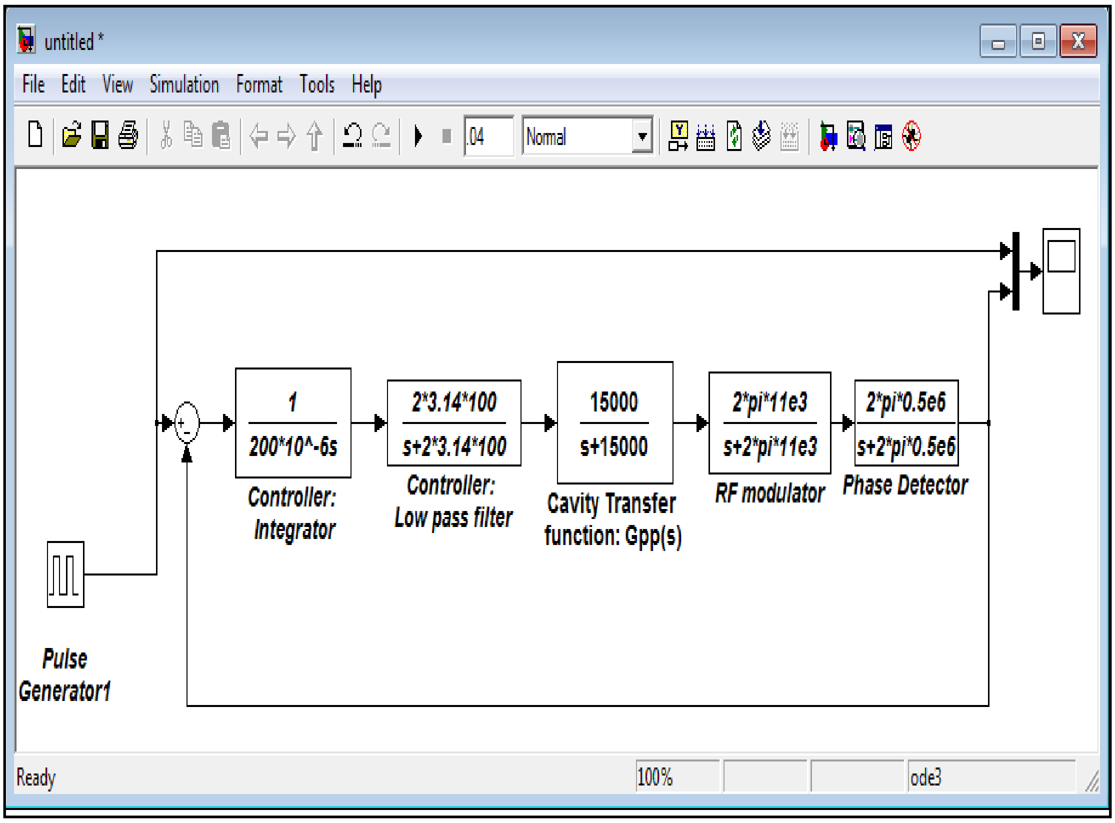

Fig.2.3.2.9 The equivalent baseband model of the control system of the phase regulation loop for the RF system of *K*500 Superconducting Cyclotron.

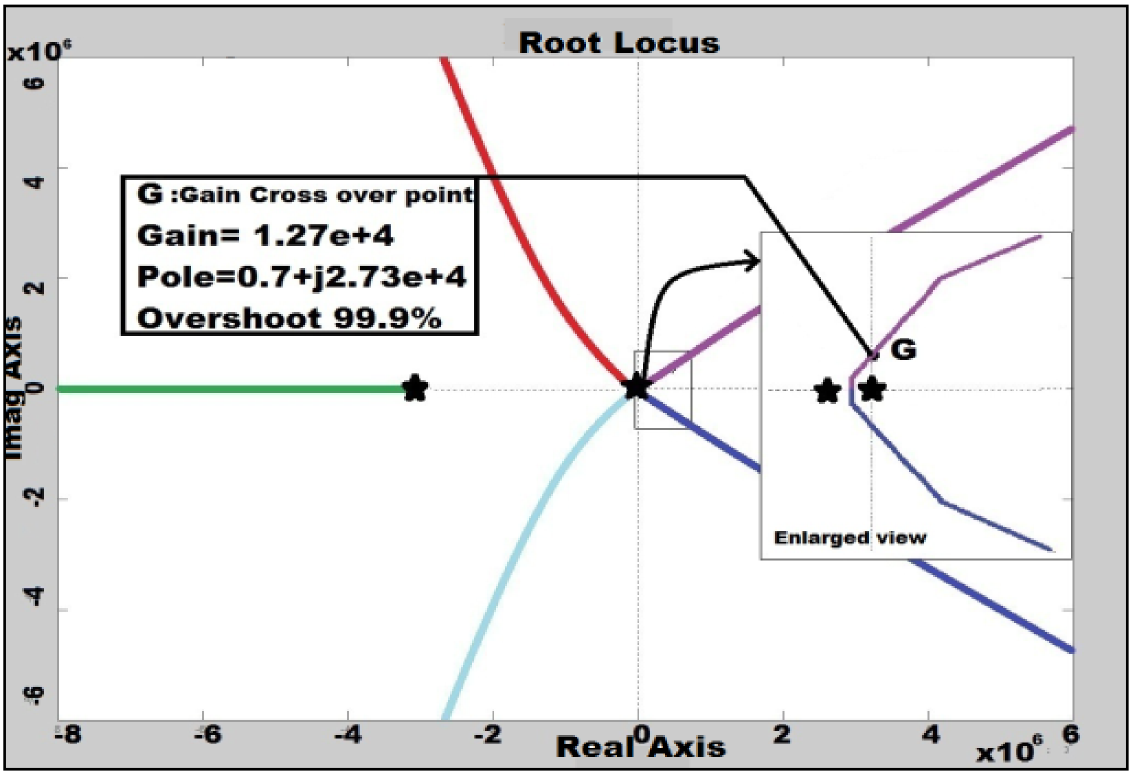

Fig.2.3.2.10 Root locus plot of the control system, where 'G' is the gain cross-over point, of the phase regulation loop for the RF system of *K*500 Superconducting Cyclotron.

The step input response of the system as obtained from MATLAB simulation has been shown in Fig.2.3.2.11. The same response has been observed with the phase loop installed in our system (as shown in Fig.2.3.2.12). The comparative plot of step responses of phase loop for experimental (in oscilloscope) and simulation has been given in Fig.2.3.2.13.

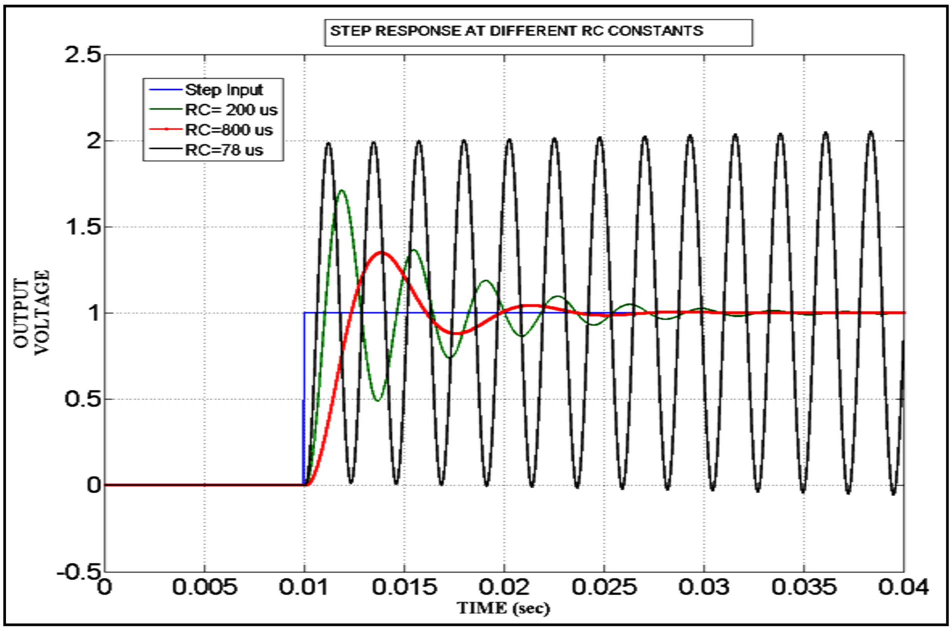

Fig.2.3.2.11 Step Response of phase loop Matlab/Simulink (simulated)for different time constants (RC), of the phase regulation loop for the RF system of *K*500 Superconducting Cyclotron.

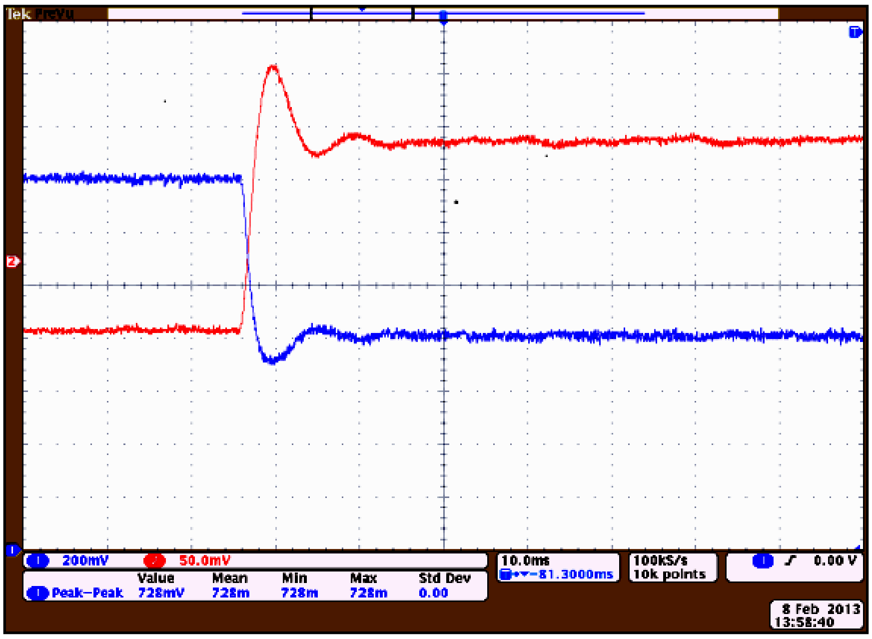

Fig.2.3.2.12 Step Response of phase loop captured in oscilloscope (experimental), where 'red' plot shows output phase and 'blue' plot shows the control signal to I/Q modulator.

The phase stability of $\pm 0.1^0$ for 30 minutes has been shown in Fig.2.3.2.14 & Fig.2.3.2.15. It is shown (in Fig.2.3.2.14) that even if the resonators are kept at constant voltages the system generates considerable amount of phase errors visible in green waveform (unregulated). The phase loop takes care of phase shifts occurred due to various cavity phenomena during voltage ramp up as shown in Fig.2.3.2.15.

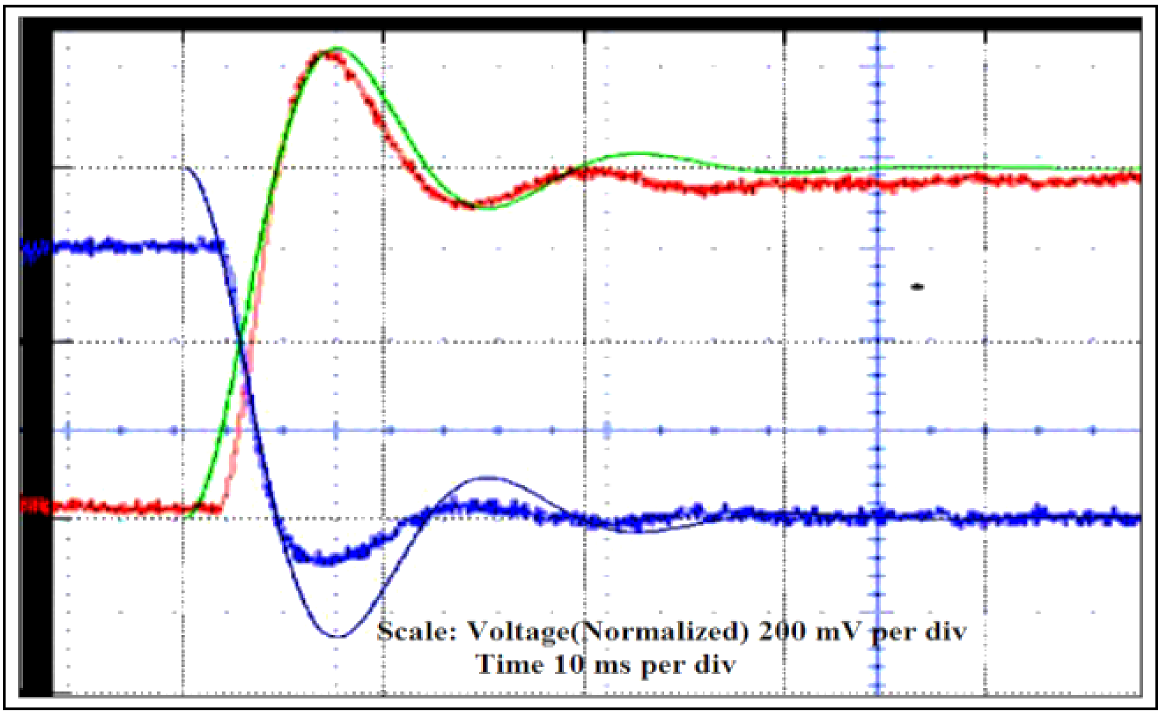

Fig.2.3.2.13Step Response of phase loop captured in oscilloscope & simulation (compared).

The RF pick off signal from resonator has been measured with spectrum analyzer to examine whether there is any residual modulation left in the waveform. The system spectrum has been shown in Fig.2.3.2.16 taken at 100 Hz span at 19 MHz.

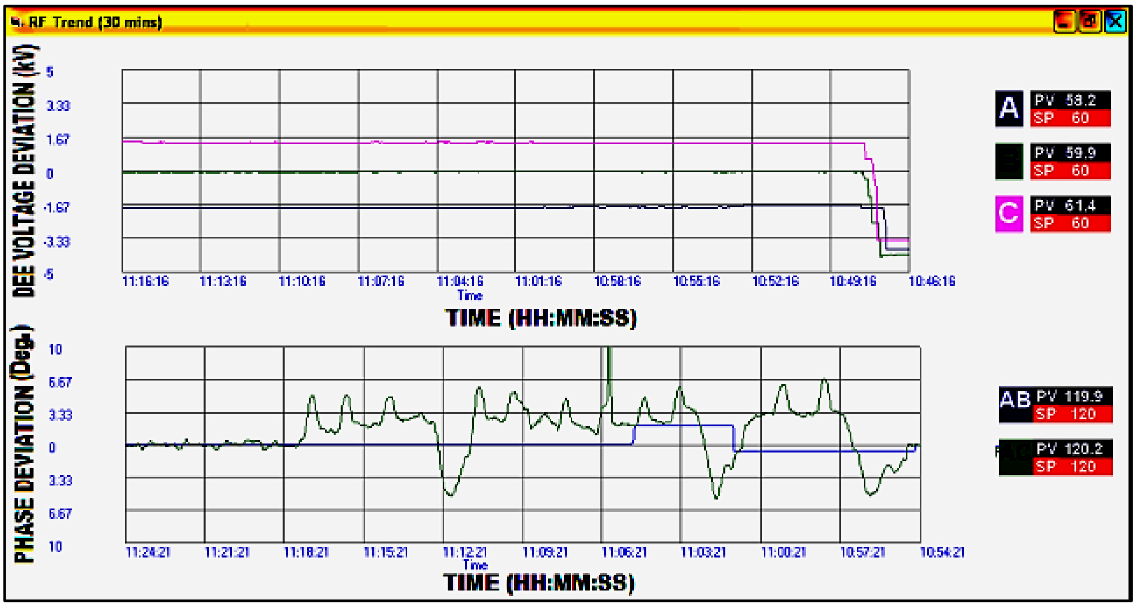

Fig.2.3.2.14 The Phase stability (Bottom Plot) for 30 minutes where AB phase loop was CLOSED, AC loop was OPEN. Although, a deliberate change in AB phase (blue) was made, it remained stable. However, AC phase (green) is not stable as the loop is OPEN. Amplitude variation in three cavities with respect to time is shown in Top plot.

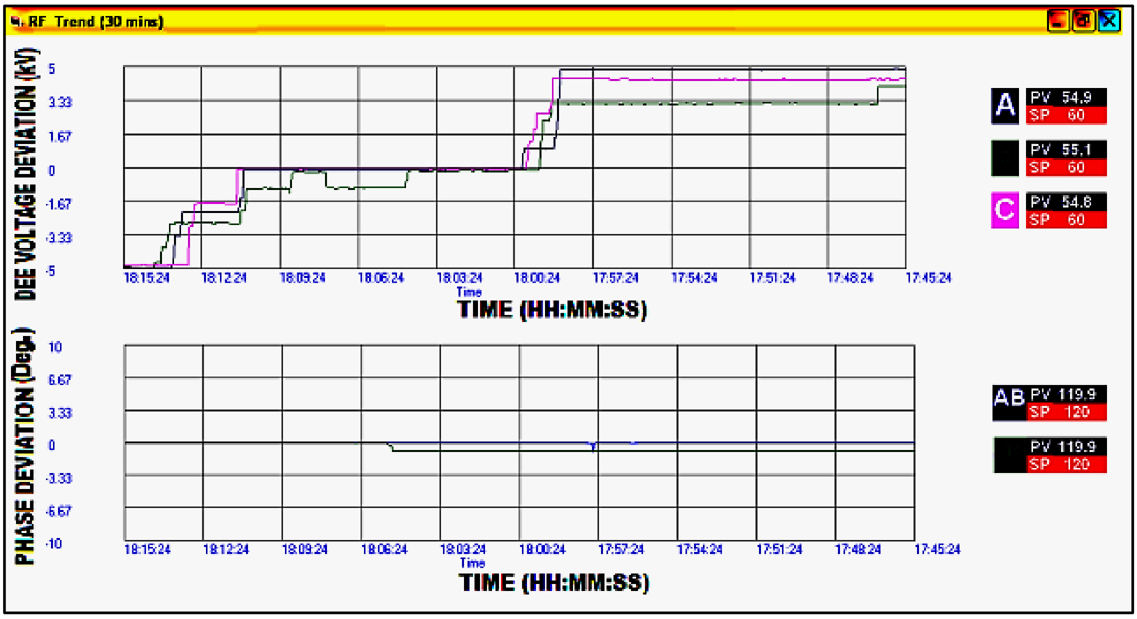

Fig.2.3.2.15 The Phase stability (Bottom Plot) for 30 minutes where both AB loop and AC loop were CLOSED. In spite of deliberate changes made, AB phase remained stable. Also AC phase is stable as it CLOSED. The glitch found in phase deviation plot (blue) is due to analog phase loop saturation. Amplitude variation in three cavities with respect to time is shown in Top plot.

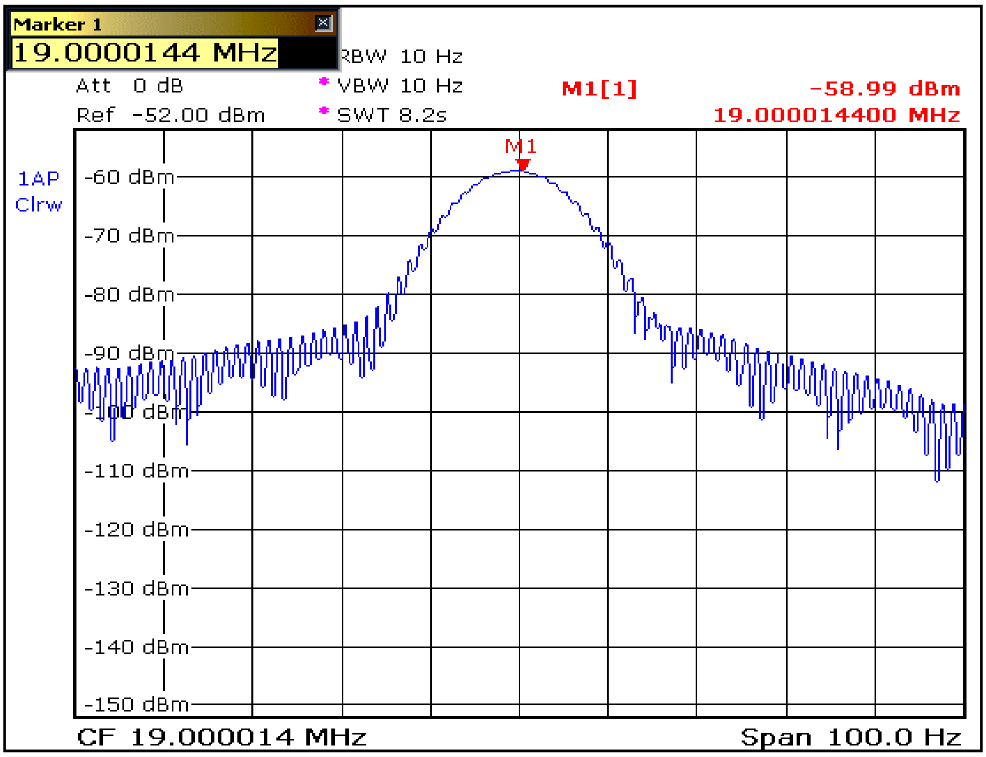

Fig.2.3.2.16 Measured RF pick up at 19 MHz in the Spectrum Analyzerwith no residual phase modulation.

2.4 Fine Tuner

Because of high quality factor, both RF amplifier-cavities and main resonator cavities are narrow band structure. From cavity simulation results[18], it is found that in case of main resonator cavities, frequency shift produced at the highest frequency (27 MHz) is around 22 kHz/mm and at the lowest frequency (9 MHz) is around 400 Hz/mm. The requirement of fine frequency tuning for RF amplifier-cavities is less than that of Main resonator cavities, as the former has much less loaded Quality factor (Q). The RF power is capacitively coupled to the dee (accelerating electrode) of the main resonant cavity through Coupler (Coupling capacitor). The coupler is also used to match the high shunt impedance of the main resonant cavity to the 50 Ohm output impedance of final RF power amplifier[8]. There is a vacuum variable capacitor formed between an adjustable insert and DEE (in each main cavity) called “trimmer capacitor”. Trimmer capacitor [19] operates in closed loop for the adjustment of a small variation in tuned frequency due to thermal effect and beam loading of the cavity.

Coupler can travel 100 mm. maximum and trimmer has a maximum of 20 mm span of travel. The Coupling capacitor and trimmer capacitor movement is hydraulically driven, not based on stepper motors because the system is very close to high field superconducting magnet. This system is responsible for the overall tuning of the cavity in closed loop [20].The critical coupling between RF amplifier and RF cavity is achieved by analyzing impedance matching and minimizing VSWR. It also ensures minimal reflection at coupler port.

After proper tuning of the cavity with Vector Network Analyzer (VNA), when RF power is fed to the cavity, it gets slightly detuned because of thermal instability arising due to RF heating. The effect of the cavity detuning isreduction in dee voltage and change in phase. The precise movement of trimmer is necessary to compensate the change in volume of the cavity due to thermal expansion. The accurate position and stability depend on the lowest piston speed of the trimmer determined by minimum fluid flow rate of the hydraulic drive system. As the hydraulic valve has dead band and hysteresis error, the dead zone inevitably brings about steady-state position error and therefore, the dead band is set according to position accuracy. The stability of Dee voltage is substantially affected by this error. Moreover, the variation in cavity dynamic impedance results in the increase of VSWR and reflected power, which is harmful to the RF amplifier. The problem is further aggravated as the vacuum level deteriorates due to variation of RF power inside the cavity.

<u>PID control of hydraulically driven couplers and trimmers</u>:

This Proportional Integral Derivative (PID) control system consists of a PID controller, hydraulic proportional control valve, position sensor and hydraulic drive system. A PID based feedback control loop is implemented for the positioning of trimmer and coupler. The block diagrams of coupler control loop and trimmer control loop are shown in Fig.2.4.1 and Fig.2.4.2 respectively.

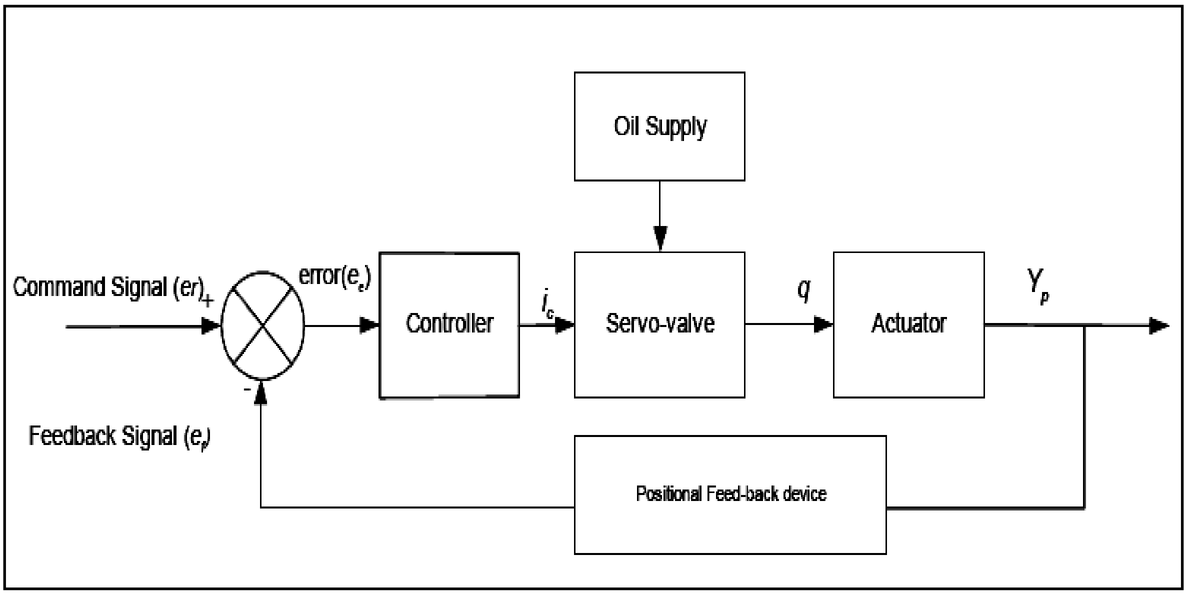

Fig.2.4.1 PID loop position control system for coupler for the RF system of *K*500 Superconducting Cyclotron.

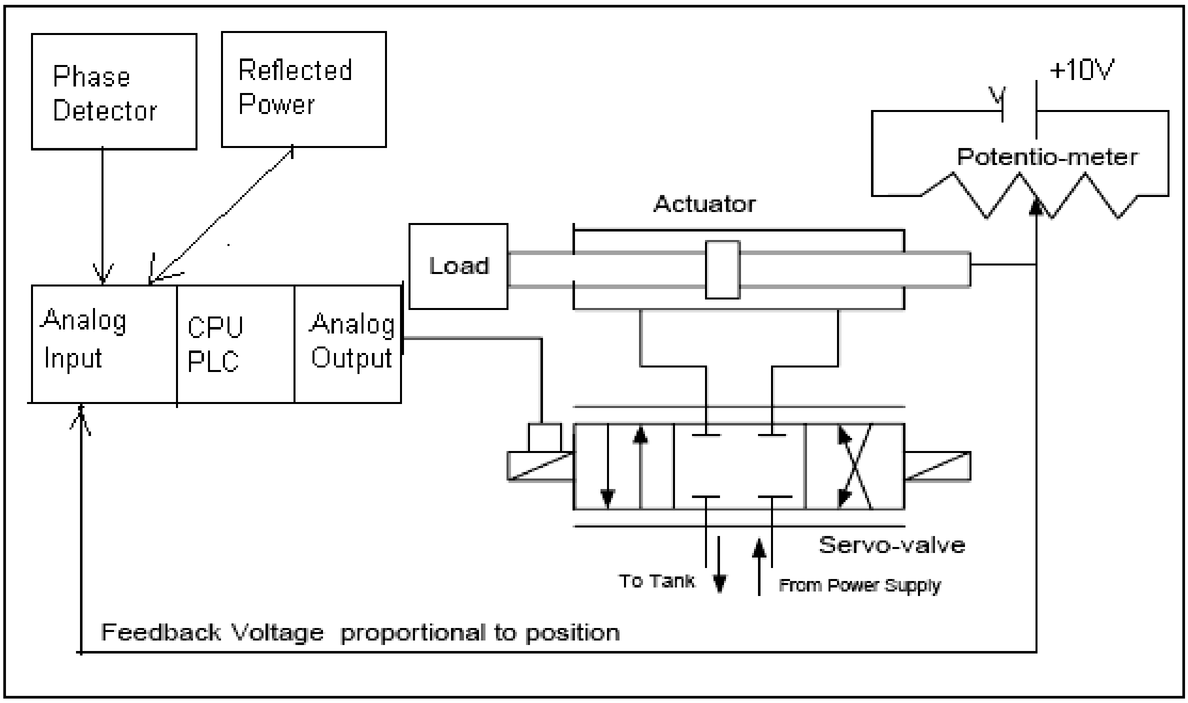

Fig.2.4.2 Closed-loop control system of trimmer (fine tuner) for the RF system of K500 Superconducting Cyclotron.

When the cavity is perfectly tuned, there will be a phase difference of $\pi/2$ radians (90 degrees) between dee-in pick-up and dee pick-up signal (as shown in Fig.2.4.3). This phase difference is detected by AD8302 IC based phase detector circuit and the phase error signal drives the trimmer to track the tuning condition of the cavity in closed loop operation. The error amplifier continuously monitors the input reference signal (U_r) and compare it with the actuator position (U_p) signal measured by a displacement transducer to yield an error signal (U_e).

$$U_e = U_r - U_p$$

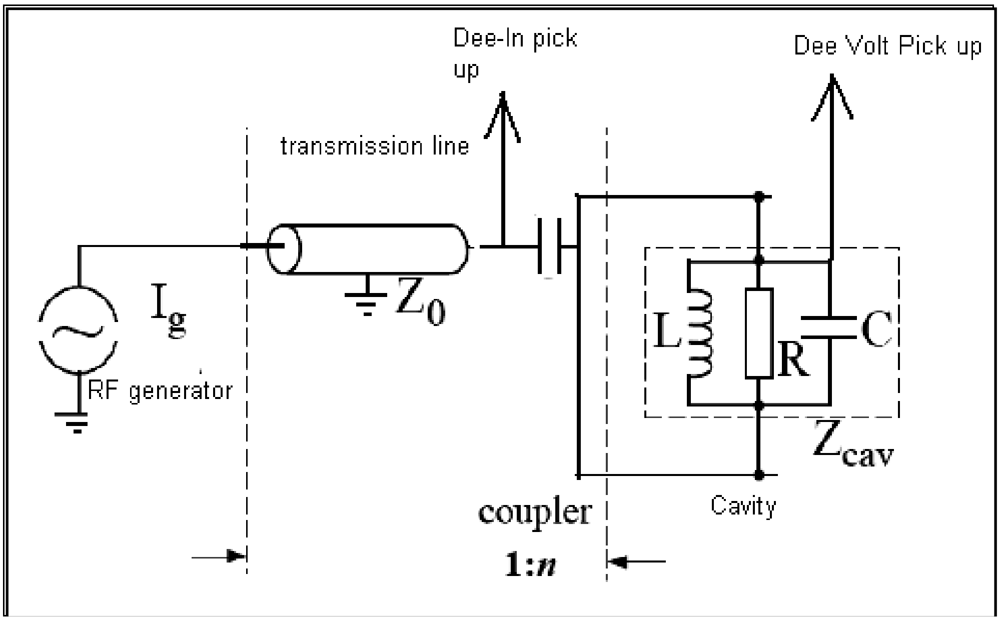

Fig: 2.4.3 Block diagram of the trimmer control signal for the RF system of K500 Superconducting Cyclotron.

The error signal is processed by the servo controller according to a pre-defined control algorithm to produce a command signal (U_v) to drive the hydraulic flow control valve. The output of the controller due to this error signal is a function of the proportional, integral, and derivative gain compensation settings according to the control algorithm.

$$U_o(t) = K_p . U_e(t) + K_i \int U_e(t)\, dt + K_d . \frac{dU_e(t)}{dt}$$

[WhereK_p,K_i and K_d are the PID constants[21], U_e is the error signal and U_o is the controller output].

Effect of static and dynamic friction of hydraulic valve and actuator:

The static friction inside the mechanical components like, valve and actuator possesses complex nonlinear behavior during the onset of the motion. It can be modeled as a discontinuous nonlinear mapping between the velocity and static friction. The frictional force depends upon both the magnitude and direction of velocity. Coulomb and viscous frictional force opposes instantaneous movement of the spool of the valve and thus limiting the motion accuracy of the valve. The high static friction and dynamic behavior of the frictional force significantly affects the performance of the valve at low signals.

Furthermore, due to hysteresis of the mechanical valve, a large error signal is required to overcome the static friction of the valve and ultimately the movement of the large trimmer. But the large signal causes significant overshoot. Trimmer cannot take fast correction at low error signal, thus resulting in increase of reflected power. The detuning will have the following undesirable effects (as shown in Fig.2.4.4).

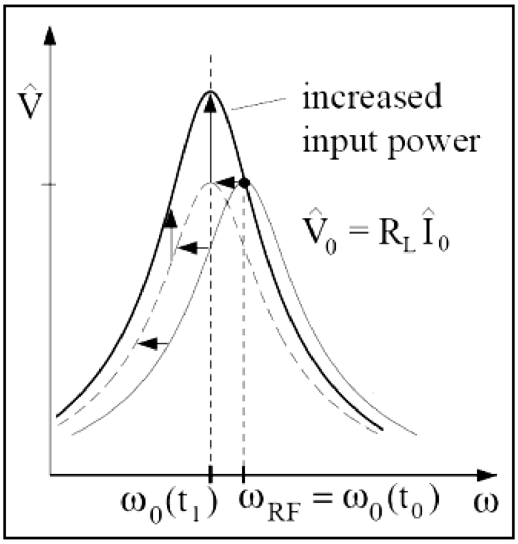

(a)

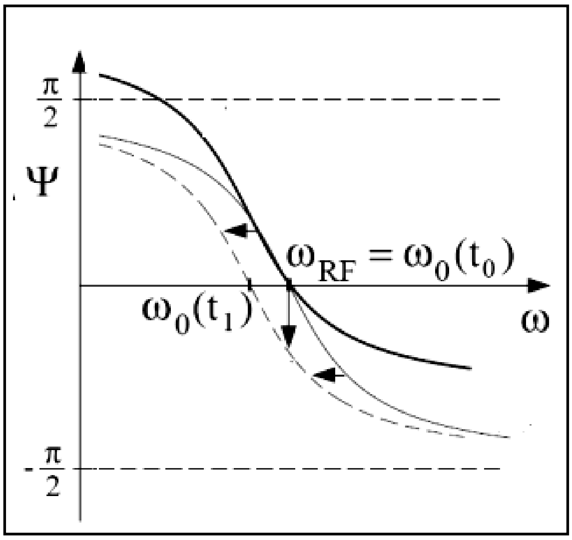

(b)

Fig. 2.4.4Effects of detuning of the cavity due to (a) increase in Power (b) change in Phase, for the RF system of *K*500 Superconducting Cyclotron

- Reduction of Dee voltage and shifting of the cavity phase and so requirement of more input power to maintain the Dee voltage.

To overcome this problem, the input phase should be regulated accordingly to compensate the phase shift.The modified transmitter power (P) and resulting phase (ψ) are as follows.

$$P = P_0.\left(1 + (\frac{\Delta\omega}{\omega_{1/2}})^2\right); \psi = \tan^{-1}\left(\frac{\Delta\omega}{\omega_{1/2}}\right)$$

[Where,P_0,$\Delta\omega$,$\omega_{1/2}$ are power at tuned condition, change in frequency and half bandwidth of the cavity]

Both amplitude stability of each Dee and relative phase stability between any two of the three Dees are very important parameters for beam acceleration. The Dee voltage regulator (DVR) maintains the dee voltages and therefore a portion of additional power will reflect back to the tetrode-based RF amplifier and increase its plate dissipation. This situation lasts until the error is accumulated to a significantly large value, which finally operates the valve to take corrective measures appropriately.

<u>Closed loop trimmer control</u>:

The closed loop trimmer control system is developed based on Siemens 315-2DP PLC. An analog input channel with 16 bit resolution analog-to-digital converter is used to sense and linear potentiometer is used to measure the position of the trimmer. The closed loop Proportional Integral (PI) controller minimizes the error signal. The analog output signal with 12 bit resolution is used for the trimmer movement. It was observed that in case of small error signal, it takes longer correction time, with some jittering effect in the trimmer movement due to the nonlinear behavior of the valve and actuator at low fluid flow condition. The dead-band of the valve causes the hysteresis effect resulting in variation in the reflected power.

To overcome the problem of jittering effect, reflected power is also considered as error signal in the closed loop. The square of the reflected power with suitable scaling factor is multiplied to the phase error signal. The sign of the product determines the required direction of the movement and also the error signal is magnified when there is substantial reflected power but the small phase error. However, the total error gets reduced drastically when reflected power is small, thus reducing the movement of trimmer. A substantial improvement in trimmer correction is observed with introduction of this technique in the trimmer control loop [22], thus removing the jittering effect completely.

Integrated RF tuning user interface:

An integrated operational interface (as shown in Fig.2.4.5) is developed for the movement of nine stepper motors (for sliding shorts of three amplifier-cavities and six main resonator cavities), three couplers, and three trimmer capacitors. It has a feature to control each of the parameter independently and store in the database. An EPICS based data archiving system is also developed to monitor the effect of movement of trimmer on dee voltage, phase, forward power and reflected power any time.

The commercially available hydraulic drive based system has its limitation of precise movement at very low flow. Even response of the control system becomes critical for the high precision system. To overcome the effect jittering due to complex friction function inside the valve and actuator limits overall performance. The developed system has been operating satisfactorily round-the-clock with K500 superconducting cyclotron.

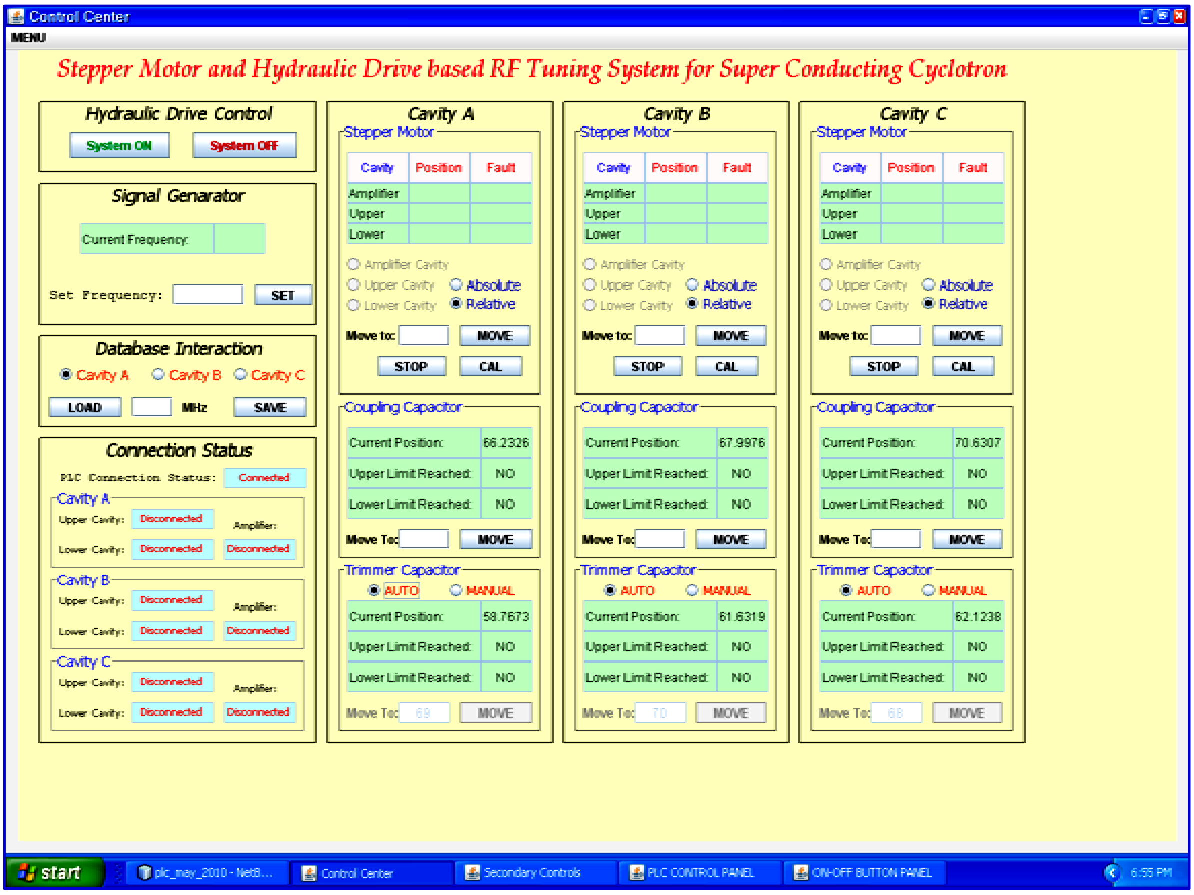

Fig.2.4.5 User Interface of the RF Tune operation control for the RF system of *K*500 Superconducting Cyclotron.

2.5 High Power RF for *K*500 Superconducting Cyclotron

2.5.1 RF Cavity Simulations, Design, Description

The geometric model of the above coaxial RF cavity (as shown in Fig.2.2.1) of *K*500 SCC has been analyzed in 3D CST MICROWAVE STUDIO (CST MWS) code, which is a general-purpose simulator based on the Finite Integration Technique (FIT). This numerical method provides a universal spatial discretization scheme applicable to various electromagnetic problems ranging from static field calculations to high frequency applications in time domain or frequency domain.

After carrying out RF cavity analysis[18] using 2D SUPERFISH code, we have presently used CST MICROWAVE STUDIO code to simulate a number of models of SCC

RF cavity (as shown in Fig.2.5.1.1) at different frequencies in the range 9 MHz to 27 MHz and electric and magnetic field profiles have been studied in different regions of the cavity. Also, the three parameters, quality factor (Q), shunt impedance (R_{sh}) and power dissipation (P),in the cavity at different frequencies have been calculated. The following diagram (as shown in Fig.2.5.1.2) shows electric field lines in the accelerating region (Dee-Liner region).

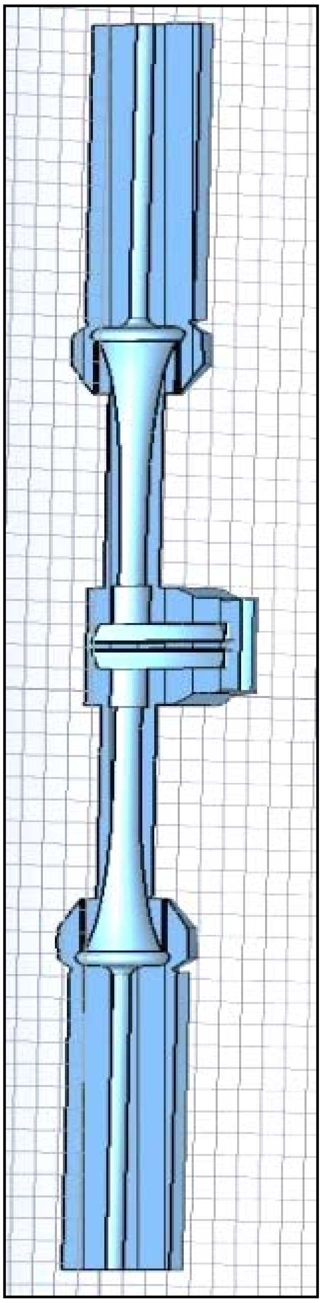

Fig.2.5.1.1 Cross-sectional CST MWS Model of half-wave resonant Cavity for the RF system of *K*500 Superconducting Cyclotron

The uncoupled Quality factor (Q_0) of the cavity (as shown in Fig.2.5.1.3) ranges from 4281 to 4925 with its peak value at about 17 MHz. It is observed from the plot (as shown in Fig.2.5.1.4) of Cavity length vs. Frequency, that the sliding short distance (from the median plane) varies from 4600 mm at 9 MHz to 1400 mm at 27 MHz. The cavity shunt impedance (R_{sh}) has been calculated as seen by the coupler. Due to the large radial extent of the Dee compared to the wavelength (λ), the Dee can be considered as a combination of many transmission line segments (as shown in Fig.2.5.1.5.) and is similar to this figure, which is the top view of the *K*1200 Dee showing the cross-sections of *K*1200 Superconducting Cyclotron [Reprinted with permission from J. Vincent, Ph.D. dissertation (MSU, USA, 1996), Copyright 1996 by J. Vincent]. Hence, the Dee voltage is a function of radius[23][24]. As SCC RF system is a high frequency system, a variation in voltage profile has been found along the Dee from the simulation. In order to have the radial voltage distribution (as shown in Fig.2.5.1.6) in the accelerating zone, voltage value was obtained by integration of the electric field in the median plane of the resonant cavity for different frequencies from 9 MHz to 27 MHz. The voltage variation is around 10% at 14 MHz, whereas 18% at 27 MHz. As the cavity volume decreases with the increase in operating frequency, the length of the Dee becomes more comparable to the wavelength at highest frequency and thus voltage variation along the Dee increases with frequency.

From the simulation, power dissipations (P) to achieve desired voltage at Dee have been found at different frequencies [25]. The RF power dissipation (for normalized Dee voltage of 80 kV) has been calculated as 26kW at 9MHz, 48kW at 27MHz and 32 kW at 14 MHz. Due to voltage variation along the dee, R_{sh} of the cavity is calculated (as shown in Fig.2.5.1.7) considering voltage at the radius of 400 mm (near Coupler region) and the calculated value is 123 kΩ at 9 MHz, 100 kΩ at 14 MHz and 67 kΩ at 27 MHz.

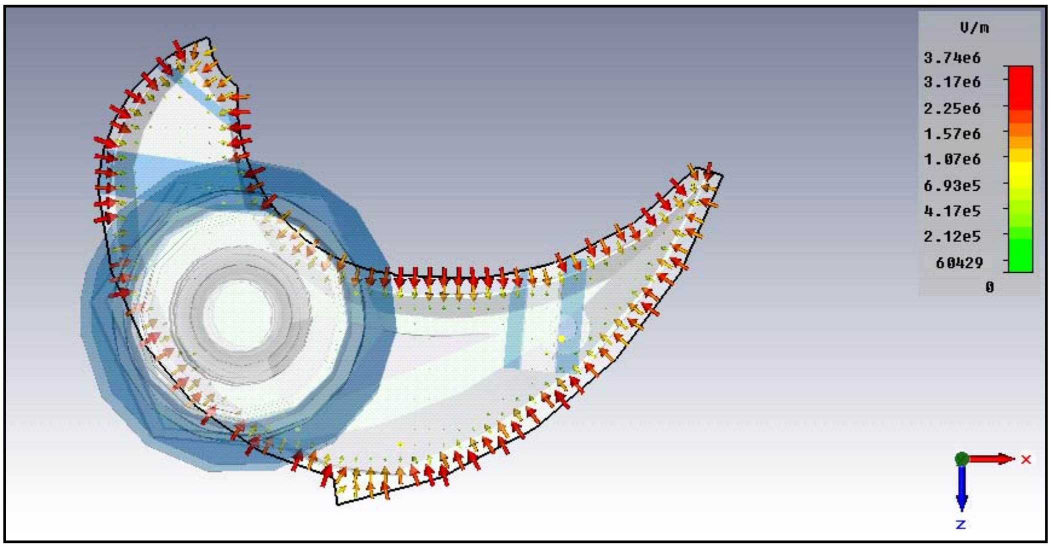

Fig.2.5.1.2 Electric Field lines in dee -liner region of the RF cavity, for the RF system of *K*500 Superconducting Cyclotron.

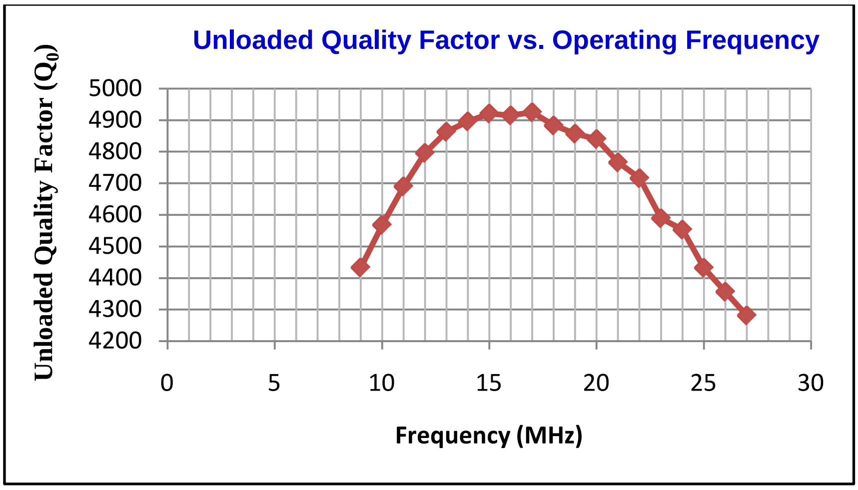

Fig.2.5.1.3 Unloaded Quality factors of the RF cavity at different frequencies, for the RF system of *K*500 Superconducting Cyclotron.

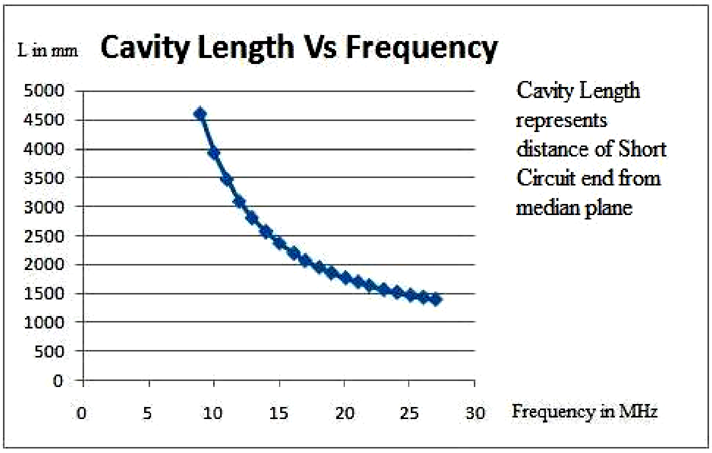

Fig.2.5.1.4 Cavity length at different frequencies, for the RF system of *K*500 Superconducting Cyclotron.

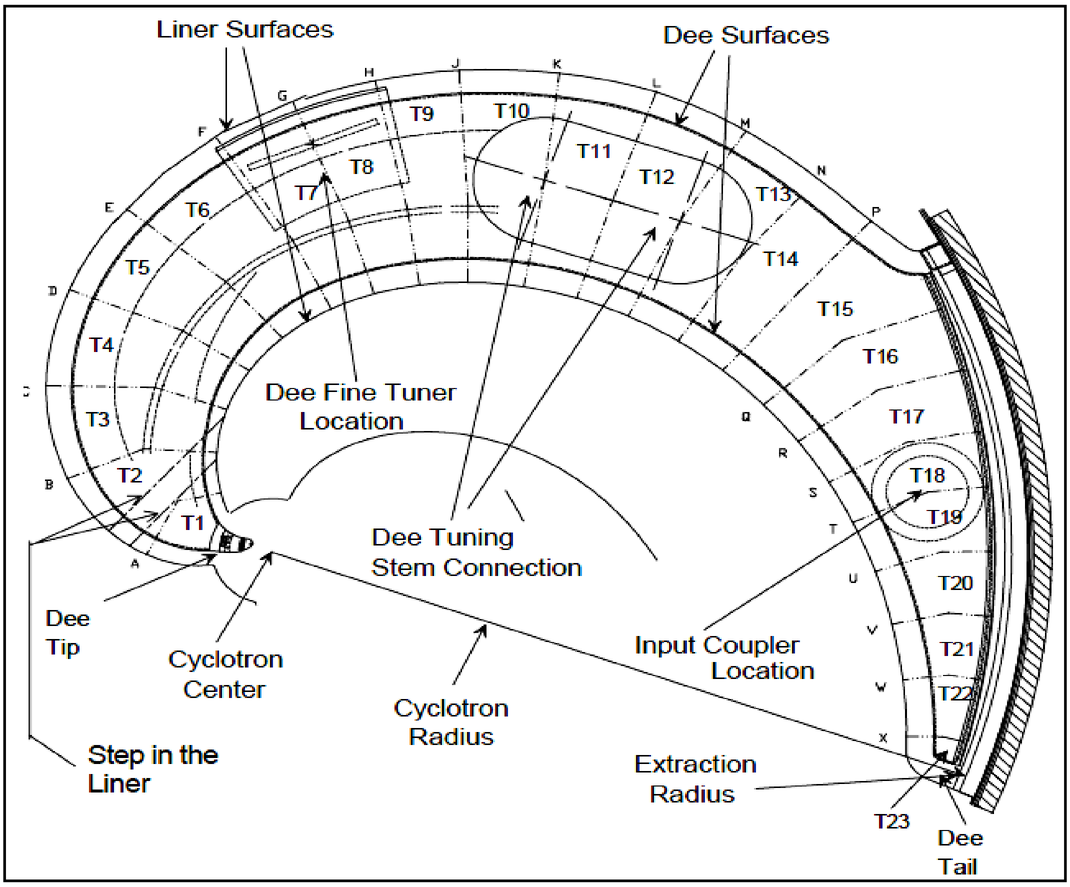

Fig.2.5.1.5 Dee as transmission line segments[23], for the RF system of *K*500 Superconducting Cyclotron.

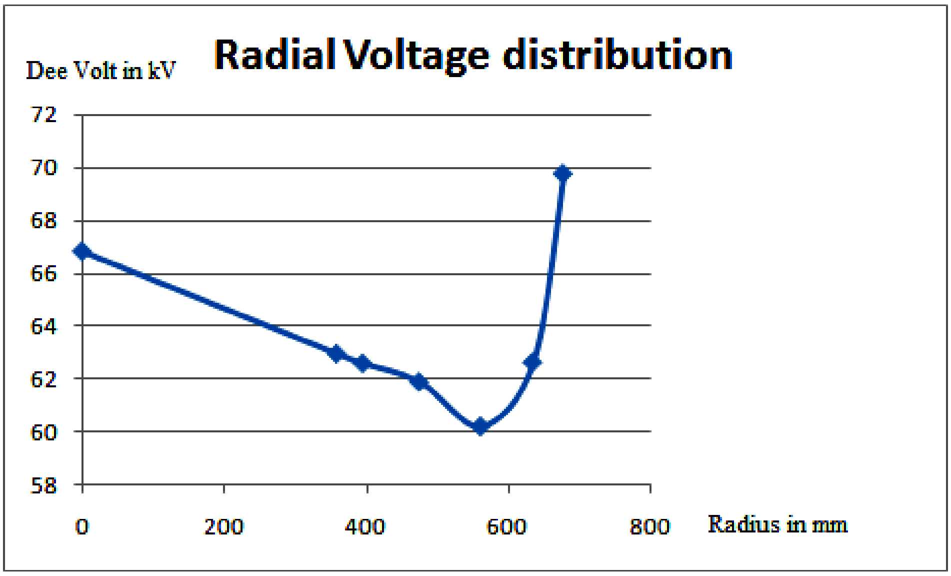

Fig.2.5.1.6 Radial Voltage distribution in the Dee of the RF cavity at 14 MHz, for the RF system of *K*500 Superconducting Cyclotron.

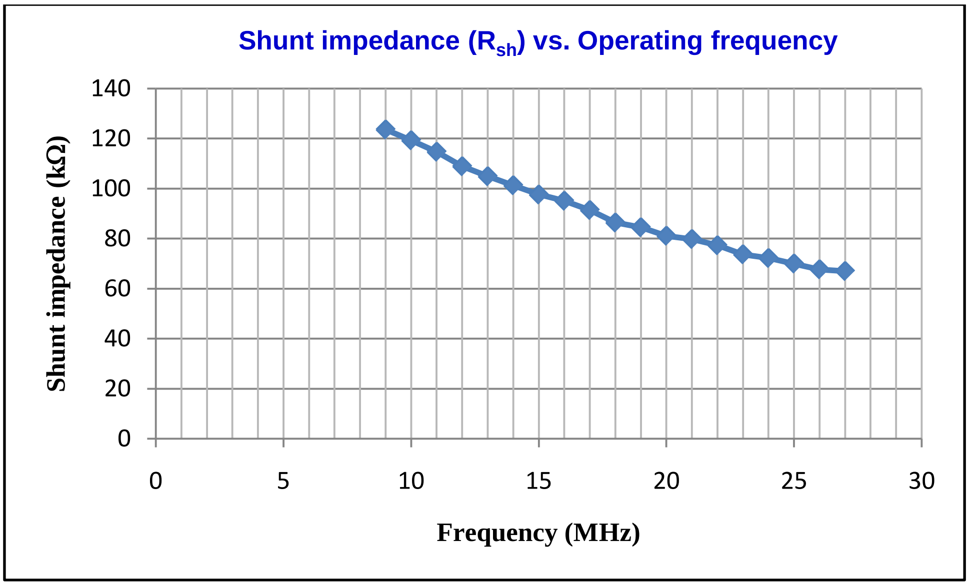

Fig.2.5.1.7 Shunt impedance variation with frequency of the RF cavity, for the RF system of *K*500 Superconducting Cyclotron.

2.5.2 High power RF Amplifiers

The high power RF amplifier (as shown in Fig.2.5.2.1) is based on Eimac 4CW 150,000E water-cooled tetrode[26] and the output tank circuit of the amplifier consists of a quarter-wave (λ/4) type variable length coaxial cavity. The short-circuited coaxial cavity is tuned by the precise movement (minimum 50 μm corresponding to tuning accuracy of 19.35 Hz at the lowest frequency and 1.135 kHz at the highest frequency) of the sliding short within the operating frequency range of 9 MHz to 27 MHz under unloaded condition.

The coaxial line is made of hexagonal outer conductor (with each side of hexagon 201.65±0.05 mm) and circular inner conductor (with outer diameter 58.42±0.05 mm). The sliding short plate is electrically connected to the outer and inner conductor of coaxial line by Be-Cu contact finger (as shown in Fig.2.5.2.2) with sliver-graphite (99%Silver+1%Graphite) contact ball at the tip. The sliding short contact must operate below the copper softening temperature (~460K), since the softening could lead to fusion welding. The inner and outer conductors are aligned concentric preferably within ±0.25 mm, because large asymmetry may give rise to uneven stress on the contact finger. The contact resistance is of the order of $0.7 m\Omega$ per finger.

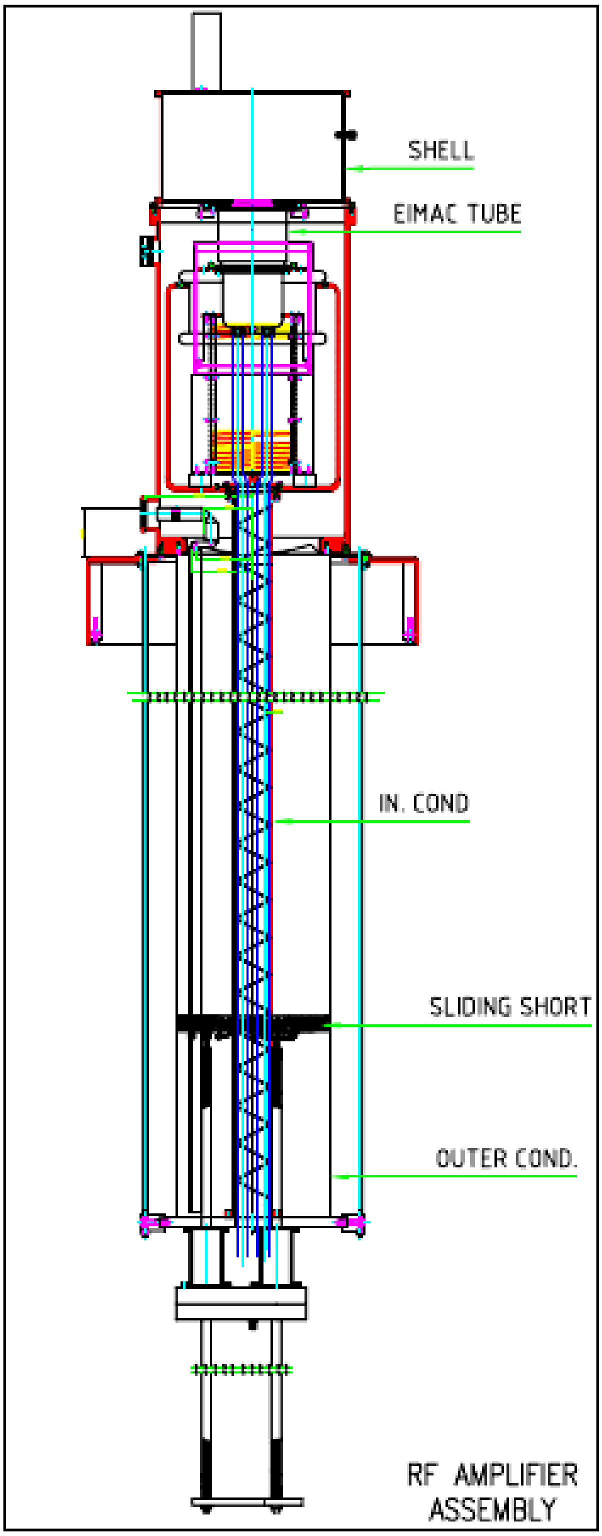

Fig.2.5.2.1 Cross-sectional view of high power rf amplifier, for the RF system of *K*500 Superconducting Cyclotron

Fig.2.5.2.2 Sliding short contact fingers for RF amplifier, for the RF system of *K*500 Superconducting Cyclotron

An inductive coupling loop is inserted along one side of the cavity (through the sliding short) at 1/5th voltage point to reflect nearly constant impedance at the anode of the tetrode. But as the length of the loop is comparable to operating wavelength, this assumption is not valid. So, by loop area trade-off it is kept in required range. Anode shell capacitance heavily loads the tank circuit and therefore, the cavity length is reduced, thus shifting the cavity higher order modes beyond 66 MHz. The output RF power (80 kW max) is taken out at 50Ω impedance through this inductive loop, which is matching the high cavity impedance to 50Ω.

The four identical Bridge-T networks (see Fig.2.5.2.3 (a) & (b)) in the control grid of the amplifier are driven with equal power levels of 250 watts each. The Voltage Standing Wave Ratio (VSWR) of the input circuit of the amplifier has been measured using Vector Network Analyzer (VNA) (See Fig.2.5.2.4) and obtained max of 1.14 at 18.18 MHz.

The precise movement of the sliding short is accomplished by a PC-based Stepper motor controlled system (as shown in Fig.2.5.2.5.), that can be operated locally or from RF Control Room through local area network (LAN).

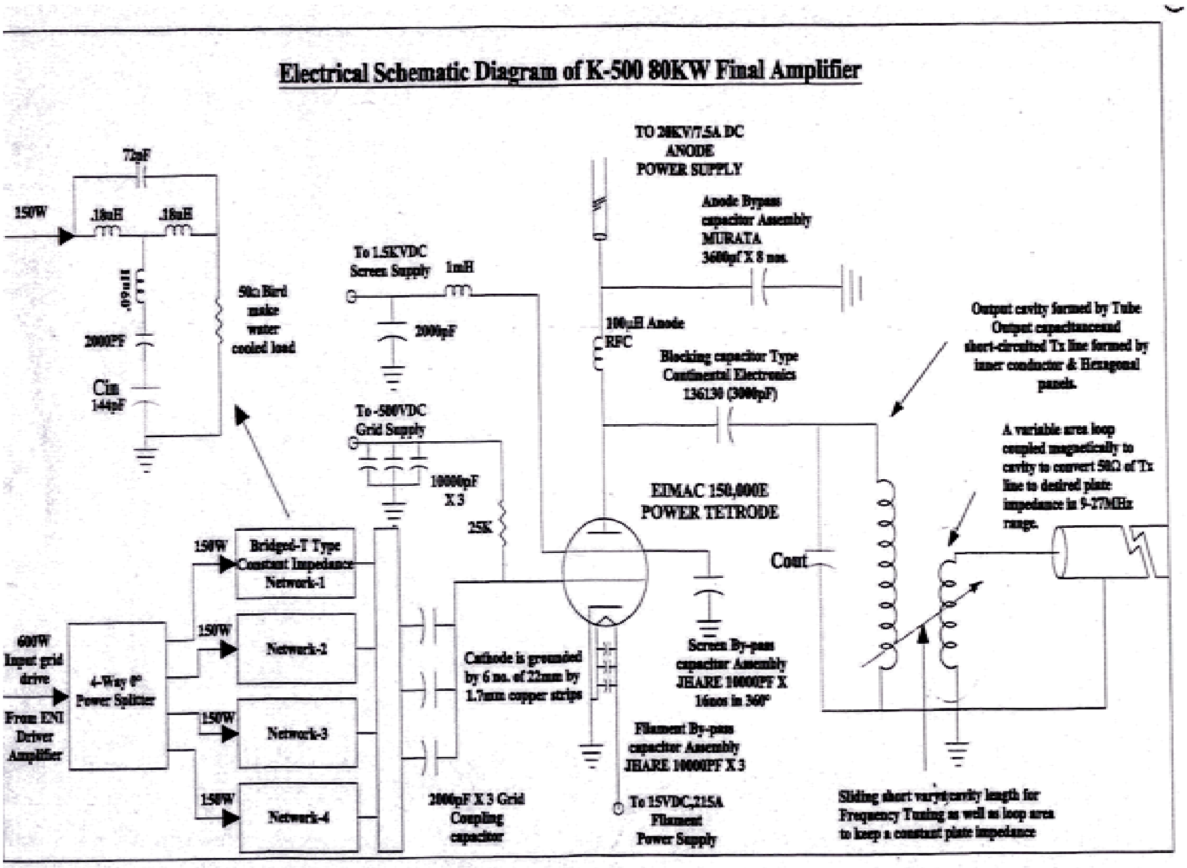

Fig.2.5.2.3(a)Electrical schematic diagram of 80 kW Final RF Amplifier for *K*500 SCC

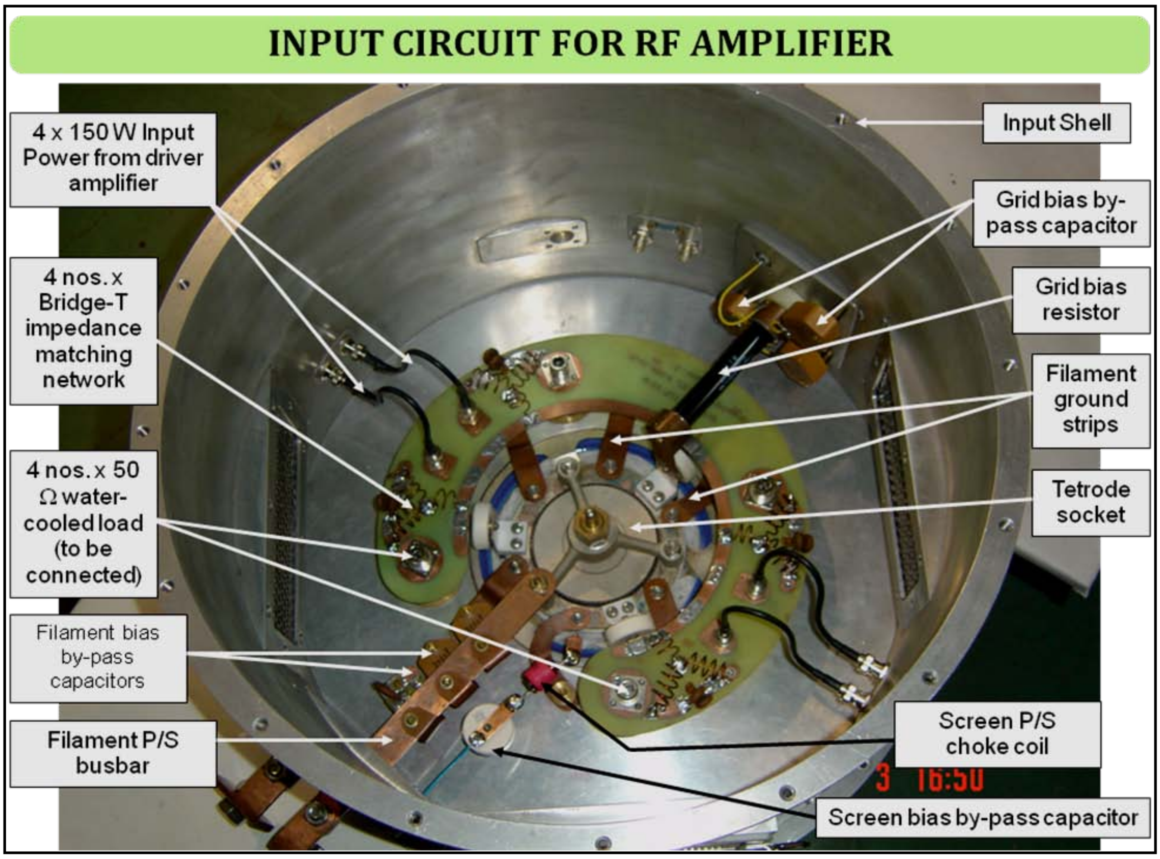

Fig.2.5.2.3(b)Input circuit (assembled) for amplifierfor *K*500 Superconducting cyclotron

Limit switches (as shown in Fig.2.5.2.6) are connected with the cavity for upper limit and lower limit of the movement. These limits are decided according to the required cavity length at 9 MHz (lowest frequency) and 27 MHz (highest frequency).

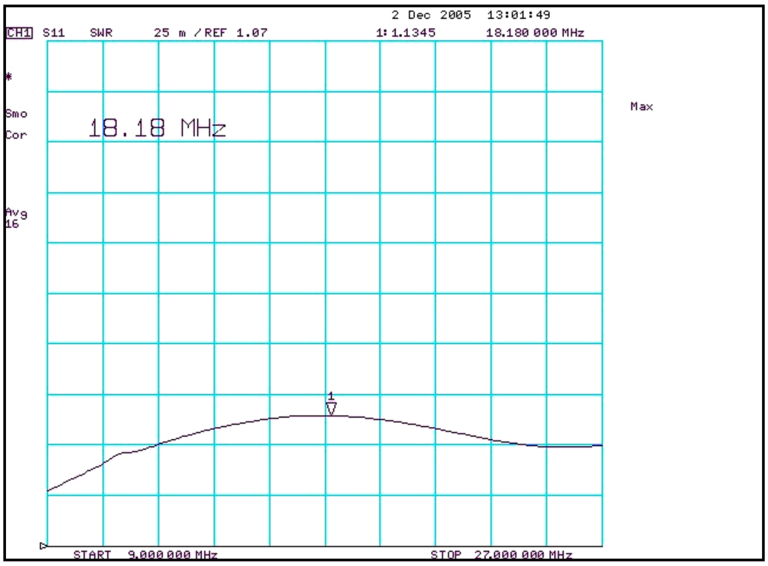

Fig.2.5.2.4 VNA measurement of input VSWR for amplifier

Fig.2.5.2.5 Stepper motor assembly with amplifier sliding short for *K*500 SCC

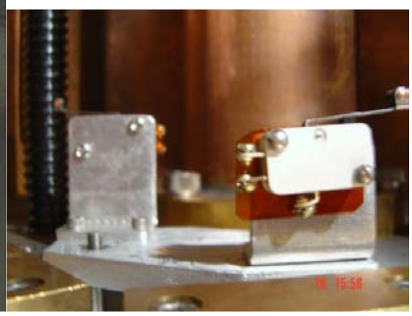

Fig.2.5.2.6 Limit switches assembly of the cavity

The anode of the tetrode is coupled to the cavity by a cylindrical Blocking capacitor (3000 pF) as shown in Fig. 2.5.2.7 (a) & (b).

(a) (b)

Fig.2.5.2.7 (a) Anode Blocking Capacitor and (b) Tetrode assembled with anode blocking capacitor for the amplifier for *K*500 Superconducting Cyclotron.

DC power supply (20kV@22.5A for three amplifiers) is fed to the anode through RF Choke (100 μH) and 8 nos. of High Voltage Filter capacitors (3600 pF, 30 kV) for each amplifier, as shown in Fig.2.5.2.8.One DC Power supply (1.5 KV@1A) is connected to screen terminal of each amplifier. The Screen by-pass capacitor (10000pF, 2.5 kV x 16 nos.) assembly (as shown in Fig. 2.5.2.9) is connected to the Screen terminal to prevent the RF from entering into the power supply.

Fig.2.5.2.8 Assembly of RF Choke & HV Filter capacitors.

Fig.2.5.2.9 Assembly of Screen by-pass capacitors.

The measured unloaded Q of the cavity varies from 4300 to 1800 (as shown in Fig.2.5.2.10) and the measured loaded shunt impedance values vary from 5kΩ to 1kΩfor 9 MHz to 27 MHz, as shown in Fig.2.5.2.11. Only for low frequency near 9 MHz presence of higher order modes is found [27]. But the values are significantly small. At 9 MHz, next higher order mode is found near 66 MHz with shunt impedance of 1.5k and at 10 MHz, next higher order mode is found near 81 MHz with shunt impedance of 1k.

Three numbers of 80 kW RF power amplifiers (as shown in Fig.2.5.2.12) have been installed in the vault area of K500 Superconducting cyclotron building. The cold RF measurement of the amplifier cavity has been successfully carried out using Vector Network analyzer (VNA). The amplifiers have been successfully tested at dummy with 70 kW output RF power at the highest design frequency of26.9999 MHz and the amplifiers being operated round-the-clock with the actual cavity load at various operating frequencies.

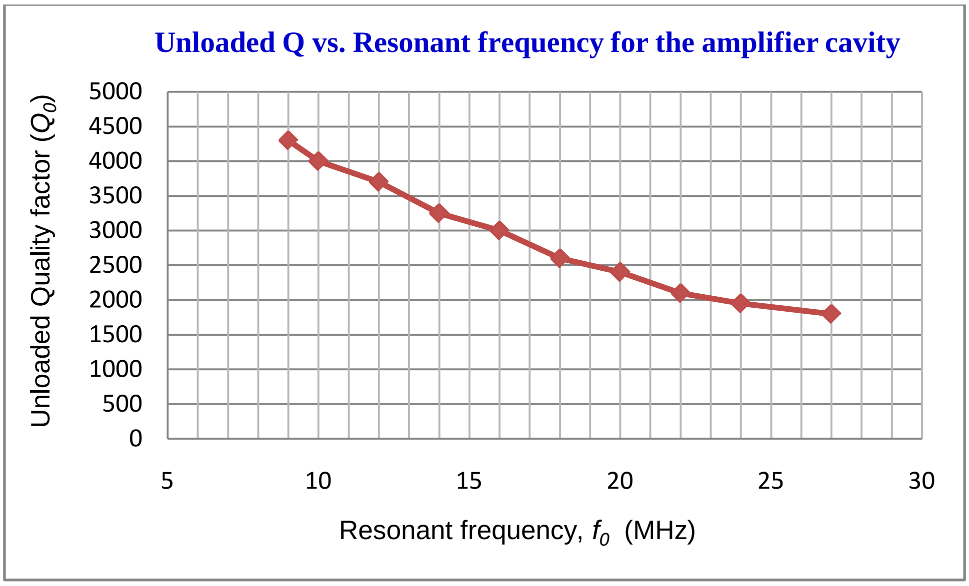

Fig.2.5.2.10 Plot of Unloaded Quality factor vs. resonant frequency for the amplifier of *K*500 Superconducting Cyclotron.

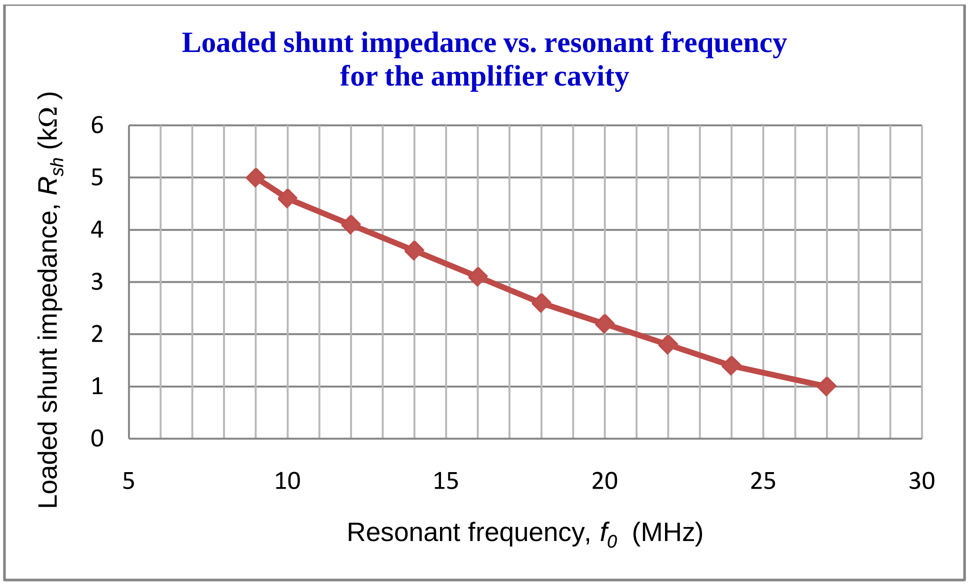

Fig.2.5.2.11 Plot of Loaded Shunt Impedance vs. resonant frequency for the high power final RF amplifier cavity of *K*500 Superconducting Cyclotron.

Fig.2.5.2.12 Installed final RF power amplifiers for the RF system of *K*500Superconducting Cyclotron.

2.6 RF Measurements of *K*500 Superconducting Cyclotron

2.6.1 Low Power measurements of RF Cavity

During the commissioning of SCC RF system, RF cavity characterisation has been carried out. Cavity size, quality factor and shunt impedance has been measured using standard methods.

SCC RF cavity is coarsely tuned at different frequencies by moving the sliding shorts of upper and lower main resonator cavity and coupling capacitor. Fine tuning is achieved by varying the trimmer capacitor[28]. Tuning is done using Vector Network Analyser (VNA) and the condition for tuning is to achieve critical coupling at the input of coupler. As the tetrode-based final power RF amplifier has output impedance of 50 Ω, we tried to match the impedance at the coupler port close to 50 Ω to achieve critical coupling. The scattering parameter S11 measurement with Vector Network Analyzer in Smith Chart format (as shown in Fig.2.6.1.1) indicates that the measured impedance at the coupler port at 14.00072 MHz operating frequency is (51.281+j0.736) Ω, which is a very good result.

The loaded or coupled Quality factor ($\boldsymbol{Q_L}$) of the cavity has been measured[25] from cavity charging and discharging time by energizing the cavity with a RF signal under pulsed condition. If U is the stored energy in a cavity, P is the power loss, and ω (= 2πf) is the operating frequency, then

$$-\frac{dU}{dt} = P \qquad \text{and} \qquad Q_L = \frac{\omega U}{P},$$

which leads to the following relation.

$$\frac{dU}{dt} = -\frac{\omega U}{Q_L} \quad \text{.....................} \quad (2.6.1.01)$$

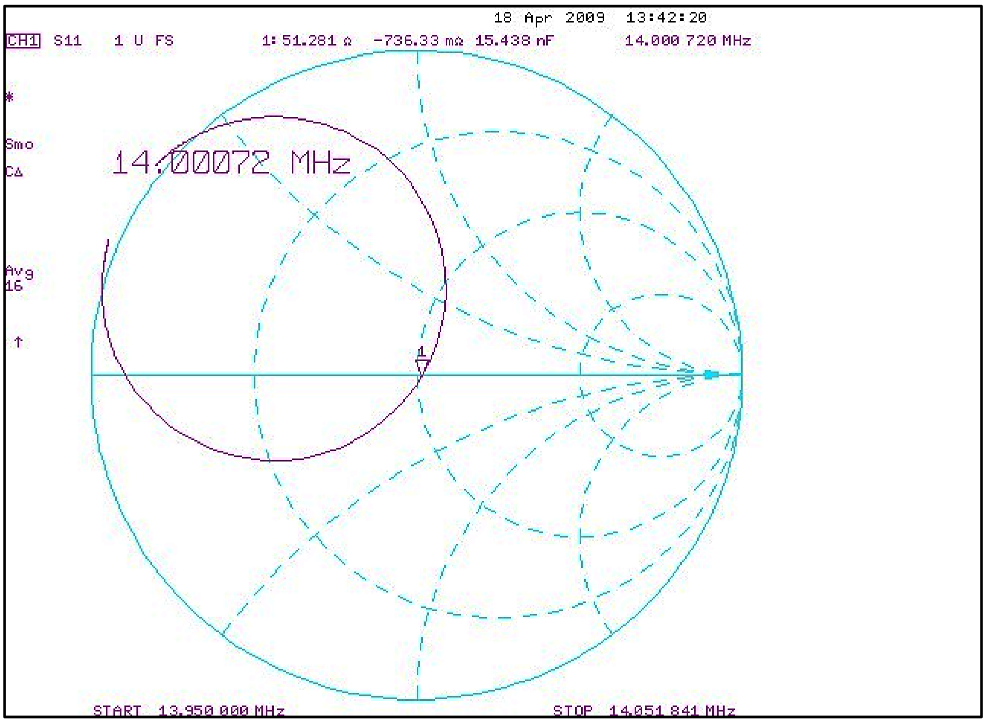

Fig.2.6.1.1 Measurement of input impedance (in Smith Chart format) with Vector Network Analyzer(VNA) of the cavity at the coupler port matched at 50 Ohm under tuned condition at 14.00072MHz.

From this equation (2.6.1.01), the stored energy in the cavity will decay according to the equation (2.6.1.02).

$$\boldsymbol{U = U_0 e^{-\frac{\omega t}{Q_L}}} \text{.............(2.6.1.02)}$$

The time constant of the cavity stored energy is, $\boldsymbol{\tau} = \frac{\boldsymbol{Q_L}}{\boldsymbol{\omega}}$. As the cavity stored energy is proportional to the square of voltage or current in the cavity, the voltage in the cavity has time constant,$\boldsymbol{\tau_V} = \boldsymbol{2\tau} = \frac{\boldsymbol{2Q_L}}{\boldsymbol{\omega}}$. The Cavity has been operated at a certain frequency, say, 14 MHz sinusoidal wave modulated with pulse (duty cycle 10% and time period 3ms). The Cavity charging/discharging time is obtained from the Dee voltage pick offsignal on the Oscilloscope (as shown in Fig.2.6.1.2). $\boldsymbol{Q_L}$of the cavity can be calculated from the measured voltage time constant. As the cavity is critically coupled to the RF source, the uncoupled Quality factor ($\boldsymbol{Q_0}$) of the cavity will be $\boldsymbol{2Q_L}$. By this procedure, we have measured cavity voltage time constant ($\boldsymbol{\tau_V}$) as 39.8 μS, which results in$\boldsymbol{Q_L = 1750}$ at 14 MHz. and$\boldsymbol{Q_0} =$

$\mathbf{3500}$. At the operating frequency of 21 MHz, the measured $\boldsymbol{\tau_V}$is 21.6 μS and the resulting $\boldsymbol{Q_0} = \mathbf{2850}$.

In order to find out the cavity shunt impedance (R_{sh}) from the relation,$\boldsymbol{R_{sh}} = \frac{\boldsymbol{V^2}}{\boldsymbol{2P}}$, it is necessary to measure power dissipation (P) and RF Dee Voltage (V) of the cavity. For this purpose, a Directional Coupler (Make-Bird electronics Corp.) has been connected with the 50 ohm transmission line ($3\frac{\mathbf{1}}{\mathbf{8}}$inch rigid coaxial line), which is used to transfer power from final RF amplifier to the main resonator cavity. Signal from directional coupler is fed to the Bird power meter which gives the forward power fed to the main resonator cavity. The absolute Dee voltage of the cavity is measured using X-ray spectrum method with high RF power applied, as discussed in the following section.

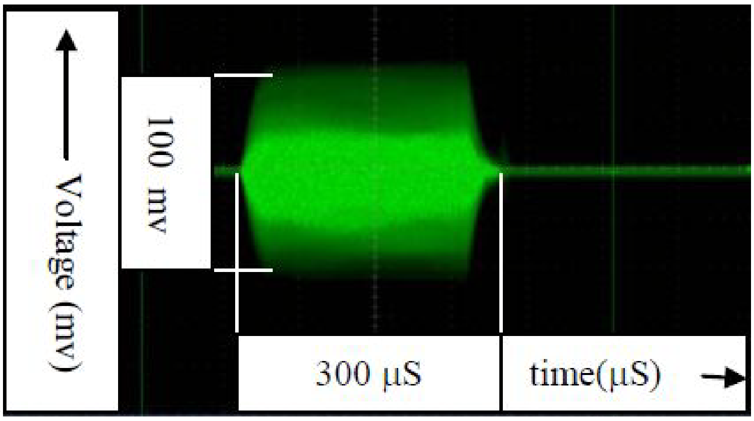

Fig.2.6.1.2 Dee Pick off Waveform in pulsed mode operating condition of the cavity with RF power

2.6.2 Absolute Dee Voltage measurement

The RF Dee voltage is an important parameter in accelerator operation. But measuring the amplitude of RF voltage precisely and accurately is very difficult with common electronics method, which depends upon coupling to the Dee. Moreover, once we used a high impedance and high voltage probe to contact RF cavity and measure RF voltage directly, as the probe was in contact with RF cavity, the resonant characteristics of RF cavity gets disturbed and the accuracy of the measured RF voltage is affected greatly.

Therefore, using a different kind of method[29] using X-ray spectrum to measure RF voltage becomes important, fairly accurate and reliable.

Under the condition of no beam injection in the cyclotron, when RF cavity generates high value of Dee voltage between acceleration gap, the field-emitted electrons are accelerated by the RF electric field between the cavity electrodes (Dee and a part of RF Liner). When the accelerated electrons impact on the electrodes, the energy of accelerated electrons is transferred to the atoms of electrode material. Meanwhile, electromagnetic radiation takes place by the transition of atomic inner electrons. Therefore, a kind of X-ray is generated with continuous energy spectrum, called "Bremsstrahlung". The energies of electrons accelerated by RF electric field are distributed continuously. The maximum electron energy corresponds to the peak value of Dee voltage. When the electrons collide with the atoms of electrode's material, the transferred energies to the atoms are from zero to the maximum kinetic energy of the accelerated electrons. Hence, the X-ray spectrums demonstrate continuous energy properties. If we detect the end-point or the maximum energy of the X-ray spectrum, the RF cavity's peak voltage can be determined.

A cadmium-telluride (CdTe) detector XR-100T-CdTe (a high performance X-ray and gamma ray detector), preamplifier, and cooler system using a 5x5x1 mm Cadmium Telluride (CdTe) diode detector, is selected for X-ray spectrum measurement. The detector can be operated in air or in vacuum down to 10^{-8}Torr. The entire detector and preamplifier box (as shown in Fig.2.6.2.1) is placed inside the vacuum chamber. In order to avoid overheating and to dissipate the 1 Watt of power (needed to operate the detector), adequate heat conduction to the chamber walls has been provided by using the four mounting holes. A Model 9DVF 9-Pin D vacuum feed-through connector on a Conflat flange is available to connect the detector to the digital pulse processor (PX5) outside the vacuum chamber. Power to the detector is provided by the PX5. The PX5 is DC powered by an AC adaptor and provides both a variable

Digital Pulse Shaping Amplifier (0.2 μs to 100 μs shaping time), the multi-channel analyzer (MCA) function, and all necessary power supplies for the detector and preamplifier. The PX5 connects via USB, to a PC (the schematic of measurement set-up as shown in Fig.2.6.2.2).A mechanical support system has been designed and fabricated to hold the X-ray detector inside the magnet iron for placing it near the DEE.

Fig.2.6.2.1 X-ray detector (AMPTEK make, XR-100T-CdTe detector) with feed through and cablings.

The detector is inserted through lower RF liner near the cavity lower Dee and the hole (of 79.5mm diameter) for the insertion of the detector is located (as shown in the following Fig.2.6.2.3) at a radius of 591.15 mm at an angle 198.5^0. The detector assembly is connected through a metal bellow for providing 20 mm movement, if required, of the detector inside the cavity vacuum.

Before measurement, the energy calibration of the XR-100T-CdTe detector is done with a known X-Ray source ^{133}Ba. The MCA channel numbers were calibrated (as shown in Fig.2.6.2.4) with centroid method as per the following quadratic calibration equation (2.6.2.01).

$$Energy\ (in\ keV) = A + Bx + Cx^2 \quad \ldots\ldots\ldots\ldots\ldots\ldots\ldots. (2.6.2.01)$$

[where, $x = channelnumber$, $A = 0.774014\ keV$, $B = 0.17737\ keV$, $C = 1.42036.10^{-5} keV$].

In the present measurement, the peak energies of a known radiation source Barium (^{133}Ba) at 30.973keV corresponds to Channel No.168,at 34.987keVcorresponds to Channel No. 190and at80.997keVcorresponds to Channel No. 437.To avoid the pile up error, the count rate has been reduced by using a lead (Pb) collimater (a lead cap with a hole of 2 mm diameter and height of 12 mm) and an aluminium cap of thickness 3 mm on the detector has been provided to stop low energy X-rays.

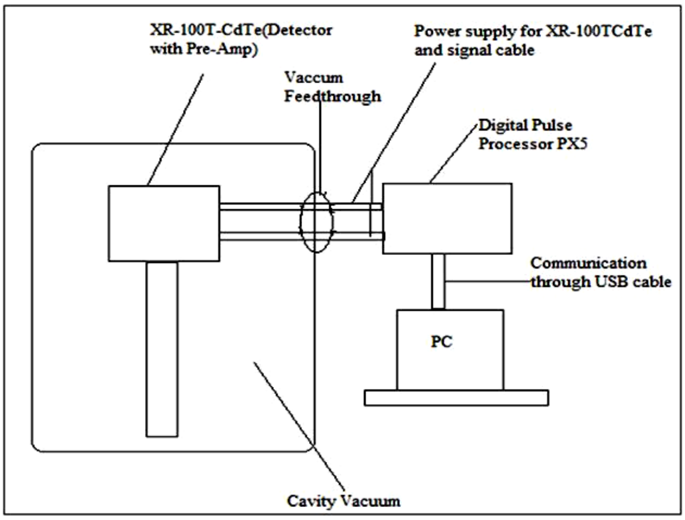

Fig.2.6.2.2 Schematic Diagram for the X-ray spectrum measurement set up for Dee voltage of *K*500 Superconducting cyclotron.

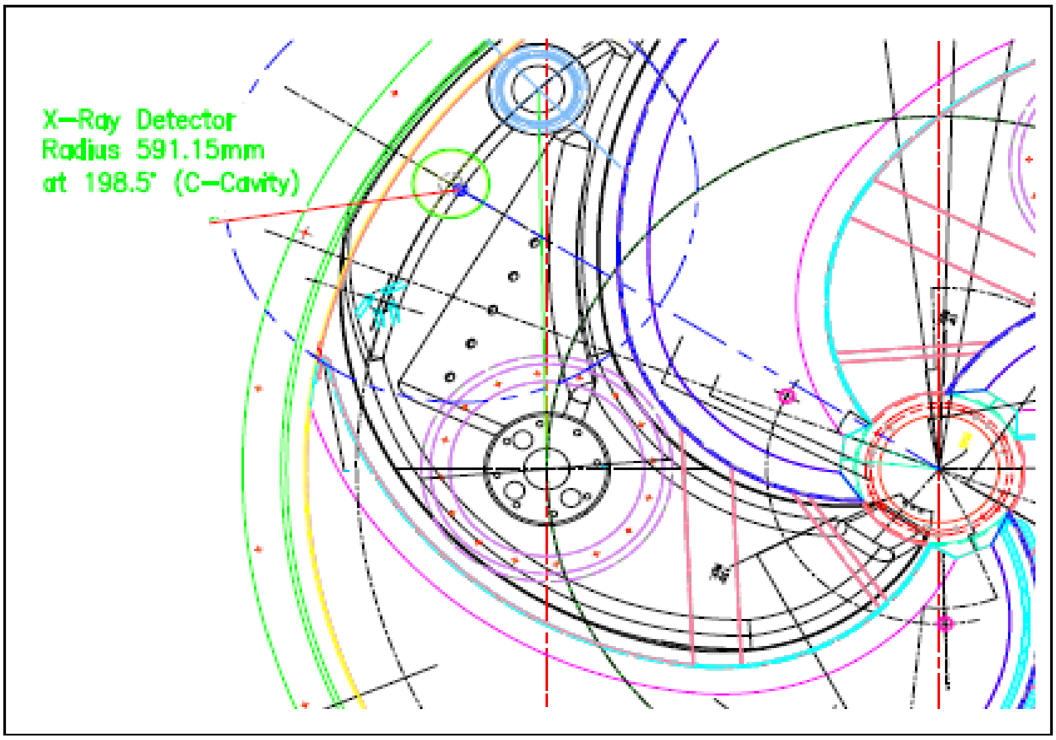

Fig.2.6.2.3 Place of insertion of X-ray Detector Probe at the Dee region (in vacuum).

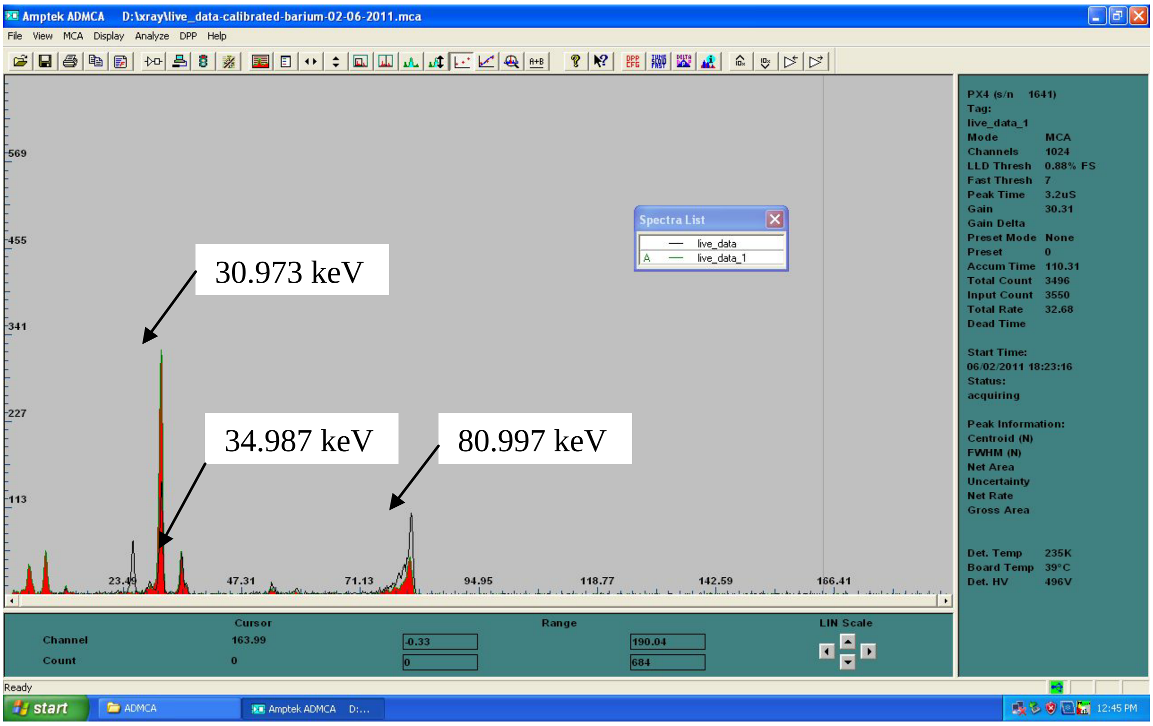

Fig.2.6.2.4 Calibrated value of the channel number of Multichannel Analyzer (MCA) with reference to the known Barium (Ba^{133}) source energy peaks.

2.6.3 Shunt Impedance measurement

In this measurement[25], SCC RF cavity was excited at 14 MHz and RF voltages were measured by X-ray spectrum method at different Dee voltage end points. The measured spectrum (as shown in Fig. 2.6.3.1, Fig.2.6.3.2, Fig.2.6.3.3) fitted with calculated X-ray spectrum, has been illustrated in following figure (Fig.2.6.3.4). Locating the endpoint energy of a measured spectrum can be troublesome because of statistical uncertainties, and background noise. To improve the measurement of the endpoint, the X-Ray bremsstrahlung spectrum is calculated and fitted to the measured data. The measured R_{sh} is 64 kΩ as compared to the simulated result of 100 kΩ.

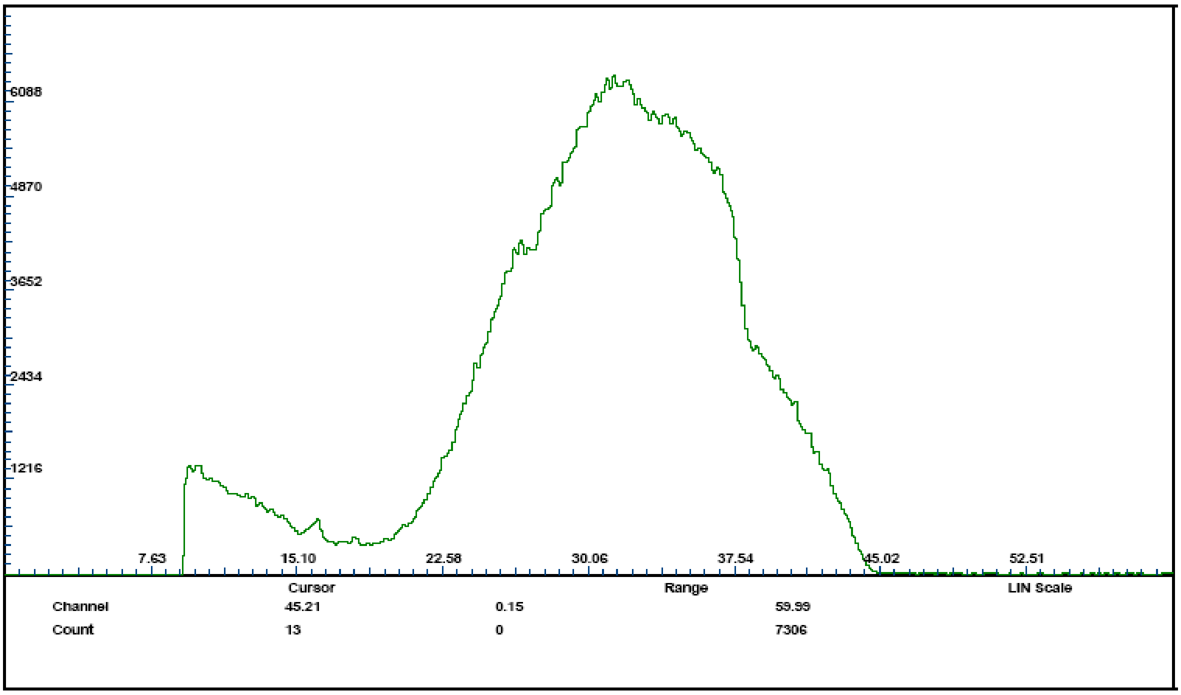

Fig.2.6.3.1 Plot of Count vs. Energy of bremstrahllung X-ray spectrum for Dee Voltage at 45 kV developed in the cavity operating at 14 MHz, for the *K*500 Superconducting Cyclotron.

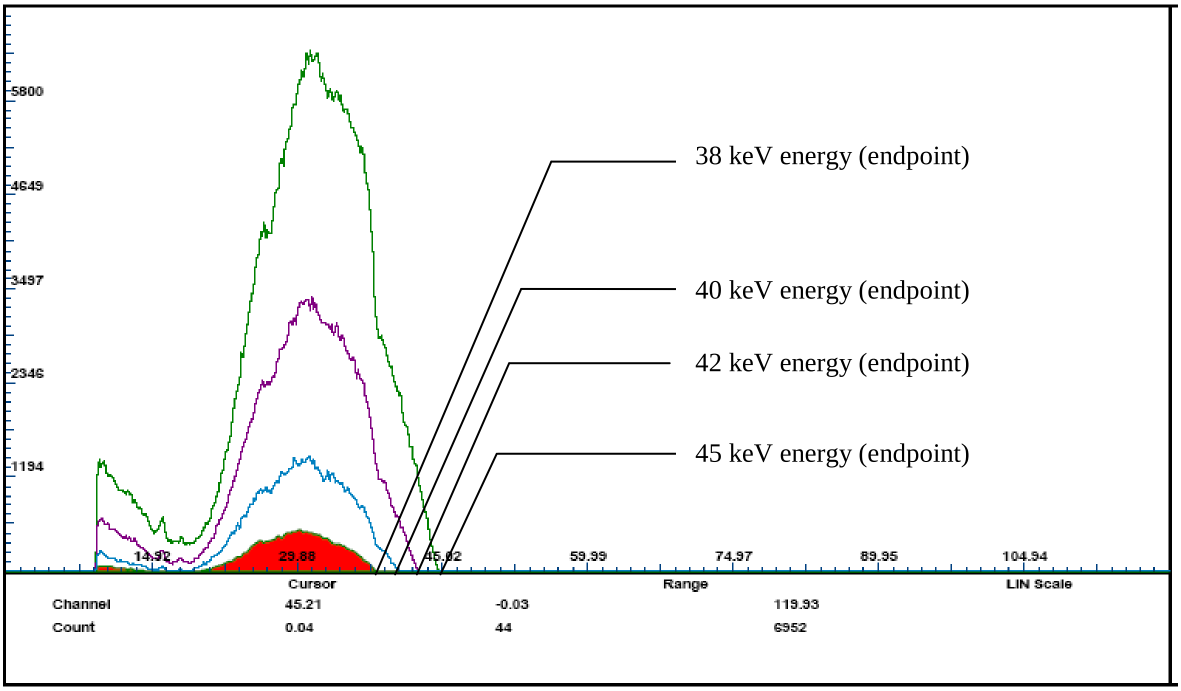

Fig.2.6.3.2 Plot of Count vs. energy of bremstrahllung X-ray spectrum for different Dee voltages at 38kV, 40 kV, 42 kV, 45 kV developed in the cavity operating at 14 MHz, for the *K*500 Superconducting Cyclotron.

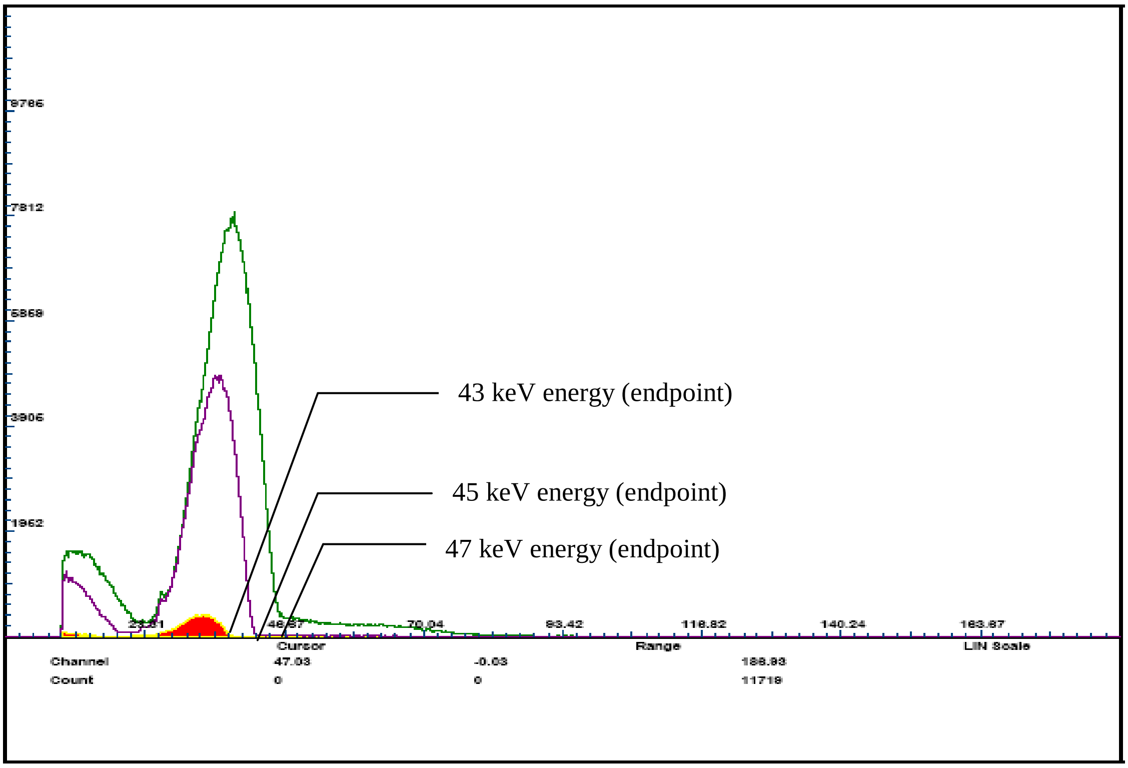

Fig.2.6.3.3 Plot of Count vs. energy of bremstrahllung X-ray spectrum for different Dee voltages at 43 kV, 45 kV, 47 kV developed in the cavity operating at 16 MHz, for the *K*500 Superconducting Cyclotron.

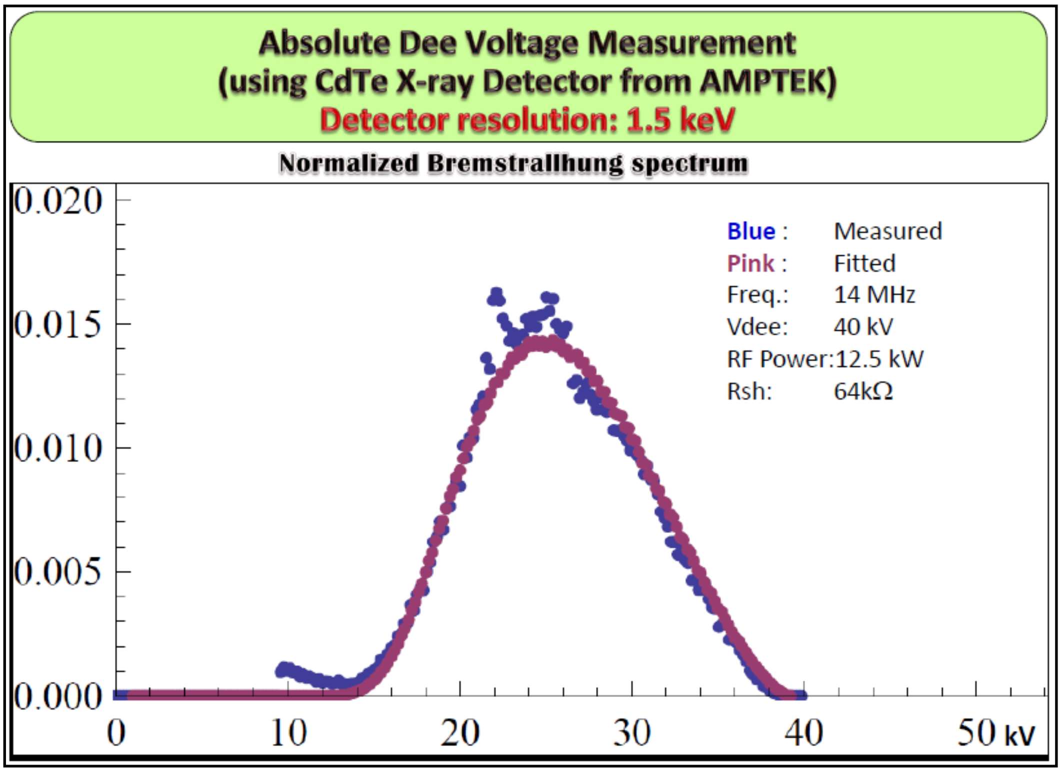

Fig.2.6.3.4 Measured X-ray Spectra at 40kV dee Voltage at 14 MHz, for the *K*500 Superconducting Cyclotron.

The simulation of the SCC RF cavity using CST Microwave Studio gives a prior knowledge about the cavity performance before commissioning the RF system. Cavity Sizes as we obtained at different frequencies from the simulation, are more or less same with the measured cavity sizes at tuned conditions. But, the measured quality factor and shunt impedance values are somewhat less than the simulated values. This may be due to a number of facts as mentioned below. Firstly, cavity is considered to be made of a copper with conductivity, $\sigma = 5.8 \times 10^{7}\ (\Omega\mathrm{m})^{-1}$ in the simulation although in practical situation, such a complicated large mechanical structure is full of brazed and welded joints and also some contacts are not made of copper. Secondly, as the power is fed to the cavity, temperature of the cavity increases causing increase of the resistance of the cavity material. These factors will increase loss in the cavity causing the reduction of quality factor and shunt impedance. Another factor will come into play in case of measurement of shunt impedance. Shunt impedance is measured from RF dee voltage measurement by X-ray spectrum method. Though this method is a absolute RF voltage measurement method, it depends on geometry of the cavity and due to variation of voltage along dee, it may give lower voltage depending on point of insertion of the probe. From the simulation, we have noticed that the voltage in the zone of X-ray detector probe is not the highest voltage at dee. So this will lower the shunt impedance by some percentage.

2.7 Cavity Conditioning for *K*500 SCC

With vacuum level inside the cavity having 1.0×10^{-8} mbar and magnetic field off, we started feeding RF power in pulse mode at 5% duty cycle (ON Time ~ 150 μS) to the cavity and kept on increasing power level gradually. Then duty cycle is raised to 10% (ON Time ~ 300 μS) and similarly the power level has been increased gradually till the any sparking inside the cavity is observed. The pick-up signal from the Dee has been observed in the oscilloscope. The normal desired signal from the Dee Pick-up port has been shown in Fig.2.6.1.2. When multipacting phenomena[30] occurs inside the cavity, the Dee pick-up signal gets distorted as shown in Fig.2.7.1and immediately the pressure inside the cavity gets increased very rapidly. When RF drive is put off, vacuum level improved very fast and came back to the original level. This indicates that the phenomena of multipactoring occurred in the virgin cavity with a lot of trapped gases and they were getting ionized under the low power RF field. After feeding RF power in pulse mode in a conservative way for a day or two, we started feeding power in continuous-wave (CW) mode. After some time,as we keep on increasing RF power to the cavity, finally we could overcome the multipacting zone and achieved steady RF field inside the cavity. Vacuum interlock was set at 1.0×10^{-7}mbar.

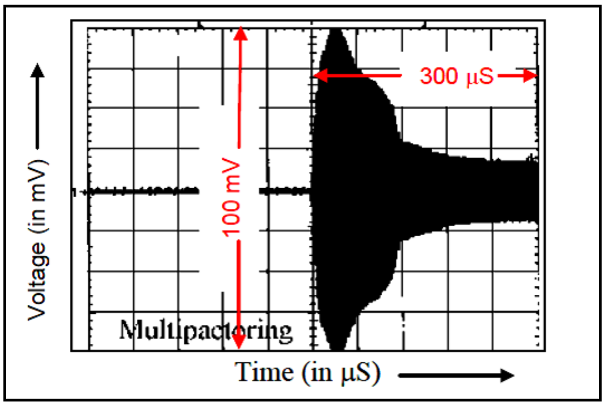

Fig.2.7.1 Dee Pick off Waveform in pulsed mode during maultipacting condition of the RF cavity, for the *K*500 Superconducting Cyclotron.

To cross the multipacting level, pulsed input RF power of around 2kW is preferred in order to reduce the conditioning time. After this we could achieve Dee voltage up to 50kV, with forward input RF power of around 25kW(at the operating frequency of 19 MHz) into the cavity and maximum reflected power reading of 200W only measured with RF power meter of make-Bird Electronic Corp.,USA. The amplitude of the dee voltage is measured by dee-pick-up signal, and also it is calibrated according to the cavity shunt impedance, as measured from the absolute dee voltage measurement by using X-Ray calibration method.

CHAPTER –3

SUPERCONDUCTIVITY IN ACCELERATORS

3.1 Basics of Superconductivity

In this chapter, a thorough literature study on superconductivity has been discussed. It is observed that a normal conducting high purity copper material does not exhibit superconductivity, when cooled down to very low temperature. The conductivity (σ) of high purity copper, at very low temperature, increases around 5000 times[31]and the surface resistance, R_s , (being proportional to $\frac{1}{\sqrt{\sigma}}$) and so, RF power loss (being proportional toR_s) is expected to be reduced by $\sqrt{5000} \approx 70$. But this does not happen due to Anomalous skin effect[31]. The skin effect, in general, takes place due to surface currents in the conducting material (copper) which short circuit the electric field parallel to the surface. In case of copper under cryogenic temperature, the mean free path of the electrons gets larger and so the surface resistance of copper does not decrease further. Instead it remains almost at a constant minimum value (as shown in Fig.3.1.1). This phenomenon is called as Anomalous Skin Effect.

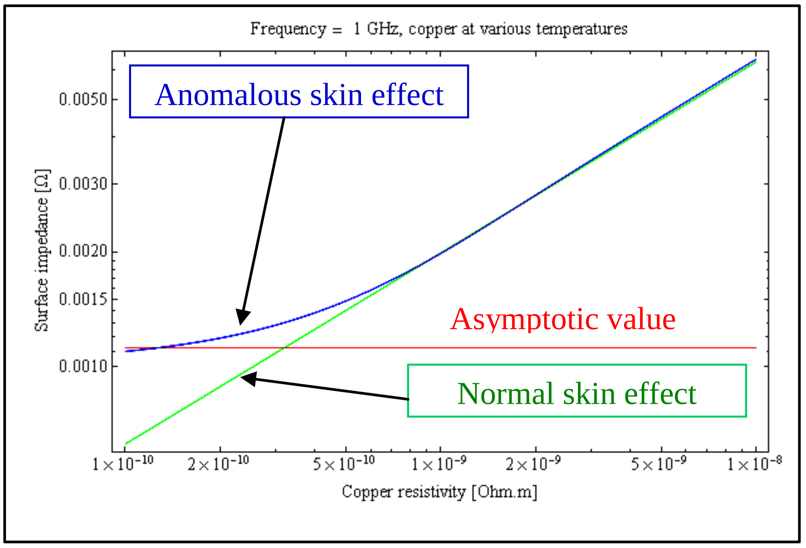

Fig.3.1.1 Plot of surface impedance vs. resistivity for copper cavity at 1 GHz [32].

A perfect superconductor, when cooled below its critical temperature (T_c), exhibits two characteristics — zero electrical dc resistance and perfect diamagnetism. Above the critical temperature (T_c) it exhibits the property of a normal metal and rather behaves as a bad conductor. For example, below T_c(<4.2K for niobium material) niobium exhibits superconductivity (as shown in Fig.3.1.2(a)) and also exhibits diamagnetism. It means that the susceptibility, $\chi = -1$. We know that,

$$B = \mu_0 H(1 + \chi) = \mu_0 (H + M)$$

This means that there can be *no* magnetic field (*B*) inside a perfect diamagnet, because the magnetization (M) is directed opposite to the H field and thereby cancels it. Here, μ_0($\approx 4\pi . 10^{-7}$ Henry/meter) is the permeability of the medium (air or vacuum).

$$M = -H$$

When a superconductor is placed between the pole pieces of a magnet (with magnetic field less than the critical magnetic field of the superconductor), B field lines from the magnet do not enter into the superconductor, but go around it, and its own internal field remains zero (as shown in Fig.3.1.2(b)). This field distribution is the resultant of the superposition of the uniform applied field and the reversely magnetized superconducting sphere. This phenomena of perfect diamagnetism shown by a superconductor is called "Miesssner effect"[33].

But in normal state, niobium is not a good conductor. However, copper, silver etc. are much better conductors in normal state. But they do not behave as superconductors when cooled to cryogenic temperature.

The ground state of a material is unstable with respect to pairs of 'bound' electrons (*i.e.*, Cooper pairs) and they are formed by electron-phonon interactions[33]. These interactions take place when an electron in the cation lattice distorts the lattice around it (as shown in Fig.3.1.3) and creates an area of greater positive charge density around itself. Another electron at some distance in the lattice is then attracted to this charge distortion (phonon). The electrons are thus indirectly attracted to each other and form a Cooper pair. This attraction between two electrons (of a cooper pair) is mediated by the lattice which creates a 'bound' state of the two electrons. Mathematically, the Cooper pair is more stable than a single electron within the lattice, it experiences less resistance (although the superconducting state cannot be made up entirely of Cooper pairs as this would lead to the collapse of the state). Physically, the Cooper pair is more resistant to vibrations within the lattice as the attraction to its partner will keep it 'on course'. Therefore, below the critical temperature, Cooper pairs move through the lattice relatively unaffected by thermal vibrations (electron-phonon interactions).

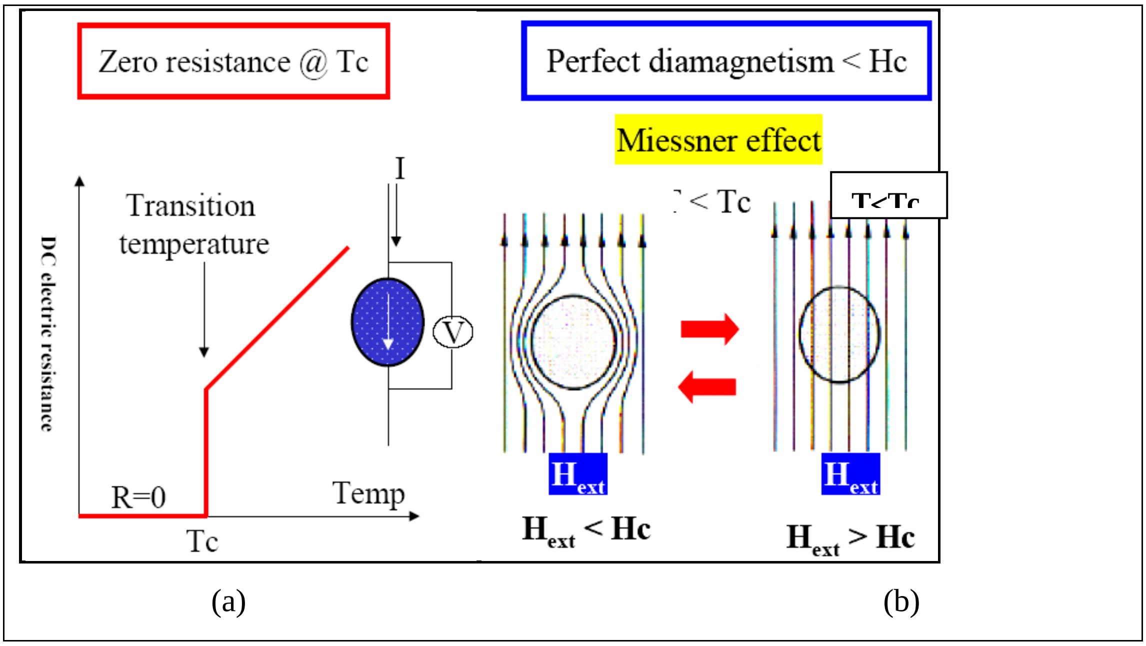

Fig.3.1.2 (a) Supercondutor exhibits zero resistance below critical temperature and (b)also exhibits perfect diamagnetism below critical magnetic field [Courtsey: K. Saito, KEK][34].

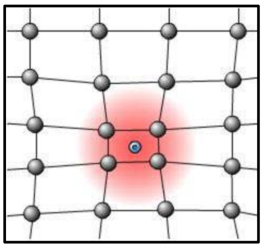

Fig.3.1.3 Schematic showing lattice distortion around an electron causes an increase in positive charge density that will propagate along the lattice with the cation vibrations.

3.2 RF Superconductivity

The BCS theory[33] of Superconductivity explains that the super-current is carried by Cooper pairs. Each cooper pair is formed by two super-electrons**.** The response of a superconductor to an alternating (ac) field is described by "Two-fluid model"[33]. According to this model, Cooper pairs are superfluid and unpaired electrons are normal fluid having conductivity (σ_n).The following paragraph discusses about the response of two fluids to a periodic sinusoidal electric field.

In presence of periodic sinusoidal electric field, the normal current obeys Ohm's law and dissipates power.

$$J_n = \sigma_n E_0 e^{-j\omega t} \quad \text{...(3.2.1)}$$

[where, J_n is the current density of normal conductor,σ_n is the conductivity of normal conductor, E_0 is the peak electric field, ω $(= 2\pi f)$ is the angular frequency of the periodic electric field ($E_0 e^{-j\omega t}$), f is the frequency of the periodic electric field, *t* is the time and$j(= \sqrt{-1}$**)** is complex number.

Cooper pairs are accelerated by the applied electric field and the force acting on the cooper pair can be expressed as,

$$m_c . \frac{dv_c}{dt} = -2eE_0 e^{-j\omega t} \quad \text{....................................(3.2.2)}$$

[where, m_c is the mass of a cooper pair, v_c is the velocity of a cooper pair,*e* is the magnitude of one electronic charge, –2*e* is the total charge of a cooper pair having two electrons].

$$\frac{dv_c}{dt} = -\frac{1}{m_c} 2eE_0 e^{-j\omega t} \quad \text{…………………………..(3.2.3)}$$

$$\int dv_c = -\int \frac{2e}{m_c} E_0 e^{-j\omega t} . dt \qquad \text{[Integrating both sides]}$$

$$v_c = -\frac{2e}{m_c} . \frac{E_0 e^{-j\omega t}}{-j\omega} = -j \frac{2eE_0 e^{-j\omega t}}{2m_e \omega} = -j \frac{eE_0 e^{-j\omega t}}{m_e \omega} \text{....................(3.2.3)}$$

[where, m_e is the mass of an electron and $m_c = 2m_e$].

The current density of cooper pair or super-current density $(J_s)$is given by the following relation.

$$J_s = n_c(-2e).v_c = j\ \frac{n_c 2e^2 E_0 e^{-j\omega t}}{m_e \omega} = j\sigma_s E_0 e^{-j\omega t} \text{ ....(3.2.4)}$$

[where, n_c is the number of cooper pairs per unit volume, $-2en_c$ is the volume charge density of cooper pairs, σ_s is the super-current conductivity].

$$\sigma_s = \frac{2n_c e^2}{m_e \omega} = \frac{1}{\mu_0 {\lambda_L}^2 \omega} \text{..(3.2.5)}$$

[where,μ_0 is the permeability of the superconductor in air or vacuum,$\lambda_L = \sqrt{\frac{m_e}{2\mu_0 n_c e^2}}$, is the London penetration depth of the superconductor. This is analogous to the skin depth of the normal conductor]

As the supper-current is in quadrature (*i.e.*,90^0 out of phase) with electric field, there is no power dissipation. The total current density (J) is the sum of normal current density and super-current density and expressed as follows.

$$J = J_n + J_s = \sigma E_0 e^{-j\omega t} \text{ ....(3.2.6)}$$

Here, σ is the complex conductivity, which is expressed as follows.

$$\sigma = \sigma_n + j\sigma_s \text{ ....(3.2.7)}$$

The complex surface impedance of the superconductor is given by the following expression.

$$Z_s = \frac{1}{\sigma \lambda_L} = \frac{1}{\lambda_L} . \frac{1}{(\sigma_n + j\,\sigma_s)} \text{ ....(3.2.8)}$$

The BCS surface resistance (R_{BCS})[31] is the real part of the complex surface impedance (Z_s).

$$R_{BCS} = Re\left[\frac{1}{\lambda_L} . \frac{1}{(\sigma_n + j\,\sigma_s)}\right] = \frac{1}{\lambda_L} . \frac{\sigma_n}{({\sigma_n}^2 + {\sigma_s}^2)} \text{ ....(3.2.9)}$$

It is observed that the normal-state conductivity (σ_n) is much less than superconducting-state conductivity (σ_s) at microwave frequencies (*i.e.*,${\sigma_n}^2 \ll {\sigma_s}^2$) and so,${\sigma_n}^2$ term in the above equation (3.2.9) can be neglected.

$$R_{BCS} = \frac{1}{\lambda_L} . \frac{\sigma_n}{{\sigma_s}^2} \text{...(3.2.10)}$$

A surprising result is observed here. *The BCS surface resistance of the superconductor at microwave frequencies is directly proportional to the normal-state conductivity* (σ_n) *of the superconducting material.* The conductivity of the normal metal is given by the following Drude expression.

$$\sigma_n = \frac{n_n e^2 l}{m_e v_F}$$

$$\textit{i.e.,} \qquad \sigma_n \propto n_n . l \text{...(3.2.11)}$$

[n_n is the density of single unpaired electrons which are created by thermal break up of Cooper pairs, *l* is the mean free path of single electrons and v_F is the Fermi velocity, m_e is mass of electron].

By analogy with the conductivity of an intrinsic semiconductor, we can write,

$$n_n \propto e^{-\frac{E_g}{2k_B T}}$$

$$n_n \propto e^{-\frac{\Delta}{k_B T}}$$

$$\text{Hence,} \quad \sigma_n \propto l . e^{-\frac{1.76 T_c}{T}} \text{..(3.2.12)}$$

[where, $E_g = 2.\Delta = 2.(1.76 k_B T_c)$ = energy gap between the superconducting ground state (BCS) and the free electron states, k_B is the Boltzman's constant and *T* is the temperature in kelvin].

Now, from the equations (3.2.5), (3.2.10) and (3.2.12), we can get the following expression of BCS resistance of the superconductor.

$$R_{BCS} \propto \omega^2 . {\lambda_L}^3 . l . e^{-\frac{1.76 T_c}{T}} \text{.......................................(3.2.13)}$$

It is observed that, in case of microwave superconductivity, the BCS surface resistance (R_{BCS}) varies

- exponentially with temperature
- quadratically with RF frequency
- cubically with London penetration depth
- linearly with the mean free path of single electrons.

One way to view the nature of the BCS RF resistance is that the superconducting cooper pairs, with zero DC resistance, have finite mass and momentum which has to alternate sinusoidally for the RF fields, thus giving rise to a small energy loss. The approximate BCS resistance for niobium is given by,

$$R_{BCS} \propto \frac{\omega^2}{T} e^{-\frac{1.76T_c}{T}} \qquad \text{[when } T < \frac{T_C}{2}\text{]}$$

[where, $f(=\frac{\omega}{2\pi})$ is the RF frequency in Hz, T is the temperature in K, and T_c=9.3 K for niobium].

In the two-fluid model, a refined expression for the surface resistance[31] can be derived as follows.

$$R_{BCS} = \frac{1}{2}\omega^2 {\mu_0}^2 \Lambda^3 \sigma_n$$

Here, Λ is the effective penetration depth and is given by the following relation.

$$\Lambda = \lambda_L \sqrt{1 + \frac{\xi}{l}}$$

[where, λ_L: London penetration depth is basically the width of an included vortex, i.e., the radius within which most of the flux is confined;

ξ: the coherence length is the distance over which the super electron (Cooper pair) density rises from n_c=0 at the centre of the vortex to its full bulk value. A long ξ prevents the superconductor's $n_c$from rising quickly enough to provide the shielding current required to contain the flux, so no vortex can form;

l : themean free path of the unpaired electrons]

From equation (3.2.11), we know that σ_n is proportional to the mean free path (l) and it gives a surprising result that the BCS surface resistance does not assume its minimum value when the superconductor is pure ($l >> \xi$), but rather in the range of $l \approx \xi$. For niobium, BCS surface resistance (as shown in Fig.3.2.a) at 1300 MHz is around 800 nΩ at 4.2K and drops to around 15 nΩ at 2K. This drop in surface resistance takes place due to exponential temperature dependence and so the niobium cavity should be operated at 1.8K–2K to achieve high accelerating gradient ($\mathrm{E_{acc}}$) along with very high quality factor ($\mathrm{Q_0}$).

In fact, the surface resistance of superconductor at microwave frequency consists of two parts--BCS resistance and Residual resistance[31].

$$R_s = R_{BCS} + R_{Res}$$

The residual resistance of superconductor arises due to impurities, frozen-in magnetic flux or lattice distortions. Random material defects, hydrides that can form on the surface due to hot chemistry and slow cool-down. One of the quantifiable residual resistance contributions is due to an external magnetic field pinning magnetic fluxons in a Type-II superconductor. The pinned fluxon cores create small normal-conducting regions in the niobium that can be summed to estimate their net resistance. For niobium, the magnetic field contribution($\mathrm{R_H}$) to R_s can be approximated by [31],

$$R_H = \frac{H_{ext}}{2H_{c2}} R_n \approx 9.49 \times 10^{-12} H_{ext} \sqrt{f}$$

[where, H_{ext} is any external magnetic field in Oe, H_{c2} is the Type II superconductor magnetic quench field, which is 2400 Oe (190 kA/m) for niobium, and R_n is the normal-conducting resistance of niobium in ohms, f is the frequency of operation].

The residual resistance is temperature independent and has a value of a few nΩ for clean niobium surface.

The plot of surface resistance as a function of $\left(\frac{T_c}{T}\right)$ for a 9-cell TESLA cavity[35] is shown in the following figure (Fig.3.2.1). Here, the residual resistance is 3Ω at a quality factor of$Q_0 = 10^{11}$ for the cavity.

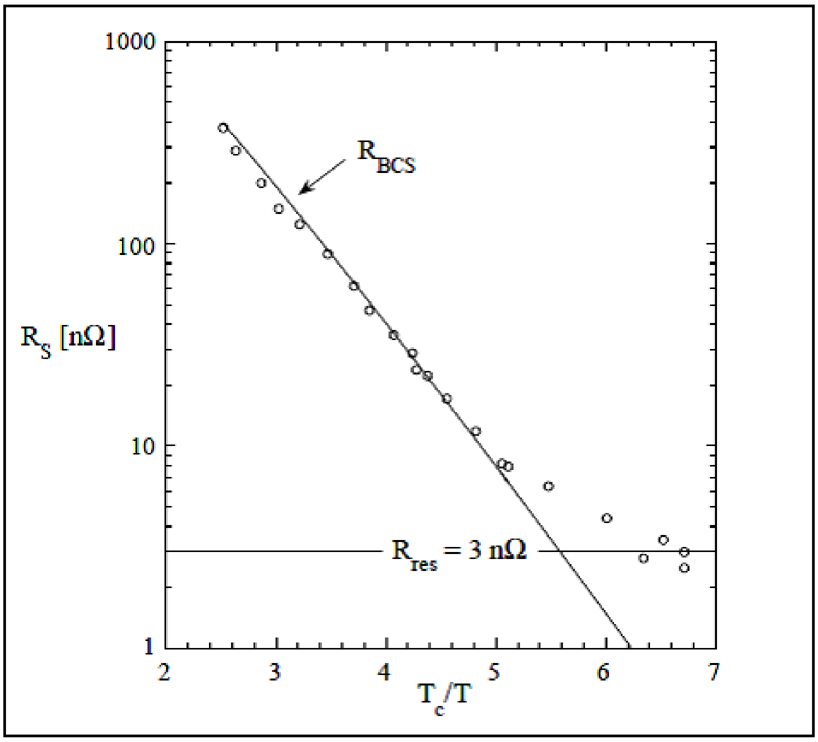

Fig.3.2.1 Plot of surface resistance vs.$\left(\frac{T_c}{T}\right)$ for a 9-cell TESLA cavity [Courtsey: W.Weingarten, CERN, Geneva][31]

The Earth's nominal magnetic flux of 50 µT translates to a magnetic field of 0.5 Oe (40 A/m) and would produce a residual surface resistance in a superconductor that is orders of magnitude greater than the BCS resistance, making the superconductor too lossy to use practically. For this reason, superconducting cavities are surrounded by magnetic shielding to reduce the field permeating the cavity within the limit of 10 mOe (0.8 A/m).

Using the above approximations for a niobium a SRF cavity at 1.8 K, 1.3 GHz, and assuming a magnetic field of 10 mOe (0.8 A/m), the surface resistance components would be R_{BCS} = 4.55 nΩ and $R_{res} = R_H$ = 3.42 nΩ, giving a net surface resistance R_s = 7.97 nΩ. If for this cavity geometrical factor (see Appendix-2 for definition), G = 270 Ω then the ideal quality factor would be $Q_o = 3.4\times10^{10}$.

The Q_o can be further improved to twice the value by performing a mild vacuum bake of the cavity. Empirically, the bake seems to reduce the BCS resistance by 50%, but increases the residual resistance by 30%.

In general, much care and attention to detail must be exercised in the experimental setup of SRF cavities so that there is not Q_o degradation due to RF losses in ancillary components, such as stainless steel vacuum flanges that are too close to the cavity's evanescent fields. However, careful SRF cavity preparation and experimental configuration have achieved the ideal Q_o not only for low field amplitudes, but up to cavity fields that are typically 75% of the magnetic field quench limit. Few cavities make it to the magnetic field quench limit since residual losses and vanishingly small defects heat up localized spots, which eventually exceed the superconducting critical temperature and lead to a thermal quench.

3.3 Type of Superconductors:

According to Schunikov's experiment in 1937 and Abrikosov's theory in 1957, there are two types of superconductors — Type-I and Type-II.

Type-I superconductors exhibit zero dc resistance and perfect diamagnetism for applied magnetic field below it's critical value (B_c). Coherence length (ξ) of this type of superconductors exceeds their London penetration depth (λ_L), which is not energetically favorable for boundaries to form between their normal and superconducting phases.

[Coherence length (ξ): a distance within which the superconducting electron concentration cannot change drastically in a spatially varying magnetic field.

London penetration depth (λ_L): depth of penetration of magnetic field]

The following figure (Fig.3.3.1), according to Ginzburg and Landau theory, shows that Ginzburg-Landau (G-L) parameter (κ) is less than $\frac{1}{\sqrt{2}}$ for Type-I superconductors and greater than $\frac{1}{\sqrt{2}}$ for Type-II superconductors.

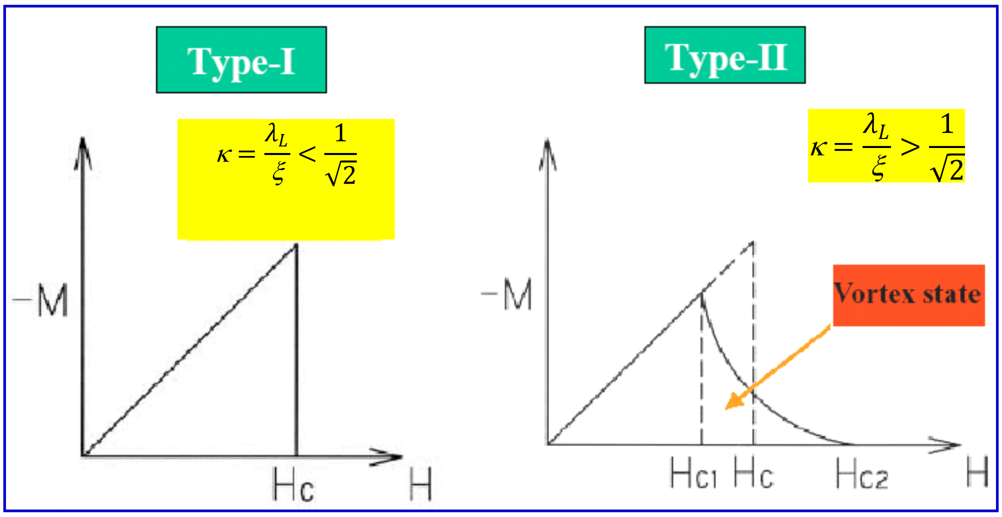

Fig.3.3.1 Magnetization curves for Type-I and Type-II superconductors [34]

Pure elements like Lead (*Pb*), Indium (*In*), Tin (*Sn*) etc. are Type-I superconductors. But Niobium (Nb) is not a Type-I superconductor.

In Type I superconductors, the external magnetic field is completely shielded from the interior of the superconductor for fields up to the critical field (H_c). The superconductivity vanishes above the critical field, because then the magnetic field penetrates completely.

In Type II superconductors, the magnetic field (for DC or steady fields at 0 K) is completely expelled up to a first critical field (H_{c1}), beyond which, the magnetic field penetrates partially, with normal conducting regions isolated on the surface of the superconductor. This behavior persists up to a second critical field (H_{c2}), above which, the superconductivity gets destroyed as the field penetrates completely. Above absolute zero temperature, the critical field depends on temperature according to the following equation.

$$H_c(T) = H_c(0)\left[1 - \left(\frac{T}{T_c}\right)^2\right]$$

[where, $\mathrm{H_c(T)}$ is critical field at temperature T kelvin, $\mathrm{H_c(0)}$ is critical field at absolute zero temperature, $\mathrm{T_c}$ is the critical temperature of the superconductor]

There are large scale applications of superconductors in accelerators- in magnets and also in accelerating cavities[35]. There are some common requirements like higher and higher critical temperature achievable for both magnets and cavities as well. There are some characteristic differences for both magnet and cavity applications. In microwave applications the limitation of superconductor is not dictated by the upper critical field but rather by the so called “superheating field” which is well below 1 Tesla (for all known superconductors). Moreover, strong flux pinning, as it coupled with hysteresis losses, appears undesirable in microwave cavities. Hence a “soft” superconductor like, pure niobium is still the best choice although its critical temperature is only 9.2K and the superheating field is 240 mT. Niobium-tin (Nb_3Sn), in spite of its higher critical temperature (18K) and superheating field (400 mT), is not yet the designer’s choice for cavity fabrication. The gradient achieved in niobium-tin coated single cell copper cavities was below 15 MV/m, probably, due to grain boundary effects in the niobium-tin layer. Again there are two alternatives exist --- *first*, cavities fabricated from bulk niobium sheets or second, the thin layer of niobium is sputtered onto the inner surface of the copper cavity. Both approaches have been successfully applied at various international laboratories. The demonstrated test results on existing cavities throughout the world conclude that higher gradients are achieved, until now, in bulk niobium cavities.

3.4 Advantages of Superconducting RF cavity

The accelerating cavities are fabricated either from normal conducting or superconducting materials. There are several attractive features in superconducting accelerating cavity (SRF) structures over the normal conducting ones. High accelerating gradient (E_{acc}) and high quality factor (Q_0) can be achieved with SRF cavities. The quality factor achieved in good copper cavities is of the order of10^4 to 10^5, while that of SRF cavities is more than 10^{10}.Therefore, the RF power loss is expected to be reduced by 5 to 6 orders of magnitude.

The main advantage of using superconducting material for making RF cavities is the reduced power losses on the cavity wall, and the loss is proportional to the surface resistance (R_s) of the cavity material (niobium) under superconducting (SC) state at the operating frequency. $R_s$is of the order of 10 nΩ at 2K and is around one-millionth (10^{-6}) times that of the normal conducting (NC) copper cavity. Unfortunately, the required mains power is not so small for SC cavities, however, because the cavities are required to be kept at liquid helium temperature (~ 2K for niobium cavity). The power requirement is reduced by a factor of at least a few hundredth times in SC cavities. Only a small fraction of incident RF power is dissipated in the SC cavity walls and most of it is transferred to the beam of charged particles.

3.5 Theoretical Potential of Superconducting RF cavities

It is well established that even at temperature below the critical temperature ($T<T_c$), a sufficiently high surface magnetic field greater than critical magnetic field ($B >B_c$) can destroy superconductivity. There are two types of classical superconductors, which have the same fundamental mechanism for superconductivity, but differ in their behavior with increasing magnetic fields. The difference in behavior can be traced to differences in the free energy associated with NC/SC boundaries on the RF surface, which are controlled by such parameters as the coherence length and the penetration depth.

In RF conditions, the requirements are relaxed somewhat, as the penetration of the magnetic field into the RF surface requires nucleation of a flux line, which requires a finite amount of time. The nucleation time has been determined [36] to be such that the complete shielding of magnetic fields can persist to fields higher than the critical field, up to a limit termed the superheating critical field, B_{sh}. In niobium, the superheating critical field is estimated to be approximately B_{sh} = 230 mT[37].

Experimentation with specially designed SRF non-accelerating cavities[38], has clearly shown that there are no fundamental limits to the peak electric field on a niobium surface up to E_p = 200 MV/m. The theoretical limit on accelerating cavity performance is therefore dependent on the cavity magnetic fields.

In typical SRF accelerating cavities, B_p = 230 mT corresponds to accelerating gradients of 50 to 60 MV/m. Nowadays, accelerators with niobium cavities generally operate at an accelerating gradient (E_{acc}) ~ 10–20 MV/m and the highest accelerating gradient (E_{acc}) achieved so far is ~ 50 MV/m for a test cavity in KEK, Japan. Still the quest for higher and higher accelerating gradient is in progress to make SRF technology economically more attractive. [39]

CHAPTER –4

SUPERCONDUCTING RFCAVITY DESIGN

4.1 Introduction to SRF Cavity design:

A particle accelerator consists of various subsystems like ion source, vacuum chamber, RF system, focusing system etc. The RF system comprising of resonant cavity provides acceleration to the ions or charged particles. Normal conducting or Superconducting materials are generally used for the fabrication of the accelerating cavities. Over the last few decades superconducting RF (SRF) technology has been evolved and matured for its attractive features, like, high accelerating field gradient (E_{acc}), high quality factor (Q_0) and minimal power dissipation. The SRF structures are classified into three distinct velocity($\beta = \frac{v}{c}$) regions.

- Low-velocity ($\beta \leq 0.2$) structures: These are based on resonant transmission line operating in transverse electromagnetic (TEM) mode and are designed for the acceleration of protons or heavy ions.
- Medium-velocity ($\beta \sim 0.2\ to\ 0.6$) structures: These are based onhalf-wave (λ/2) resonant transmission line mode or TEM-like (*e.g.,* coaxial half-wave or spoke geometry) and transverse magnetic (TM) mode (e.g., elliptical geometry), and are designed for the acceleration of protons etc.
- High-velocity ($\beta \sim 0.6\ to\ 1.0$) structures: These are based on elliptical shape cavities in transverse magnetic (TM) mode and designed for the acceleration of light particles (*e.g.,* electrons, positrons or high energy protons).

The design and analysis[40] of medium-velocity or medium-βSRF cavities are discussed elaborately in the following subsections.

4.2 Medium-β superconducting cavities:

According to the applications, medium energy superconducting accelerators are of three broad categories: high-current continuous-wave (CW), high-current pulsed, and low-to-medium current cw accelerators. High current CW accelerators are generally used for accelerator driven sub-critical systems (ADSS), either for energy production or waste transmutation. The SRF technologies are applied for the development of cavities with high acceptance and high shunt impedances, development of high CW fundamental power couplers (FPC), development of higher order mode (HOM) damper. High current pulsed accelerators are mostly H^- or proton accelerators for neutron production (*e.g.*, Spallataion Neutron Source (SNS) in USA or European Spallation Source (ESS)). Low-to-medium current CW Accelerators (e.g., Rare Isotope Accelerators (RIA)) poses major technical challenges, such as microphonics and frequency control, cryogenic losses, multi-charge-state acceleration etc. The SRF technologies are applied for the development of cavities with low sensitivity to vibrations, high shunt impedance, large velocity acceptance, large beam acceptance and the development of microphonics control and compensation technique.

4.2.1 Resonant Transmission line modes:

The cavities with resonant transmission line modes are of two categories−Quarter - wave resonator (QWR) and half-wave resonator (HWR). QWR consists of a quarter-wavelength (λ/4) transmission line. The structure may include a single loading element (as shown in Fig.4.2.1.1) as in QWR [41] or several loading elements(as shown in Fig.4.2.1.2)as in the split ring [41] or the twin-quarter-wave structure (as shown in Fig. 4.2.1.3) [41].

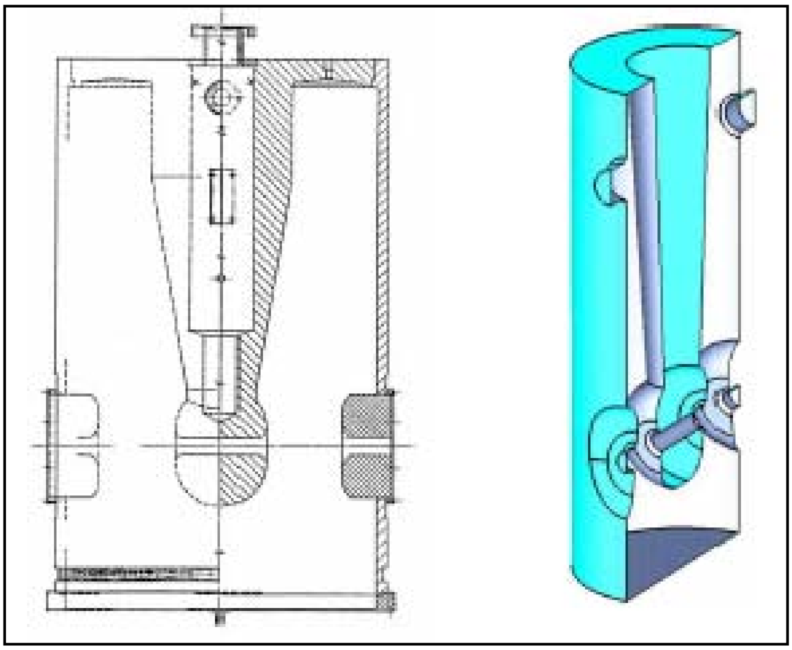

Fig.4.2.1.1 Quarter-wave resonator with single element loading (SRF) [41].

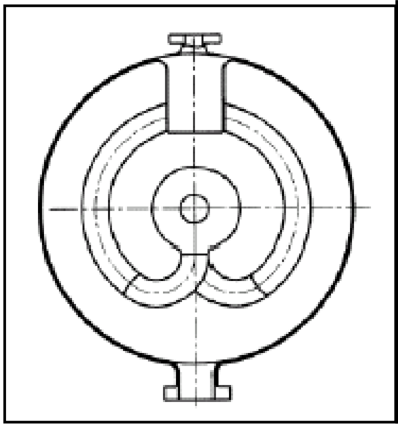

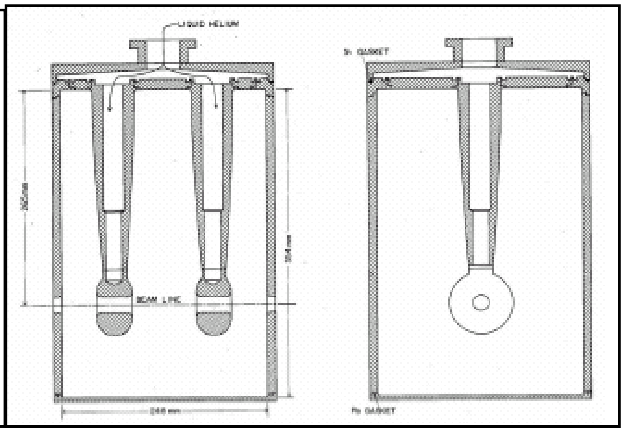

Fig.4.2.1.2 Split Ring resonator (SRF) Fig.4.2.1.3Twin-quarter-wave resonator (SRF)

HWR structures are of two types – coaxial half-wave geometry (as shown in Fig.4.2.1.4) [41] and spoke geometry (as shown in Fig.4.2.1.5) [41]. The spoke cavity can be used as a building block for longer multi-gap structures. When the number of loading elements is large and they are rotated by 90 degrees from one to the next, those cavities (as shown in Fig.4.2.1.6)are called H-type cavities[41].

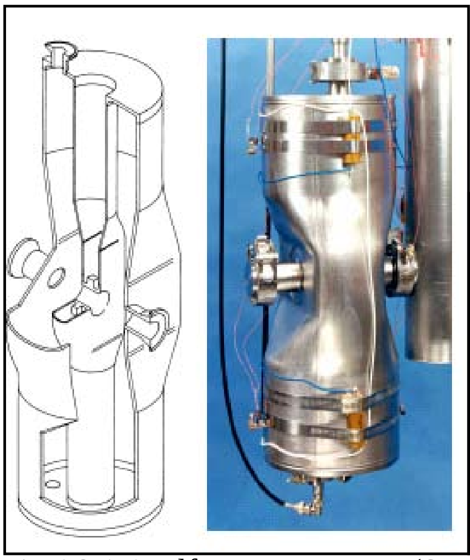

Fig.4.2.1.4Half-wave resonator (SRF)

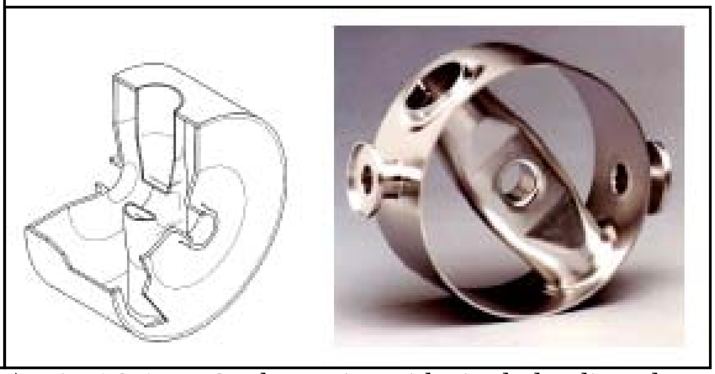

Fig.4.2.1.5 Spoke cavity with single loading element (SRF)[41]

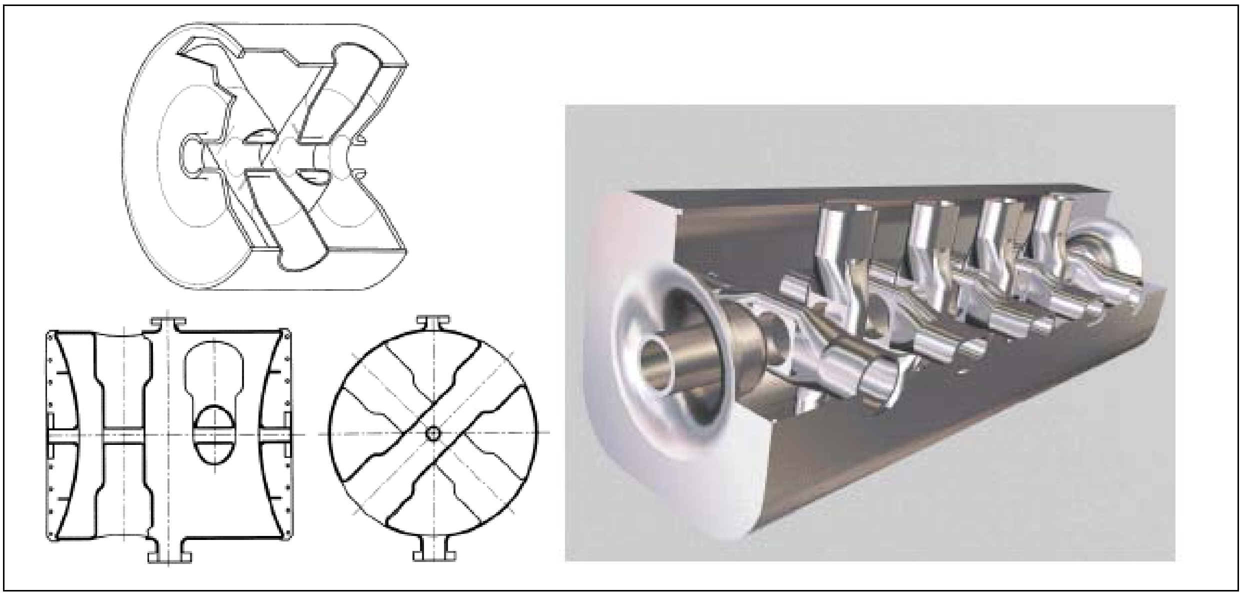

Fig.4.2.1.6 Multi-element spoke cavities (SRF)[41]

4.2.1.1 Transverse magnetic modes:

The elliptical geometry is generally used in almost all the operational high-β (~1) superconducting cavities (operating in TM_{010} mode) in the world. A few number of TM mode cavities designed and tested for β value as low as 0.47 are shown in Fig.4.2.1.1.1(a) & (b) [41].

(a) **(b)**

Fig.4.2.1.1.1MulticellTM010 cavity (a) at 805 MHz, β=0.82; (b) at 805 MHz, β=0.62 [41].

4.2.2 Design considerations for medium-βsuperconducting cavity:

The medium-β or intermediate-velocity CW (continuous-wave) accelerator cavities with high shunt impedances are usually designed to operate at an accelerating gradient of around 17 to 20 MV/m. In high current applications, the gradients are limited by the capability of the fundamental power couplers (FPC).However, the gradients, in low current applications, are limited by the RF power required for field control. Beam losses and activation are important fundamental issues in the design of the accelerating structures for medium-β accelerators. An ample frequency control window should be provided for the cavity operation.

In an accelerating module the cavity is the main part and its design cannot be separated from the system as a whole. The complicated relationship among the accelerator requirements, associated effects, cavity parameters and the cryomodule and cavity design issues have been illustrated in some paper [40]. The main considerations [42] in the design of the superconducting structures are given in APPENDIX-2.

In a 5-cell TM-class cavity, five resonant modes form a fundamental pass-band. The plot of frequencies of these modes vs. mode number (as shown in Fig. 4.2.2.1) gives a dispersion curve, where the 5th point corresponds to the π-mode or the accelerating mode of the proposed 5-cell, β = 0.61, 650 MHz superconducting cavity for Indian SNS/ Fermilab Proton Improvement Plan (PIP-II).

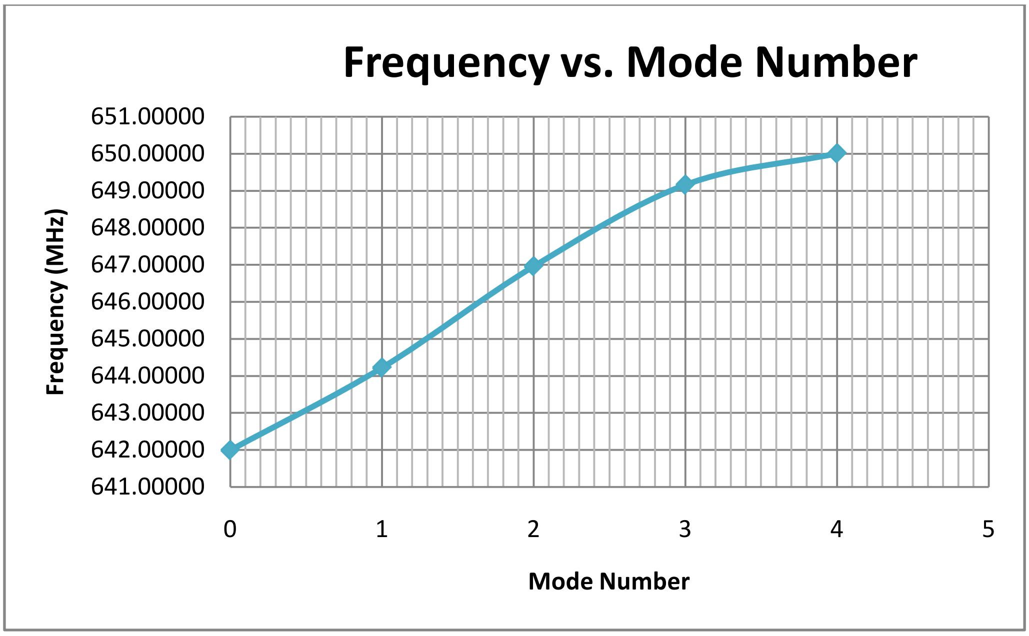

Fig.4.2.2.1 Plot of Frequency vs. Mode Number (for 5-cell, β = 0.61, 650 MHz elliptical cavity).

4.2.3 Influence of cell geometry on RF parameters:

The criteria for multi-cell superconducting cavity design[43] are discussed in the following paragraphs. The standard elliptical cavities are for $0.47 \leq \beta \leq 1$ with a schematic cross-sectional view is given in Fig.4.2.3.1.

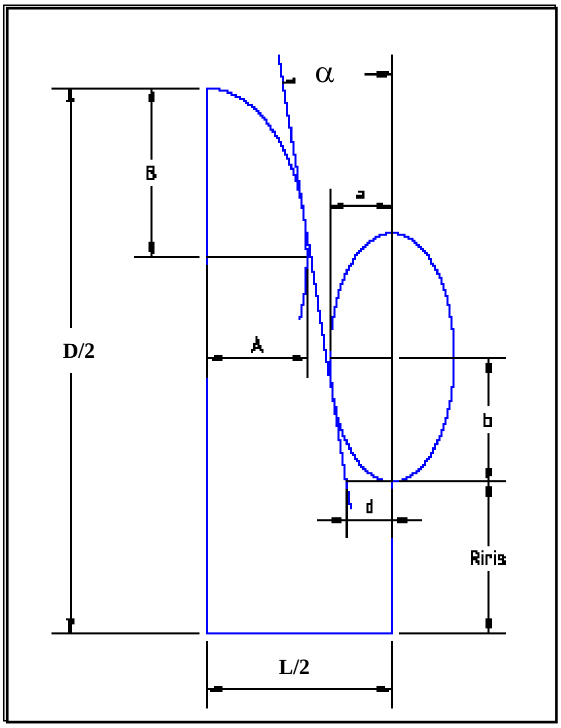

Fig.4.2.3.1 Cross-sectional view of an elliptical cavity[43]

The geometry or the shape of the cavity is determined by the following parameters as discussed[43]below.

- The cell length (L) determines the geometrical β value of the cavity.
- The cell Iris radius (R_{iris}) is primarily determined by the required cell-to-cell coupling.
- The selection of slope angle (α) of the side wall and position (d) with respect to the Iris plane is done by trading-off between peak surface electric field $\left(E_p\right)$ and peak surface magnetic field $\left(B_p\right)$, with a very little effect on cell-to-cell coupling.
- The Iris ellipse aspect ratio uniquely influences the peak surface electric field.
- There is a very negligible effect of equator ellipse aspect ratio on the RF parameters, but it has significant influence on the mechanical behavior of the cavity.
- The frequency tuning of the cavity is done by varying the equator diameter or cell diameter (D), without affecting any electromagnetic or mechanical parameters of the cavity.

The effect of the variation of each geometrical parameter of the cavity is reviewed [43] in the following sub-sections.

Equator ellipse aspect ratio $\left(\frac{\boldsymbol{B}}{\boldsymbol{A}}\right)$:

The equator ellipse aspect ratio $\left(\frac{B}{A}\right)$can be chosen freely from the electromagnetic design of the cavity operating in accelerating mode (π-mode). From Fig.4.2.3.2 it is observed that the electromagnetic parameters such as, $\frac{E_p}{E_{acc}}$, $\frac{B_p}{E_{acc}}$, R/Q and percentage cell-to-cell coupling (k_c%) do not vary with the equator ellipse aspect ratio. In this case, $\left(\frac{B}{A}\right)$ is varied from 1 (i.e., circle) to 2 (i.e., ellipse) keeping stored energy constant at 1 Joule.

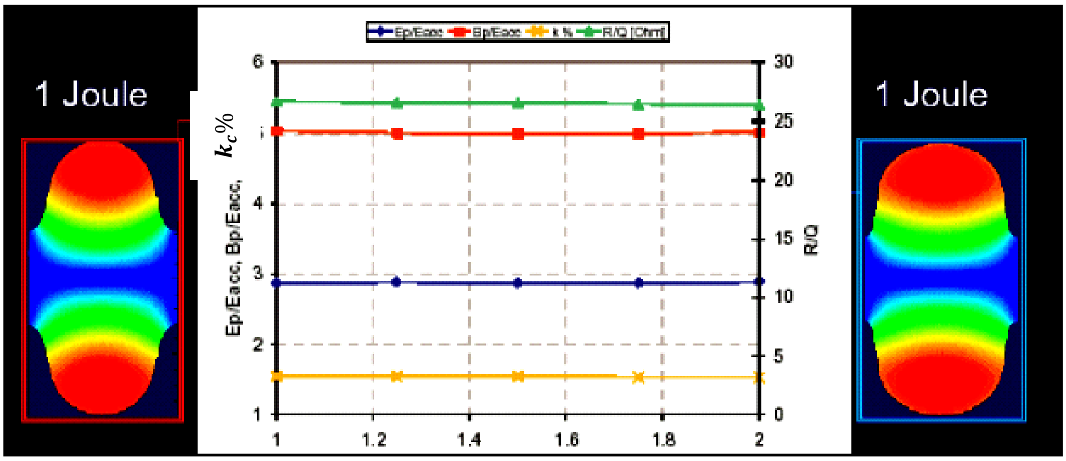

B/A ⟶

Fig.4.2.3.2. Plot of electromagnetic parameters vs. equator ellipse aspect ratio[43]

Iris ellipse aspect ratio $\left(\frac{b}{a}\right)$:

It is observed from Fig.4.2.3.3 that the electromagnetic parameters vary with the iris ellipse aspect ratio $\left(\frac{b}{a}\right)$, varying from 1 (i.e., circle) to 2 (i.e., ellipse). For any cavity geometry and parameters, there is an optimal value for iris ellipse aspect ratio, that minimizes the peak surface electric field with a very little influence on the other electromagnetic parameters.

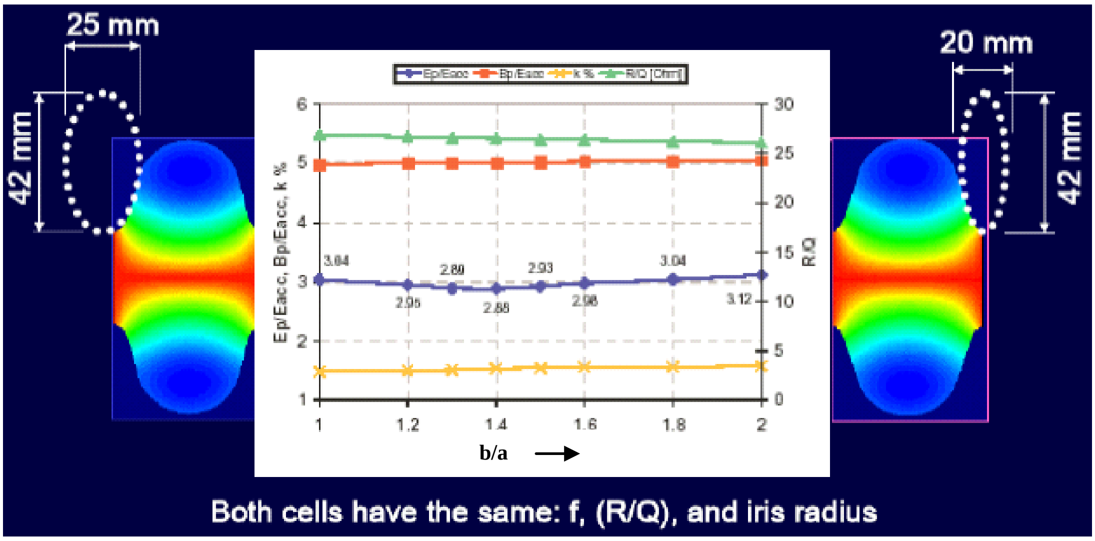

Fig.4.2.3.3.Plot of electromagnetic parameters vs. Iris ellipse aspect ratio[43]

Wall slope angle (α):

It is observed from Fig.4.2.3.4that the wall slope angle (α) has relatively small effect on the electromagnetic parameters. As the wall slope angle is increased, magnetic volume gets reduced, thus resulting in higher peak surface magnetic field (B_p). Conversely, as the wall slope angle is increased, electric volume gets increased, thus resulting in lower peak surface electric field (E_p).It is also to be noted that the wall slope angle has practical constraints on cavity fabrication and treatments, since small value of slope angle can be critical for the cavity chemistry and cleaning procedure[43].

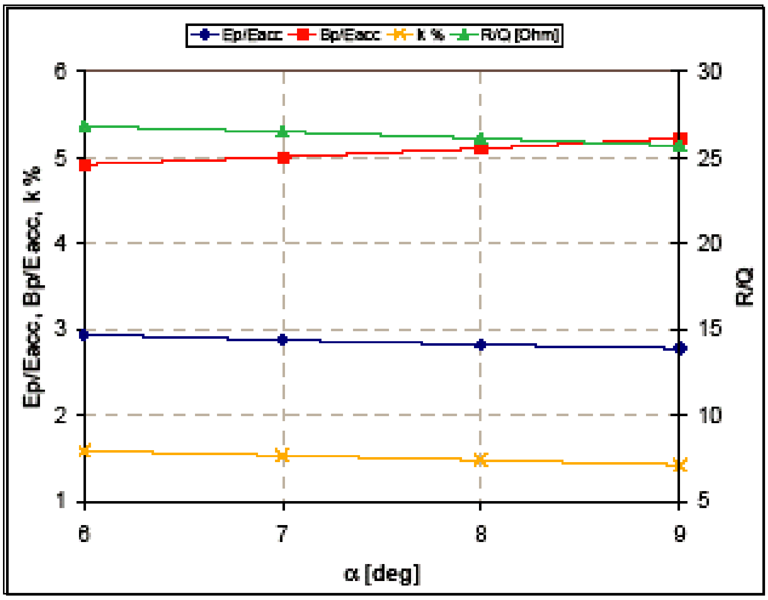

Fig.4.2.3.4Plot of electromagnetic parameters vs. wall slope angle[43]

4.3 650 MHz, β = 0.61 superconducting cavities:

As the SRF technology has evolved and matured in the last few decades, it is established that the high accelerating gradient SRF cavities are the most favorable choice for future energy frontier accelerators. A lot of progress on achieving higher and higher accelerating gradient (E_{acc}) has been made by various laboratories around the world over the past few decades. The E_{acc} of a single-cell re-entrant shape cavities[44] made of fine-grain and large grain niobium has been reached up to the world record value of 59 MV/m at 1.3 GHz at Cornel University, USA for International Linear Collider (ILC) and also a low-loss shape niobium cavity[45] of 53.5 MV/m at 1.3 GHz in KEK, Japan. It is well established that the peak surface electric field $\left(E_p\right)$, and peak surface magnetic field $\left(B_p\right)$ are the two deciding parameters to achieve the maximum accelerating gradient[46]. Both E_p and B_p increase proportionally as E_{acc} is raised. However, it is desirable to minimize the ratios $\frac{E_p}{E_{acc}}$ and $\frac{B_p}{E_{acc}}$ both, which is a contradictory requirement. If one of them is reduced, the other one gets increased. So,proper optimization is necessary in the design. These ratios are solely determined by the cavity geometry[43]. Theoretically, there is no fundamental limit to E_p, although field emission control is practically a challenging task[47]. But there is a hard limit to B_p and this limit is referred to as RF critical magnetic field $\left(B_{critical\ ,RF}\right)$above which the superconductor quenches to become normal conducting material. The $B_{critical\ ,RF}$ depends on the material property. The maximum accelerating gradient $\left(E_{acc\ ,max}\right)$ allowed, within this hard limit[48] can be written as follows.

$$E_{acc\ ,max} = \frac{B_{critical\ ,RF}}{\left(\frac{B_p}{E_{acc}}\right)}$$

The predicted $B_{critical\ ,RF}$ value is 230 mT for the niobium cavity at 1.8K temperature and this critical value is the limiting value as of now, until the discovery of new superconducting material for the cavity. The other alternative to achieve higher E_{acc} is to reduce the ratio $\frac{B_p}{E_{acc}}$ by optimizing the cavity shape or geometry.

A new design, optimization and analysis of β = 0.61, 650 MHz,5-cell elliptical shape SRF linac cavity has been done at VECC, Kolkata, with aperture of 96 mm and wall slope angle 2.4 degree (for the Mid cells) and 4.5 degree (for the End cells). Influence of geometric parameters on different RF design parameters has been analyzed for the said cavity and the shape optimization has been done using 2D SUPERFISH and 3D CST MICROWAVE STUDIO codes. The following paragraphs also discuss the comparative study of RF design parameters for two types of cell shapes, re-entrant and elliptical, for single-cell 650 MHz, β= 0.61 SRF cavity.

4.3.1 RF DESIGN:

The elliptical shaped cavity cell (as shown in Fig. 4.3.1.1),consisting of two elliptic arcs and, possibly, a straight line between them, is determined by geometric parameters[49] like, cell length(L), equator radius(D/2), iris radius or aperture radius (R_{iris}), iris ellipse ratio $\left(\frac{a}{b}\right)$, equator ellipse ratio $\left(\frac{A}{B}\right)$, slope of the side wall (α) and the distance (*d*) measured from the iris plane. The main figures of merit for an elliptical-cell design of a Superconducting RF cavity are $\frac{E_{pk}}{E_{acc}}$, $\frac{B_{pk}}{E_{acc}}$, geometric factor (G) and the ratio of shunt impedance to quality factor $\left(\frac{R}{Q}\right)$. Iris radius has very strong influence on the above mentioned figures of merit [50] .With the decrease of R_{iris}, both the ratios $\frac{E_{pk}}{E_{acc}}$ and $\frac{B_{pk}}{E_{acc}}$get reduced, but the other two parameters, G and $\frac{R}{Q}$, get increased [51]. By choosing proper value of geometric parameters, optimal values of figures of merit have been determined for 650 MHz, β = 0.61, 5-cell elliptical cavity.

Re-entrant and elliptical shape single-cell Cavities:

The two parameters, E_{pk}, B_{pk}, determine the desired accelerating gradient (E_{acc}) in elliptical shape cavity. Both E_{pk} and B_{pk} increase proportionally as E_{acc} is raised. The cavity geometry solely determines the ratios $\frac{E_{pk}}{E_{acc}}$ and $\frac{B_{pk}}{E_{acc}}$.As the field emission increases with $\frac{E_{pk}}{E_{acc}}$and limits the value of accelerating gradient (E_{acc}), $\frac{E_{pk}}{E_{acc}}$is reduced by optimizing the shape of the cavity. Further, by proper treatment on the inner surface, field emission in a cavity can be reduced. But there is a fundamental limit to E_{acc}, due to an intrinsic limit referred to as the RF critical magnetic field $\left(B_{critical\ ,RF}\right)$ on the surface of the superconducting material used for the construction of the cavity. To overcome this hard limit, the ratio $\frac{B_{pk}}{E_{acc}}$ can be lowered by changing the cavity shape to the re-entrant shape (as shown in Fig. 4.3.1.2). Re-entrant shape cavities have negative value of wall slope angle(α) [52].

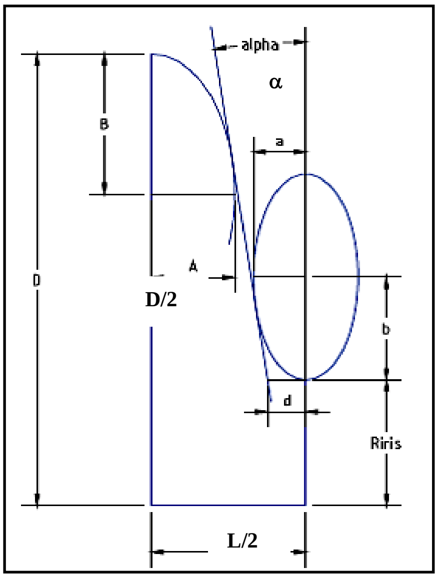

Fig.4.3.1.1.$\frac{1}{4}$th cell Geometry of elliptical shape cavity

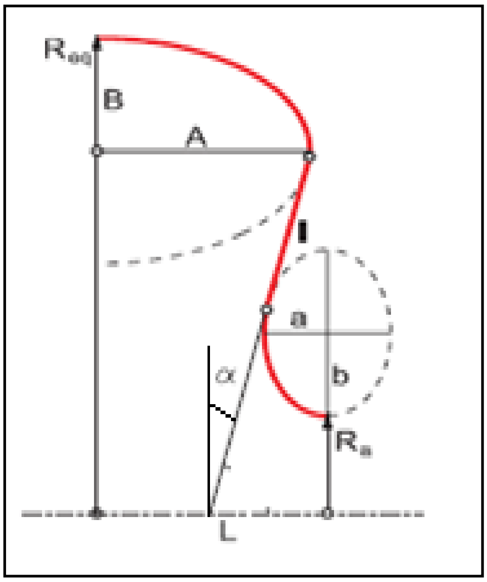

Fig.4.3.1.2. $\frac{1}{4}$th cell Geometry of Re-entrant shape cavity

Along with the lower value of $\frac{B_{pk}}{E_{acc}}$, the other advantages of re-entrant shape are to achieve higher values of G and $\frac{R}{Q}$, which are beneficial in terms of less RF power dissipation on the cavity wall and smaller heat load on the cryogenic system. The major disadvantage of the re-entrant shape cavity[52] is that the value of $\frac{E_{pk}}{E_{acc}}$ is somewhat higher.

The geometry or the shape of the cavity is determined by several parameters as discussed below in detail. The cell length (L) determines the geometrical β value of the cavity from the following relation.

$$L = \frac{\beta\lambda}{2}\ [\lambda\text{=wavelength of the electromagnetic wave}]$$

The cell Iris radius (R_{iris}) is primarily determined by the required cell-to-cell coupling. The wall slope angle (α) of the side wall and position (d) with respect to the Iris plane can be set to achieve a trade-off between peak surface electric $(E_{pk})$and magnetic (B_{pk}) fields with a very little effect on cell-to-cell coupling. The Iris ellipse aspect ratio $\left(\frac{a}{b}\right)$ uniquely influences the peak surface electric fields[43]. The equator ellipse aspect ratio $\left(\frac{A}{B}\right)$ has a marginal effect on the RF parameters, but has a significant effect on the mechanical behavior of the cavity. The frequency tuning of the cavity is done by varying the equator diameter or cell diameter (D), without affecting any electromagnetic or mechanical parameters of the cavity. The tuning of the cell at the right frequency is accomplished by varying the cell diameter (D) without changing any other independent parameters, namely, cell length (L), wall slope angle (α), side wall position (d) with respect to the Iris plane, Iris ellipse aspect ratio $\left(\frac{a}{b}\right)$, equator ellipse aspect ratio $\left(\frac{A}{B}\right)$. This is practically achieved by varying the equator ellipse parameters (A, B), but keeping their ratio$\left(\frac{A}{B}\right)$ fixed. In this manner the cavity shape, uniquely determined by the six independent parameters, is not affected by the tuning procedure.

RESULTS AND DISCUSSION:

The comparative study on single-cell cavities with two different types of geometry, re-entrant shape and elliptical shape for $\beta = 0.61$, operating at 650 MHz has been carried out. The single-cell length of the cavity is 140.67 mm and the Iris diameter is 96 mm.

The simulations results are tabulated in Table-1 for elliptical and re-entrant shape single-cell cavities. The wall slope angle is negative (-10.48 degree) for the re-entrant shape as compared to positive wall slope angle (+2.38 degree) for the elliptical one. For the re-entrant cavity geometry, $\frac{B_{pk}}{E_{acc}}$ value (4.525 mT/(MV/m)) is slightly better (4%) with respect to that (4.7172 mT/(MV/m)) for elliptical geometry. However, $\frac{E_{pk}}{E_{acc}}$value (3.085)for re-entrant cavity has been deteriorated a little bit, by around 1.2% compared to that (3.048) for elliptical shape cavity. The desired higher values of geometric factor (G = 202.5) and the ratio of shunt impedance-to-quality factor $\left(\frac{R}{Q} = 63.2\right)$ have been achieved for re-entrant ones compared to those values (G=192.9 and $\frac{R}{Q} = 58.6$) for elliptical cavity. For the re-entrant shape cavity, as desired, the value of G gets increased by around 5% and $\left(\frac{R}{Q}\right)$gets increased by 8% as compared to those of the elliptical cavity. This simulation result confirms that RF power loss and heat load on cryogenic system will be less for re-entrant cavity.

To achieve the accelerating gradient of 17 MV/m, the energy (22.13 Joule) to be supplied to the re-entrant cavity is around 7.3% less than the energy (23.87 Joule) for the elliptical ones. However, there are some practical problems of cavity treatment like, high pressure water rinsing etc., in case of re-entrant cavities [52].

Five-cell elliptical cavity:

After the comparative study of the single-cell cavities of different shapes, the simulation of 5-cell elliptical cavity (as shown in Fig.4.3.1.3) for 650 MHz, β = 0.61, has been carried out[53].

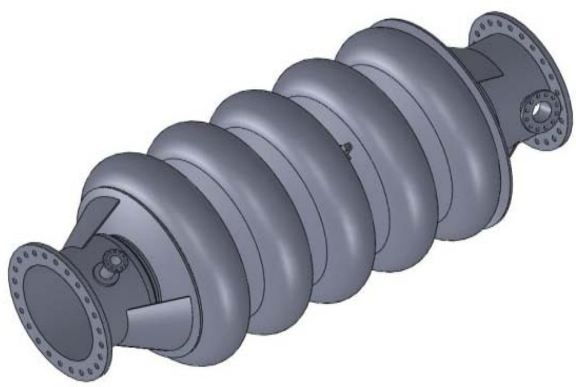

Fig.4.3.1.3 Isometric view of 5-cell elliptical cavity

The electric field lines for four non-accelerating modes, *i.e.*,π/5-mode (or 0-mode) to 4π/5-modes have been plotted in Fig.4.3.1.4 and the same for fundamental accelerating mode (or π-mode) has been shown in Fig.4.3.1.5. The simulation results for two slightly different five-cell elliptical cavities with same aperture or Iris radius (48 mm) have been presented in Table-2. The same accelerating cavities are designed to achieve accelerating gradient of 17 MV/m.

CAVITY-1 with uniform wall slope angle (α) of 3.6 degrees in all half cells (mid-cells and end-cells), has equator ellipse aspect ratio $\left(\frac{\mathrm{A}}{\mathrm{B}}\right)$ and iris ellipse aspect ratio $\left(\frac{\mathrm{a}}{\mathrm{b}}\right)$ for the end-cells different from that of the mid cells. CAVITY-2 has α = 2.4 degrees in all mid-cells and 4.5 degrees in the two end-cells, but $\left(\frac{\mathrm{a}}{\mathrm{b}}\right)$ for the end-cells are different from that of the mid cells, with $\left(\frac{\mathrm{A}}{\mathrm{B}}\right)$ kept unchanged for all cells.

It is observed from Table-2 that all RF parameters for CAVITY-2, are better than those for CAVITY-1. As desired, the values of $\frac{\mathrm{B_{pk}}}{\mathrm{E_{acc}}}$ and $\frac{\mathrm{E_{pk}}}{\mathrm{E_{acc}}}$ for CAVITY-2 are little lower (i.e., better) than those values for CAVITY-1.

The Iris radius (R_{iris}) is a very powerful knob to trim RF parameters. $\frac{B_{pk}}{E_{acc}}$ and $\frac{E_{pk}}{E_{acc}}$ both get increased as the Iris radius (R_{iris}) increases. But the increase of $\frac{E_{pk}}{E_{acc}}$ is much faster than that of $\frac{B_{pk}}{E_{acc}}$. However, the value of $\frac{R}{Q}$gets decreased as the Iris radius (as shown in Fig.4.3.1.6) increases and consequently the RF power loss and hence the thermal load on the cryogenic system increases with Iris aperture. So, the smaller iris aperture (R_{iris}) is preferable because of higher $\frac{R}{Q}$ value and lower $\frac{B_{pk}}{E_{acc}}$ and $\frac{E_{pk}}{E_{acc}}$ values.

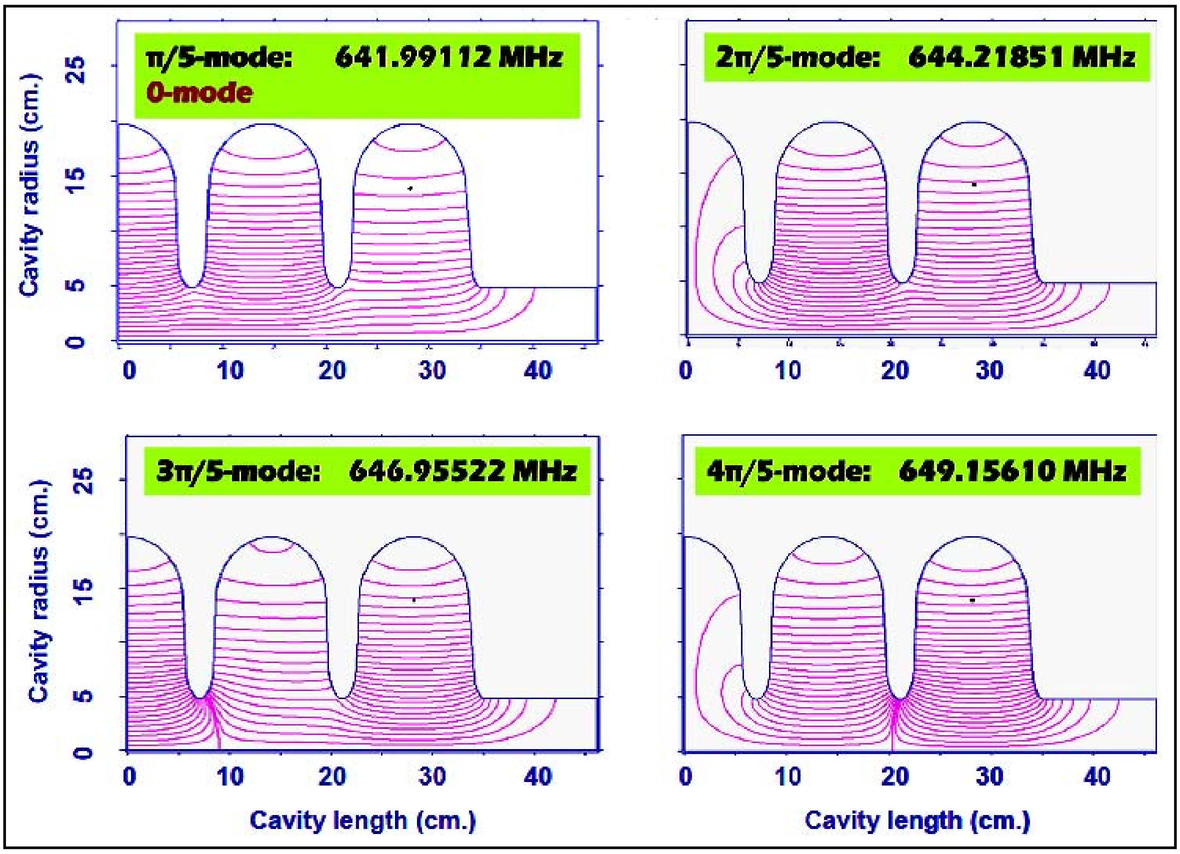

Fig.4.3.1.4 Plot of Electric field lines for π/5 mode(0-mode), 2π/5, 3π/5 and 4π/5 modes of elliptical shape, 5-cell cavity ($\frac{1}{4}th$ geometry shown)

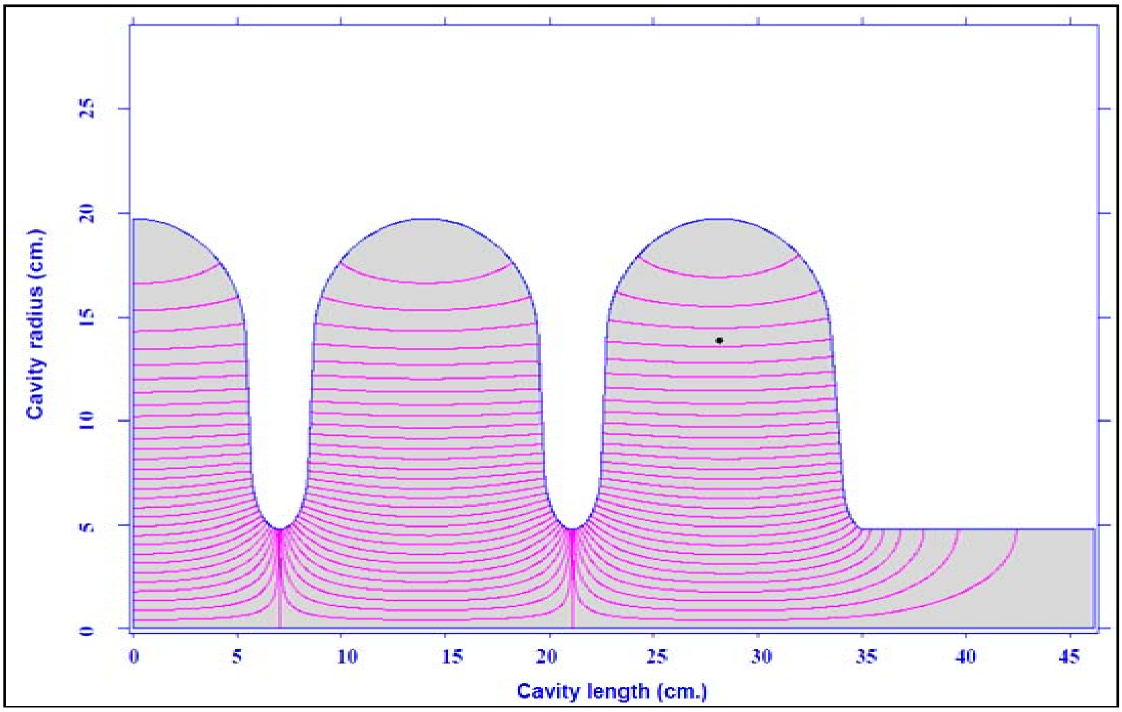

Fig. 4.3.1.5 Plot of Electric field lines for accelerating mode (π-mode) elliptical shape 5-cell cavity ($\frac{1}{4}th$ geometry shown)

For the mid-cells, the maximum accelerating gradient (E_{acc}) increases with the Iris radius (R_{iris}) as shown in Fig.4.3.1.7. However, for the two end-cells, the maximum E_{acc} decreases with R_{iris} and the field flatness is not maintained. So the optimized value of R_{iris} is 48 mm in this case. Besides this, proper end-cell tuning is done to achieve better field flatness throughout all cells. In this case, for end cells the Iris ellipse ratio is optimized to $\left(\frac{a}{b}\right)_{endcell} = \frac{10.67}{24.02}$ as compared to $\frac{13.68}{30.82}$ for mid-cells. However, the equator ellipse ratio $\left(\frac{A}{B}\right) = \frac{54}{58}$is kept constant for both mid-cells and end-cells. The wall slope angle for end-cells is optimized to $\alpha_{endcell} = 4.5$ degree as compared to 2.4 degree for mid-cells. The different geometry of end-cells require a different half-cell die or former from that of mid-cells.

The variation of equator radius ($R_{equator}$) has a very little effect on electromagnetic parameters (as shown in Fig.4.3.1.8) like, $\frac{B_{pk}}{E_{acc}}$, $\frac{E_{pk}}{E_{acc}}$ and $\frac{R}{Q}$. Also, the maximum accelerating gradient (E_{acc}) on the axis throughout the 5-cell cavity almost unchanged with the variation of the equator radius. The field flatness does not depend on the variation of the equator radius $(R_{equator}$).

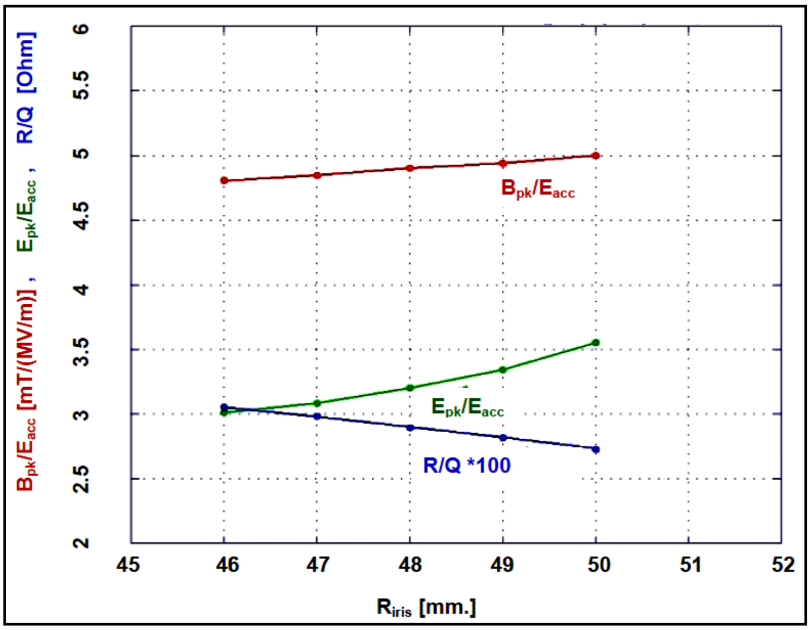

Fig.4.3.1.6 Plot of normalized peak surface magnetic field $\left(\frac{B_{pk}}{E_{acc}}\right)$, normalized peak surface electric field $\left(\frac{E_{pk}}{E_{acc}}\right)$ and normalized shunt impedance $\left(\frac{R}{Q}\right)$ vs. Iris radius (R_{iris}) of the cavity.

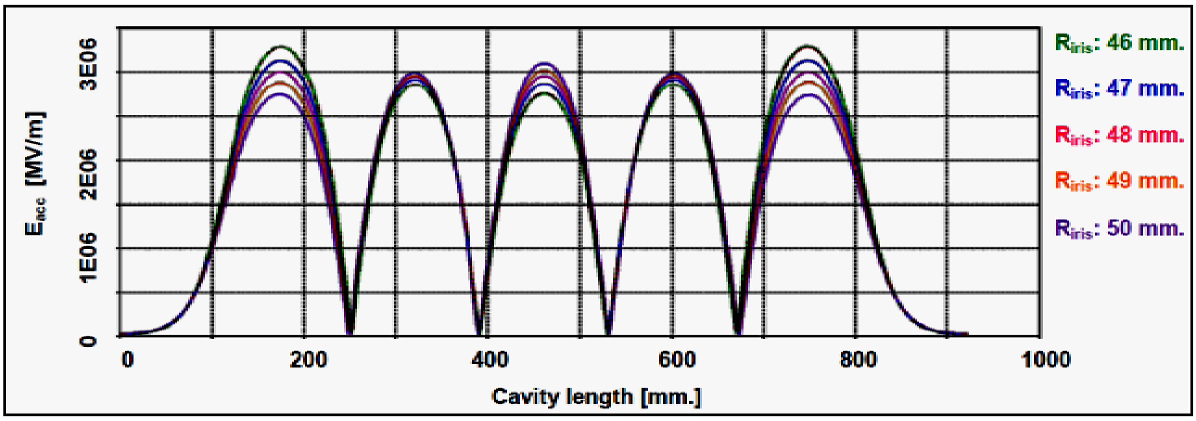

Fig.4.3.1.7 Plot of accelerating gradient (E_{acc}) along the cavity axis for different Iris radius(R_{iris})

A plot of Transit time factor vs. velocity factor (β) for 650 MHz, β=0.61, 5-cell SRF cavity has been shown in Fig.4.3.1.9. The said cavity with geometric velocity factor (β_G) ~0.61 is intended to use for the proton beam of energy range from 177 MeV to 480 MeV corresponding to velocity factor (β) ranging from 0.55 to 0.75. The kinetic energy (in MeV) of the proton under relativistic region is given by the following equation.

$$K.E. = (\gamma - 1)m_0.c^2$$

[where, $\gamma = \frac{1}{\sqrt{1-\beta^2}}$, $\beta = \frac{v}{c}$, v is the velocity of proton, c is the velocity of light, m_0 is the rest mass of proton].

The rest mass energy of proton is 938 MeV. Therefore, for the accelerated proton energy of 177 MeV and 480 MeV, the velocity factor (β) is 0.55 and 0.75 respectively. It is observed from Fig. 4.3.1.9 that the transit-time factor for wider βranging from 0.55 to 0.75is obtained higher with no end cells tuning than that obtained with end cells tuning done.In fact, Transit-time factor is highest (~0.72) for the designed β ~ 0.61-0.65. Although the higher transit-time factor, with no end cell tuning, is desirable for acceleration at the higher electric field,the end cell tuning is necessary to achieve better field flatness.

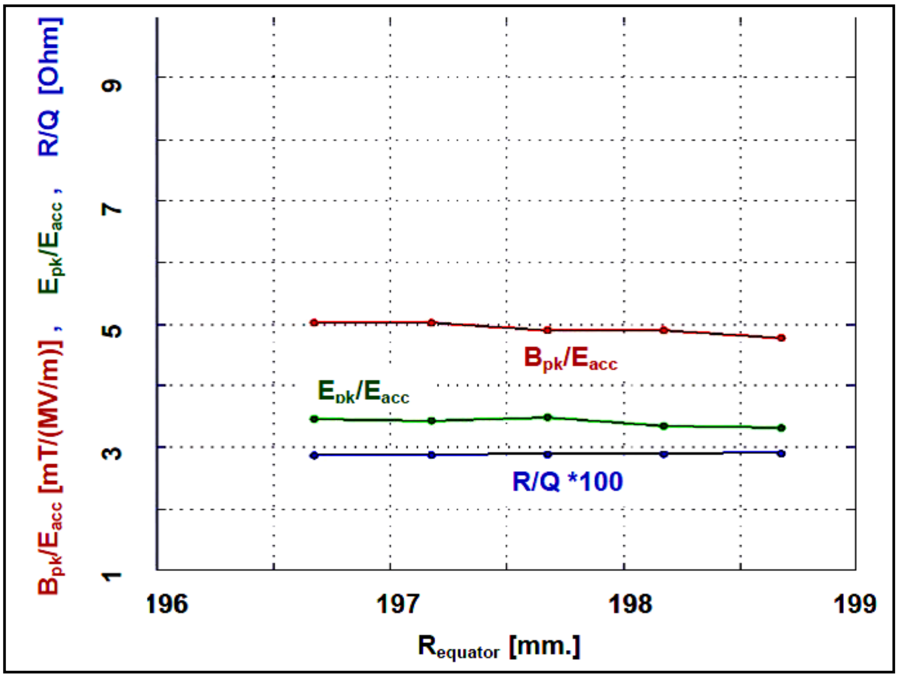

Fig.4.3.1.8 Plot of normalized peak surface magnetic field $\left(\frac{B_{pk}}{E_{acc}}\right)$, normalized peak surface electric field $\left(\frac{E_{pk}}{E_{acc}}\right)$ and normalized shunt impedance $\left(\frac{R}{Q}\right)$ vs. Equator radius $(R_{equator})$ for the elliptical cavity.

A plot of $\frac{B_{pk}}{E_{acc}}$ vs. equator ellipse aspect ratio (Fig.4.3.1.10) shows that $\frac{B_{pk}}{E_{acc}}$ is almost unchanged (*i.e.*, varying between 4.82 and 4.9 mT/(MV/m)) as equator ellipse aspect ratio, A/B. However, the value of $\frac{B_{pk}}{E_{acc}}$ varies (as in Fig.4.3.1.11) from 5.2 to 4.7 mT/(MV/m) as iris ellipse aspect ratio, a/b and it has a minimum value of 4.6 mT/(MV/m) at a/b=0.5.

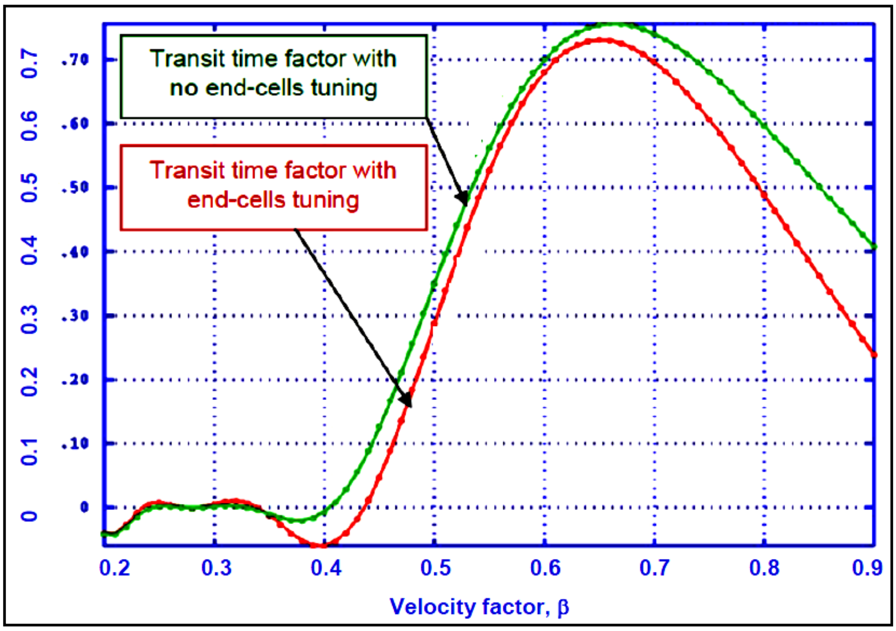

Fig.4.3.1.9 Plot of Transit time factor vs. β for 650 MHz, β = 0.61, 5-cell SRF cavity

It is observed that $\frac{E_{pk}}{E_{acc}}$ increases from 2.9 to 3.9 (as shown in Fig.4.3.1.12) as equator ellipse aspect ratio, A/B. However, the value of $\frac{E_{pk}}{E_{acc}}$ decreases (as shown in Fig.4.3.1.13) from 3.5 to 3.0 with the increase of iris ellipse aspect ratio, a/b.

Finally, after analyzing all pros and cons between CAVITY-1 & CAVITY-2 and also considering the better field flatness factor, the design of CAVITY-2 has been frozen as the best one. The engineering drawings for the half-cell of mid-cells and end-cells of CAVITY-2 have been given in Fig.4.3.1.14 and Fig.4.3.1.15 respectively.

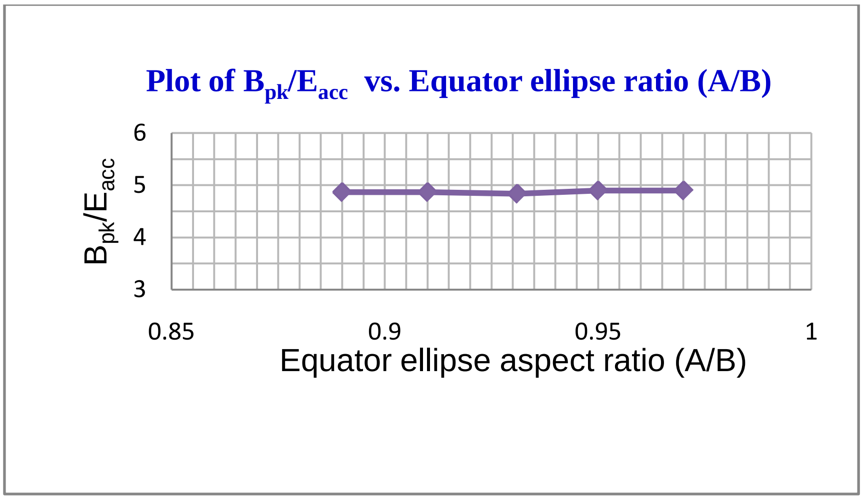

Fig.4.3.1.10 Plot of normalized peak surface magnetic field $\left(\frac{B_{pk}}{E_{acc}}\right)$ vs. Equator ellipse aspect ratio $\left(\frac{A}{B}\right)$ for the elliptical cavity.

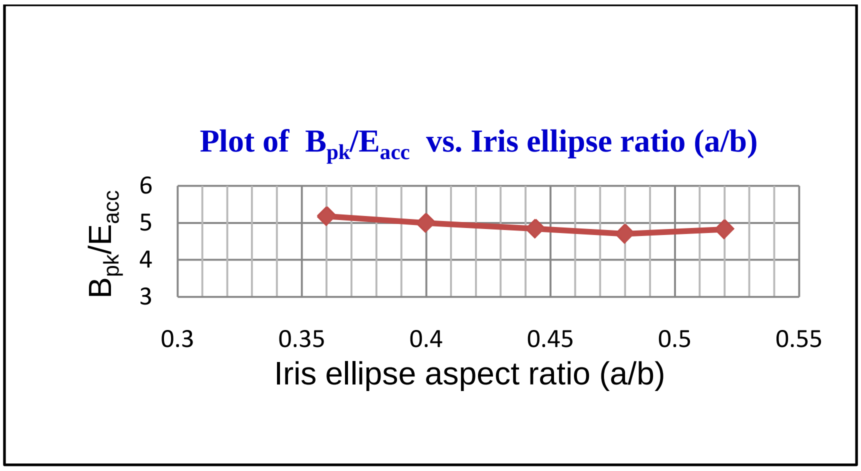

Fig.4.3.1.11 Plot of normalized peak surface magnetic field $\left(\frac{B_{pk}}{E_{acc}}\right)$ vs. Iris ellipse aspect ratio $\left(\frac{a}{b}\right)$ for the elliptical cavity.

A Comparative chart of design parameters [54] from three different laboratories, Jefferson Lab (JLab), Fermilab and VECC for five-cell elliptical cavities at 650 MHz, β = 0.61 has been given in Table-3. It is observed that JLab design has larger iris radius of 50 mm in comparison to 42 mm of Fermilab and 48 mm of VECC. The larger iris radius will increase cell-to-cell coupling coefficient as well as peak surface electric and peak surface magnetic fields. Jlab design has some flat equator region. But, Fermilab and VECC design do not have any such region. The wall slope angle for JLab design is 0 degree (for both mid-cells and end-cells) as compared to 2 degree (mid-cells) and 2.7 degree (end-cells) in case of Fermilab and 2.4 degree (mid-cells) and 4.5 degree (end-cells) in case of VECC design. So, for JLab design, the same half-cell die or former can be used for mid-cells and end-cells. However, for Fermilab and VECC designs, the different half-cell die or former will be required for mid-cells and end-cells. There are little difference in equator and iris ellipse aspect ratios among the three designs. This new design of the cavity, with different aperture and wall angle, has better field flatness and mechanical stability, reliable surface processing facility and less beam loss.

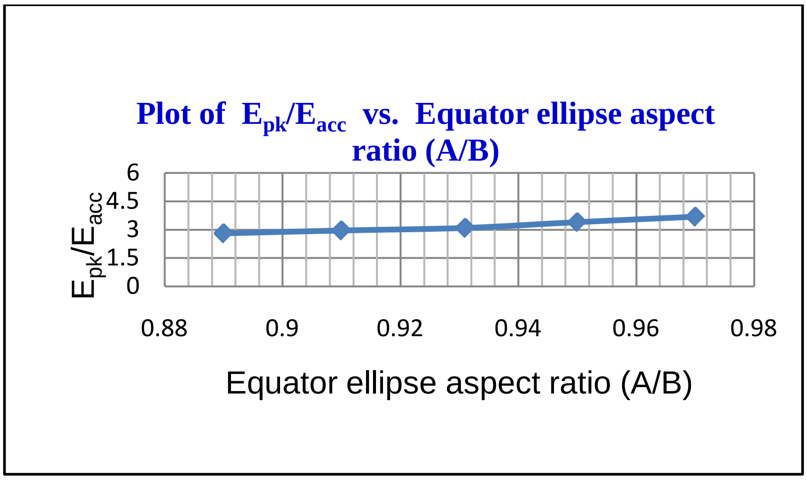

Fig.4.3.1.12 Plot of normalized peak surface electric field $\left(\frac{E_{pk}}{E_{acc}}\right)$ vs. Equator ellipse aspect ratio $\left(\frac{A}{B}\right)$ for the elliptical cavity.

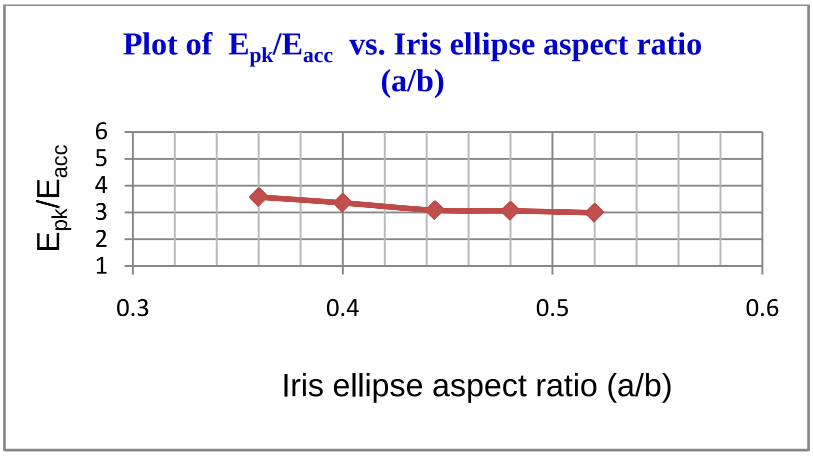

Fig.4.3.1.13 Plot of normalized peak surface electric field $\left(\frac{E_{pk}}{E_{acc}}\right)$ vs. Iris ellipse aspect ratio $\left(\frac{a}{b}\right)$ for the elliptical cavity.

Table-1–Simulation results for single-cell elliptical and Re-entrant cavities at 650 MHz, β = 0.61

$\frac{A}{B}$ (mm./mm.)	$\frac{a}{b}$ (mm./mm.)	Equator radius (D/2) (mm.)	Iris radius (R_{iris}) (mm.)	Half-cell length L/2 (mm.)	$\frac{R}{Q}$ (Ω)	G (=Q.R_S) (Ω)	E_{acc} (MV/m)	$\frac{E_{pk}}{E_{acc}}$	$\frac{B_{pk}}{E_{acc}}$ [mT/(MV/m)]	$f_{\pi-mode}$ (MHz)	Remarks
Elliptical Cavity											2D SUPERFISH, 3D CST MWS α=2.38 deg. Energy=23.87 J
$\frac{54}{58}$	$\frac{13.7}{30.876}$	197.346	48	70.335	58.6	192.9	17	3.048	4.7172	650.008	
Re-entrant cavity											2D SUPERFISH, 3D CST MWS α = −10.48 deg. Energy=22.13 J
$\frac{65}{54}$	$\frac{13.67}{30.8}$	188.1	48	70.335	63.2	202.5	17	3.085	4.525	650.008	

Table-2: Simulation results for five-cell elliptical cavities at 650 MHz, β = 0.61

$\frac{A}{B}$ (mm./mm.)	$\frac{a}{b}$ (mm./mm.)	Equator radius D/2 (mm.)	Iris radius R_{iris} (mm.)	Half-cell length L/2 (inner) (mm.)	$\frac{R}{Q}$ (Ω)	G (=Q.R_S) (Ω)	E_{acc} (MV/m)	$\frac{E_{pk}}{E_{acc}}$	$\frac{B_{pk}}{E_{acc}}$ [mT/(MV/m)]	$f_{\pi-mode}$ (MHz)	Remarks
***CAVITY-1**: Wall slope angle is 3.6 deg. for all cells and two half end cells have different geometry from mid cells.*											2D SUPERFISH 3D CST MWS $\left(\frac{a}{b}\right)_{end} = \frac{20.66}{46.54}$ $\left(\frac{A}{B}\right)_{end} = \frac{45.94}{49.35}$ α=3.6 deg Energy=118.8 J Mesh size=0.05
$\frac{54}{58}$	$\frac{11.99}{27}$	198.175	48	70.335	290	197	17.00	3.34	4.90	650.	
***CAVITY-2**: Wall slope angle is 2.4 deg. (mid cells) & 4.5 deg.(end cells) and two half end cells have different geometry from mid cells.*											2D SUPERFISH 3D CST MWS $\left(\frac{a}{b}\right)_{end} = \frac{10.67}{24.02}$ $\left(\frac{A}{B}\right)_{end} = \frac{54}{58}$ α =2.4 deg (mid) =4.5 deg (end) Energy=118.8 J Mesh size=0.05
$\frac{54}{58}$	$\frac{13.68}{30.82}$	197.4	48	70.335	296	200	17.00	3.00	4.84	650.	

Table-3: Comparative chart of design parameters for five-cell elliptical cavities at 650 MHz, β = 0.61

Name of the lab designed	$\frac{A}{B}$ (mm./ mm.)	$\frac{a}{b}$ (mm./ mm.)	Equator radius D/2 (mm.)	Iris radius R_{iris} (mm.)	Half-Cell Length L/2 (inner) (mm.)	$\frac{R}{Q}$ (Ω)	G (=Q.R_s) (Ω)	E_{acc} (MV/m)	$\frac{E_{pk}}{E_{acc}}$	$\frac{B_{pk}}{E_{acc}}$ [mT/ (MV/m)]	$f_{\pi-mode}$ (MHz)	Remarks
Fermilab (FNAL)	$\frac{54}{58}$	$\frac{14}{25}$	194.95	42	70.335	378	191	17.0	2.26	4.21	650	2D SLANS code L/2 = 71.385 (end-cell) α = 2.0 deg. (mid-cell) = 2.7 deg. (end-cell) E = 92.7 J
Jefferson Lab (JLAB)	$\frac{50.46}{45}$	$\frac{15}{22}$	192.10	50	65.456	297	190	17.3	2.71	4.78	650	2D SUPERFISH code Equator flat = 0.976 mm.(mid-cell) = 0.5047 (end-cell) α = 0 degree E = 118.8 J
VECC	$\frac{54}{58}$	$\frac{13.68}{30.82}$	197.40	48	70.335	296	200	17.0	3.00	4.84	650	2D SUPERFISH, 3D CST MWS, α = 2.4 deg. (mid-cells) = 4.5 deg. (end-cells), $\left(\frac{a}{b}\right)_{end-cells} = \frac{10.67}{24.02}$ Energy = 118.8 J

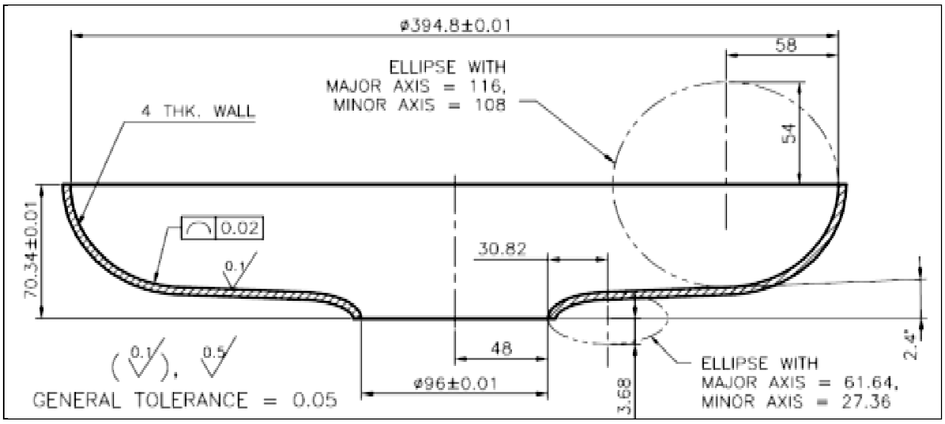

Fig.4.3.1.14–Engineering drawing for half-cell (mid-cell) of CAVITY-2

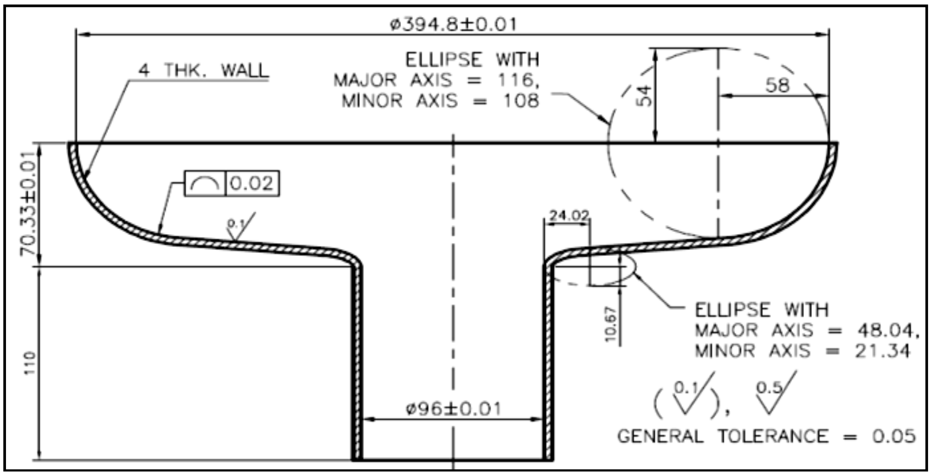

Fig.4.3.1.15–Engineering drawing for half-cell (end-cell)of CAVITY-2

4.3.2 Cavity Shrinkage

The cavity is designed at room temperature and it will be operated at 2K. The niobium cavity will shrink due to thermal contraction of the material at cryogenic temperature. Therefore, it is necessary to adjust the dimensions of the cavity by taking into account the 150 μm of material removal (t_{ch}) due to chemical treatment like buffered chemical polish (BCP), electro-polishing (EP) etc. and thermal shrinkage from room temperature (293K) to 2K. The aperture and equator radius is decreased by 150 μm. The ellipse centers and half-cell length do not change appreciably. Half axis in Iris area are increased by 150 μm, while that in equator area are decreased by the same quantity. Although the thermal expansion/contraction coefficient (α_{Nb}) of niobium is actually non-linear (as shown in Fig. 4.3.2.1) with respect to temperature (inK), the linear approximation of thermal expansion[55]gives,$k_{Nb} = \frac{(L_{293} - L_2)}{L_{293}} = 142 \times 10^{-5}$. If the inside dimension of the cavity under cold and warm condition are L_{COLD} and L_{WARM}, the relation between them is established as follows. The cold and warm dimensions (as shown in Fig.4.2.3.1) of the cavity are tabulated in Table-4.

$$L_{COLD} = \frac{(L_{WARM} + t_{ch})}{(1 + k_{Nb})}$$

Table-4 Cold and Warm Dimensions of 650 MHz, β=0.61, SRF Cavity

Dimensional Parameters	COLD Dimension(inside) (*as designed*) (mm)	COLD Dimension (pre-BCP treatment of 150 μm) (mm)	WARM Dimension (inside) (*as fabricated*) (mm)
Equator radius (D/2)	197.400	197.250	197.53
Iris radius (R_{iris})	48.000	47.850	47.92
A	54.000	53.850	53.93
B	58.000	57.850	57.93
a	13.680	13.830	13.85
b	30.820	30.970	31.01
a (for end-cell)	10.670	10.820	10.84
b (for end-cell)	24.020	24.170	24.21
Half-cell length (L/2)	70.335	70.335	70.44

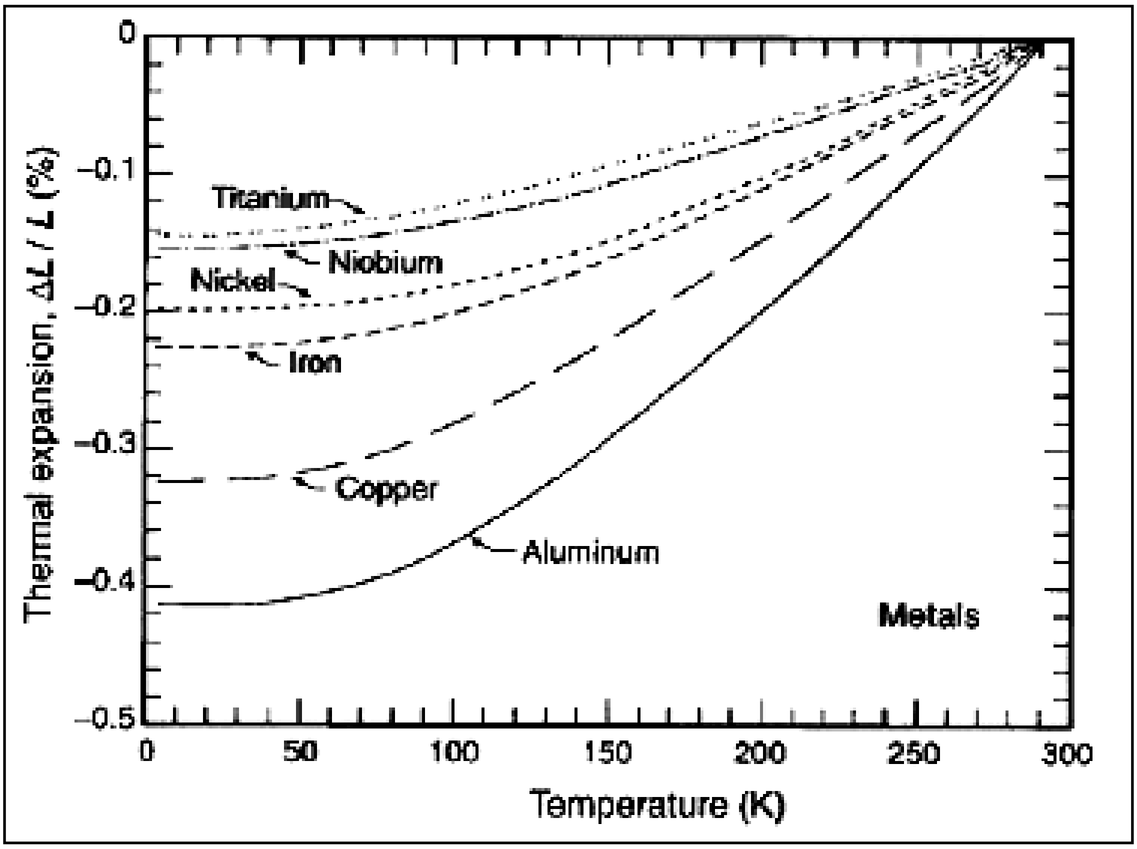

Fig. 4.3.2.1. Plot of percentage linear thermal expansion [$\Delta L/L = (L_T - L_{293})/L_{293}$] of common metals including niobium (compiled by Clark 1983 from Data of Corruccini and Gniewek 1961, and Hann 1970)

4.3.3 Higher Order Modes (HOMs)

As the beam of charged particles passes through the cavity, it generates higher order modes with higher resonant frequencies. Mainly, the existence of dipole and monopole higher order modes (HOMs) may create problems, especially, in well collimated on-axis beam, thereby limiting the performance of the cavity. Besides, beam instability, the presence of HOMs also has adverse effect of producing heat on the cavity wall, thereby adding thermal load to the cryogenic system. The existence of transverse (dipole) and longitudinal (monopole) HOMs of the cavity has been investigated using CST Microwave Studio code. CST results of some of the transverse higher order modes are shown in Fig.4.3.3.1(a), (b), (c), (d) & (e) and longitudinal higher order modes are shown in & Fig.4.3.3.2(a) & (b). However, it is observed (from Fig.4.3.3.3&Fig.4.3.3.4) that there is no trapped higher order modes(transverse or longitudinal) with high effective impedance. Hence, HOM dampers are not necessary for the cavity operating at the beam current limited to 2 mA. For higher beam current applications, HOM damper may be necessary.

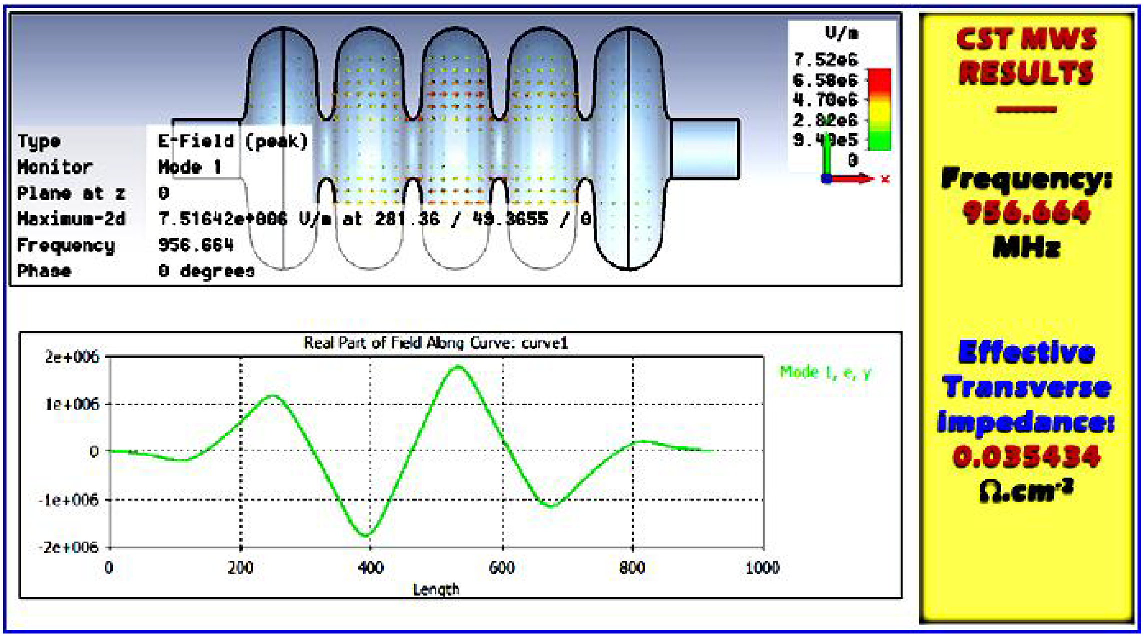

Fig.4.3.3.1(a) CST MWS result for one of the transverse HOMs for the cavity

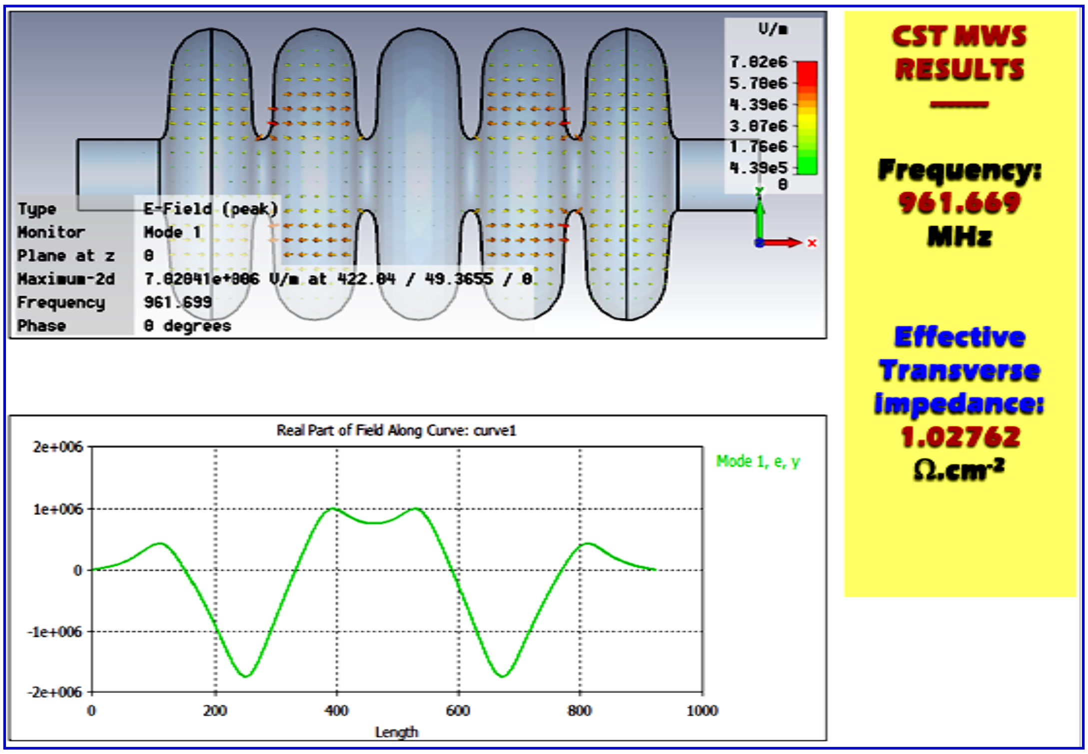

Fig.4.3.3.1(b) CST MWS result for one of the transverse HOMs for the cavity

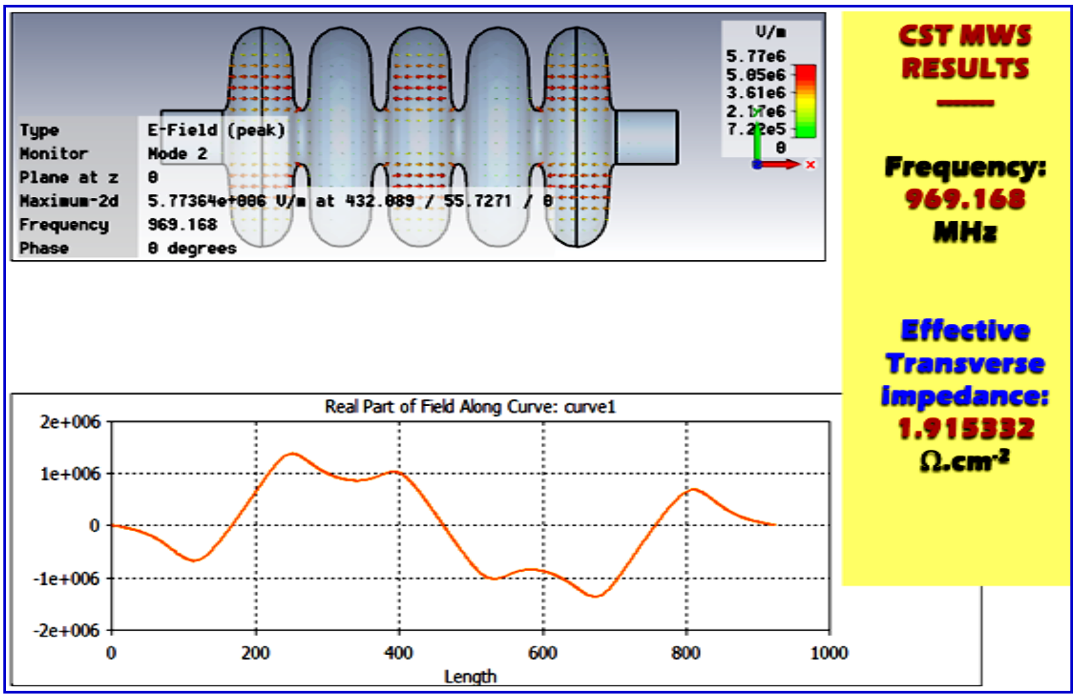

Fig.4.3.3.1(c) CST MWS result for one of the transverse HOMs for the cavity

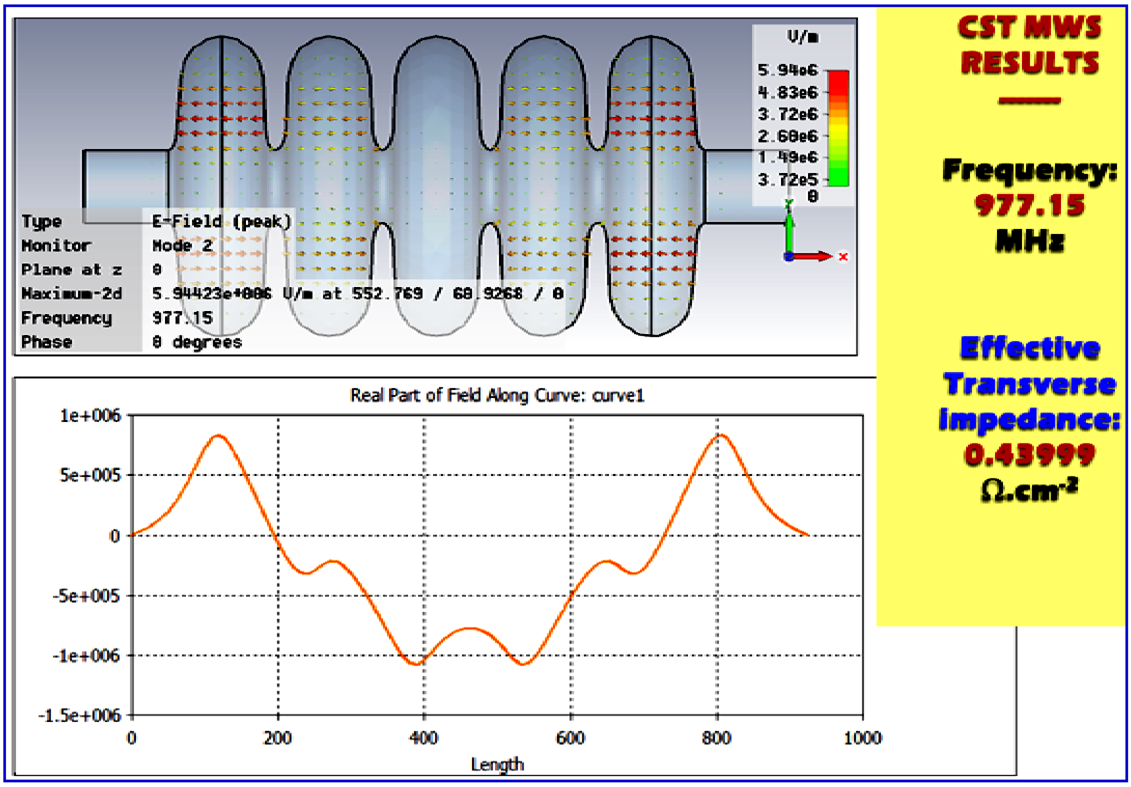

Fig.4.3.3.1(d) CST MWS result for one of the transverse HOMs for the cavity

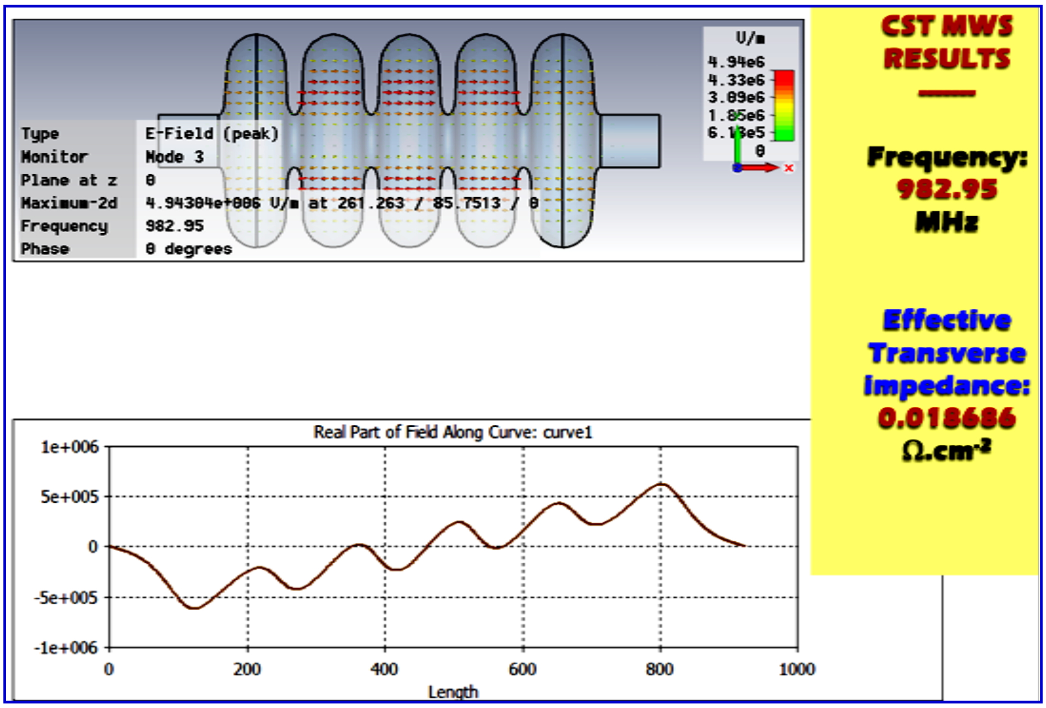

Fig.4.3.3.1(e) CST MWS result for one of the transverse HOMs for the cavity

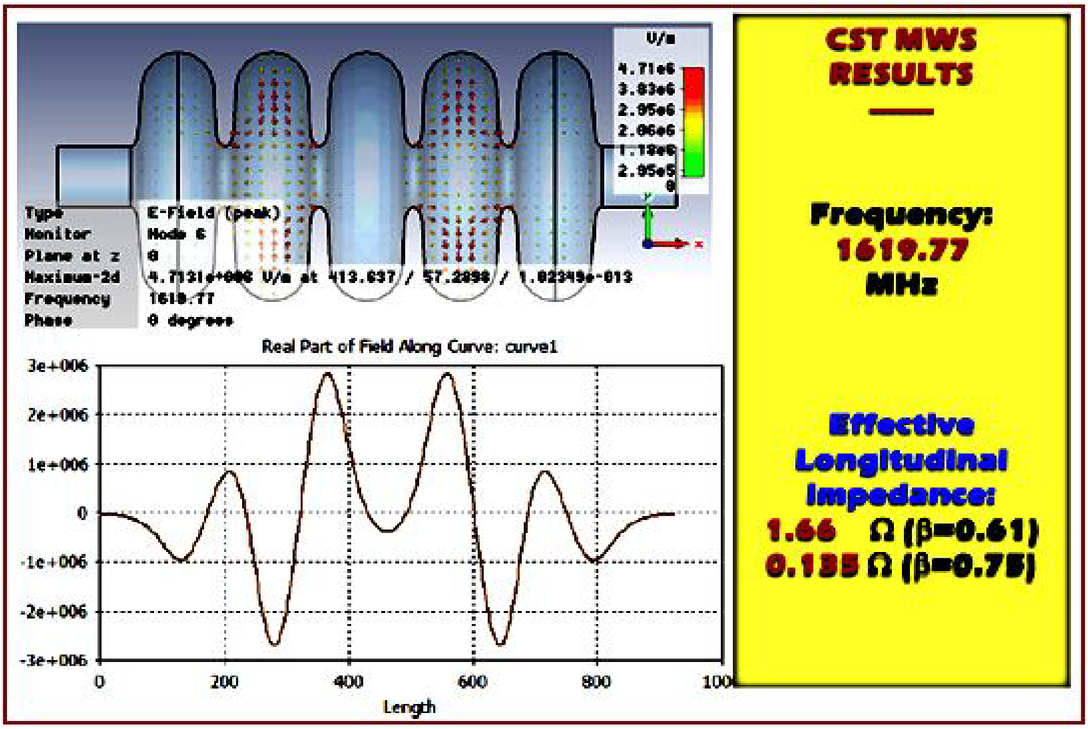

Fig.4.3.3.2(a) CST MWS result for one of the longitudinal HOMs for the cavity

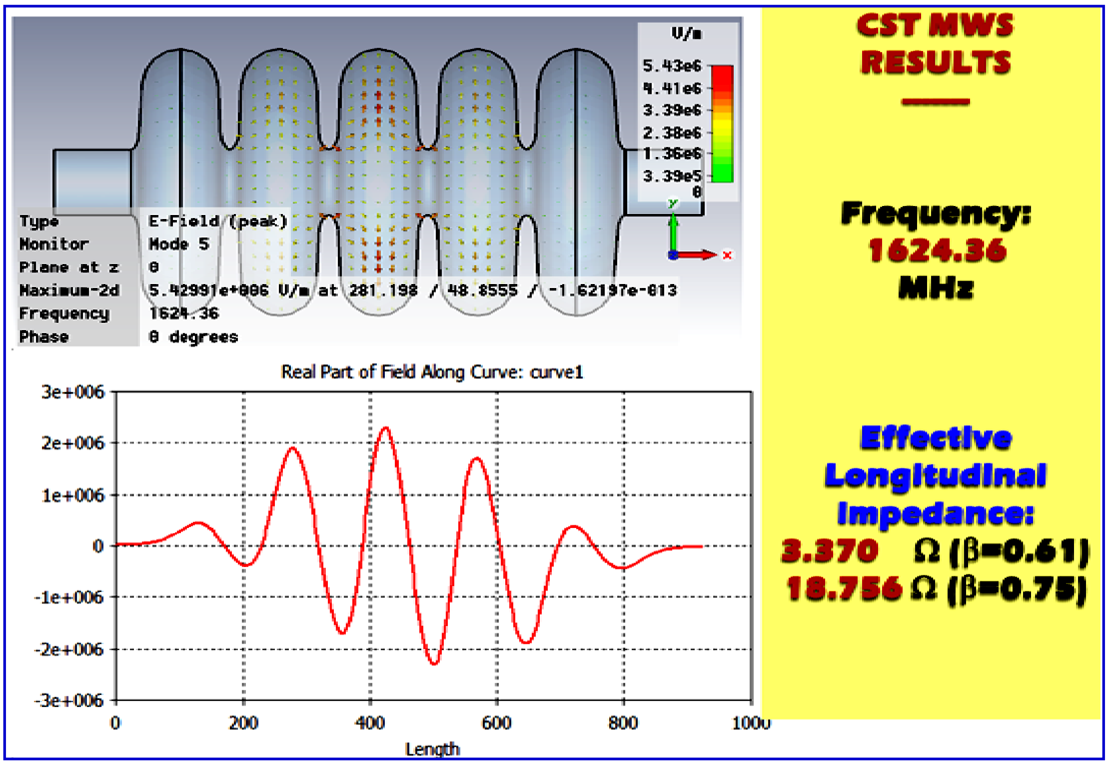

Fig.4.3.3.2(b) CST MWS result for one of the longitudinal HOMs for the cavity

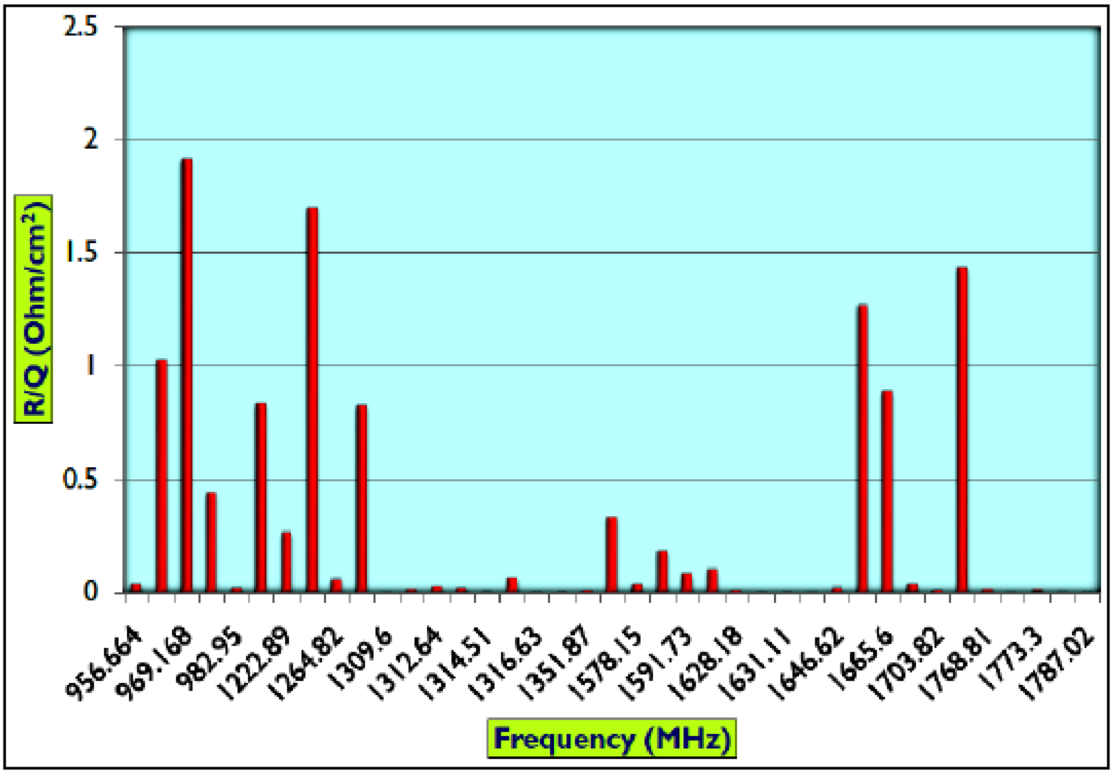

Fig.4.3.3.3 Effective impedance for transverse HOMs

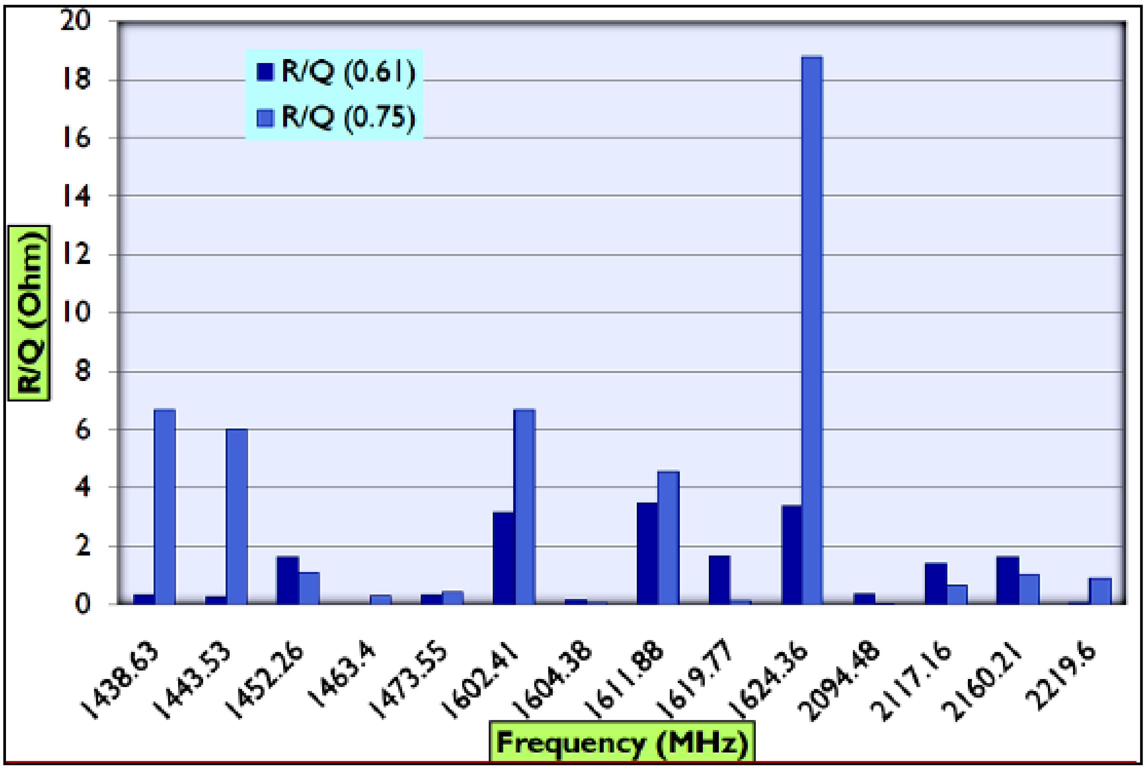

Fig.4.3.3.4 Effective impedance for longitudinal HOMs

4.3.4 Multipacting

A few decades ago, Multipacting, or Resonant Field Emission, was a limitation on SRF cavities. The evacuated cavity structures containing RF fields have a tendency of multipacting, which is resonant coupling between the fields and emitted electrons. The primary electrons emitted from the inside RF surface of the cavity get accelerated by the RF fields and follow a trajectory or closed orbital paths such that they impact back at the surface of the cavity an integral number of RF cycles after emission. The impacting primary electrons then produce secondary electrons from the surface and the cycle is repeated causing an avalanche effect, until all available power goes into this process[56]. Due to this effect the required accelerating gradient cannot build up in the cavity. Multipacting is an undesirable effect in the cavity and it can be overcome by appropriately choosing the cavity shapes. In order to eliminate the multipacting the fields should be produced such that emitted electrons will drift towards the equator, eventually ending up in a region with zero surface electric field. In this way the avalanche effect can be stopped. In the elliptical cavity, the emitted electrons drift towards the cavity equator, where the electric field is not strong enough for secondary emission to recur.

In general, the lower order of multipacting resonance is more problematic since it is spatially broader and more stable. Anyway, it is desirable to avoid lower order multipacting (less than 6^{th} or 7^{th} cycle) for the entire operating range, and to avoid any multipacting resonances that coincide with operating power level of the coupler.

A preliminary study of multipacting analysis for 650 MHz, β = 0.61, 5-cell SRF cavity has been carried out using 2D code MultiPac2.1 (Windows version). The analysis has been done for both mid-cells and end-cells and the inputs for mid cells and end cells are shown in Fig.4.3.4.1(a)& Fig.4.3.4.1(b). The secondary electron emission coefficient is greater than 1, if the impact energy of electron is above 50 eV. In the present multipact analysis, 30 impacts of electrons have been considered, which is a sufficient proposition for the analysis.

The result of the multipacting analysis for the mid-cell and end-cell of the said cavity is discussed below. Fig.4.3.4.2(a) &Fig.4.3.4.2(b) show the variation of three parameters, electron counter function (c_{30}/c_0), average impact energy (Ef_{30}) and enhanced electron counter function (e_{30}/c_0), with Peak electric field for mid-cell and end-cell cavities respectively.

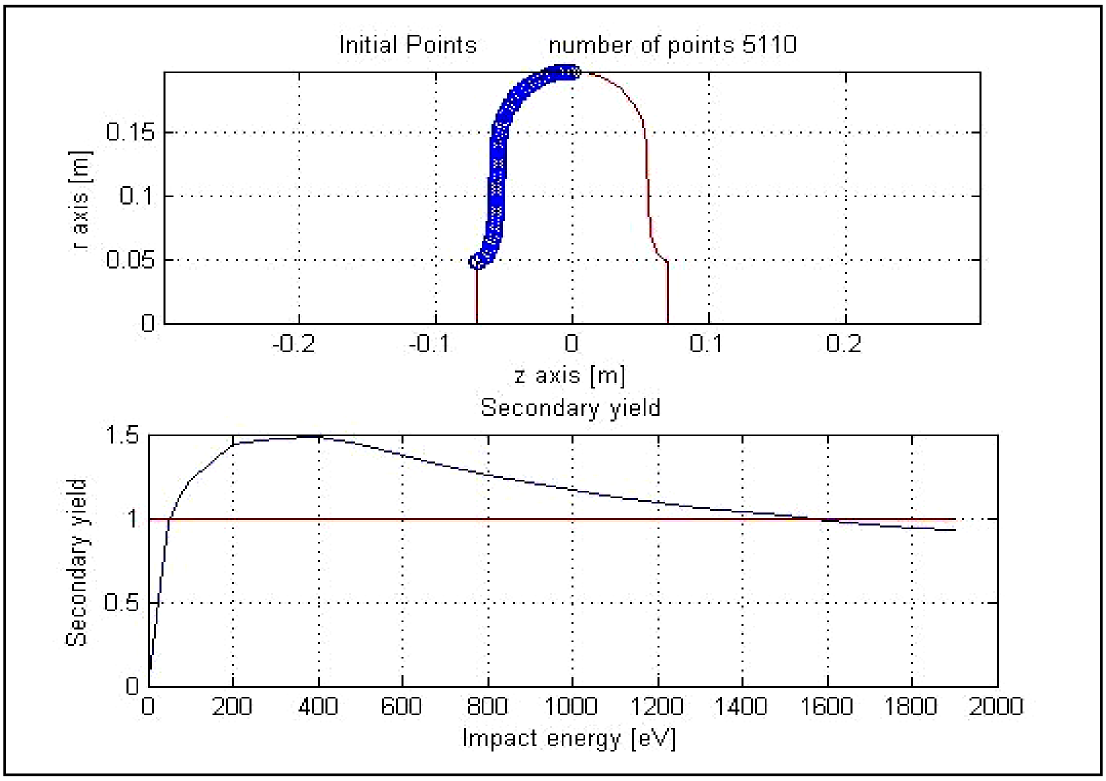

Fig.4.3.4.1(a)

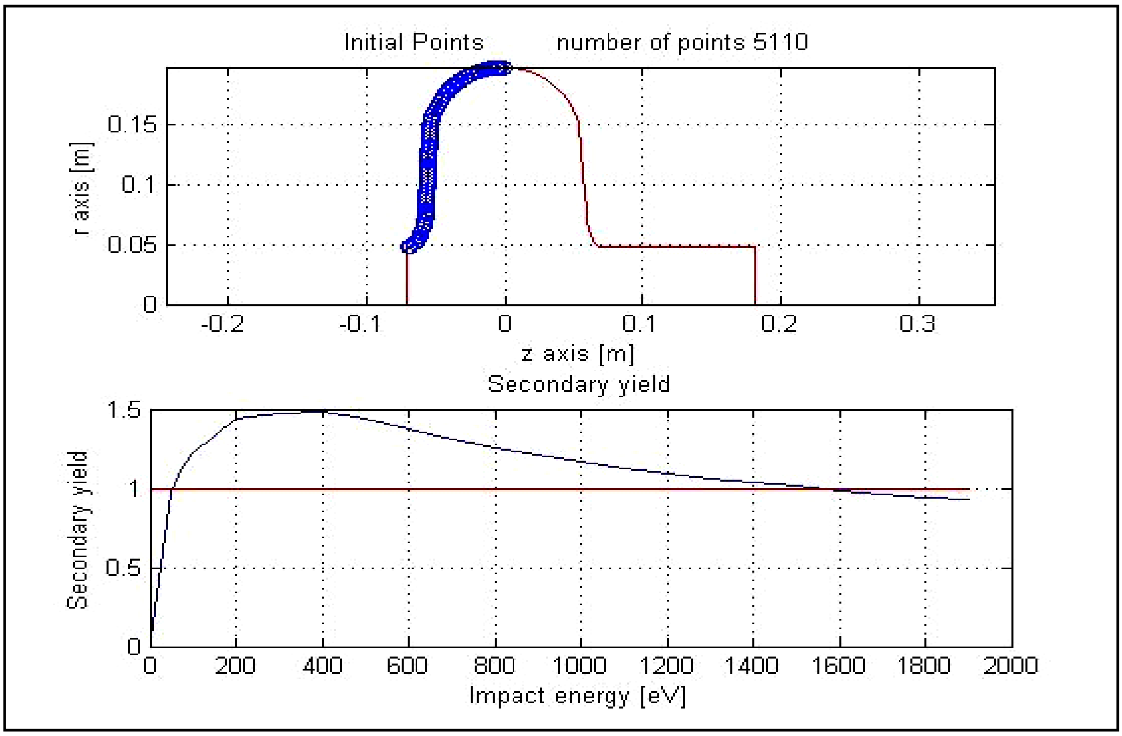

Fig.4.3.4.1(b)

Fig.4.3.4.1 (a)Input for mid-cell of the 5-cell cavity;(b)Input for end-cell of the 5-cell cavity

c_0 is the initial number of electrons which can impact on the surface of the cavity, c_{30} is the total number of electrons (with and/or without proper impact energy and phase synchronization to cause multipacting) available after 30 impacts on the surface of the cavity and e_{30} is the number of secondary electrons (with proper impact energy and phase synchronization to cause multipacting). The impact energy is less than 50 eV for all peak electric fields excepting a small region between 30–35 MV/m, where it is around 200 eV. However, we can conclude that no multipacting can take place in the said cavity as the relative enhanced electron counter function is less than 1 for the whole range of peak electric field up to 60 MV/m.

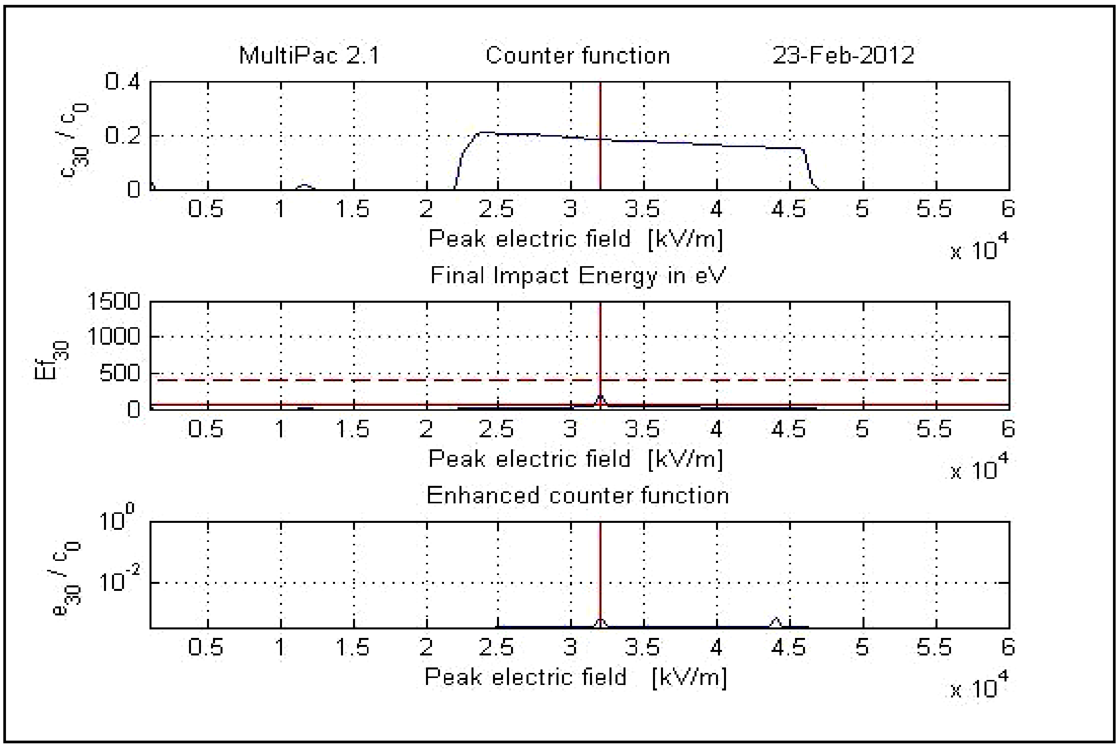

Fig.4.3.4.2(a)

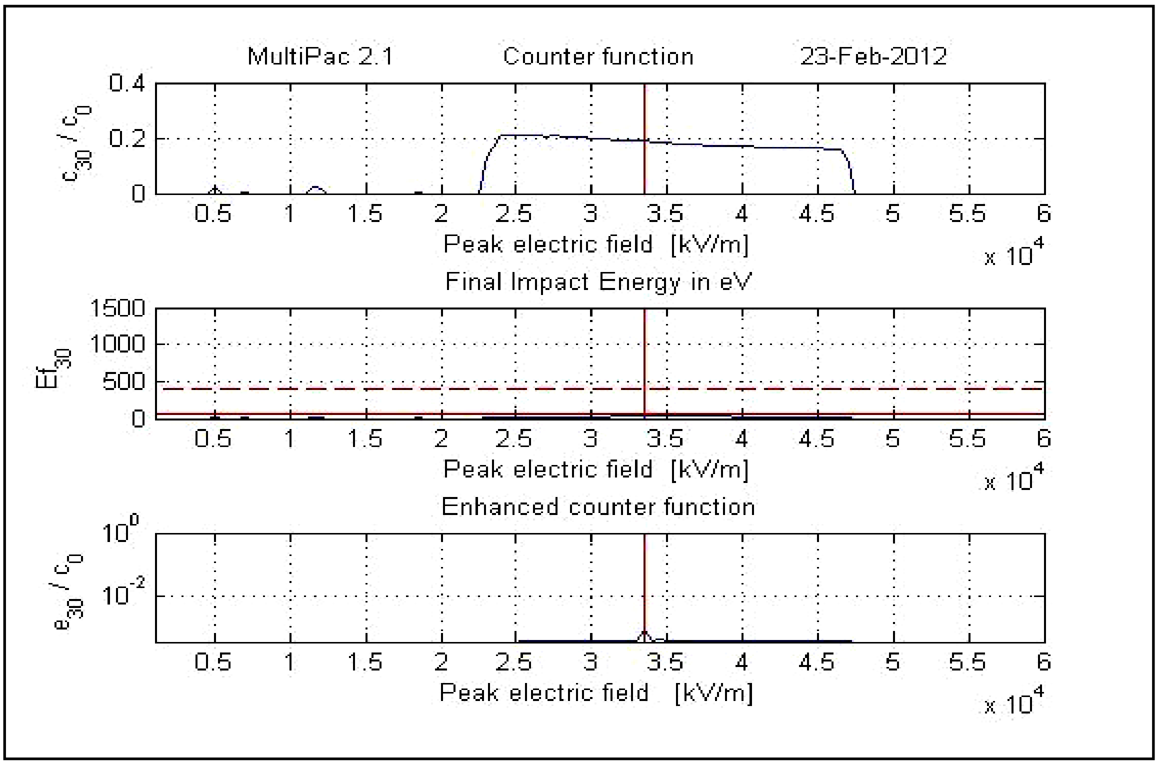

Fig.4.3.4.2(b)

Fig.4.3.4.2 Plot of electron counter function, impact energy and enhanced electron counter function with peak electric field for (a) mid-cell and (b) end-cell of the 5-cell cavity

It is observed from Fig.4.3.4.3(a) & Fig.4.3.4.3(b) for mid-cells and end-cells that even after 30 impacts of electrons at the equator region (at the radius of 197 mm) of the cavity, the final impact energy is 28.4364 eV, which is well below 50eV and hence it is unlikely to cross secondary electron emission yield for producing multipacting.

2D MultiPac 2.1 code with simplified model of secondary electron emission predicted that the probability of Multipacting in the above cavity is negligible. However, it is necessary to carry out 3D simulation for the same cavity to confirm the presence of Multipacting. In the present case Multipactinganalysis for 650 MHz, β = 0.61, SRF cavity has been carried out using 3D CST Partcle Studio code. In this code, the model for secondary electron emission is based on Furman model [57] that includes three types of secondary electrons like, elastic back scattered, rediffused and also true secondary particles (as shown in Fig. 4.3.4.4).

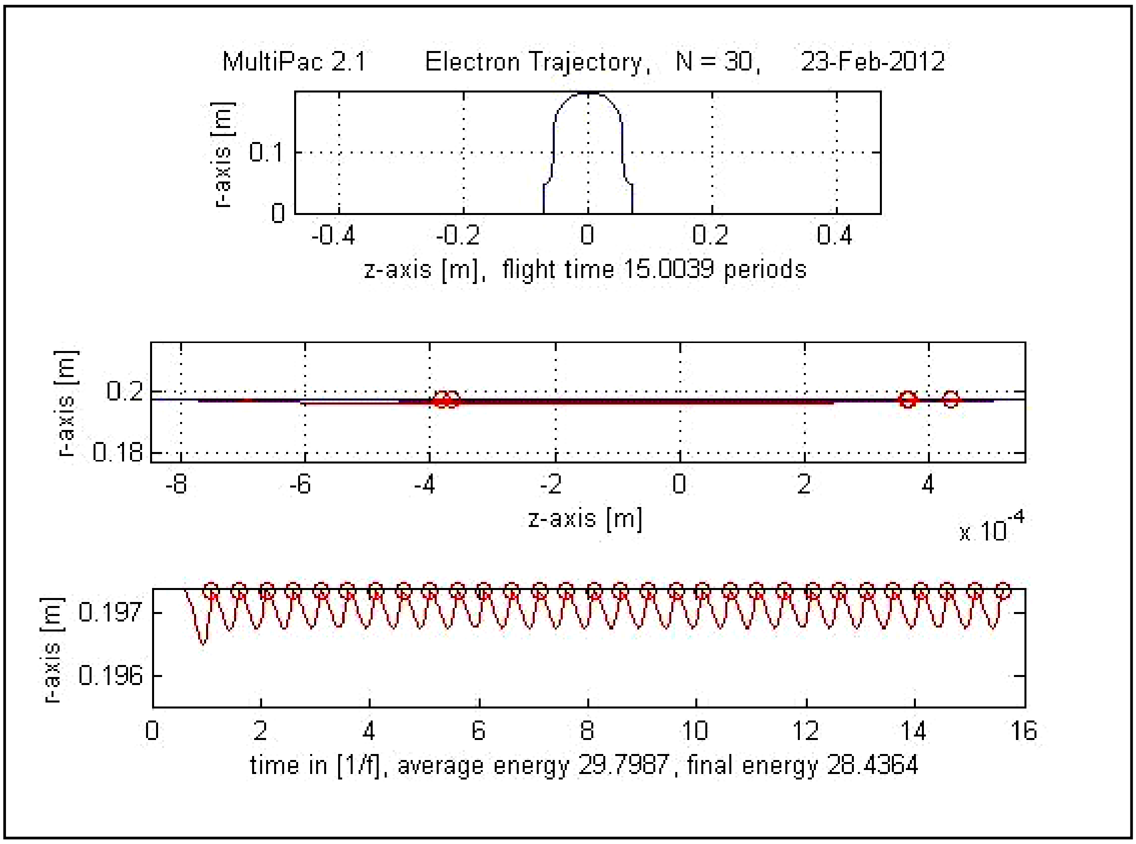

Fig.4.3.4.3(a)

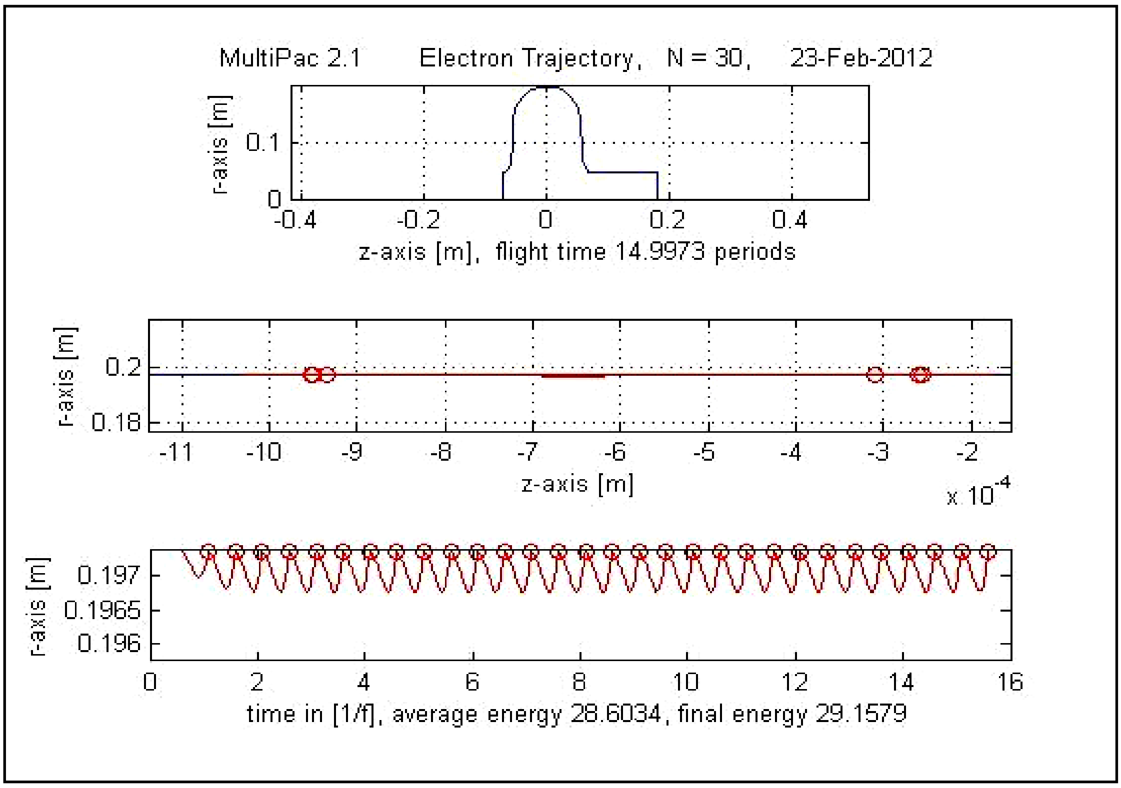

Fig.4.3.4.3(b)

Fig.4.3.4.3 Plot of electron impact at the equator region (zoomed scale) with RF period for (a) mid-cell and (b) end-cell of the 5-cell cavity

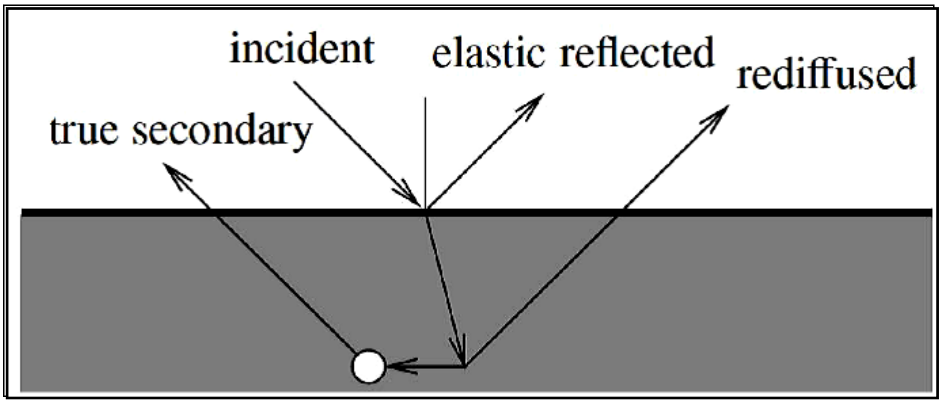

Fig.4.3.4.4 An incident electron strikes a surface yielding three types of secondary electrons.

Furman model is a mathematically self-consistent probabilistic model for the secondary electron emission process. According to this model[57] when a steady current (I_0) of electrons strikes a surface at a given energy and angle, a certain portion of current (I_e) is reflected elastically while the remaining ones penetrate into the material. Some of these electrons (called "rediffused" electrons corresponding to rediffused electron current, I_r) scatter from one or more atoms inside the material and are reflected back out. The rest of the electrons (called "true secondary" electrons corresponding to true secondary current, I_{ts}) interacts in a more complicated way with the material. The secondary emission yields for the elastically reflected, rediffused and true secondary electrons are $\delta_e = \frac{I_e}{I_0}$, $\delta_r = \frac{I_r}{I_0}$ and $\delta_{ts} = \frac{I_{ts}}{I_0}$ respectively. So the total secondary emission yield (SEY) is $\delta = \frac{(I_e+I_r+I_{ts})}{I_0} = \delta_e + \delta_r + \delta_{ts}$. The inputs for this model are the three components of SEY and the secondary energy spectrum. The main assumptions[57] in this model are given below.

- The secondary electrons are generated instantaneously when a primary electron strikes on a surface.
- The backscattered electrons are generated only in a single-electron event.
- The true secondary electrons generated in events for arbitrary n≥1 with a distribution in "n" whose mean is the true secondary component of the SEY.

Actually, the elastic back scattered and rediffused secondary electrons change the situation drastically and have to be included into the model. Here, 30 mm of equator region has been simulated in order to limit the memory requirement of the computer. The minimum mesh size has been chosen as 0.37 mm, which provides convergence. Multipacting starts at electric field 5.8 MV/m (as shown in Fig.4.3.4.5 & Fig.4.3.4.6). It actually takes place at electric field between 5.8 MV/m and 11.5 MV/m and the rate of producing secondary electrons is very fast at 6.8 MV/m (as shown in Fig. 4.3.4.7& Fig.4.3.4.8). At 9 MV/m, the rate of increase in particle starts reducing (as shown in Fig. 4.3.4.9 & Fig.4.3.4.10). At 11.5 MV/m, the rate of increase in particle due to multipacting is very low (as shown in Fig. 4.3.4.11& Fig. 4.3.4.12). There is no occurrence of multipacting below 4.5 MV/m and beyond 22.5 MV/m (as shown in Fig. 4.3.4.13& Fig.4.3.4.14).

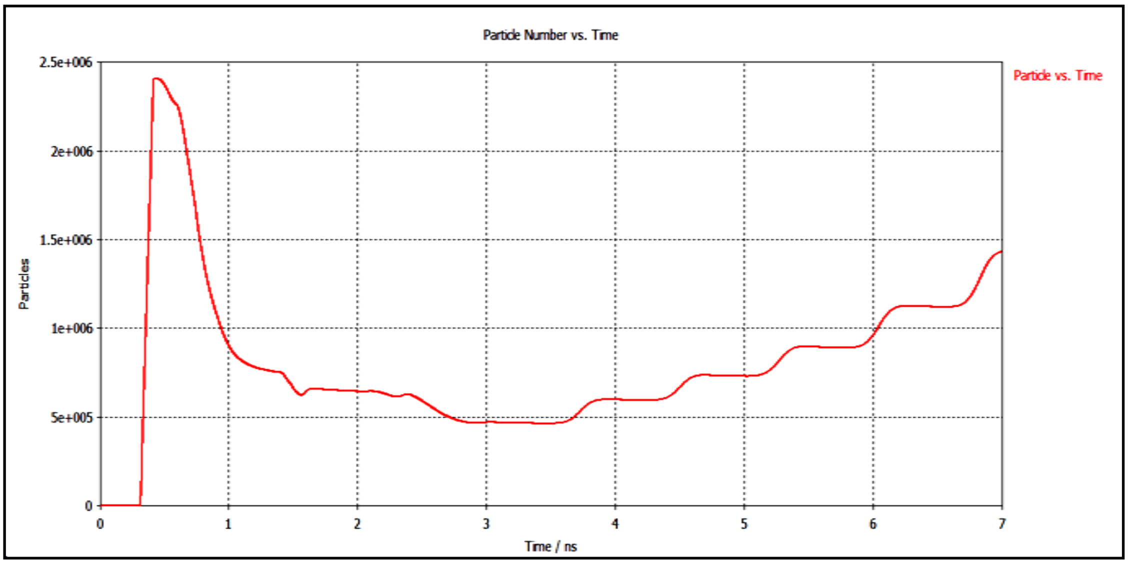

Fig.4.3.4.5 Plot of Particle counts vs. time (ns) at accelerating gradient of 5.8 MV/m in the cavity (as simulated with 3D CST article Studio Code)

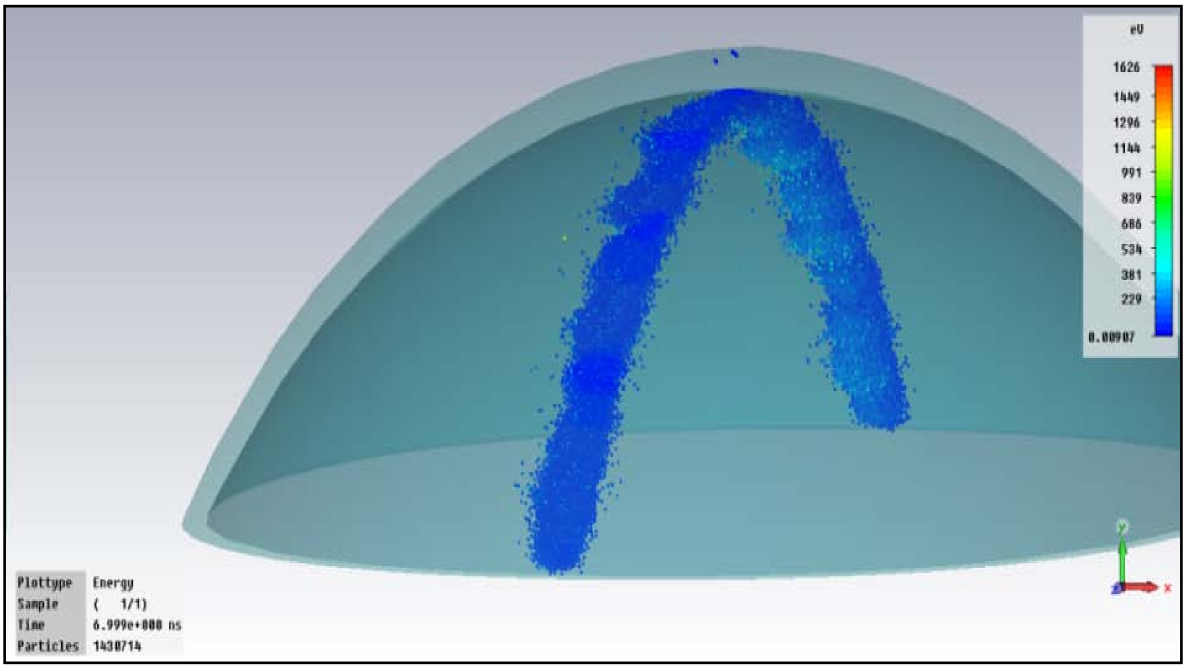

Fig.4.3.4.6 View of fast rate of Particle growth at the equator region of the cavity after 7 ns at accelerating gradient of 5.8 MV/m (as simulated with 3D CST Particle Studio Code)

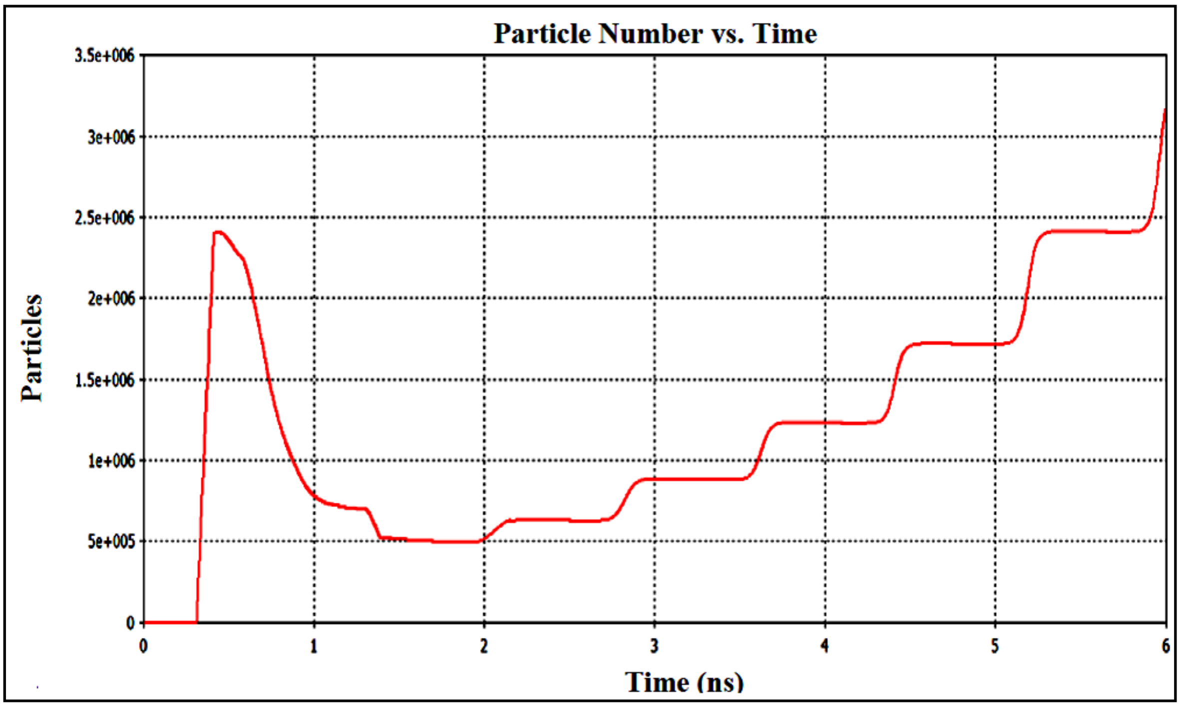

Fig.4.3.4.7 Plot of Particle counts vs. time (ns) at accelerating gradient of 6.8 MV/m in the cavity (as simulated with 3D CST Particle Studio Code)

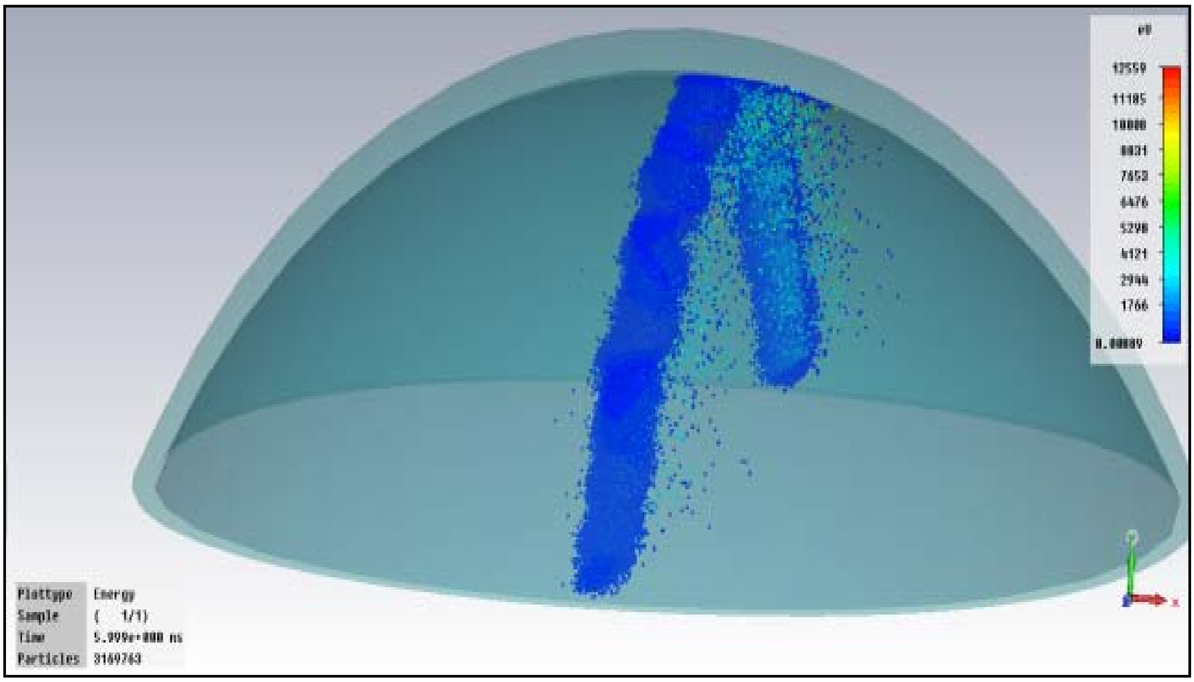

Fig.4.3.4.8 View of fast rate of Particle growth at the equator region of the cavity after 6 ns at accelerating gradient of 6.8 MV/m (as simulated with 3D CST Particle Studio Code)

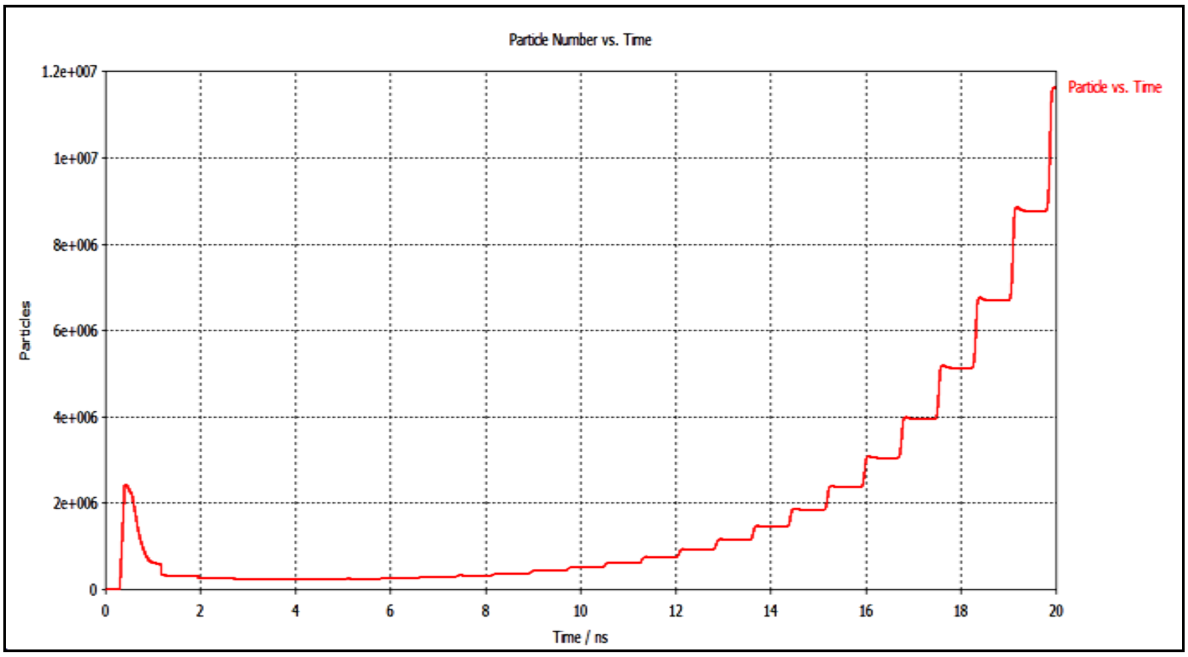

Fig.4.3.4.9 Plot of Particle counts vs. time (ns) at accelerating gradient of 9 MV/m in the cavity (as simulated with 3D CST article Studio Code)

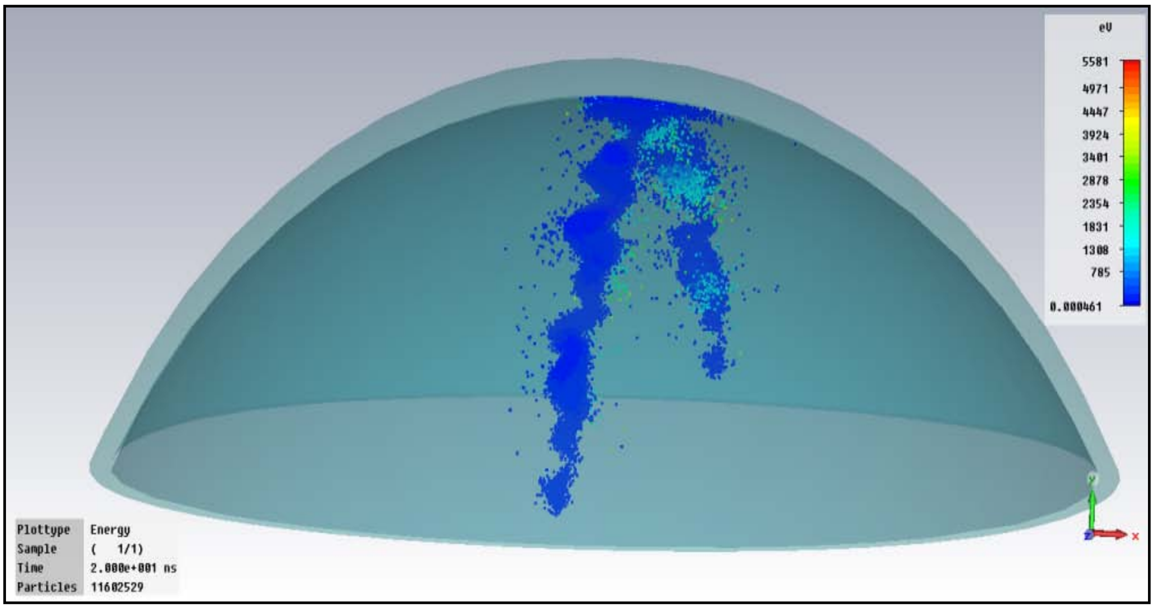

Fig.4.3.4.10 View of fast rate of Particle growth at the equator region of the cavity after 20 ns at accelerating gradient of 9 MV/m as simulated with 3D CST Particle Studio Code

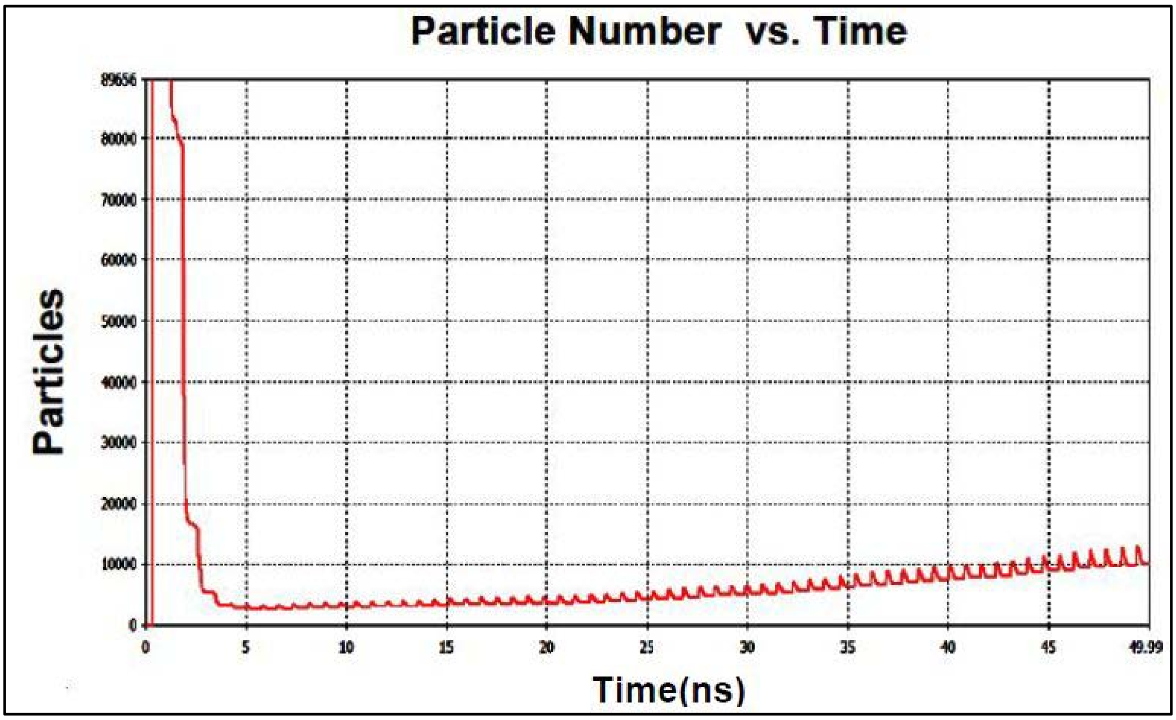

Fig.4.3.4.11 Plot of Particle counts vs. time (ns) at accelerating gradient of 11.5 MV/m in the cavity (as simulated with 3D CST article Studio Code). A very low rate of particle growth is seen.

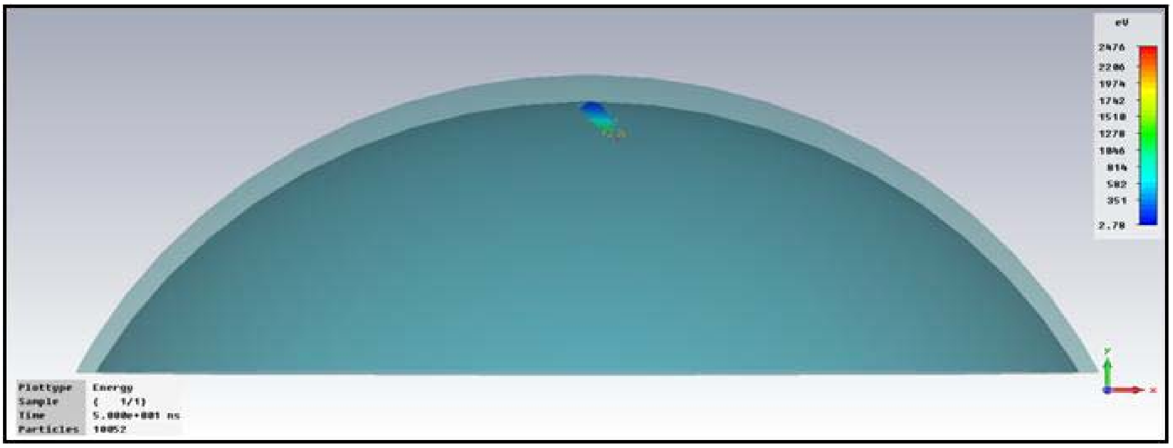

Fig.4.3.4.12 View of very low rate of Particle growth at the equator region of the cavity after 50 ns at accelerating gradient of 11.5 MV/m (as simulated with 3D CST Particle Studio Code)

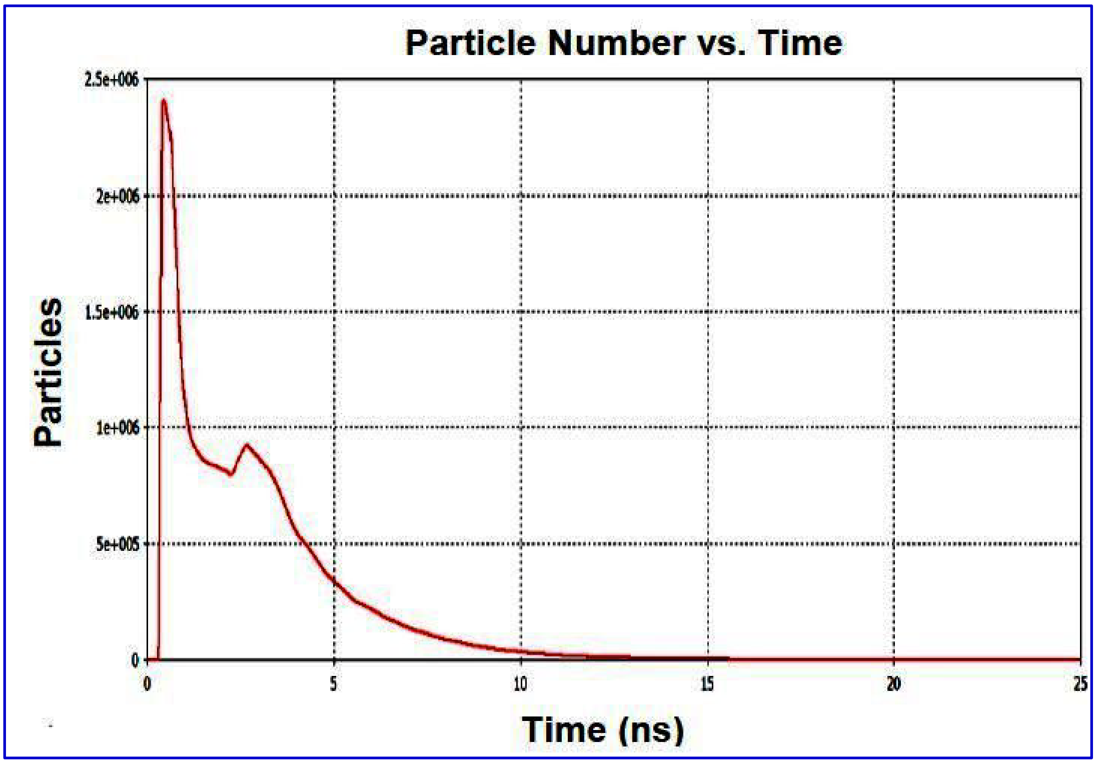

Fig.4.3.4.13 Plot of Particle counts vs. time (ns) at accelerating gradient of 4.5 MV/min the cavity (as simulated with 3D CST article Studio Code). No particle growth or multipacting is observed.

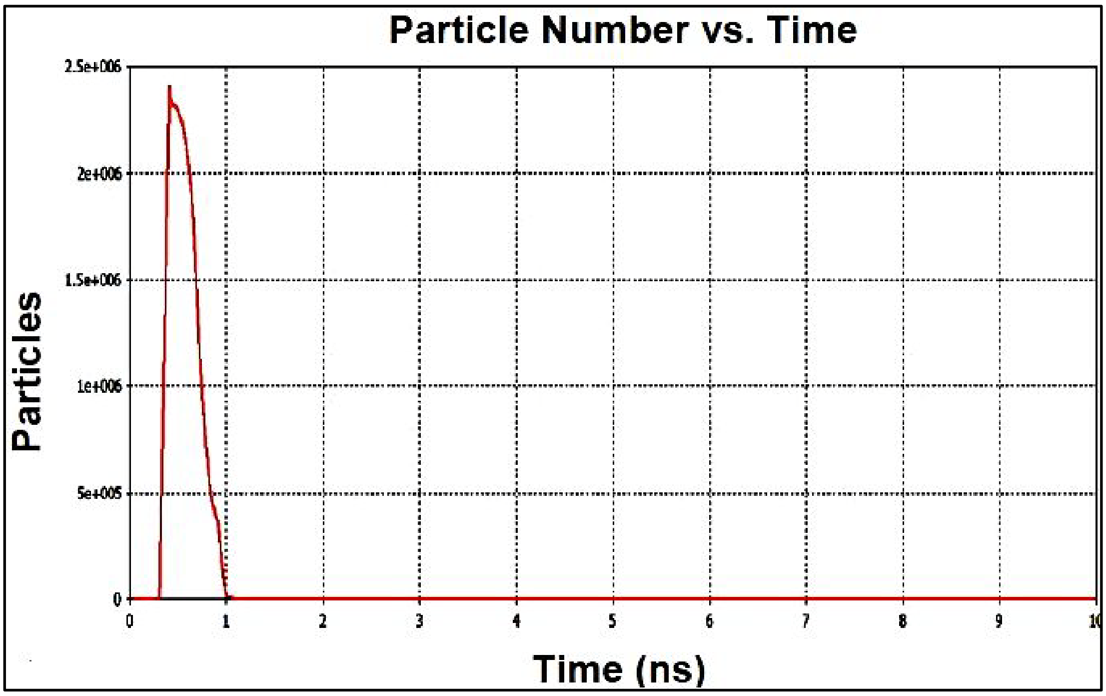

Fig.4.3.4.14 Plot of Particle counts vs. time (ns) at accelerating gradient of 22.5 MV/min the cavity (as simulated with 3D CST article Studio Code). No particle growth or multipacting is seen.

A small convexity in the equator region (as shown in Fig.4.3.4.15) suppresses the multipacting significantly, probably, because the remaining electric field lines at the equator region, vanishes, due to this convexity, as the electric field lines cannot be parallel with the metal boundaries. However, the small convexity does not change appreciably the cavity parameters, like, peak surface fields, quality factor, R/Q etc. Practically, this small convexity gets introduced automatically during electron beam welding, which in turn may become beneficial, as far as multipacting is concerned.

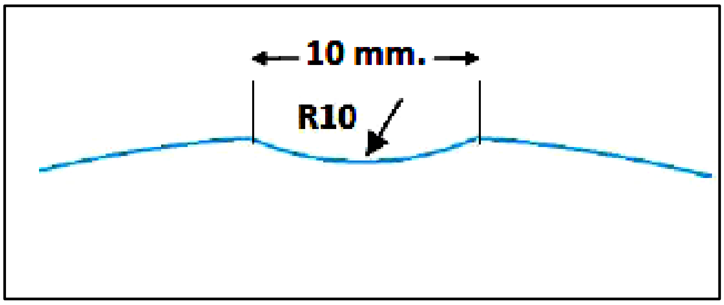

Fig.4.3.4.15 convexity in the equator region of the cavity

4.3.5 Mechanical Analysis

4.3.5.1 Modal Analysis

The preliminary mechanical modal analysis (as shown in Fig. 4.3.5.1.1) of the cavity (using 3D Finite Element Model) shows that the natural frequencies of mechanical modes[58] without stiffener are present below 100 Hz, which is not desirable for operation. Because, in that case the cavity may get detuned due to any household low frequency vibrations. However, with stiffener, the frequencies are increased beyond 100 Hz. The natural frequencies and mode shapes are determined (as shown in Table-5) for 5-cell cavity under different support conditions. The stiffener (made of stainless steel) needs to be placed at the radius of 133 mm (as shown in Fig. 4.3.5.1.2) in order to raise the mechanical mode above 100 Hz. The modal analysis result for stiffened 5-cell cavity has been shown in Fig.4.3.5.1.3.

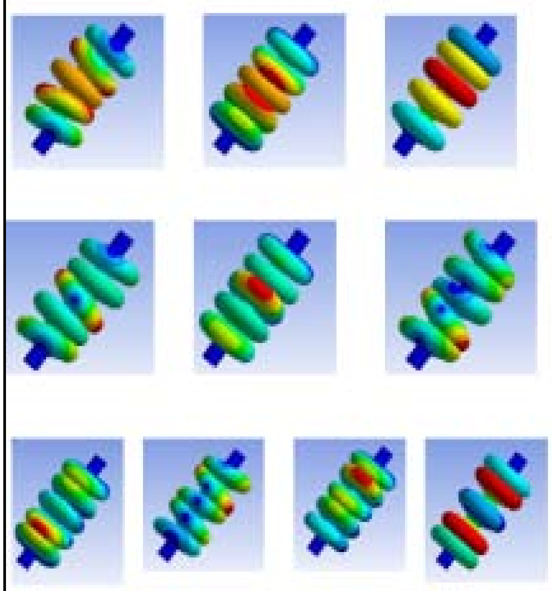

Mode	Frequency [Hz]
1.	3.0625
2.	5.9953
3.	8.6136
4.	10.776
5.	11.161
6.	24.688
7.	26.005
8.	27.449
9.	28.538
10.	57.485

Fig.4.3.5.1.1 Frequencies of mechanical modes of the cavity without stiffener

Table-5 Modal frequencies of 5-cell cavity under different support conditions

Modal frequencies (Hz)	
Both End Fixed	One End Fixed
51.952	24.705
101.72	73.351
146.16	119.15
182.75	158.05
189.39	186.75
419.78	353.67
442.33	421.16
467.10	444.88
485.80	469.09
975.59	486.47

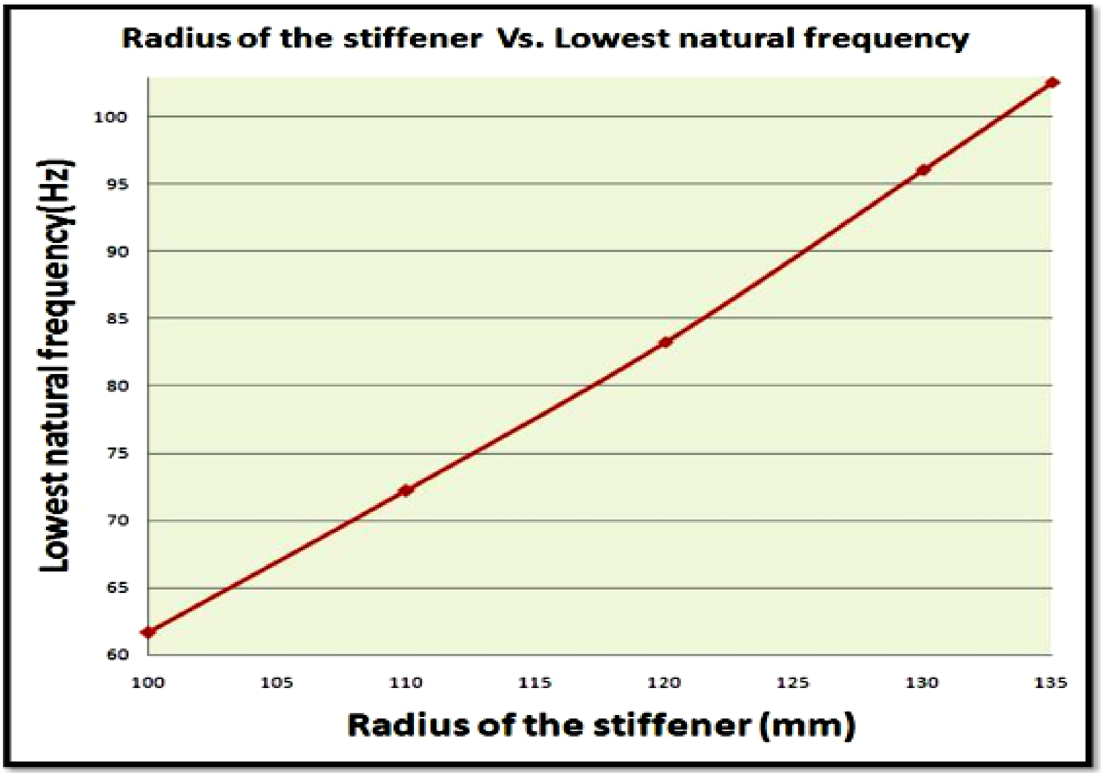

Fig.4.3.5.1.2 Plot of lowest natural frequency (Hz) in mechanical modes vs. Stiffener position (mm) from the cavity axis in the radial direction

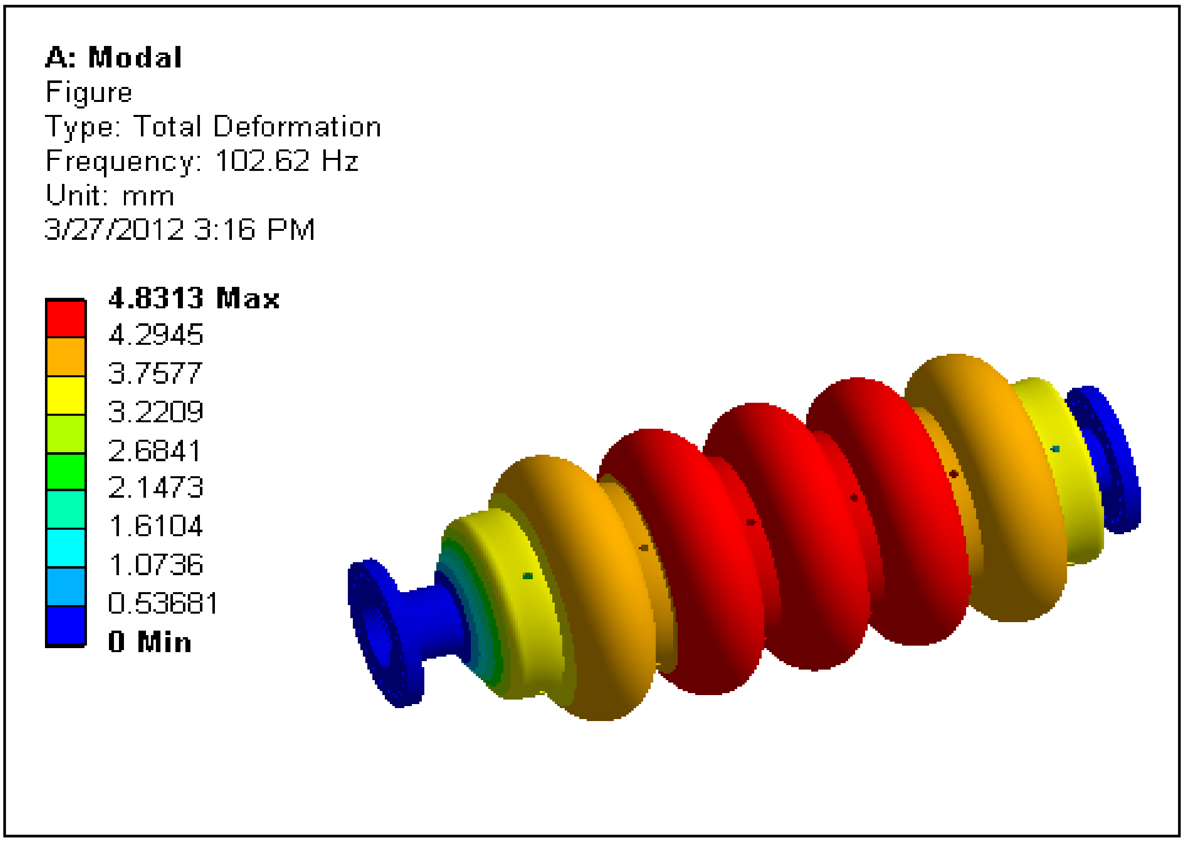

Fig.4.3.5.1.3 Modal analysis result for stiffened 5-cell cavity (using 3D ANSYS code)

4.3.5.2 Structural Analysis

The SRF cavity is subjected to cryogenic temperature (~ 2K) and external pressure under operating conditions. The simulation and preliminary structural analysis[58][59]of the cavity has been carried out using 3D ANSYS code, assuming operating temperature at 2K and external pressure of 3 atm (which is taken much higher compared to the operating pressure), with boundary conditions of both ends being fixed. As the 5-cell cavity is axis symmetric, the Finite Element Axis-Symmetric Modeling has been done (as shown in Fig. 4.3.5.2.1). Stress calculations have been done as per ASME Pressure Vessel Code Section-III for niobium with mechanical properties as mentioned in Table-6. On carrying out primary stress linearization along the thickness of iris (where the stress intensity value is maximum), it is found (as shown in Fig. 4.3.5.2.2) that the primary membrane stress integral intensity is

44 MPa, which is well within the allowable limit of 103 MPa. The combined stress intensity of primary membrane and bending is 120 MPa, which is well within allowable limit of 154 MPa (=1.5 x 103 MPa). The combined stress integral intensity (as shown in Fig. 4.3.5.2.3), comprising of primary membrane stress, bending stress and secondary stress, of 4 mm thick niobium sheet has been obtained as 131 MPa, which is well within the allowable limit of 309 MPa (=3 x 103 MPa), as per ASME code. Various stress plots indicate that they are within allowable limits. The maximum deformation due to combined loading is obtained as 0.465 mm (as shown in Fig. 4.3.5.2.4). The stress intensity (at Iris) across the thickness of the 5-cell niobium cavity is shown in Fig. 4.3.5.2.5.

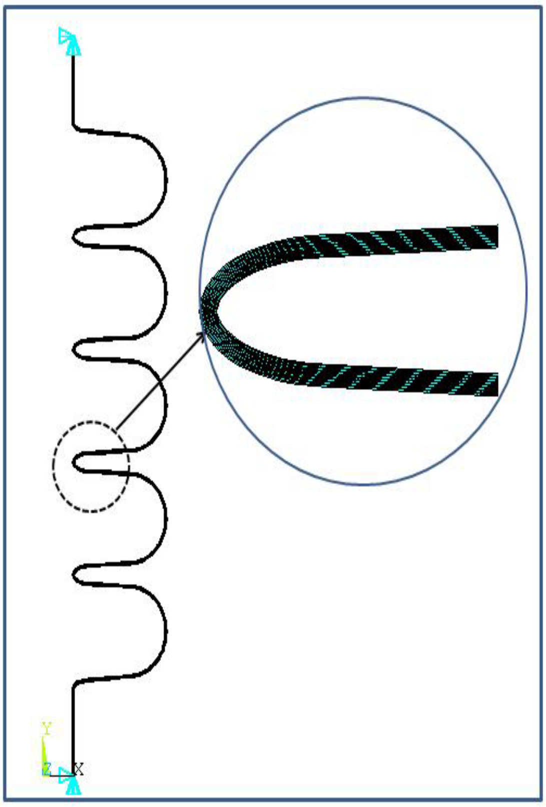

Fig. 4.3.5.2.1 Finite Element Model(axis symmetric) of 5-cell SRF cavity

Table-6 Mechanical properties of niobium

Temperature (K)	Young's Modulii (GPa)	Yield Strength (MPa)	Tensile Strength (MPa)	Design Allowable Strength (MPa)
295	97.9	50	100	33.33
2	97.9	310	310	103.3

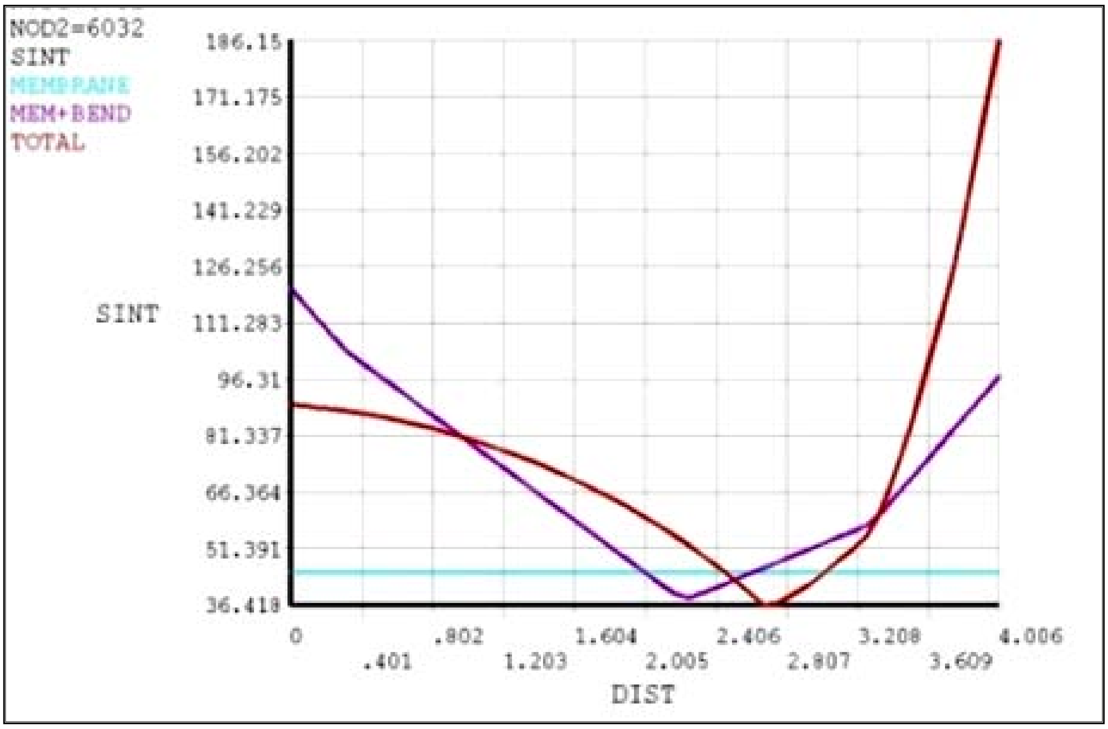

Fig. 4.3.5.2.2 Plot of stress integral across thickness (4 mm) of the niobium cavity wall(for stress linearization of Primary stress)

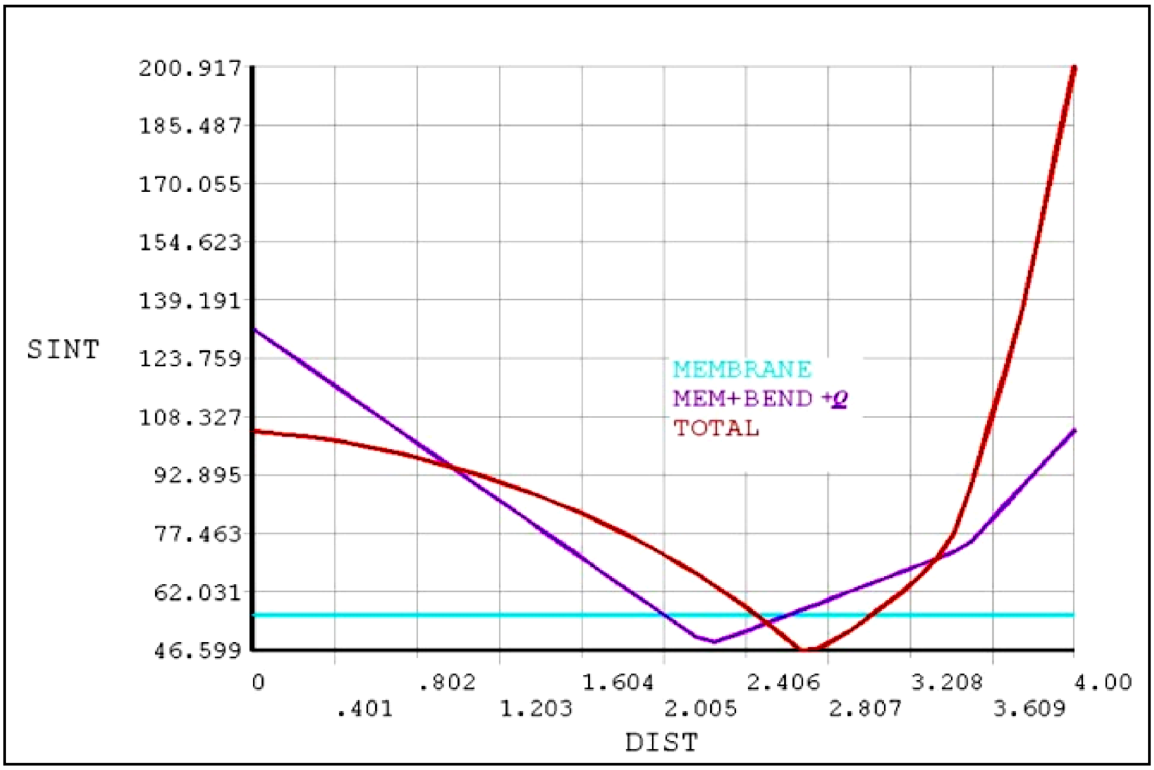

Fig. 4.3.5.2.3 Plot of stress integral across thickness (4 mm) of the niobium cavity wall (for stress linearization including thermal stress)

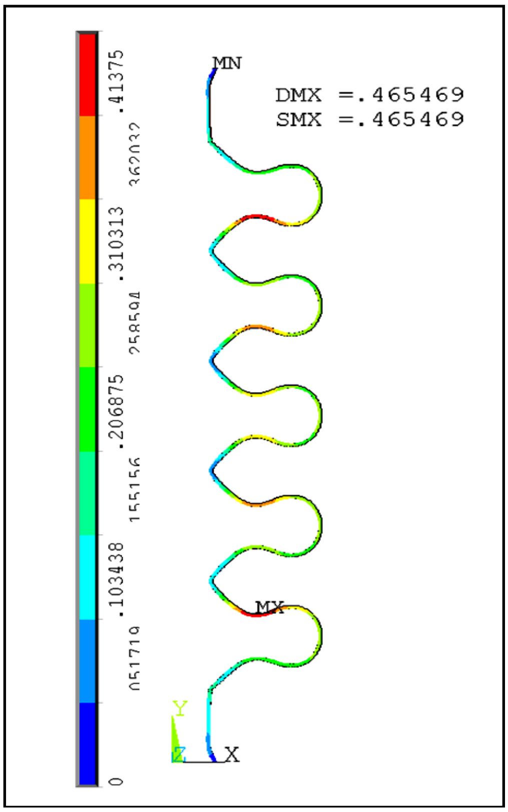

Fig. 4.3.5.2.4 Plot of deformation for 5-cell,650 MHz, β = 0.61cavity

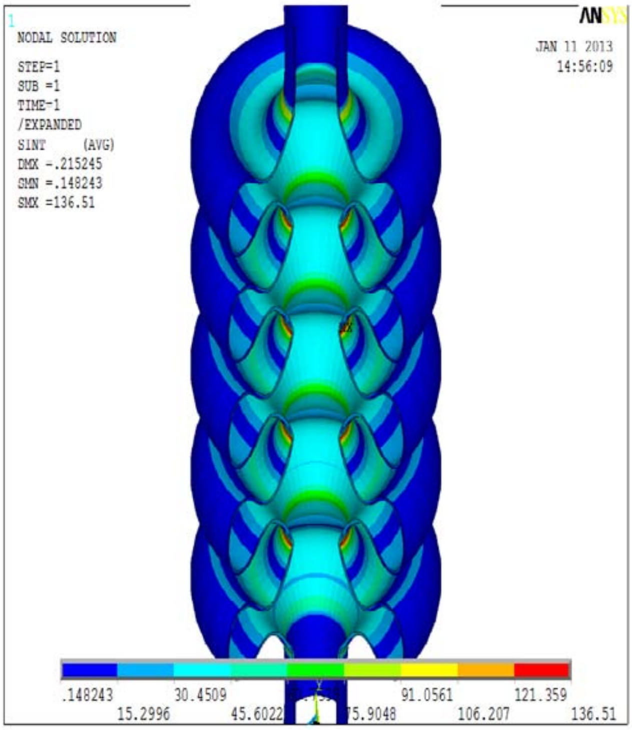

Fig. 4.3.5.2.5 Stress intensity (at Iris) across the thickness of 5-cell, 650 MHz, β = 0.61, cavity

4.3.6 Bead-pull Measurement on Cavity

The multi-cell(say, N cells) accelerating cavities have as many numbers (N) of degenerated modes and the desired accelerating mode is the π-mode [60]. The different modes have different field profile distributions. The bead-pull measurement system is used to measure the field profile for different modes. The bead-pull measurement using the technique of cavity field perturbation with a small bead is the most commonly used method to measure the field distribution inside the Radio frequency (RF) cavity. The information about the field distribution and mode orientation can be obtained by observing the coupling to electric field (E) and magnetic field (H) components at various positions in the cavity. This can be done by introducing a perturbing object (called ‘bead’) of dielectric material or metal in the cavity. The perturbation method involves drawing a perturbing object through the central axis of the cavity while monitoring the cavity's resonant frequency shifts as the object travels its entire length at a predetermined precise step.

Relevant theory of bead-pull measurement:

According to the classical Slater perturbation theory [61], a tiny perturbing object, or more commonly referred to as bead, perturbs the stored energy (U) of the resonant system of the cavity by a very small amount, resulting in a small shift or change in the resonant frequency (*f*). This frequency shift (*Δf*) is related to the relative electric field (E) and magnetic field (H) strengths in the area of the bead. Introduction of a dielectric object in a region of electric field produces a negative shift or decrease in the resonant frequency while introducing a metal object into a region of magnetic field causes a positive shift or increase in frequency. If both fields are present when a metal object is inserted the resulting frequency shift will depend on the relative strengths of the E and H fields. So the small object or bead on a string pulled through the cavity can be used to map the field distributions of the modes. In case of a small non-conducting sphere (or bead) with radius "r", where the unperturbed field may be considered uniform over a region larger than the bead, it can be shown [62] [63] in the following equation (4.3.6.01).

$$\frac{\Delta f}{f} = \frac{\Delta U}{U} = -\frac{\pi r^3}{U}\left[\mathcal{E}_0 \frac{\mathcal{E}_r - 1}{\mathcal{E}_r + 2} E_0{}^2 + \mu_0 \frac{\mu_r - 1}{\mu_r + 2} H_0{}^2\right] \text{ .... (4.3.6.01)}$$

For a dielectric bead ($\mu_r = 1$), the magnetic field perturbation is almost zero or negligible and so the above expression reduces to the equation (4.3.6.02).

$$\frac{\Delta f}{f} = -\frac{\pi r^3}{U}\left[\mathcal{E}_0 \frac{\mathcal{E}_r - 1}{\mathcal{E}_r + 2} E_0{}^2\right] \text{ .... (4.3.6.02)}$$

[where, Δf = frequency shift, f = unperturbed frequency, E_0=amplitude of electric field, H_0=amplitude of magnetic field strength, $\mathcal{E}_r$=relative permittivity of the bead, $\mathcal{E}_0$=permittivity of vacuum, , μ_r=relative permeability of the bead, μ_0=permeability of vacuum, U=energy stored in the cavity, ΔU=change in stored energy due to its perturbation].

So, with the displacement of the bead along the cavity beam axis, if frequency shift of the cavity can be measured with synchronization, electric field distribution of the linac cavity along its length on the axis can be obtained. In the present measurement technique, instead of measuring the frequency-shift, phase-shift has been measured for more stable data and then translated it into frequency-shift.

$$\frac{\Delta f}{f_0} = \frac{f_p - f_0}{f_0} = \frac{tan\ \phi(f_0)}{2Q} \quad \ldots\ldots\ldots\ldots\ldots\ldots\ldots\ldots\ldots\ldots\ldots\ldots \text{(4.3.6.03)}$$

[where, f_p= perturbed frequency, f_0 = unperturbed resonant frequency, Q = quality factor of the unperturbed cavity, $\phi(f_0)$ = shift in phase angle as a function of f_0].

Measurement set-up:

A fully automated bead pull measurement system (schematic of measurement set up as shown in Fig.4.3.6.1) has been developed to provide movement of the bead in very small steps along the cavity beam axis, measurement of the phase data using a vector network analyzer (VNA) for different positions of the bead and storing these data in a database and displaying and plotting the data. The Graphical User Interface (GUI) based software has been developed in JAVA language for automation, data acquisition, storage and display. Bead-pull measurement set up consists of a VNA (Agilent 8753ES), GPIB to Ethernet converter (GPIB-ENET/100 from National Instrument), a 1.8° hybrid stepper motor (TS41 B from Compumotor division) coupled with a gear-box (10:1) arrangement for the movement of the bead and GT6k stepper motor driver. A dielectric bead (special type of alumina) with diameter of 10mm and relative permittivity of $\mathcal{E}_r$=11 has been used for the perturbation of the cavity. The bead is attached to an insulating Kevlar thread, which is inserted in the linac cavity along its central beam axis. Kevlar is used because of its inelasticity and strength as well under tension. A pulley system guides the Kevlar thread supporting the bead to move through the central axis of the cavity. Stepper motor-gear box arrangement provides the movement of the bead and the minimum step size of the movement is less than 1 μm. The movement of the stepper motor is controlled by the GT6k controller which receives command from the GUI based software running on computer through LAN (local area network). RF measurement of the cavity is done by the vector network analyzer (VNA). The software communicates with VNA having GPIB interface through LAN using GPIB-ENET/100. It transmits command to the VNA for the RF measurement of the cavity and receives the measured data. The photograph of bead pull measurement set-up for 5-cell, 650 MHz, $\beta = 0.61$, elliptical shape prototype copper cavity is shown in Fig.4.3.6.2.

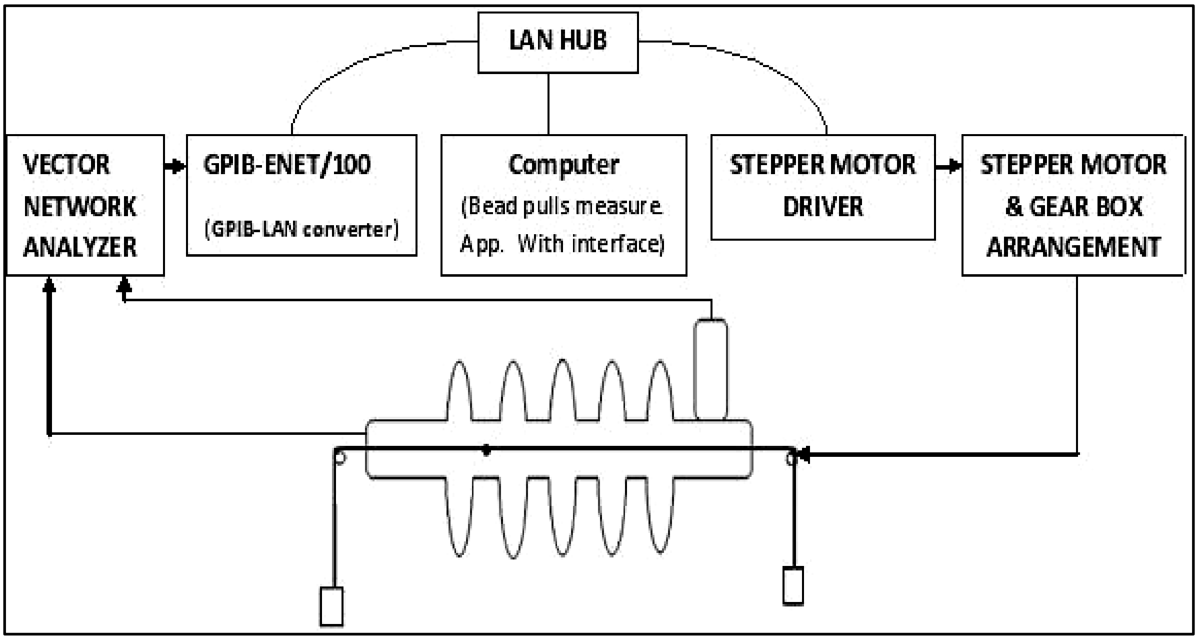

Fig.4.3.6.1 Schematic Block diagram of bead-pull measurement set-up

Fig.4.3.6.2 Bead pull measurement set up for 650 MHz, 5-cell, $\beta = 0.61$, Elliptical shape prototype copper cavity

Graphical User Interface (GUI) based software for bead-pull measurement:

The Graphical User Interface (GUI) based software, developed in JAVA language, takes care of the automation of the bead pull measurement system, storing the measured data in a database and displaying the data. Vector Network Analyzer (VNA) measures the variation of the phase of transmission coefficient of scattering parameter (S_{21}) at unperturbed resonant frequency with the displacement of the bead and phase variation is converted into frequency shift using equation (4.3.6.03). The resonant frequency of the unperturbed cavity and the quality factor of the cavity at unperturbed frequency are also measured by the VNA. A program has been developed which automates the above measurement procedure. Flow Chart for the measurement procedure is self-explanatory as given in Fig.4.3.6.3.

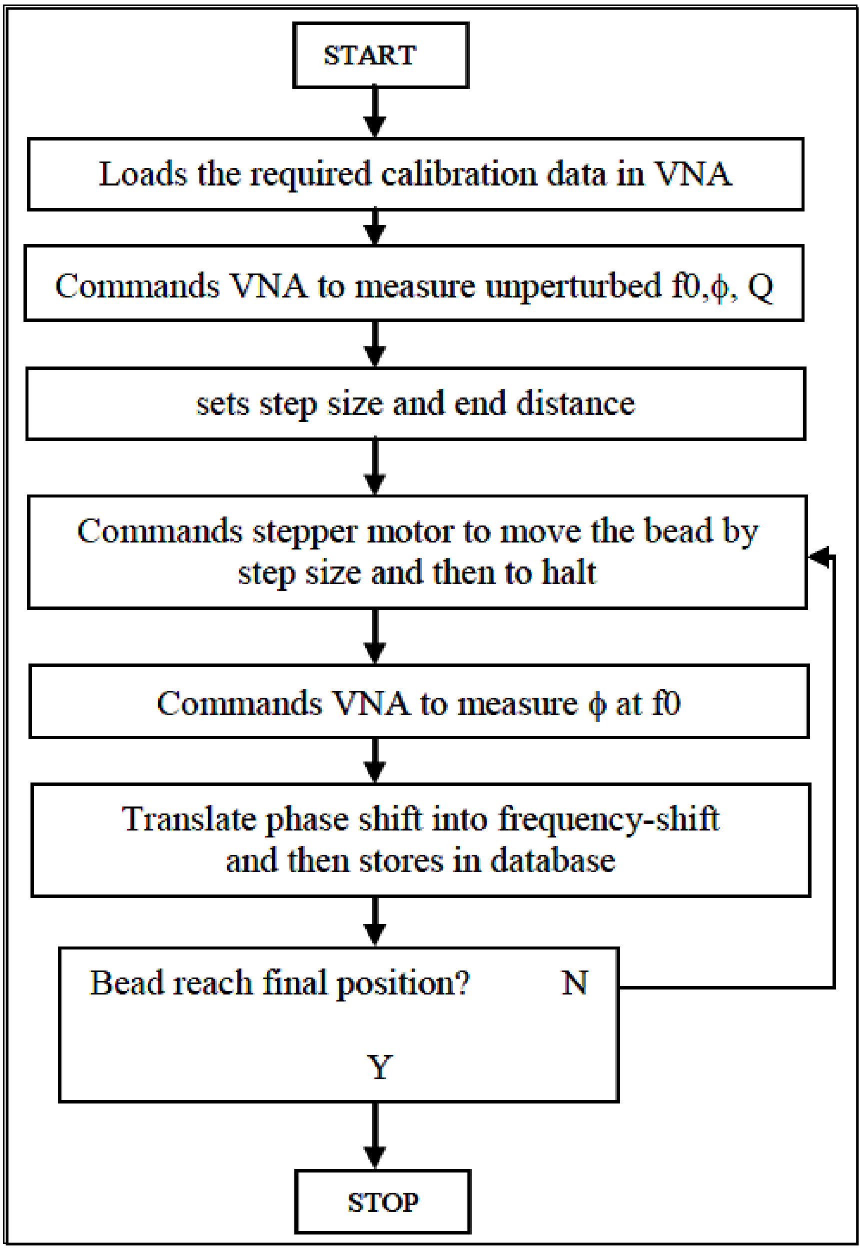

Fig.4.3.6.3 Flow chart for bead-pull measurement procedure of five-cell elliptical cavity

As the five-cell linac cavity has five distinct modes at five different frequencies, GUI based software gives mode selection facility (as shown in Fig.4.3.6.4) and also for measurement at different modes, start frequency and stop frequency can be sent to VNA. MySQL database has been used for data storage and data can be displayed in both tabular form and graphical form.

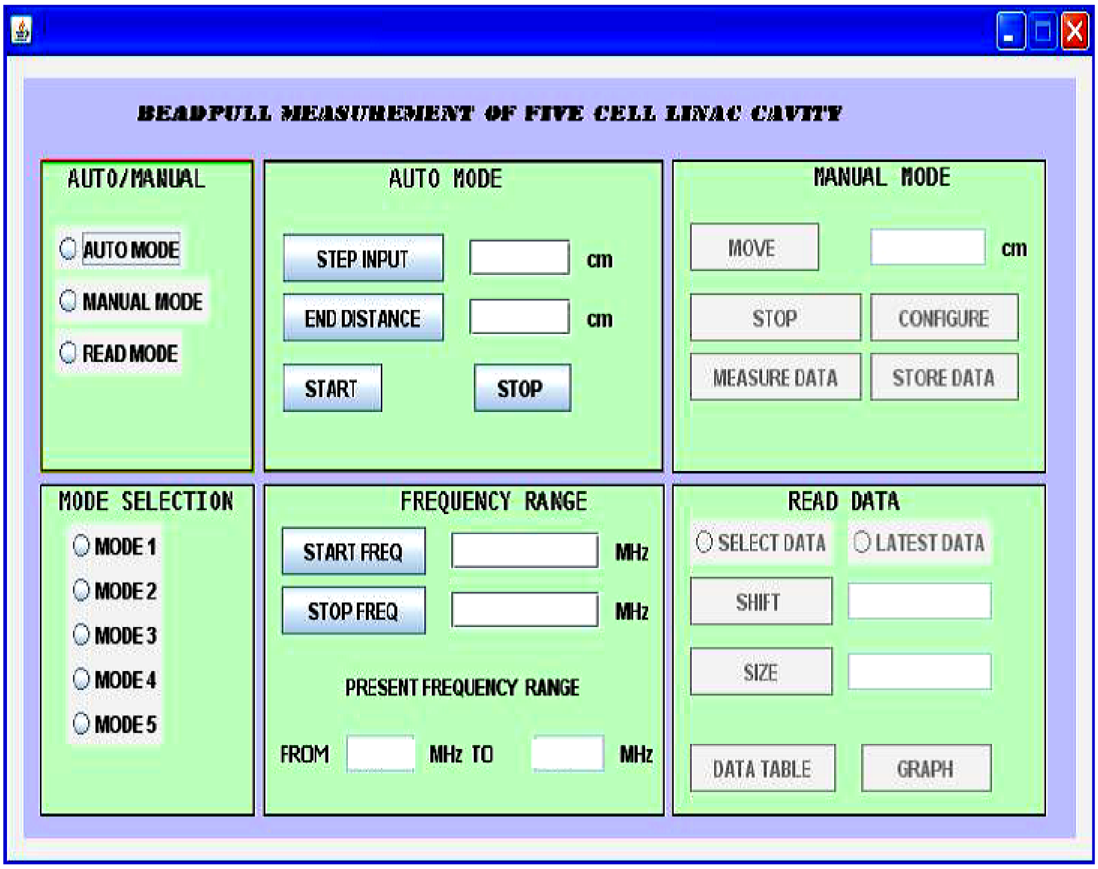

Fig.4.3.6.4 Graphical User Interface (GUI)of bead-pull measurement set-up for the five cell elliptical cavity

Bead-pull measurement result of 5-cell elliptical shape copper cavity & discussion:

In a multi-cell elliptical cavity, the resonant cells are coupled to each other capacitively. In case of an N-cell cavity, there are N distinct modes with frequency of m[th] mode expressed[64] in terms of frequency of single cell f_0, with k being coupling parameter between the cells.

$$f_m = \frac{f_0}{[1+2k\cos(\frac{m\pi}{N})]^{1/2}} \quad \ldots\ldots\ldots\ldots\ldots\ldots\ldots\ldots(4.3.6.04)$$

The accelerating (π-mode) mode, as given by m = N, has the highest frequency. Using this automated bead pull system, RF field measurement has been carried out for 5-cell copper prototype cavity and five modes (from mode-4 to mode-0) have been measured at 651.395MHz, 649.46MHz, 647.055MHz, 645.14MHz and 643.61 MHz respectively. The desired accelerating mode, i.e., π-mode or mode-4 is located at 651.395 MHz [65]. The plot of normalized Electric field (E)vs. Bead position (from the end of beam pipe on the axis) for all five modes, mode-4 (*i.e.*, π-mode), 0-mode, mode-1, mode-2 and mode-3are shown in Fig.4.3.6.5, Fig.4.3.6.6, Fig.4.3.6.7, Fig.4.3.6.8, Fig.4.3.6.9 respectively.

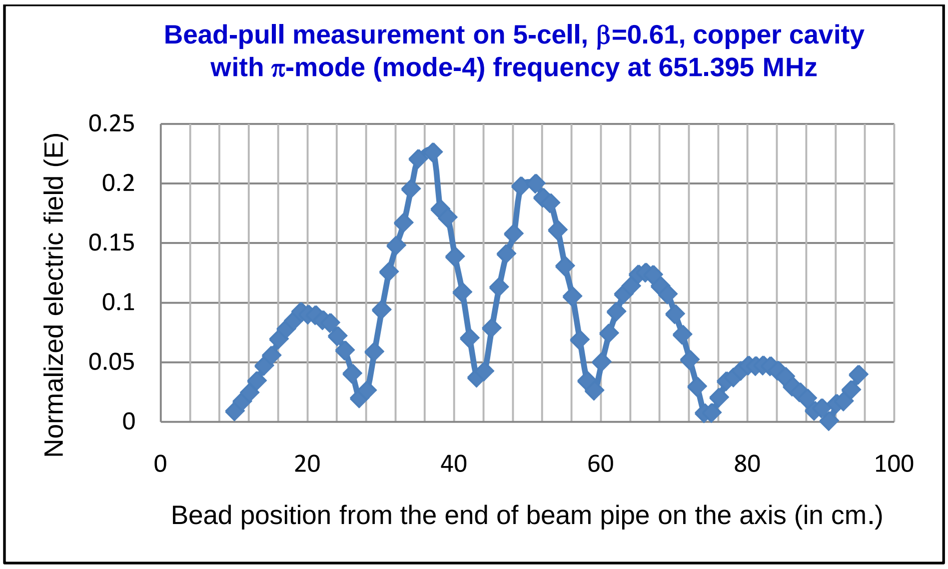

Fig.4.3.6.5Plot of Normalizedelectric field (E)vs. Bead position on the axis (for π-mode) for 1 watt power of 5-cell, β = 0.61, copper cavity

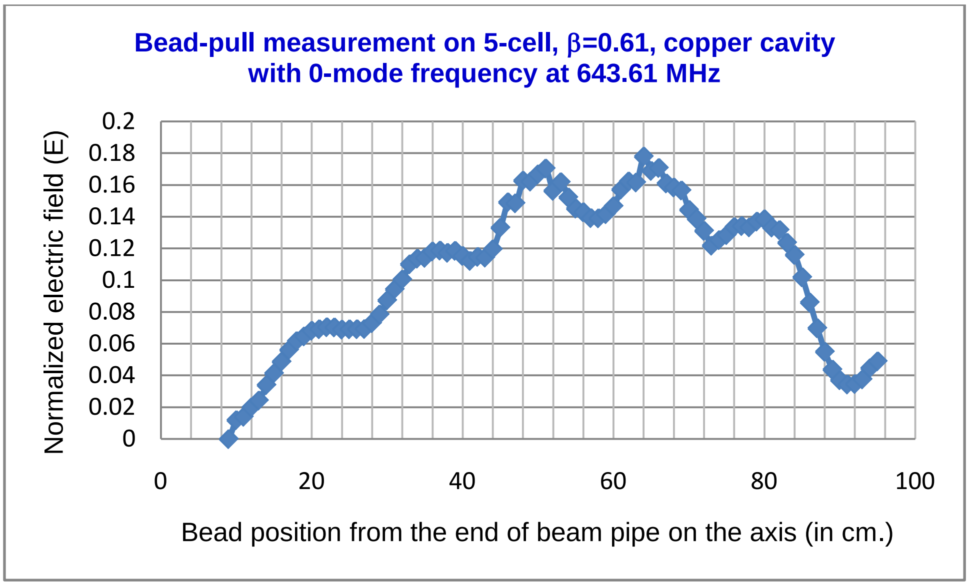

Fig.4.3.6.6Plot of Normalized electric field (E) vs. Bead position on the axis (for 0-mode) for 1 watt power of 5-cell, β = 0.61, copper cavity

At each of the zero-crossing in the field profile curves, there is phase reversal of the electric field and thus we can conclude that π-mode (accelerating mode) is located at 651.395 MHz where phase difference is 180° between two neighbouring cells. Similarly, for the 0-mode located at 643.61 MHz, the phases in all cells are same and the corresponding measured plot is successfully represented in Fig.4.3.6.6.

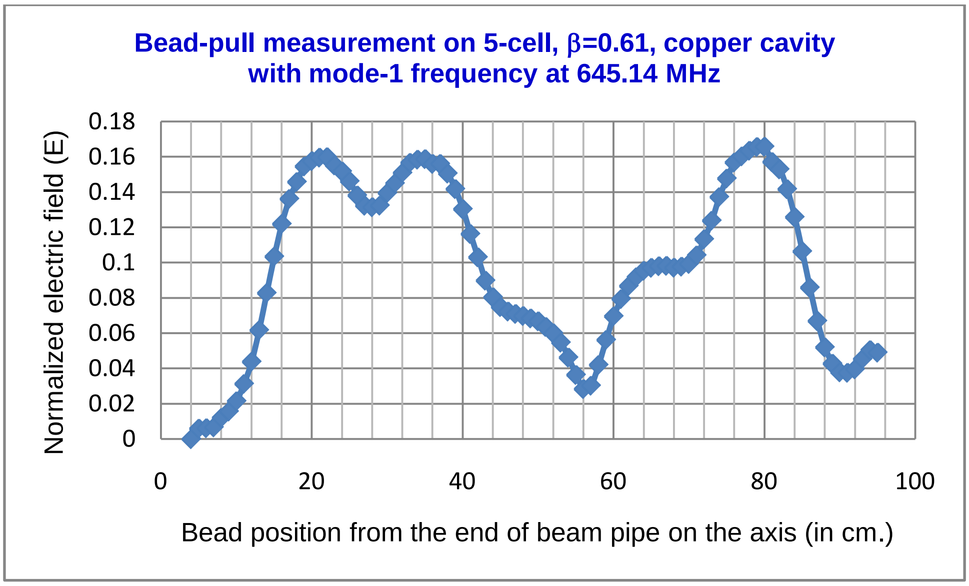

Fig.4.3.6.7Plot of Normalized electric field (E) vs. Bead position on the axis (for mode-1) for 1 watt power of 5-cell, β = 0.61, copper cavity

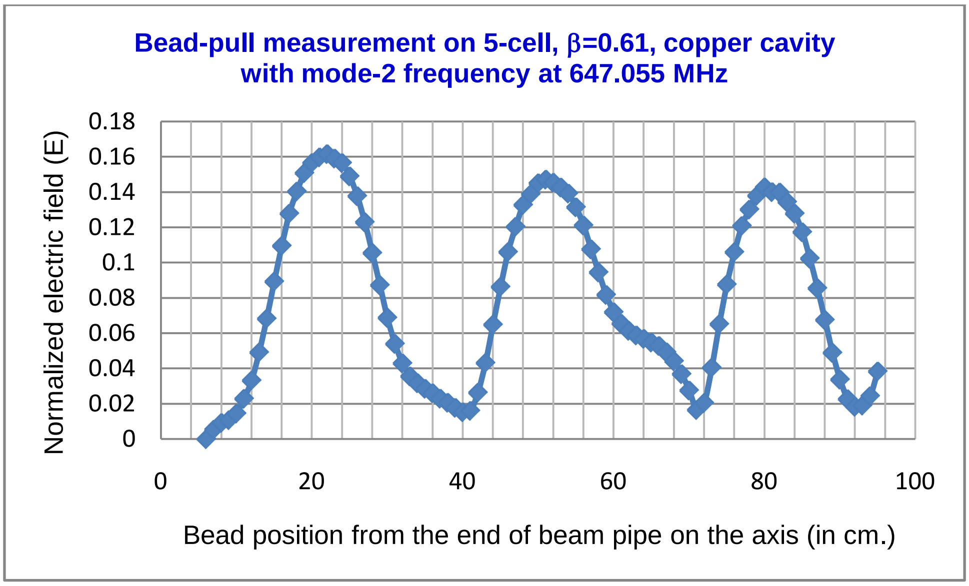

Fig.4.3.6.8Plot of Normalized electric field (E) vs. Bead position on the axis (for mode-2) for 1 watt power of 5-cell, β = 0.61, copper cavity

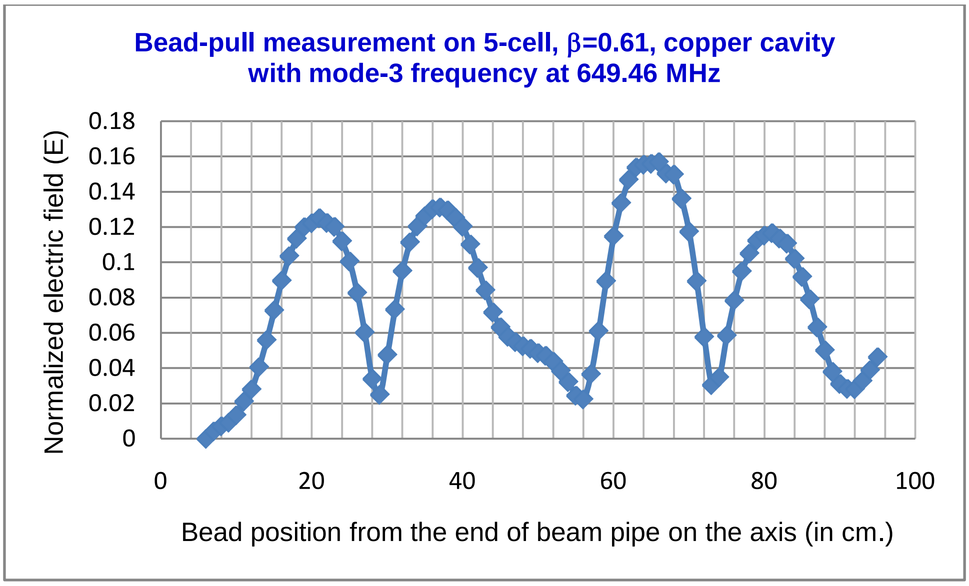

Fig.4.3.6.9Plot of Normalized electric field (E) vs. Bead position on the axis (for mode-3) for 1 watt power of 5-cell, β = 0.61, copper cavity

One of the most important parameters, the ratio of shunt impedance and quality factor orR/Q or R-over-Q, has been calculated (as shown in Table-7) from the measured frequency shift vs. bead position data for all modes considering β = 0.61. For the accelerating mode (π-mode or Mode-4), the value of R-over-Q is278 ohm as compared to 296 ohm, obtained from simulation with CST Microwave Studio/SUPERFISH.

Table-7 Calculated R/Q from bead-pull measurement data for accelerating mode (π-mode) of a 5-cell, β = 0.61 cavity

ε_r	27	35	45
Bead diameter (cm)	R/Q(ohm)		
1.00	278	272	267
1.05	240	235	230
1.10	209	204	200

The value of R-over-Q for π-mode, obtained from bead-pull measurement data, highly depends on the accurate measurement of bead diameter, relative permittivity (ε_r) and unloaded quality factor (Q) of the cavity. The filed profile remains same as only the absolute value of field depends on bead diameter, ε_r and Q. Table-7 contains the values of R/Q for accelerating mode of a 5-cell, β = 0.61, 650 MHz copper cavity, varying bead diameter from 1.0 to 1.1 and also varying ε_r from 27 to 35. The measurement result shows that R-over-Q decreases with bead diameter and also with ε_r. The values of R-over-Q obtained from simulation with CST Microwave Studio and also calculated from bead-pull measurement data for all five modes of a 5-cell, β = 0.61, 650 MHz cavity have been given in Table-8.

Table-8 R/Q from simulation with CST Microwave Studio and calculated from bead-pull measurement data for all five modes of a 5-cell, β = 0.61 cavity

For bead diameter 1 cm. and ε_r = 27			
		Obtained from simulation with CST Microwave Studio	Calculated from Bead-pull measurement
Mode number	Frequency (MHz)	R/Q (ohm)	R/Q (ohm)
Mode-0 (*i.e.*, 0-mode)	643.610	2.56	10.5
Mode-1	645.140	1.53	0.005
Mode-2	647.055	27.25	49.9
Mode-3	649.460	1.36	2.4
Mode-4 (*i.e.*,π-mode)	651.395	296	278

It is observed from Table-8 that the magnitudes of R-over-Q for other four modes (non-accelerating modes) are very small, as obtained from simulation and also from bead-pull measurement data. The smaller values of R-over-Q are desirable in case of non-accelerating modes (i.e., mode-0 to mode-3), especially, for accelerating cavity. The plot of R-over-Q vs. Mode frequencies for all five modes of a 5-cell, β = 0.61, 650 MHz cavity has been shown in Fig.4.3.6.10. As end cells are coupled to neighbouring cell at one side only, electric fields at end cells are lower than that in inner cells and end cell modifications and/or tuning is required to have a flat E-field profile in π-mode with equal amplitude at each cell [64]. For very small perturbation, it is very difficult to measure the frequency shift in the peak of the cavity response using Vector Network Analyzer (VNA). Phase locked loop (PLL) may be required to track the frequency deviation in π-mode. However, the phase shifts at the unperturbed resonant frequency are much easier to measure with VNA. For this reason, the present measurement system has been developed using phase shift measurement technique and performed very well and satisfactorily.

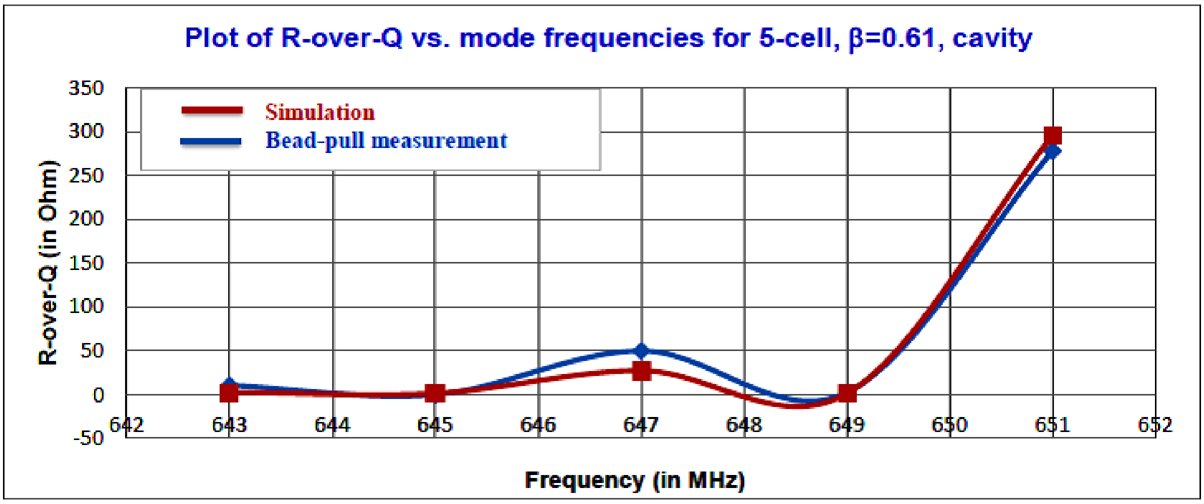

Fig.4.3.6.10Plot of R-over-Q vs. mode frequencies for 5-cell, β = 0.61, copper cavity

CHAPTER – 5

SUMMARY AND DISCUSSION

5.1 Summary

The dissertation comprises of studies on two types of RF cavities: a) Normal conducting cavities for *K500* Superconducting Cyclotron at VECC and b) Superconducting cavity for proton acceleration around β=0.61 and resonating at 650 MHz for 1 GeV proton linear accelerator. The studies carried out are summarized below.

- The electromagnetic modeling and simulations, design and analysis of a large size high power TEM-class coaxial type copper cavities with complicated geometry for the *K500* Superconducting cyclotron and the measurements of RF parameters of the cavities at low power and high power level as well, have been carried out in detail.
- An indirect method using continuous X-ray spectrum (called "Bremsstrahlung") has been employed to measure RF voltage at the accelerating gap of the cavity, fairly accurately (within ± 1.5 kV) and quite reliably, without perturbing the fields inside.
- The necessary design and successful implementation of low-level closed loop radiofrequency (LLRF) feedback control system has been accomplished achieving the amplitude stability of 10 ppm. The stringent requirement of phase stability within ±0.1 degree between any two cavities, during the continuous high power operation of the machine, has been achieved remarkably with the help of automatic phase control system with a design feature of having both analog in-phase/quadrature (I/Q) modulator based phase regulator and Direct Digital Synthesis (DDS) based phase shifter in order to achieve faster response along with wide dynamic range (± 180 degree) as well.

- Besides normal conducting copper cavities, the superconducting cavity technology has matured enough for the future energy frontier accelerators. A new electromagnetic design of five-cell elliptical SRF cavity operating at 650 MHz inβ = 0.61 region for the proposed 1GeV, 2mA proton linear accelerator, has been carried out with targeted accelerating gradient of 17 MV/m. The cavity design offered some new features, comprising of wide aperture (96 mm) for better acceptance and moderate value of wall slope angle (2.4 degree for mid cells and 4.5 degree for end cells) for better mechanical rigidity and also better accessibility for surface processing.
- The 3D multipacting study and analysis based on Furman model with due consideration of three kinds of secondary electron emissions – true secondary, elastic back scattered secondary and rediffused secondary electrons, for 650 MHz, β = 0.61, SRF cavity, have been performed. Unlike true secondary electrons, the elastic back scattered and rediffused secondary electrons, are actually responsible for the probable occurrence of multipacting at the electric fields between 5.8 MV/m and 11.5 MV/m in the above cavity. A small convexity in the equator region suppresses the multipacting significantly, probably, because the remaining electric field lines at the equator region, vanishes, due to this convexity, as the electric field lines cannot be parallel with the metal boundaries.

5.2 Discussion

The research issues for further development are wide open for room temperature cavities and also for superconducting cavities, in terms of achieving higher and higher accelerating gradients. The on-going progress in the development of new cavity materials will definitely improve the performance of the cavities. The continuously developing and upgraded manufacturing and fabrication processes and also improved measurement techniques have the scope of achieving better performance of the cavity and its associated controls. The design of LLRF controller, especially, the high stability phase controller, as discussed in the thesis, has a great scope of utilization in any high power accelerator cavities.

The state-of-the-art design of multi-cell superconducting RF elliptical cavity operating at 650 MHz, β=0.61, with some new features would be a strong choice of the global accelerator communities, as major accelerator components for the proposed 1GeV, high intensity Proton linear accelerators for FERMILAB Proton Improvement Plan (PIP-II) project and/or Indian Spallation Neutron Source (SNS) or Accelerator Driven Subcritical System (ADSS) projects.

REFERENCES

[1] Haus, Hermann A., and James R. Melcher, "Electromagnetic Fields and Energy", *Eaglewood Cliffs NJ: Prentice-Hall, 1989.*

[2] P.K. Sigg, “RF for Cyclotrons”, *Proceedings of CERN Accelerator School on Small Accelerators, Zeegse, The Netherlands, 2005 (p231).*

[3] M. Puglisi, “Conventional RF cavity design”, *Proceedings of CERN Accelerator School on RF Engineering for Particle Accelerators, Oxford, UK, 1991 (p156).*

[4] S. Belomestnykh& V. Shemelin, “High-β cavity design-a tutorial”, *12th International workshop on "RF Superconductivity" (SRF-2005), Cornell University, New York, USA, 2005 (SRF-060424-03).*

[5] John D. Kraus, Keith R. Carver, "Electromagnetics", 2nd Edition, Mcgraw-HillKogakusha Ltd., Tokyo, 1973.

[6] M. Stanley Livingstone, "Particle accelerators - a brief history" published by Harvard University Press, 1969.

[7] SumitSom, Rakesh Kumar Bhandari, Saikat Pal, Ajoy Kumar Mukherjee, ProbalGangopadhyay, Aditya Mandal, Sudeshna Seth, J.S. Prasad, P.R. Raj, SubimalSaha, “Development of RF system for K500 Superconducting Cyclotron at VECC, Kolkata”, *Proceedings of 18th International Conference on Cyclotrons and their Applications (Cyclotrons-2007), LNS, INFN, Catania, Italy, 2007 (p473).*

[8] S. Som, Saikat Paul, A.K. Mukherjee, D.S. Bhattacharyay, P. Gangopadhyay, J.S. Prasad, A. Mandal, S. Seth, P.R. Raj, S.K. Manna, M. Banerjee, K.V. Krishnaiah, M.S. Saha, S. Biswas, S. Saha, “Development of 100 kW RF Amplifier for Superconducting Cyclotron at VECC”, *Proceedings of Asian Particle Accelerator Conference (APAC-2007) held at RRCAT, Indore, 2007 (p476).*

[9] SumitSom, Surajit Ghosh, Sudeshna Seth, Aditya Mandal, , Saikat Paul, Suprakash Roy, "Precision phase control for the radiofrequency system of K500 superconducting cyclotron at Variable Energy Cyclotron Centre, Kolkata", *Review of Scientific Instruments in Vol.84, issue-11, 113303 (2013).*

[10] A. Caruso, F. Consoli, A. Sparta, A. Loghitano, "A Compact solution for DDS-generator, turn-on and protections in Radiofrequency accelerator systems", *Proceedings of 19th International Conference on Cyclotrons and their Applications (Cyclotrons-2010), Lanzhou, China, 2010 (institute of Modern Physics, Chinese Academy of Sciences, 2011),* p.159.

[11] A. Bosotti, A. Caruso, M. Di Giacomo, V. Lovati, C. pagani, G. Varisco, F. Zibra, "Accelerating voltage amplitude and phase stabilization for the Milan K800 cyclotron", *Proceedings of 1st European Particle Accelerator Conference (EPAC-1988), Rome, Italy, 1998 (World Scientific Publication,1989), p.1303.*

[12] HoomanHassanzadegan,, Robert Grino, *Nuclear Instruments and Methods in Physics Research A*615, 143–157 (2010).

[13] R. Garoby in "Low level RF and feedback", CERN PS/RF Note. *(DOI:http://cdsweb.cern.ch/record/328252/files/ps-97-034.ps.gz).*

[14] Data Sheet for AD9959 4-Channel, 500 MSPS DDS with 10-Bit DACs A product of *Analog Devices,*Norwood, MA, USA (*www.analog.com*).

[15] Data Sheet for AD8302, LF–2.7GHz RF/IF Gain and Phase Detector, A product of *Analog Devices,*Norwood, MA, USA (*www.analog.com*).

[16] JH-6-4 V2 Quadrature Hybrid, 2-32 MHz, Tyco Electronics, MACOM. *http://www.alldatasheet.com/datasheet-pdf/pdf/185380/MACOM/JH-6-4.html.*

[17] MadanGopal, I.J.Nagrath, "Control Systems Engineering", *5th Edition, New Age International (2011).*

[18] S. Som, P.K. Khemka, "RF cavity analysis using PC-SUPERFISH code", *1997 IEEE Conference on High power microwave electronics: measurements, identification, applications (MIA-ME’97) held at Novosibirsk State Technical University, Russia, 1997 (p179).*

[19] Aditya Mandal, S. Som, S. Saha, Saikat Paul, S. Seth, R.K. Bhandari, P.R. Raj, B.C. Mondal, B.K. Das, U.S. Panda, “ Closed loop RF tuning for superconducting cyclotron at VECC", *Proceedings of 19th International Conference on Cyclotrons and their Applications (Cyclotrons-2010), Lanzhou, China, 2010 (institute of Modern Physics, Chinese Academy of Sciences, 2011),* p.180.

[20] S. Som, Saikat Paul, A.K. Mukherjee, D.S. Bhattacharyay, P. Gangopadhyay, J.S. Prasad, A. Mandal, P.R. Raj, S.K. Manna, M. Banerjee, K.V. Krishnaiah, M.S. Saha, S. Biswas, S. Seth, “An overview of the RF system of K500 Superconducting Cyclotron at VECC”, *Proceedings of Indian Particle Accelerator Conference (InPac-2005) held at VECC, Kolkata, 2005 (paper_Id:C-139).*

[21] SPRAA76 Datesheet, Texas Instrument Application Report, January 2005, (*http://www.datasheetarchive.com/dl/Datasheet-082/DASF0044192.pdf*).

[22] S.Som, Saikat Paul, Aditya Mandal, S. Seth, S. Saha, R.K. Bhandari, P. Gangopadhyay, P.R. Raj, “ Commissioning experience of the RF system of K500 Superconducting cyclotron at VECC”, *Proceedings of 19th International Conference on Cyclotrons and their Applications (Cyclotrons-2010) held at Lanzhou, China, 2010 (institute of Modern Physics, Chinese Academy of Sciences, 2011), p162.*

[23] John Vincent, "Modeling and analysis of Radio Frequency Structures using an equivalent circuit methodology with Application to Charged Particle Accelerator RF Resonators", *NSCL, MSU, USA, PhD Thesis, 1996 (p143).*

[24] C. Pagani, G. Varisco, V. Venturini and F. Alessandria, "RF system design of the Milan superconducting Cyclotron", *9th International Conf. on Cyclotrons and their Applications held at Caen, France,1981 (p423).*

[25] SumitSom, Sudeshna Seth, Aditya Mandal, Saikat Paul, AnjanDuttagupta, "Radio frequency cavity analysis, measurement and calibration of absolute Dee voltage for K-500 superconducting cyclotron at VECC, Kolkata", *Review of Scientific Instruments in Vol.84, issue-2, 023303 (2013).*

[26] S.Paul, S. Som, D.S. Bhattacharyay, A.K. Mukherjee, P. Ganguly, A. Mandal, S. Seth, M. Banerjee, S.K. Manna, P.R. Raj, M.S. Saha, K.V. Krishnaiah, S. Biswas, “Overview of control and low-power electronics of K500 RF system”, *Proceedings of Indian Particle Accelerator Conference (InPac-2005) held at VECC, Kolkata,2005 (Paper_Id: C-141).*

[27] S. Som, Saikat Paul, A.K. Mukherjee, D.S. Bhattacharyay, P. Gangopadhyay, J.S. Prasad, A. Mandal, S. Seth, P.R. Raj, S.K. Manna, M. Banerjee, K.V. Krishnaiah, M.S. Saha, S. Biswas, S. Saha, “Present status of Radiofrequency system of Superconducting Cyclotron at VECC”, *Proceedings of 3rd Indian Particle Accelerator Conference (InPac-2006) held at BARC, Mumbai,2006.*

[28] Aditya Mandal, Surajit Ghosh, Sudeshna Seth, SumitSom, S. Paul, P.R. Raj, S. Roy, S. Saha, R.K. Bhandari, “Advanced closed-loop trimmer control system for fine tuning the RF cavity of K500 superconducting cyclotron", *Proceedings of Indian Particle Accelerator Conference (InPac-2011), IUAC, New Delhi, India, 2011, (Paper_Id:240).*

[29] P. Miller and E. Kashy, "Absolute calibration of Dee voltage by X-ray endpoint", *Proceedings of 7th International Conference on Cyclotrons and their Applications (Cyclotrons-1975) held at Zurich, Switzerland, 1975 (p171).*

[30] Chuan Wang, Bin Ji, Pengzhan Li, Zhiguo Yin, Yu Lei, Jiansheng Xing, Tianjue hang, Andreas Adelmann, AchimGsell, Mike Siedel, "A study of multipacting effects in large cyclotron cavities by means of fully 3-dimensional simulations", *Proceedings of 20th International Conference on Cyclotrons and their Applications (Cyclotrons-2013) held at TRIUMF, Vancuber, Canada, 2013, (p142).*

[31] W. Weingarten, "Superconducting Cavities", *Proceedings CERN Accelerator School on "RF Engineering for Particle Accelerators", Oxford, UK, April,1991, p318.*

[32] Wiren Chou, Francesco Ruggiero, "Anomalous skin effect and resistive wall heating", LHC Project Note 2 (SL/AP), CERN, Geneva, 1995. *(http://cds.cern.ch/record/691905/files/project-note-2.pdf).*

[33] H. Padamsee, J. Knobloch, T. Hays, *"RF Superconductivity for Accelerators"*, 2nd edition,Wiley-VCH Publication, Germany (2008).

[34] K. Saito, "Superconducting RF-1 - Basics for SRF cavity", *2nd International Accelerator School for Linear Colliders (ILC School-2007), Erice, Italy, 2007.*

[35] B. Aune, R. Bandelmann, D. Bloess, B. Bonin, A. Bosottti, M. Champion, C. Crawford, G. Deppe, B. Dwersteg, D.A. Edwards, H.T. Edwards, M. Ferrario, M. Fouaidy, P.D. Gall, A. Gamp, A. Gossel, G. Graber, D. Hubert, M. Huning, M. Juillard, T. Junquera, H. Kaiser, G. Kreps, M. Kuchnir, R. Lange, M. Leenen, M. Liepe, L. Lilje, A. Matheison, W.D. Moller, A. Mosnier, H. Padamsee, C. Pagani, M. Pekeler, H.B. Peters, O. Peters, D. Proch, K. Rehlich, D. Reschke, H. Safa, T. Schilcher, P. Schmuser, J. Sekutowicz, S. Simrock, W. Singer, M. Tigner, D. Trines, K. Twarowski, G. Weichert, J. Weisend, J. Wojtkiewicz, S. Wolff, K. Zapfe, *"The superconducting Tesla cavities", http://arxiv.org/pdf/physics/0003011.pdf.*

[36] J. Matricon and D. St. James, "Superheating fields in superconductors", *Phys. Lett.* Vol.24A, number-5, p241 (1967)

[37] H. Piel, "Superconducting cavities", *Proceedings of the CERN Accelerator School 1988*, S. Turner ed., DESY, Hamburg, West Germany, CERN 89-04, p149 (1988).

[38] J.R. Delayen, C.L. Bohn, W.L. Kennedy, G.L. Nichols, C.T. Roche, L. Sagalovsky, "Recent developments in the application of RF superconductivity to high-brightness, high-gradient ion accelerators", *Proceedings of the 5th Workshop on RF Superconductivity, SRF91E03, p376 (1992).*

[39] K. Saito, "State-of-the-art and future prospects in RF superconductivity", *Proceedings of the 3rd International Particle Accelerator Conference (IPAC-2012) held at New Orleans, Louisiana, USA, 20112 (p11).*

[40] Sergey Belomestnykh, Valery Shemelin, "High-β cavity design-A Tutorial", *Proceedings of the 12th International Workshop on RF Superconductivity (SRF-2005), Ithaka, New York, USA, 2005.*

[41] J.R. Delayen, "Medium-β superconducting accelerating structures", *Proceedings of the 10th Workshop on RF Superconductivity, Tsukuba, KEK, Japan, 2001 (p152).*

[42] J.R. Delayen, "Intermediate-velocity superconducting accelerating structures", *Proceedings of XXII International Linear Accelerator Conference (LINAC-2004), Lubek, Germany, 2004 (p589).*

[43] Carlo Pagani, "SRF activities at INFN Milano-LASA", *Proceedings of the 10th Workshop on RF Superconductivity (SRF-2001), Tsukuba, Japan, 2001 (p115).*

[44] R L Geng, G.V. Eremeev, H. Padamsee, V.D. Shemelin, "High Gradient Studies for ILC with Single Cell Re-entrant Shape and Elliptical Shape Cavities made of Fine-grain and Large-grain Niobium", *Proceedings of 22nd Particle Accelerator Conference (PAC'07), New Mexico, USA, 2007 (p.2337).*

[45] P Kneisel, "Results from a Nearly Defect-Free Niobium Cavity",*Proceedings of the 7th International Workshop on "RF Superconductivity", France, 1995 (p.449).*

[46] H. Padamsee, et. al., "RF Superconductivity for accelerators", *John Willey & Sons Inc.,1998.*

[47] J. Graber, C. Crawford, J. Kirchgessner, H. Padamsee, D. Rubin, P. Schmueser, "Reduction of field emission in superconducting cavities with high power pulsed RF", *Nuclear Instruments & Methods in Physical Research A, 350, 1994 (p572).*

[48] R L Geng, "Review of new shapes for higher gradients", *Physica C: Superconductivity Vol.441, issue 1-2, July 2006 (p.145).*

[49] P Kneisel, "State of the art of multicell SC cavities and perspectives", *Proceedings of European Particle Accelerator Conference 2002 (EPAC 2002), Paris, France (p.139).*

[50] B Aune, et al, "Superconducting Tesla cavities", Physical Review Special topics-Accelerators and Beams,Vol.3, 092001 (2000).

[51] Sudeshna Seth, SumitSom, Aditya Mandal, S. Saha, R.K. Bhandari, “Design study on 650MHz, high-β multi-cell elliptical shape superconducting RF linac cavity”, *Proceedings of Indian Particle Accelerator Conference (InPac-2011), IUAC, New Delhi, India, 2011, (Paper_Id: 208).*

[52] R L Geng, H. Padamsee, A. Seaman, J. Sears, V. Shemelin," Testing the First 1300 MHz Reentrant Cavity", *Proceedings of the Workshop on "Pushing the limits of RF superconductivity", held at ANL, USA (Sep'2004), p11.*

[53] SumitSom, S. Seth, A. Mandal, S. Ghosh, "Design, Analysis and Multipacting Studies of 650 MHz, β=0.61 Superconducting RF Cavity", *Indian Journal of Pure and Applied Physicsin Vol.53 (3), p.160-168 (2015).*

[54] SumitSom, "Development of 650 MHz Cavities for the GeV Proton Accelerator in Project-X", *Proceedings of the16th International Conference on RF Superconductivity (SRF-2013)* held in Paris, France during 23–27 September, 2013 (*p.1193*).

[55] Steven Van Scivor, "Low temperature properties of materials", *Proceedings of USPAS Accelerator School on Principle of Cryogenic Engineering, MIT, USA, 2010 (http://uspas.fnal.gov/materials/10MIT/Lecture_1.2.pdf).*

[56] W. Hartung, F. Krawczyk, H. Padamsee, "Studies of multipacting in axisymmetric cavities for medium-velocity beams", *Proceedings of the 10th Workshop on RF Superconductivity (SRF-2001), at KEK, Japan (2001).*

[57] M.A. Furman, M.T.F. Pivi, "Probabilistic model for the simulation of secondary electron emission", *Physical Review Special Topics-Accelerators and Beams,Vol.5, 124404(2002).*

[58] Pranab Bhattacharyya, Javed Akhtar, Chinmay Nandi, AnjanDuttagupta, SumitSom, Gautam Pal, AlokChakraborty, "Structural Design of 650MHz β=0.6, Superconducting Radio-Frequency Cavity",*Proceedings of National Symposium on Cryogenics, IPR, Ahmedabad, 2013.*

[59] M. Cola, G. Ellis, R. Gentzlinger, R. Mitchell, "Structural Analysis of the APT Superconducting Cavities", *Proceedings of the 9thWorkshop on RF Superconductivity, New Mexico, USA ,1999, (p405).*

[60] P. Pierini, D. Barni, A. Bosotti, G. Ciovati, C. Pagani, "Cavity design tools and applications to the TRASCO project", *Proceedings of the 9thWorkshop on RF Superconductivity, New Mexico, USA ,1999, (p380).*

[61] E.L. Gintzton, "Microwave Electronics", Van Nostrand, Princeton, New Jersy, p81.

[62] P.A. McIntosh, "Perturbation measurements on RF cavities at Daresbury", *Proceedings of the 4th European Particle Accelerator Conference (EPAC-1994), Daresbury, U.K., 1994 (p1283).*

[63] John Byrd, “RF cavity bead-pull measurements”, *Microwave Measurement Laboratory, USPAS & CCAST, Beijing China, 2-6 Nov’1998.*

[64] Peter Schmuser, “Tuning of multi-cell cavities using bead-pull measurements”, *(http://www.lns.cornell.edu/public/SRF/1992/SRF920925-10/SRF920925-10.pdf).*

[65] Sudeshna Seth, SumitSom, Aditya Mandal, P.R. Raj, S. Saha, R.K. Bhandari, “RF characterization and measurement of a full scale copper prototype of 5-cell elliptical shape Superconducting RF linac cavity”, *Proceedings of Indian Particle Accelerator Conference (InPac-2011), IUAC, New Delhi, India, 2011, (Paper_Id: 207).*

[66] C.C. Compton, T.L. Grim, W. Hartung, H. Podlech, R.C. York, G. Ciovati, P. Kneisel, D. Barni, C. Pagani, P.pierini, "Prototyping of a multicell superconducting cavity for acceleration of medium-velocity beams", *Physical Review Special Topics - Accelerators and Beams 8, 042003 (2005).*

[67] J.R. Delayen, G.J. Dick, J.E. Mercereau, “A microprocessor-based feedback system for phase and amplitude stabilization of superconducting resonators”, *IEEE Transaction on Nuclear Science, Vol. NS-24, No.3 (1977), p1759.*

[68] J.M. Bogaty, B.E. Clifft, K.W. Shepard, G.P. Zinkann, “An improved phase-control system for superconducting low-velocity accelerating structures”, *Proceedings of the 1989 IEEE Particle Accelerator Conference (PAC’89), Chicago, 1989 (p.1978).*

APPENDIX-1

A1. RF Cavity theory

An infinite number of eigen modes can exist in a resonant pill-box cavity. The different eigen modes have different field distributions (as shown in Fig.A1.1& Fig.A1.2) and generally have different resonant frequencies. Two types of modes exist in a pill-box cavity – transverse electric (TE) or H-modes and transverse magnetic mode (TM) or E-modes. In some special cases two modes can have same resonant frequency and are called degenerate modes. The modes can have different number of variations along each of the three cylindrical co-ordinates *(θ, r, z)* and are designated accordingly. For example, the TM mode with two variations along azimuth (θ), one variations along the radius (r) and no variation along longitudinal coordinate is called TM_{210}. The fundamental or the lowest rf frequency mode (TM_{010}), which has no variation along azimuth, one variation along the radius and no variation along longitudinal coordinate is usually employed for particle acceleration as it has the highest shunt impedance.

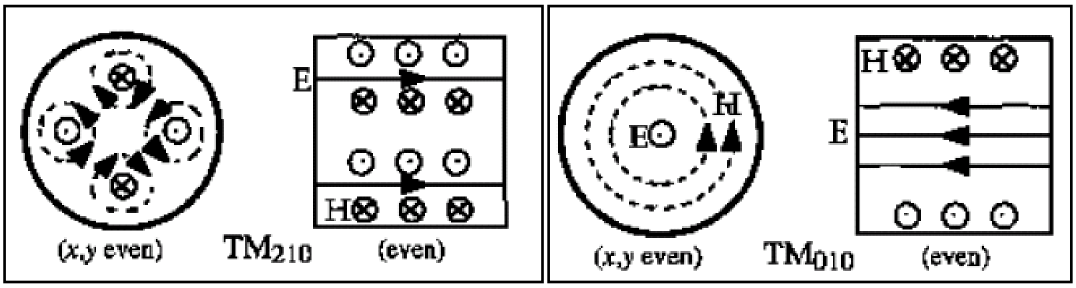

Fig. A1.1 Electric and magnetic field for two different modes (TM_{210} and TM_{010}) of a pillbox cavity. The left-hand member of each figure pair shows field patterns in the x-y plane and the right-hand, the y-z plane. The notations below the x-y view indicate the transverse symmetries and the notations below the y-z view indicate the longitudinal symmetry

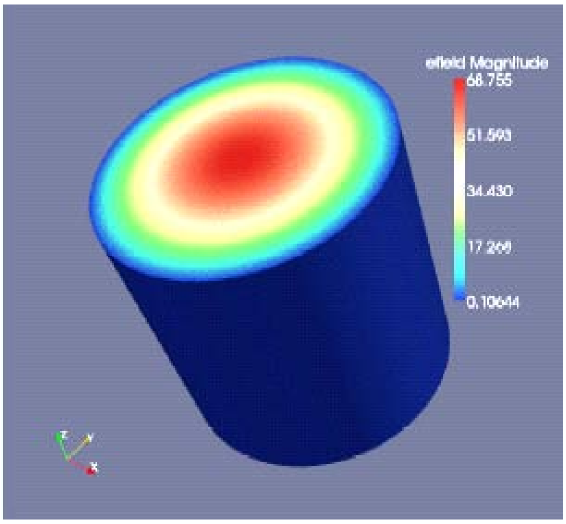

Fig.A1.2 Electric field distribution pattern for TM_{010} mode of a pillbox cavity

RF cavity theory deals with the problem to find out the electromagnetic resonance frequencies and evaluate the field components in a cavity surrounded by perfectly conducting walls. In this case, the cavity (as shown in Fig.A1.3) having three-dimensional geometries with cylindrical symmetry has been considered.

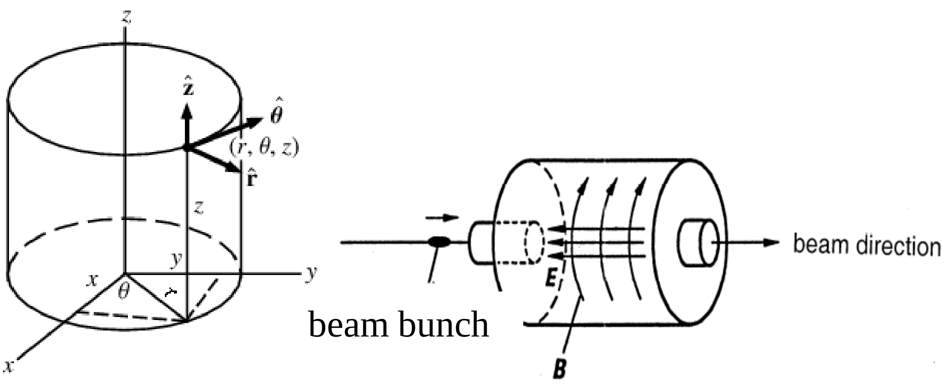

Fig.A1.3 Pillbox cavity geometry in cylindrical co-ordinate system

Although there are no real currents or charges in the cavity, a fictitious magnetic current density **K**, and magnetic charge density σ that will "drive" the fields in the cavity, is introduced. At resonance, the amount of current needed to drive the cavity approaches zero. The medium in the cavity is assumed as vacuum, which is homogeneous, isotropic, and non-conducting, with piecewise constant permittivity (ε) and permeability (μ).

$$\mathbf{D} = \varepsilon\,\mathbf{E} \text{ ....(A1.1.1)}$$

$$\mathbf{B} = \mu\,\mathbf{H} \text{ ....(A1.1.2)}$$

[Where, **D** is the displacement density vector, **E** is the Electric field vector, **B** is the magnetic field and **H** is the magnetic field intensity vector.]

With cylindrical symmetry **E**, **H**, **K**, and σ are independent of ϕ. Maxwell's equations[4]can be written in two sets, which are

$$\left[\nabla\times\mathbf{E}+\frac{\partial\mathbf{B}}{\partial t}\right]_r = K_r \quad \text{or} \quad -\frac{\partial E_\phi}{\partial z}+\mu\frac{\partial H_r}{\partial t} = K_r \text{ ....(A1.1.3)}$$

$$\left[\nabla\times\mathbf{E}+\frac{\partial\mathbf{B}}{\partial t}\right]_z = K_z \quad \text{or} \quad \frac{1}{r}\frac{\partial\left(rE_\phi\right)}{\partial r}+\mu\frac{\partial H_z}{\partial t} = K_z \text{ ....(A1.1.4)}$$

$$\left[\nabla\times\mathbf{H}-\frac{\partial\mathbf{D}}{\partial t}\right]_\phi = 0 \quad \text{or} \quad \frac{\partial H_r}{\partial z}-\frac{\partial H_z}{\partial r}-\varepsilon\frac{\partial E_\phi}{\partial t} = 0 \text{ ....(A1.1.5)}$$

$$\nabla\cdot\mathbf{B} = \sigma \quad \text{or} \quad \frac{1}{r}\frac{\partial\left(rH_r\right)}{\partial r}+\frac{\partial H_z}{\partial z} = \frac{\sigma}{\mu} \text{ ....(A1.1.6)}$$

and

$$\left[\nabla\times\mathbf{H}-\frac{\partial\mathbf{D}}{\partial t}\right]_r = 0 \quad \text{or} \quad -\frac{\partial H_\phi}{\partial z}-\varepsilon\frac{\partial E_r}{\partial t} = 0 \text{ ....(A1.1.7)}$$

$$\left[\nabla\times\mathbf{H}-\frac{\partial\mathbf{D}}{\partial t}\right]_z = 0 \quad \text{or} \quad \frac{1}{r}\frac{\partial\left(rH_\phi\right)}{\partial r}-\varepsilon\frac{\partial E_z}{\partial t} = 0 \text{ ....(A1.1.8)}$$

$$\left[\nabla\times\mathbf{E}+\frac{\partial\mathbf{B}}{\partial t}\right]_\phi = K_\phi \quad \text{or} \quad \frac{\partial E_r}{\partial z}-\frac{\partial E_z}{\partial r}+\mu\frac{\partial H_\phi}{\partial t} = K_\phi \text{ .....(A1.1.9)}$$

$$\nabla\cdot\mathbf{D} = 0 \quad \text{or} \quad \frac{1}{r}\frac{\partial\left(rE_r\right)}{\partial r}+\frac{\partial E_z}{\partial z} = 0 \text{ ....(A1.1.10)}$$

where H_ϕ is the azimuthal component of the magnetic field expressed in electric field units. The true magnetic field is $\sqrt{\varepsilon/\mu}$ times H_ϕ. The permittivity and permeability are related to the speed of light as

$$c = \frac{1}{\sqrt{\varepsilon\mu}}.$$

[The permittivity is ε , and the permeability is μ.]

It is to be noted that, the first four equations involve the field components H_r, E_ϕ, and H_z, while the last four are nearly identical but involve E_r, H_ϕ, and E_z. This grouping corresponds to a separation into transverse electric (TE) modes for which $E_\phi \neq 0$ and transverse magnetic (TM) modes for which $H_\phi \neq 0$. It is usually the TM modes of the cavity that are of interest to accelerator designers, because they have nonzero axial E_z, which can be used to accelerate a beam of charged particles.

Equations (A1.1.3) through (A1.1.5) can be combined to give a second-order partial differential equation for E_ϕ alone. Differentiate Equation (A1.1.3) by z, differentiate Equation (A1.1.4) by r, subtract the two results, and make use of Equation (A1.1.5) to eliminate the combination $\partial H_r/\partial z - \partial H_z/\partial r$. The result is

$$-\frac{\partial}{\partial r}\left[\frac{1}{r}\frac{\partial}{\partial r}\left(rE_\phi\right)\right] - \frac{\partial^2 E_\phi}{\partial z^2} + \mu\varepsilon\frac{\partial^2 E_\phi}{\partial t^2} = \frac{\partial K_r}{\partial z} - \frac{\partial K_z}{\partial r} = \left[\nabla \times \mathbf{K}\right]_\phi \text{...............(A1.1.11)}$$

Similarly, we can obtain an equation for H_ϕ by using Equations (A1.1.7) through (A1.1.8).

$$-\frac{\partial}{\partial r}\left[\frac{1}{r}\frac{\partial}{\partial r}\left(rH_\phi\right)\right] - \frac{\partial^2 H_\phi}{\partial z^2} + \mu\varepsilon\frac{\partial^2 H_\phi}{\partial t^2} = \varepsilon\frac{\partial K_\phi}{\partial t} \text{..................................(A1.1.12)}$$

We are interested in solutions that are periodic in time. Let us arbitrarily assume that

$$\mathbf{K}(r,z,t) = \overline{\mathbf{K}}(r,z)\sin\omega t \text{..(A1.1.13)}$$

where ω is an angular frequency ($\omega = 2\pi f$). It then must follow from Equations (A1.1.11) and (A1.1.12) that

$$E_\phi(r,z,t) = \overline{E}_\phi(r,z)\sin\omega t \text{ .... (A1.1.14.1)}$$

$$H_\phi(r,z,t) = \sqrt{\frac{\varepsilon}{\mu}}\,\overline{H}_\phi(r,z)\cos\omega t\,. \qquad \text{(A1.1.14.2)}$$

This definition of $\overline{H}_\phi$ makes $\overline{E}_\phi$ and $\overline{H}_\phi$ have the same dimensions. When these assumptions are put into Equation A1.1.11 and Equation A1.1.12, the results are

$$\nabla^2\overline{E}_\phi - \frac{1}{r^2}\overline{E}_\phi + k^2\overline{E}_\phi = -\left[\nabla \times \overline{\mathbf{K}}\right]_\phi \text{ ....(A1.1.15)}$$

$$\nabla^2\overline{H}_\phi - \frac{1}{r^2}\overline{H}_\phi + k^2\overline{H}_\phi = -\varepsilon\,\omega\,\overline{K}_\phi = -\sqrt{\frac{\varepsilon}{\mu}}k\,\overline{K}_\phi \text{ ....(A1.1.16)}$$

$$k = \sqrt{\mu\varepsilon}\,\omega \text{ ....(A1.1.17)}$$

Where, k is called the eigenvalue.

$$\nabla^2 f = \frac{1}{r}\frac{\partial}{\partial r}\left(r\frac{\partial f}{\partial r}\right) + \frac{\partial^2 f}{\partial z^2} \text{ ....(A1.1.18)}$$

The equation (A1.1.18) is the two-dimensional Laplacian in cylindrical coordinates. Given $\overline{E}_\phi$ and $\overline{H}_\phi$ from these equations, one can use Equation (A1.1.3) through Equation (A1.1.8) to find H_r, H_z, E_r, and E_z. The integration over time is trivial. The constants of integration just determine the initial phase of the fields at time t = 0 and can be set equal to zero for our purposes. The results are

$$H_r = -\sqrt{\frac{\varepsilon}{\mu}}\frac{1}{k}\left(\frac{\partial\overline{E}_\phi}{\partial z} + \overline{K}_r\right)\cos\omega t \text{ ....(A1.1.19)}$$

$$H_z = \sqrt{\frac{\varepsilon}{\mu}}\frac{1}{k}\left[\frac{1}{r}\frac{\partial}{\partial r}\left(r\overline{E}_\phi\right) - \overline{K}_z\right]\cos\omega t \text{ ....(A1.1.20)}$$

$$E_r = -\frac{1}{k}\frac{\partial \overline{H}_\phi}{\partial z}\sin\omega t \text{ ....(A1.1.21)}$$

$$E_z = \frac{1}{k}\left[\frac{1}{r}\frac{\partial}{\partial r}\left(r\overline{H}_\phi\right)\right]\sin\omega t \text{ ....(A1.1.22)}$$

It is easily seen that Equation (A1.1.10) is identically satisfied and that Equation (A1.1.6) is satisfied if

$$\nabla \cdot \mathbf{K}\sin\omega t = -\frac{\partial \sigma(r,z,t)}{\partial t} \text{ ....(A1.1.23)}$$

The equation of continuity for magnetic current with the magnetic charge given by

$$\sigma(r,z,t) = \overline{\sigma}(r,z)\cos\omega t \text{ ....(A1.1.24)}$$

Note that in the TM mode, the electric field lines are parallel to the lines of constant rH_ϕ, which can be seen as follows. A field line is a curve r(z) whose tangent is proportional to the ratio of the electric field components, thus

$$\frac{dr}{dz} = \frac{E_r}{E_z} = \frac{-\frac{\partial H_\phi}{\partial z}}{\frac{1}{r}\frac{\partial}{\partial r}\left(rH_\phi\right)} \text{ ....(A1.1.25)}$$

This equation implies that

$$\frac{1}{r}\frac{\partial}{\partial r}\left(rH_\phi\right)dr + \frac{\partial H_\phi}{\partial z}dz = 0 \text{ ....(A1.1.26)}$$

or, multiplying through by r,

$$\nabla\left(rH_\phi\right)\cdot d\mathbf{r} = 0 \text{ ....(A1.1.27)}$$

which implies that rH_ϕ is a constant along an electric field line.

Poynting's theorem:

Poynting's theorem in this case can be written as

$$\oint(\mathbf{E}\times\mathbf{H})\cdot d\mathbf{a}+\frac{\partial}{\partial t}\int\frac{1}{2}\left[\varepsilon E^2+\mu H^2\right]dv=\int\mathbf{H}\cdot\mathbf{K}\,dv \text{ ....(A1.1.28)}$$

where the first term on the left is the outflow of energy over the cavity surface **a**, enclosing the volume v. The second term on the left is denoted by the change in energy of the electromagnetic fields in the enclosed volume. The term on the right is interpreted as the rate of work being done on the field by the magnetic current.

Since the cavity is closed, the surface integral must be zero. The generalized equation for cavities containing dielectric or permeable material is given below.

$$\int\sqrt{\frac{\varepsilon}{\mu}}\,\overline{\mathbf{H}}\cdot\overline{\mathbf{K}}\,dv=\omega\int\varepsilon\left(\overline{E}^2-\overline{H}^2\right)dv \text{ ....(A1.1.29)}$$

$$\text{Where, } \overline{E}^2=\overline{E}_r^2+\overline{E}_\phi^2+\overline{E}_z^2 \quad \text{and} \quad \overline{H}^2=\overline{H}_r^2+\overline{H}_\phi^2+\overline{H}_z^2 \text{ ....(A1.1.30)}$$

<u>Energy per unit volume</u>:

In a high-Q rf cavity, the electric and magnetic fields are very nearly 90 degrees out of phase. The energy stored in the field oscillates back and forth between the magnetic and electric field, but remains a constant, independent of time. Therefore, the energy per unit volume can be evaluated when the magnetic field is maximum and the electric field is zero, without loss of generality. The integral is over the z-r cross-section of the cavity.

$$U=\frac{\mu}{2}\frac{\int_S\left[H_\phi(z,r)\right]^2 r\,dr\,dz}{\int_S r\,dr\,dz} \text{ ....(A1.1.31)}$$

Power losses on walls:

If the electrical resistivity ρ of the cavity walls were zero, there would be no power loss and the electric field amplitude would go to zero at the wall. For walls with finite resistivity, the electric field penetrates into the wall and causes a current to flow. The power loss is given by the formula

$$P_{wall} = \pi\sqrt{\frac{k\rho}{2\mu^3 c^3}}\oint_C \left[H_\phi(z,r)\right]^2 r\,dl \text{ ....(A1.1.32)}$$

The main approximation is that the field energy in the wall is much less than the field energy in the cavity. In cylindrical coordinates, the integral over the surface of the cavity is easily changed to a line integral around the cross section of the cavity in the z-r plane.

Average accelerating field:

The average accelerating field E_0 is defined as the integral of the z component of the field along the beam direction:

$$E_0 = \frac{1}{L}\int_{-L/2}^{L/2} E_z(z, r=0)\,dz \text{ ....(A1.1.33)}$$

The rf cell has length L and, in this formula, is assumed to be symmetric with the center of the gap between drift tubes located at z = 0.

Shunt impedance:

Shunt impedance Z has dimensions of Ω/m and serves as a figure of merit for the accelerating efficiency. The larger the accelerating field for a given power loss per unit length, the more efficient the accelerator. For a total power loss P_T, the shunt impedance is given by

$$Z = \frac{E_0^2}{P_T/L} \text{ ....(A1.1.34)}$$

Quality factor:

The quality factor Q is a ratio of the energy stored in the cavity to the energy dissipated in the walls per rf cycle. A high Q is desirable if it means low power dissipation, but is not necessarily desired if it means large stored energy because it implies sensitivity to frequency errors. For pulsed systems, high Q also implies a long time constant for filling the cavity with rf energy.

Maximum electric field:

The maximum electric field E_{max} on a metal boundary is important because it determines whether and where electrical breakdown will occur.

Frequency perturbations:

The resonant frequency is very sensitive to errors in the size of the cavity. The frequency sensitivity is determined from the Slater-perturbation theorem, which states that for small perturbations the relative change in resonant frequency caused by a perturbation that decreases the volume of the cavity by an amount δV is given by

$$\frac{\delta f}{f} = \frac{\int_{\delta V} \left\{ \left[H_{\phi}(z,r) \right]^2 - \left[E_z(z,r) \right]^2 - \left[E_r(z,r) \right]^2 \right\} dv}{2\int_{V} \left[H_{\phi}(z,r) \right]^2 dv} \quad \text{.....................(A1.1.35)}$$

[Where, the integral in the denominator is over the cavity volume.]

APPENDIX-2

The main considerations [41] in the design of the superconducting structures are as follows.

- Cryogenic losses: In order to minimize this loss, R_{sh}/Q should be higher, frequency should be lower. When the SRF cavities are operated in CW mode at moderate accelerating gradients, there will be a significant RF power dissipation on the cavity walls and hence a considerable amount of cryogenic load. The cavity shape is required to be optimized to increase the shunt impedance, thereby reducing the cryogenic load. The selection of operating frequency and temperature is influenced by the operating mode (CW or pulsed) of the cavity. It is necessary to carry out proper thermal analysis of cryo-module and also all cryogenic piping optimization.
- Accelerating gradient (E_{acc}): In order to achieve high accelerating gradient, the ratios $\frac{E_p}{E_{acc}}, \frac{B_p}{E_{acc}}$ both should be minimized. However, achieving lower values for both the ratios simultaneously are contradictory and should be properly optimized and traded-off.
- Velocity acceptance**:** In order to achieve large velocity acceptance, number of cells of a multicell cavity has to be minimized and the frequency should be lowered.
- Frequency control: In order to achieve proper frequency control, the cavity should have low sensitivity to microphonics and also low energy content.During acceleration with low beam power, it is desirable to maximize external quality factor (Q_{ext}) to reduce the RF power requirement. The limiting effect of microphonic noise can be reduced by careful mechanical design of the cryomodule and use of special feedbacks.
- Beam acceptance: In order to achieve large beam acceptance, large aperture should be provided for transverse acceptance and the operating frequency should be low for the longitudinal acceptance. In order to preserve beam emittance, unwanted interaction of the beam with higher order modes (HOMs) has to be reduced.

- In high current operation, the active part of heavy beam loading of the accelerating structure is responsible for high power demand, while the reactive part should be compensated by appropriate detuning of the cavity (with proper tuner design) or can be dealt with RF feedback control loops or both.

Properties of cavity**:**

The performance of superconducting cavities in various applications depends on some basic properties of cavity. In this section, TM-class cavity design in the medium-β region will be discussed thoroughly.

Peak surface electric field(E_{pk}) :

It is always necessary to minimize the ratio of peak surface electric field (E_{pk}) to the accelerating electric field (E_{acc}) gradient in the superconducting accelerating cavity structure. For TM-class cavity structure, the typical value of $\frac{E_{pk}}{E_{acc}}$ is around $2.7-3.0$ for the medium-β ($0.6 \leq \beta \leq 0.7$) structure and the surface electric field is maximum at the Iris.

Peak surface magnetic field (B_{pk}):

It is also necessary to minimize the ratio of peak surface magnetic field (B_{pk}) to the accelerating electric field (E_{acc}) gradient in the superconducting accelerating cavity structure. For TM-class cavity structure, the typical value of $\frac{B_{pk}}{E_{acc}}$ is around $4.7-6.0$ mT/(MV/m) for the medium-β ($0.6 \leq \beta \leq 0.7$) structure and the peak surface magnetic field occurs at the equator region.

Geometrical Factor (G=Q.R_s):

This is the product of quality factor (Q) and the surface resistance (R_s) of the cavity. The Q-factor is a dimensionless quantity and the unit of surface resistance is Ohm (Ω). The geometrical factor (G) of the cavity does not depend on the size of the cavity and the material (niobium or copper etc.). However, *'G'* depends on the shape or the geometry of the cavity structure.

The surface current in the cavity is proportional to the magnetic field intensity (H) and the power dissipated per unit area $\left(\frac{dP_d}{ds}\right)$ in the cavity is given below.

$$\frac{dP_d}{ds} = \frac{1}{2} R_s |H|^2$$

[where, R_s is the RF surface resistance of the cavity material, P_d is the power dissipation, 's' is the surface]

$$dP_d = \frac{1}{2} R_s |H|^2 .ds$$

Integrating both sides, we get the surface integral as follows.

$$P_d = \frac{1}{2} R_s \iint_s |H|^2 \, ds$$

As the time averaged energy in the electric field is equal to that in the magnetic field inside the cavity, the stored energy (U) can be written as follows in the form of volume integral [40] [42].

$$U = \frac{1}{2} \mu_0 \iiint_V |H|^2 \, dV = \frac{1}{2} \varepsilon_0 \iiint_V |E|^2 \, dV$$

The quality factor (Q) of a cavity structure is defined as 2π times the ratio of the energy stored (U) inside the cavity to the power dissipated (P_d) per cycle in the cavity.

$$Q = \frac{\omega_0 U}{P_d} = \frac{\omega_0 \mu_0 \iiint_V |H|^2 \, dV}{R_s \iint_s |H|^2 \, ds} = \frac{G}{R_s}$$

[Where, $\omega_0 = 2\pi f_0$, f_0 is the fundamental cavity resonant frequency]

$$G = \frac{\omega_0 \mu_0 \iiint_V |H|^2 \, dV}{\iint_s |H|^2 \, ds} = Q R_s$$

Shunt impedance(R_{sh}):

The shunt impedance of cavity is an important figure of merit. It is a measure of the RF power dissipation and of the efficiency of the cavity structure. The shunt impedance determines the quantity of acceleration particle gets for a given RF power dissipation.

$$R_{sh} = \frac{{V_{acc}}^2}{2P_c} \qquad \text{[where, } V_{acc} \text{ is the peak cavity accelerating voltage]}$$

In SRF cavity structure, the shunt impedance directly influences the cryogenic load. The higher the shunt impedance, the lower is the cryogenic load. R_{sh} is material-dependent parameter. It can be made independent of material by multiplying with the surface resistance(R_s). So, $R_{sh}.R_s\left(= \frac{R_{sh}}{Q}.QR_s\right)$ is a material-independent parameter, which depends only on the shape of the cavity structure, not on the size.

Specific or geometric shunt impedance(R_{sh}/Q):

The ratio of the shunt impedance to the Q-factor of a cavity is an important figure of merit which also depends only on the shape of the cavity. It does not depend on the size or the material of the cavity fabricated with. In TM class cavity, the specific shunt impedance (R_{sh}-over-Q or sometimes called R-over-Q) is proportional to the number of cells and therefore, it is written in 'Ω per cell' unit. R_{sh}/Q relates to the integrated voltage developed along a given path (usually the axis) to the energy required to produce the voltage. At parallel resonance condition, the cavity impedance is resistive since the inductive and capacitive reactances cancel. The simple relations are given below.

$$P = \frac{1}{2}.\frac{V^2}{R_{sh}}; \qquad Q = \frac{\omega.U}{P};$$

$$\frac{R_{sh}}{Q} = \frac{V^2}{2.\omega.U}; \qquad U = \int_V \frac{\varepsilon.E^2}{2} dV;$$

The voltage (V) for the resonant cavity can be defined as the integral of the axial electric field (Ez) at r = 0.

$$\frac{R_{sh}}{Q} = \frac{\left(\int_{-\infty}^{\infty} |E_z|\, dz\right)^2}{2.\,\omega.\,U} = \frac{|V|^2}{2.\,\omega.\,U}$$

<u>Stored energy</u>(U):

The effect of the stored energy is already included in the previous paragraphs. It has importance in the low current applications, like, Radio Isotope Accelerators (RIA). When the beam loading is negligible, the quantity of RF power (P) involved in phase stabilizing [66] a structure at a given electric field gradient with a given amount of detuning (due to microphonics) is given by the product of the stored energy (U) and detuning $\left(\Delta f = \frac{\Delta\omega}{2\pi}\right)$. When phase stabilization is obtained by negative feedback the RF power that needs to be available from the RF source is as follows.

$$P = U.\,\Delta\omega$$

When stabilization is obtained through an externally controlled reactance the amount of reactive RF power must be switched or controlled as given by the following relation [67].

$$P = 4.\,U.\,\Delta\omega$$

The stored energy is proportional to the number of cells. It also depends on the electric field gradient (E) and frequency (*f*) as given in the following relation.

$$U \propto \frac{E^2}{f^3}$$

For TM class cavities, the stored energy is proportional to β (up to a certain value of β) and as β is reduced, the linear relation with β does not follow. Hence, TM structure becomes less and less efficient at generating on-axis field from fields at the iris diameter. The stored energy at constant accelerating gradient is roughly independent of β and may even increase as β decreases below 0.5. A typical value of stored energy for the proposed 5-cell cavity (for

Indian SNS/ Fermilab Proton Improvement Plan (PIP-II) operating at 650 MHz, β = 0.61, will be 118 Joule for accelerating gradient 17 MV/m.

<u>Multi-cell cavity modes & Cell-to-cell coupling</u>**:**

A multi-cell cavity can oscillate at different modes with different frequencies. The fields in the adjacent cells can have the same directions (for 0-mode) or opposite directions (for π-mode). The difference in frequencies of two modes is larger if the coupling between cells is stronger. The cell-to-cell coupling is characterized by the coupling coefficient (k_c) as given by the following relation [39][68].

$$k_c = 2.\frac{f_\pi - f_0}{f_\pi + f_0}.100\%$$

[where, f_π and f_0 are π-mode and 0-mode frequencies respectively].

In case of TM-class cavity structure, the cell-to-cell coupling takes place due to the penetration of electric field through iris holes. If iris diameter is increased, more electric field lines penetrate through iris holes and cell-to-cell coupling is increased. But at the same time, the peak surface electric field is increased near the iris region. This is of course undesirable. For this reason, to minimize the peak surface electric field, cell-to-cell coupling is kept within 2 – 3% or even less. In case of medium-β region, the small value of cell-to-cell coupling gives rise to higher sensitivity of the field flatness due to mechanical deformation. As the coupling is small, it is of the order of the perturbation caused in the end-cells by the beam. So, in order to achieve better field flatness near the end-cells, one has to modify the end-cell design.